PROGRAMA DE DOCTORADO EN INGENIERÍA QUÍMICA, DE LA ENERGÍA Y DE PROCESOS

TESIS DOCTORAL

MICRODISPOSITIVOS MAGNETOFORÉTICOS PARA LA ELIMINACIÓN DE LIPOPOLISACÁRIDOS DE LA SANGRE: DISEÑO MEDIANTE TÉCNICAS DE SIMULACIÓN AVANZADA

PhD THESIS

MAGNETOPHORETIC MICRODEVICES FOR LIPOPOLYSACCHARIDE REMOVAL FROM BLOOD: DESIGN THROUGH ADVANCED SIMULATION TECHNIQUES

AUTOR

Cristina González fernández

DIRECTORES

Prof. Dra. Inmaculada Ortiz Uribe

Dr. Eugenio bringas elizalde

UNIVERSIDAD DE CANTABRIA

Escuela de Doctorado de la Universidad de Cantabria

Santander 2022

UNIVERSIDAD DE CANTABRIA

ESCUELA DE DOCTORADO DE LA UNIVERSIDAD DE CANTABRIA

Doctorado en Ingeniería Química, de la Energía y de Procesos

MAGNETOPHORETIC MICRODEVICES FOR LIPOPOLYSACCHARIDE REMOVAL FROM BLOOD: DESIGN THROUGH ADVANCED SIMULATION TECHNIQUES

Microdispositivos magnetoforéticos para la eliminación de lipopolisacáridos de la sangre: diseño mediante técnicas de simulación avanzada

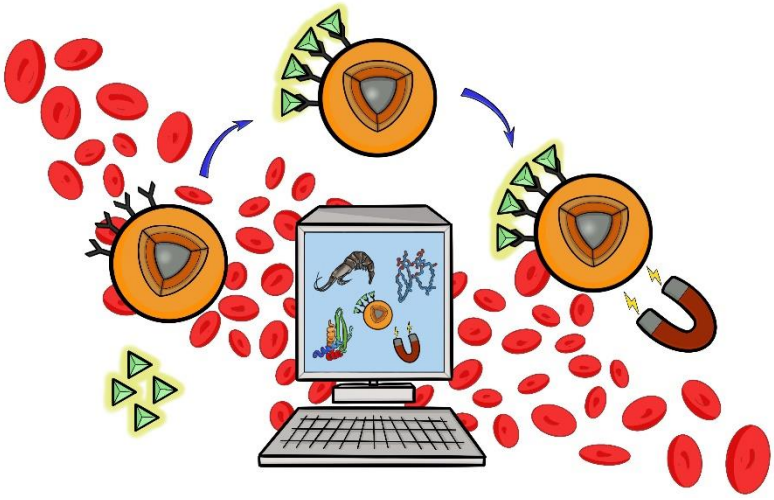

Cristina González Fernández

Dirigida por:
Prof. Dra. Inmaculada Ortiz Uribe
Dr. Eugenio Bringas Elizalde

Santander, 2022

UNIVERSIDAD DE CANTABRIA

ESCUELA DE DOCTORADO DE LA UNIVERSIDAD DE CANTABRIA

PROGRAMA DE DOCTORADO EN

INGENIERÍA QUÍMICA, DE LA ENERGÍA Y DE PROCESOS

MAGNETOPHORETIC MICRODEVICES FOR LIPOPOLYSACCHARIDE REMOVAL FROM BLOOD: DESIGN THROUGH ADVANCED SIMULATION TECHNIQUES

Microdispositivos magnetoforéticos para la eliminación de lipopolisacáridos de la sangre: diseño mediante técnicas de simulación avanzada

Memoria de Tesis Doctoral presentada al título de Doctora por la Universidad de Cantabria

Cristina González Fernández

Dirigida por:
Prof. Dra. Inmaculada Ortiz Uribe
Dr. Eugenio Bringas Elizalde

Santander, 2022

The research described in this dissertation was conducted at the Advanced Separation Processes research group of the Department of Chemical and Biomolecular Engineering at the University of Cantabria. This research was financially supported by the Spanish Ministry of Economy and Competitiveness and the Spanish Ministry of Science, Innovation and Universities through the R&D projects CTQ2015-66078-R and RTI2018-093310-B-I00, respectively.

Cristina González Fernández thanks the Concepción Arenal (granted by resolution December 19, 2017) and the FPU (FPU18/03525) postgraduate research grants from the University of Cantabria and the Spanish Ministry of Science, Innovation and Universities, respectively for the financial support. Additionally, the predoctoral mobility grant for short stays from the University of Cantabria (granted by resolution of May 20, 2019) is gratefully acknowledged.

Cristina González Fernández also thanks the web-based tool BioRender for facilitating the creation of several figures included in this dissertation.

A mis abuelos,
Cristina y Miguel

AGRADECIMIENTOS

A lo largo de estos años han sido muchas las personas tanto del ámbito laboral como personal que han contribuido de una u otra manera a la realización de la presente tesis doctoral. Una vez que el trabajo más complejo ya está realizado, es momento de expresar mi más sincero agradecimiento a todas ellas, ya que sin su granito de arena este trabajo no hubiera sido posible.

En primer lugar, quiero agradecer a mis directores de tesis, la Prof. Dra. Inmaculada Ortiz y el Dr. Eugenio Bringas. A pesar de que esta tesis nos ha dado más de un quebradero de cabeza, siempre habéis confiado en mí y me habéis valorado y animado a seguir adelante. Inma, ha sido un auténtico placer trabajar bajo tu supervisión. Muchas gracias por tu constancia y dedicación, pero sobre todo por enseñarme que "el gerundio de conseguir es insistiendo". Eugenio, me ha encantado aprender de tu experiencia y consejos. Muchas gracias por contar conmigo, por tu motivación, orientación y apoyo, especialmente en los momentos de mayor debilidad.

También quiero dar las gracias a los directores, profesores y personal técnico y de administración del Departamento de Ingenierías Química y Biomolecular por su ayuda y apoyo durante estos años. En especial, me gustaría agradecer a la Prof. Dra. Raquel Ibáñez y a la Dra. María Fresnedo San Román por transmitirme su experiencia como profesoras de la asignatura de experimentación y por hacerme sentir una más, a pesar de la evidente diferencia de conocimiento que nos separa.

Al Prof. Dr. Gabriel Moncalián, por acogerme en su laboratorio y poner a mi disposición todos los medios disponibles para sacar adelante mi investigación. Gracias por toda tu ayuda y esfuerzo.

También me gustaría agradecer al Prof. Dr. Felipe Jiménez Blas por toda su ayuda para iniciarme en las simulaciones de dinámica molecular. Muchas gracias por tu familiaridad, predisposición y apoyo. Del mismo modo, gracias a los compañeros del grupo de "Física de Líquidos Complejos", Jesús, Paula, José Manuel y María por los buenos ratos y por hacerme sentir como en casa en tierras onubenses.

I would like to thank Prof. Chris Oostenbrink for offering me the great opportunity to learn from his experience and collaborate with him. To all colleagues from BOKU for their patience and assistance.

A todos los compañeros que me han acompañado durante estos años, en especial a los que han formado parte del 335-H. A Sophie, Carmen y Carolina, gracias por vuestra generosidad, buen humor y por los ratucos que hemos pasado. A Gema, porque siempre estás ahí para echarnos una mano.

Sin duda alguna y a pesar de toda la gente que he podido conocer durante estos años, hay dos personas, mis "comums", que merecen una mención especial. A Lauri, has sido una compañera excepcional. Gracias por animarme, entenderme, y por aquellas largas conversaciones que solucionaban todos los problemas. A Jeny, sabes que siempre ha sido y seguirá siendo un honor ser tu padawan. Gracias por todo lo que me has enseñado, tanto en lo laboral como en lo personal, eres un auténtico ejemplo de superación y valentía. Muchas gracias a las dos porque sé que siempre estáis dispuestas a ayudar con la mejor de las intenciones. También me gustaría aprovechar para agradecer a nuestra tabla de salvación en más de una ocasión, quien combina los "bombazos" con "paramount" de la mejor de las maneras, Ioannis, y por supuesto, a la última incorporación, mi Uly.

A "Las de siempre", las que hemos sobrevivido desde los inicios. Sandra, hace ya unos cuantos años que nos disfrazamos en la guardería. Gracias por tu humor que siempre nos saca unas cuantas sonrisas. A Cris, por ser la que nos mantiene unidas, por preocuparte por mí en estos últimos tiempos y por hacer que me guste "un poco más" hacer rutas por el monte. A Pili, a la que le gustan las rutas tanto como a mí, la que siempre saca un rato para quedar y la que me ayudó a "cruzar el río" (aunque sin mucho éxito dada mi torpeza). A la Marquesa del grupo, la mejor compañera de piso que se puede tener, inigualable descubridora de canciones y una excelente guía turística (aunque en alguna ocasión hayas puesto en riesgo mi vida). Muchas gracias Marina por estar siempre ahí. Gracias a todas por los buenos ratos que hemos pasado juntas… y los que nos quedan!

Al primo Antonio y a la prima Charo por haber estado presentes en mis momentos más importantes, por enseñarme a bailar sevillanas y enviarme los trajes de flamenca "recién salidos de la romería" para poder demostrar en tierras cántabras cómo se bailan de verdad las sevillanas.

Gracias por hacernos sentir que no hay tanta distancia entre El Rompido y el norte.

Si hay alguien a quien tengo que agradecer porque desde luego sin ellos nada de esto hubiera sido posible es a mi familia. A mis padres, Begoña y Manuel, por vuestro esfuerzo, cariño, comprensión y apoyo incondicional. Siempre habéis confiado en mí, me habéis ayudado a ver el lado positivo de las cosas y me habéis hecho sentir que no tenía límites. Gracias por haber sido partícipes de cada uno de los pequeños pasos que he dado, sois mi ejemplo a seguir. A mis tíos, Cristina y Ramón, por estar siempre pendientes y dispuestos a ayudarme. A mi primo Adrián, un hermano, por los consejos y alguna que otra reprimenda, pero sobre todo por estar siempre para lo que necesite. A mis abuelos, Cristina y Miguel, a quienes dedico esta tesis, os lo merecéis. Muchísimas gracias por darme valiosas lecciones entre refranes y quehaceres diarios y por estar siempre conmigo por muy lejos que estéis. Sois nuestro pilar fundamental, nuestro mayor tesoro, y un ejemplo de esfuerzo y sacrificio. ¡Esta tesis es vuestra!

Cristina

Santander, 2022

TABLE OF CONTENTS

LIST OF FIGURES

LIST OF TABLES

ABSTRACT

Lipopolysaccharide (LPS or endotoxin) is the primary component of the outer leaflet of Gram-negative bacterial outer membranes. LPS elicits an overwhelming immune response during infection, which can lead to life-threatening sepsis for which no suitable treatment is available so far. As a result of the worldwide expanding antibiotic resistant bacteria, the occurrence and frequency of sepsis is expected to increase; thus, there is an urge to develop novel strategies for treating bacterial infections. In this regard, the use of affinity sorbents has been recognized as a promising strategy for the capture and removal of toxic agents (i.e., bacterial LPS) from blood, that eventually could be applied in treatment therapies. Hence, the use of functionalized magnetic micro- or nanoparticles as LPS sequestration agents offers outstanding possibilities. More specifically, extracorporeal blood detoxification using functionalized magnetic beads comprises two steps: firstly, the target LPS is captured by the biotargeting agent that decorates the beads surface, and subsequently, the LPS-bead complexes are magnetically recovered in a second stage. This process can be carried out in microfluidic devices, thus taking advantage of the unique features of microfluidics. Thereby, the coupling of both functionalized magnetic beads and microfluidics gives rise to the development of magnetic cleansing microdevices (MCMDs).

This doctoral dissertation is focused on advancing in the rational design of MCMDs to promote their successful implementation for capturing endotoxins as part of blood detoxification alternatives. Specifically, two key challenges for the development of MCMDs have been addressed. Hence, progress on the design of biotargeting agents able to capture LPS with high affinity has been made, and the optimization of the magnetic recovery stage in order to enhance its efficiency has been tackled. For performing such investigation, advanced simulation techniques, namely molecular dynamics (MD) and computational fluid dynamics (CFD), have been employed.

From the different (bio)molecules that can interact with bacterial LPS, anti-LPS factors (ALFs) have been recognized as potential candidates to develop therapeutics against sepsis. In this dissertation, the ALF from the black tiger shrimp *Penaeus monodon* (ALFPm3) has been selected for designing biotargeting agents that capture with high affinity the endotoxin.

For that purpose, understanding how ALFPm3 and lipid A (the constituent of LPS that harbors its endotoxic principle) interact is of paramount importance. In this regard, MD is used as a computational microscope since it provides atomistic insights into the molecular system of interest. Thereby, the interaction mechanism between ALFPm3 and lipid A, as well as their binding mode and the key ALFPm3 residues involved in the interaction have been *in silico* identified for the first time. In order to further confirm the predicted insights, *in silico* results were validated *in vitro*.

Besides, the optimization of the magnetic recovery stage was addressed through CFD simulations so that systems that provide complete bead capture while processing relatively high blood flow rates could be developed. For enhancing the performance of continuous-flow magnetophoretic microseparators (CMMSs), two tactics were pursued. The first strategy involved the optimization of the microchannel geometrical features (namely, cross section shape, thickness, length and volume). Once the microchannel geometry that yielded entire particle recovery and high volumetric throughput simultaneously was identified, the second strategy, which consisted of increasing the magnetic gradient exerted on the particles by selecting a more appropriate magnet arrangement, was tackled.

Collectively, the methodology herein provided, combining MD and CFD simulations as predictive tools, has proven valuable to move forward in the design of MCMDs for contributing to blood detoxification alternatives. It can be considered that this methodology, along with the insights derived from this work, paves the way to the development of MCMDs in their application to endotoxins capture as part of innovative sepsis treatments, thus contributing to the fight against antibiotic resistance.

RESUMEN

El lipopolisacárido (LPS o endotoxina) es el principal componente de la membrana externa de las bacterias Gram negativas. El LPS desencadena una respuesta inmune abrumadora durante la infección, que puede conducir a una sepsis potencialmente mortal, para la que no se dispone de un tratamiento adecuado hasta la fecha. Debido a la expansión a nivel mundial de las bacterias resistentes a antibióticos, es esperable que la ocurrencia y frecuencia de la sepsis aumenten. Por tanto, urge desarrollar nuevas estrategias para tratar infecciones bacterianas. En este sentido, el uso de adsorbentes se concibe como una estrategia prometedora para la captura y eliminación de agentes tóxicos (es decir, el LPS) de la sangre, posibilitando su uso final en terapia clínica. Por ello, el uso de micro- o nanopartículas magnéticas funcionalizadas como agentes de captura del LPS ofrece posibilidades excepcionales. Concretamente, la detoxificación de la sangre utilizando partículas magnéticas funcionalizadas comprende dos etapas: en primer lugar, la molécula que decora la superficie de las partículas captura al LPS objetivo y, posteriormente, se recuperan magnéticamente los complejos LPS-partícula en una segunda etapa. Este proceso se puede llevar a cabo en dispositivos microfluídicos, aprovechando así las características exclusivas de la microfluídica. De esta manera, el acoplamiento de la acción secuestrante de las partículas magnéticas funcionalizadas y la microfluídica da lugar al desarrollo de novedosos microdispositivos magnetoforéticos (MCMDs por sus siglas en inglés) para la captura de endotoxinas.

La presente tesis doctoral se centra en avanzar en el diseño racional de MCMDs para fomentar su exitosa implementación con la finalidad de llevar a cabo la captura de endotoxinas como parte de las alternativas de detoxificación sanguínea. Específicamente, se han abordado dos retos clave del desarrollo de los MCMDs. Por una parte, se ha progresado en el diseño de moléculas capaces de captar con elevada afinidad al LPS y, por otra, se ha abordado la optimización de la etapa de recuperación magnética. Para llevar a cabo esta investigación, se han utilizado técnicas de simulación avanzada, concretamente dinámica molecular y dinámica de fluidos computacional (MD y CFD respectivamente por sus siglas en inglés).

De las diferentes (bio)moléculas que pueden interaccionar con el LPS, las proteínas anti-LPS son concebidas como potenciales candidatas para

desarrollar terapias para combatir la sepsis. En esta tesis, se ha seleccionado la proteína anti-LPS procedente del langostino *Penaeus monodon* (ALFPm3) para diseñar moléculas que capturen con elevada afinidad a la endotoxina. Para este propósito, entender cómo interaccionan ALFPm3 con el lípido A (el componente del LPS que alberga su principio endotóxico) es de suma importancia. En este sentido, se ha utilizado la MD como un microscopio computacional, ya que proporciona detalles a nivel atómico de los sistemas moleculares de interés. De este modo, se ha identificado por primera vez *in silico* el mecanismo de interacción entre el ALFPm3 y el lípido A, así como su modo de unión y los residuos de ALFPm3 involucrados en la interacción. A fin de confirmar los resultados obtenidos *in silico*, estos se validaron *in vitro*.

Por otro lado, se abordó la optimización de la etapa de recuperación magnética mediante simulaciones CFD con el objetivo de desarrollar sistemas que proporcionen una recuperación completa de las partículas mientras procesan caudales relativamente altos de sangre. Para mejorar el rendimiento de los microseparadores magnetoforéticos de flujo continuo (CMMSs por sus siglas en inglés) se siguieron dos estrategias. En primer lugar, se llevó a cabo la optimización de las características geométricas del microcanal (es decir, forma de la sección transversal, espesor, longitud y volumen). Una vez identificada la geometría del microcanal de proporciona simultáneamente la recuperación completa de partículas y rendimientos volumétricos elevados, se abordó la segunda estrategia, que consistió en aumentar el gradiente magnético ejercido a las partículas mediante la selección de una disposición de imanes más adecuada.

En conclusión, la metodología desarrollada en este trabajo combinando simulaciones MD y CFD como herramientas predictivas ha demostrado ser valiosa para avanzar en el diseño de MCMDs para llevar a cabo la captura de endotoxinas contenidas en la sangre. Esta metodología, junto con el conocimiento derivado de este trabajo, avanza en el desarrollo de MCMDs que puedan ser utilizados para la captura de endotoxinas como parte de tratamientos novedosos para la sepsis, contribuyendo así a la lucha frente a la resistencia antibiótica.

NOMENCLATURE

LATIN SYMBOLS

$\mathbf{a}_i$	Acceleration of particle i (Chaper 2) ($nm \cdot ps^{-2}$)
A_p	Particle cross sectional area (Chapter 3) (m^2)
B	Magnetic field induction (T)
b	Bond length (nm)
b_0	Bond length at equilibrium (nm)
B_0	Maximum field at the magnet pole tips (T)
$(BxH)_{max}$	Maximum energy product of the magnet ($kJ \cdot m^3$)
C6	Attractive Lennard-Jones parameter ($kJ \cdot mol^{-1} \cdot nm^6$)
C12	Repulsive Lennard-Jones parameter ($kJ \cdot mol^{-1} \cdot nm^{12}$)
C_D	Drag coefficient (-)
CL	Characteristic length of microchannels (m)
D_h	Hydraulic diameter of microchannels (Chapter 3) (m)
D_p	Particle diameter (Chapter 3) (m)
$\mathbf{F_{drag}}$	Drag force (N)
$\mathbf{F_{ext}}$	Total force (N)
$\lvert F_{ext} \rvert$	Magnitude of the total force (N)
$\mathbf{F_{hd}}$	Hydrodynamic force (N)
$\mathbf{F}_i$	Force acting on particle i (Chapter 2) ($kJ \cdot mol^{-1} \cdot nm^{-1}$)
$\mathbf{F_m}$	Magnetic force (N)
$\mathbf{F_p}$	Counter drag force (N)
H	Microchannel depth (m)
$\mathbf{H_a}$	Applied magnetic field ($A \cdot m^{-1}$)
$\lvert H_a \rvert$	Magnitude of the applied magnetic field ($A \cdot m^{-1}$)
IA	Interface area (nm^2)
J	Dimensionless number for magnetophoretic analysis (-)
k	Boltzmann's constant ($1.38 \cdot 10^{-23}$ $J \cdot K^{-1}$)
K_b	Bond force constant ($kJ \cdot mol^{-1} \cdot nm^{-2}$)
$K_{binding}$	Binding constant (M^{-1})
K_θ	Bond angle force constant ($kJ \cdot mol^{-1} \cdot degrees^2$)
K_ξ	Improper dihedral force constant ($kJ \cdot mol^{-1} \cdot degrees^{-2}$)

K_ϕ	Force constant of torsional dihedral interactions (kJ·mol^{-1})
L	Microchannel length (m)
m	Multiplicity (-)
M_{added}	Added mass (kg)
m_i	Mass of particle i (Chapter 2) (atomic mass units)
$\mathbf{M_{m,s}}$	Magnetization of the magnetic element (A·m^{-1})
m_p	Particle mass (Chapter 3) (kg)
$\mathbf{M_{s,p}}$	Particle saturation magnetization (A·m^{-1})
P	Pressure (Chapter 3) (Pa)
q_i	Charge of particle i (electron charge)
q_j	Charge of particle j (electron charge)
Re_p	Particle Reynolds number (-)
R_f	Fluidic resistance (Pa·s·m^3)
R_g	Ideal gas constant (8.31·10^{-3} kJ·mol^{-1}·K^{-1})
R_h	Hydraulic radius of microchannels (m)
$\mathbf{r}_i$	Position of every atom i (Chapter 2) (nm)
$\overline{\mathbf{r}_i}$	Atom coordinate mean (Chapter 2) (nm)
$\mathbf{r}_i^{ref}$	Position of every atom i in the reference structure (Chapter 2) (nm)
$\mathbf{r}_{ij}$	Distance between particles i and j (Chapter 2) (nm)
RMSD	Root mean square deviation (nm)
RMSF	Root mean square fluctuation (nm)
r_{NOE}	Effective distance sensed by the nuclear Overhauser effect (nm)
r_{NOE}^{exp}	Effective distance sensed by the nuclear Overhauser effect experimentally (nm)
r_{NOE}^{sim}	Effective distance sensed by the nuclear Overhauser effect in simulations (nm)
r_{out}	Outer QMS radius (m)
r_p	Particle radius (Chapter 3) (m)
r_{rod}	Rod radius of the QMS (m)
$SASA_{complex}$	Solvent accessible surface area of the ALFPm3-lipid A complex (nm^2)
$SASA_{lipid}$	Solvent accessible surface area of lipid A (nm^2)
$SASA_{protein}$	Solvent accessible surface area of ALFPm3 (nm^2)
Sep_y	Magnet-channel distance in y-direction
Sep_z	Magnet-channel distance in z-direction

T	Absolute temperatura (K)
t	Time (ps in Chapter 2 and s in Chapter 3)
t_m	Time required to the beads to travel from the upper to the lower channel wall perpendicularly to the flow direction (s)
t_{res}	Residence time (s)
t_{total}	Total Simulation time (Chapter 2) (ps)
U	Potential energy function ($kJ \cdot mol^{-1}$)
v	Fluid velocity vector ($m \cdot s^{-1}$)
V_{dead}	Dead volume of flow channel in the QMS (m^3)
$\mathbf{v}_i$	Velocity of particle i (Chapter 2) ($nm \cdot ps^{-1}$)
V_{magnet}	Volume of the Magnet arrangement (m^3)
V_p	Particle volumen (Chapter 3) (m^3)
$\mathbf{v}_p$	Particle Velocity vector ($m \cdot s^{-1}$)
V_{total}	Total volume of the QMS (m^3)
W	Microchannel width (m)
W_{min}	Minimum channel width (m)
x	Etching mask opening (m)

GREEK SYMBOLS

α	Weight coefficient for van der Waals interactions in the LIE method (-)
β	Weigh coefficient for electrostatic interactions in the LIE method (-)
δ	Phase shift (degrees)
ΔG_{bind}	Binding free energy ($kJ \cdot mol^{-1}$)
ΔG_{bind}^{elec}	Electrostatic contribution to the binding free energy ($kJ \cdot mol^{-1}$)
ΔG_{bind}^{vdw}	Van der Waals contribution to the binding free energy ($kJ \cdot mol^{-1}$)
Δt	Simulation time step (Chapter 2) (fs)
ε_0	Vacuum dielectric permittivity ($F \cdot m^{-1}$)
ε_1	Relative permittivity of the medium ($F \cdot m^{-1}$)
η	Fluid viscosity (Pa·s)
θ	Bond angle (Chapter 2) (degrees); dimensionless number for analyzing magnetophoresis and microchannel geometry (Chapter 3) (-)

θ_0	Bond angle at equilibrium (degrees)
μ_0	Permeability of free space ($4\pi \cdot 10^{-7}$ H·m^{-1})
ξ	Improper dihedral angle (degrees)
ξ_0	Improper dihedral angle at equilibrium (degrees)
ρ	Fluid density (kg·m^3)
$\boldsymbol{\tau}$	Shear stress (kg·m^{-1}·s^{-2})
ϕ	Dihedral angle (Chapter 2) (degrees) Exploitation of the magnetic energy (Chapter 3) (m·s^{-1}·kJ^{-1})
$\phi_{\mathrm{protein/LPS}}$	Protein/LPS ratio (-)
χ_f	Magnetic susceptibility of the particle (-)
χ_p	Magnetic susceptibility of the particle (-)
$\chi_{p,e}$	Magnetic effective susceptibility of the particle (-)

ABBREVIATIONS

AA-MD	All atom-molecular dynamics
ABF	Adaptive biasing force
ALFPm3	Anti-lipopolysaccharide factor from *Penaeus monodon*
ALFs	Anti-lipopolysaccharide factors
AMPs	Antimicrobial peptides
BPI	Bactericidal/permeability-increasing protein
CD14	Cluster of differenciation 14
CDC	Centers for Disease Control and Prevention
CFD	Computational fluid dynamics
CG-MD	Coarse-grained molecular dynamics
CMMSs	Continuous-flow magnetophoretic microseparators
CV	Column volumes
DNA	Deoxyribonucleic acid
DSSP	Dictionary of Secondary Structures of Proteins
DTT	Dithiothreitol
E. coli	*Escherichia coli*
EBI	European Bioinformatics Institute
ECDC	European Centre for Disease Prevention and Control
FF	Force field
FITC	Fluorescein isothiocyanate
FPLC	Fast protein liquid chromatography
Gn	Gentamycin
GPUs	Graphic processing units
Grace	GRaphing, Advanced Computation and Exploration of data
HREST	Hamiltonian replica-exchange with solute tempering
IM	Inner membrane
IMAC	Immobilized metal affinity chromatography
IPTG	Isopropyl β-D-1-thiogalactopyranoside
K37E-LALF	*Limulus* anti-lipopolysaccharide factor with the K37E substitution
KDO	3-deoxy-D-manno-oct-2-ulosonic acid
Kn	Kanamycin
l	Ligand

L. polyphemus	*Limulus polyphemus*
LALF	*Limulus* anti-lipopolysaccharide factor
LB	Luria-Bertani
LBP	Lipopolysaccharide-binding protein
LIE	Linear interaction energy
LPS	Lipopolysaccharide
MBP	Maltose binding protein
MCMDs	Magnetic cleansing microdevices
MD	Molecular dynamics
MD2	Myeloid differentiation factor 2
mDNA	Mutated deoxyribonucleic acid
mLALF	Mutated *Limulus* anti-lipopolysaccharide factor
MM	Molecular mechanics
MM-GBSA	Molecular mechanics generalized Born surface area
MM-PBSA	Molecular mechanics Poisson-Boltzman surface area
MOE	Molecular Operating Environment
N	Number of particles in the system (Chapter 2)
NMR	Nuclear magnetic resonance
NOE	Nuclear Overhauser effect
NPT	Constant number of particles, pressure and temperature
NTA	Nitriloacetic acid
OD	Optical density
OD_{600}	Optical density at a wavelength of 600 nm
OM	Outer membrane
p	Protein
P	Pressure
P. monodon	*Penaeus monodon*
PAMP	Pathogen associated molecular pattern
PBC	Periodic boundary conditions
PCR	Polymerase chain reaction
PDB	Protein Data Bank
PMB	Polymyxin B
PMMA	Poly (methyl methacrylate)
PMSF	Phenylmethylsulfonyl fluoride

PMX-F	Polymixyn B-immobilized fiber
QMS	Quadrupole magnetic sorter
R	Rectangular-shaped
R-LPS	Rough-lipopolysaccharide
RMSD	Root mean square deviation
RMSF	Root mean square fluctuation
SA	Simulated annealing
SAP	Spatial agreggation propensity
SASA	Solvent accesible surface area
SDM	Site-directed mutagenesis
SDS	Sodium dodecyl-sulfate
SDS-PAGE	Sodium dodecyl-sulfate polyacrylamide gel electrophoresis
SIB	Swiss Institute of Bioinformatics
SIE	Solvated interaction energy
S-LPS	Smooth-lipopolysaccharide
SMD	Steered molecuar dynamics
SN	Supernatant
SPC	Simple point charge
T	Temperature
T. tridentatus	*Tachypleus tridentatus*
TALF	*Tachypleus tridentatus* anti-lipopolyssaccharide factor
TIP4P	Transferable intermolecular potential 4P
TLR4	Toll-like receptor 4
U	U-shaped
US	Umbrella sampling
VMD	Visual Molecular Dynamics
WHAM	Weighted histogram analysis method
WHO	World Health Organization
WT	Wild-type
WT-DNA	Wild-type deoxyribonucleic acid
WT-LALF	Wild-type *Limulus* anti-lipopolysaccharide factor
Y47F-LALF	*Limulus* anti-lipopolysaccharide factor with the Y47F substitution

CHAPTER 1

Lipopolysaccharide: implications in Gram-negative bacterial infections

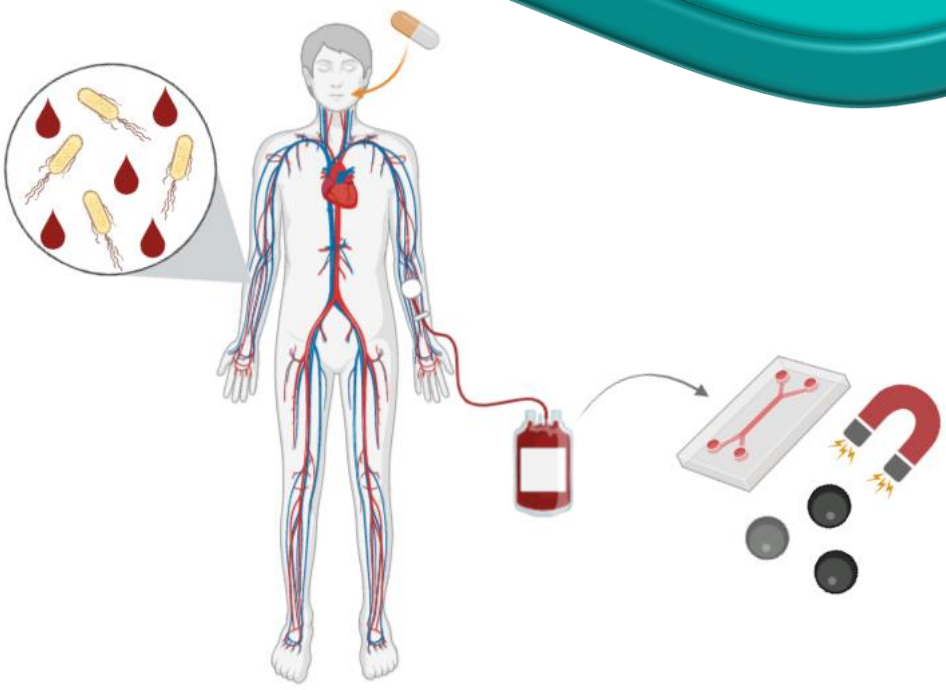

1.1. Gram-negative bacteria and lipopolysaccharides

In 1884, Hans Christian Gram developed a method in order to differentiate Gram-positive and Gram-negative bacteria, which was based on the use of a crystal violet-iodine complex and a safranin counter stain. According to this staining technique, Gram-positive bacteria stain violet or purple, while Gram-negative bacteria do not retain the stain, and thus they take a pink colour. This difference arises from the composition or the morphology of the cell wall in each bacterial type [1,2].

Gram-negative bacteria are characterized by the complex structure of their cell envelope. Thereby, contrary to Gram-positive bacteria, the cell envelope of Gram-negative bacteria is composed of two membranes, which differ in their structure and composition; these membranes are separated by the periplasm, an aqueous compartment that includes a peptidoglycan cell wall (Figure 1.1) [3–7]. The inner membrane (IM) is a symmetric bilayer that consists of phospholipids. Conversely, the outer membrane (OM), which represents the first line of defense from environmental threats in Gram-negative bacteria, is asymmetric; thus, the inner leaflet has the same phospholipid composition as the IM, whereas the outer leaflet is mainly composed of lipopolysaccharide (LPS) molecules [3,5,8–12]. LPS, also referred as endotoxin, is the major constituent of Gram-negative bacterial OM. LPS is an amphipathic molecule that consists of three domains, namely, lipid A, core oligosaccharide and O-antigen [4,9,13–17]. LPS molecules that comprise these three constituents are referred to as smooth LPS (S-LPS), whereas rough LPS (R-LPS) lacks the O-antigen and/or parts of the core oligosaccharide [9,15]. The lipid A moiety is the most conserved portion and also the main toxic constituent of LPS [13,17–19]; it consists of a β(1→6)-linked glucosamine disaccharide that generally bears several saturated fatty acids (from four to eight acyl tails), and is typically phosphorylated [3,5,15,16,18,20]. The core oligosaccharide is covalently attached to the glucosamines of lipid A; it presents a relatively conserved structure that comprises two regions, namely, the inner and outer cores, which are proximal and distal to lipid A, respectively. The inner core oligosaccharide incorporates at least one residue of 3-deoxy-D-manno-oct-2-ulosonic acid (KDO) and various heptoses, whereas the outer core oligosaccharide often comprises substituents, such as phosphate or 4-amino-4-deoxy-L-arabinose [5,6,15,16]. The O-antigen, which is linked to the core oligosaccharide, is the most variable

component of LPS. It is constituted of repeating oligosaccharide units (up to 40) made of three to eight sugar residues [4,5,15,20–22]. While lipid A is embedded in the outer leaflet of the bacterial OM and acts as a hydrophobic anchor for LPS to the OM, both the core oligosaccharide and the O-antigen are extended outwards [5,11,15].

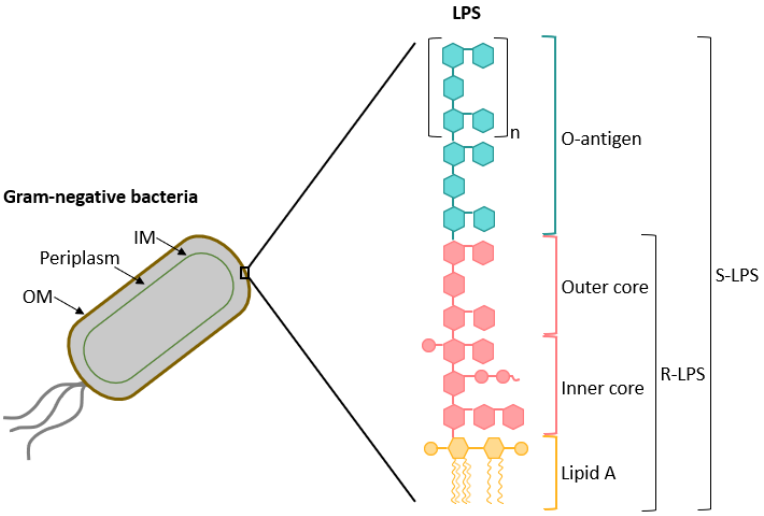

Figure 1.1. Cell envelop architecture and structure of LPS of Gram-negative bacteria.

Bacterial LPS is involved in several processes of pathophysiological relevance as it has been schematized in Figure 1.2 [4,17,23,24]. Specifically, LPS provides Gram-negative bacteria with an effective protective barrier against noxious substances, such as small molecules, antimicrobial peptides, or antibiotics (Figure 1.2a). Hence, LPS is the primary contributor to the resistance to antibiotics that Gram-negative bacteria display, which has become a major health threat globally [4,8,10,23–26]. On the other hand, LPS is a potent stimulator of the host immune system (Figure 1.2b). Particularly, LPS is a pathogen associated molecular pattern (PAMP) and thus it can be recognized by the mammalian innate immune system, which can initiate the eradication of the bacterial infection. Thereby, upon bacterial infection, LPS is recognized by the complex comprised of Toll-like receptor 4 (TLR4) and myeloid differentiation factor 2 (MD2); as a result of the LPS recognition, the TLR4-MD2 complex triggers a pro-inflammatory response in order to provide an immediate host defense against invading bacteria [4,13,27–29]. This

immune response is advantageous for fighting against the invading bacteria as long as it is controlled. However, uncontrolled activation of the immune system can lead to life-threatening sepsis [4,13,19,23,30,31]. As a result of the worldwide challenge of antibiotic resistance, occurrence and frequency of sepsis will predictably increase, which remains one of the major public health concerns of the 21st century [27,32].

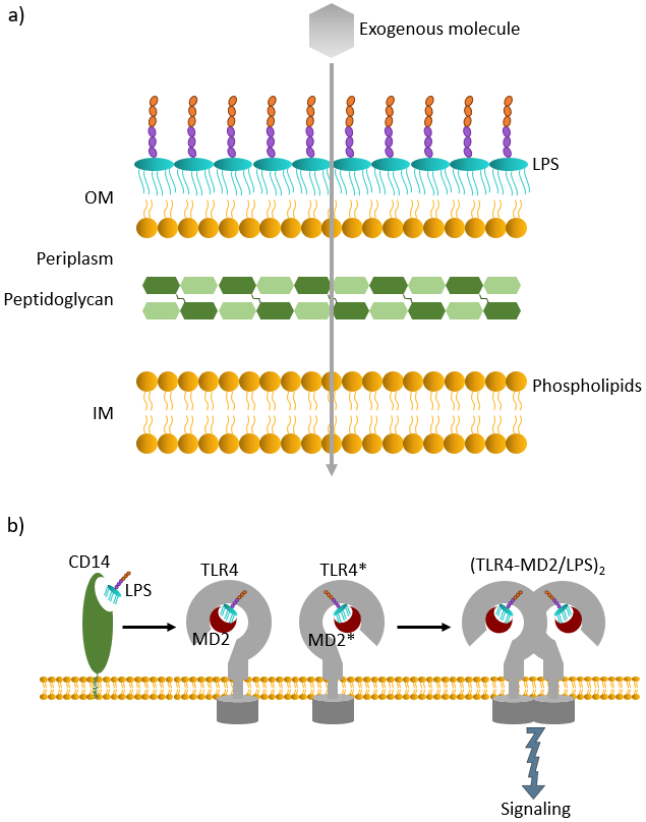

Figure 1.2. Schematic illustrating the two major LPS functions, namely (a) barrier, and (b) immunostimulatory.

1.2. The challenge of antibiotic resistance

1.2.1. Overview

The beginning of the modern era of antibiotics is generally identified with Paul Ehrlich and Alexander Fleming, who made important contributions to antibiotic research in the 1900s. Since then, a variety of antibiotics has been developed, thus revolutionizing medicine and enhancing human health and well-being [33–35]. Particularly, antibiotics have outstandingly contributed to the control of infectious diseases; thereby, their ability for treating infections has yielded a considerable mortality reduction, lifespan lengthening, and an enhancement of life quality [33,34]. Therefore, antibiotics have been recognized as one of the most valuable discoveries of the 20th century [36].

Unfortunately, the misuse of antibiotics has led to the rapid and extensive development of antibiotic resistance in Gram-negative bacteria, which renders antibiotic ineffective. Antibiotic resistance takes place when bacteria are able to defeat the effect of antibiotics; hence, they are not killed, and their growth is not inhibited [33,37–39]. Gram-negative bacteria have evolved different strategies for increasing their viability within the host, such as the use of efflux pumps to extrude antibiotics, or the introduction of modifications to LPS structure [33,40–44]. For example, in *Salmonella enterica*, the remodeling of the LPS structure is accomplished through the PhoPQ two-component regulatory system and involves the addition of a hydroxyl group, a positively charged aminoarabinose and a palmitoyl chain to the lipid A moiety; these modifications result in a stronger impermeability of the OM [42,43]. From the growing list of antibiotic resistant bacteria, the so-called "ESKAPE" pathogens (*Enterococcus faecium*, *Staphylococcus aureus*, *Kblebsiella pneumoniae*, *Acinetobacter baumannii*, *Pseudomonas aeruginosa* and *Enterobacter* species) exhibit noticeable levels of antibiotic resistance and are associated with significant morbidity and mortality. It is worth mentioning that four out of six "ESKAPE" pathogens are Gram-negative bacteria [33,45,46].

The fact that bacteria fail to respond to conventional antibiotics makes challenging the treatment of infections; hence, the frequency and occurrence of sepsis, which remains the primary cause of death from infection, will predictably increase. Thus, the emergence of antibiotic resistance has

become one of the greatest threats to public health globally [27,33,47,48]. According to the Centers for Disease Control and Prevention (CDC), the number of antibiotic-resistant infections in the United States exceeds 2.8 million every year, which leads to more than 35,000 deaths [49]. On the other hand, the European Centre for Disease Prevention and Control (ECDC) declared that in the European Union/European Economic Area, over 670,000 infections caused by antibiotic bacteria resistant are reported each year, with approximately 33,000 people dying as a result of the infection. The World Health Organization (WHO) has long recognized the urgency of a global effort in order to fight against the worldwide expanding antimicrobial resistance (i.e., the resistance of bacteria, viruses, fungi and parasites to an antimicrobial agent to which they were originally sensitive) [50,51]. In this regard, WHO published in 2014 the report "Antimicrobial Resistance: Global Report on Surveillance", where they elucidated the extent of the phenomena of antimicrobial resistance in several parts of the world and the existence of huge gaps in the surveillance [52]. Additionally, they claimed that the problem of antimicrobial resistance is "so serious that it threatens the achievements of modern medicine. A post-antibiotic era—in which common infections and minor injuries can kill—far from being an apocalyptic fantasy, is instead a very real possibility for the 21st century".

In view of this serious threat to human health, there is an urge to develop alternatives to conventional antibiotics for successfully treating Gram-negative bacterial infections and sepsis. In the following section, novel strategies that are currently being investigated to address this global concern are reported and discussed.

1.2.2. Strategies for treating LPS-caused infections

The scientific community has devoted great effort to the development of novel tactics in order to fight against the challenge of treating Gram-negative bacterial infections and sepsis [48]. Depending on the purpose of these strategies, they could be classified as approaches that target LPS and those that target the host. Strategies targeting the host rather than bacterial LPS include immunomodulatory therapies, such as vaccination or the use of immunomodulatory approaches [48,53]. Special attention has received the discovery of immunomodulatory molecules that act as TLR4 antagonists inhibiting TLR4 signalling by competing with LPS in the binding to MD2 (Figure

1.3) [27,28]. On the other hand, strategies targeting LPS encompass the development of antibacterial agents able to either circumvent the LPS defenses provided to the bacterial OM or disrupt LPS synthesis, since LPS truncation entails an increase of the sensitivity of bacteria towards hydrophobic antibiotics [3,54,55]. This group also comprises the systems for extracorporeal LPS sequestration using affinity sorbents, which have immobilized molecules that exhibit high affinity towards the endotoxin [16,56,57].

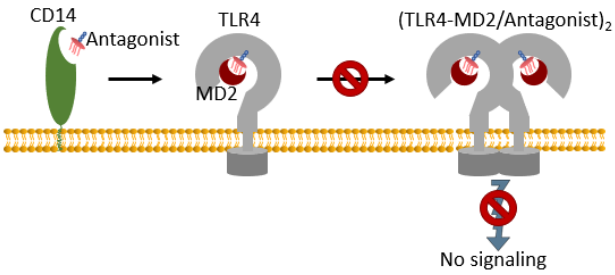

Figure 1.3. Overview of the inhibition of TLR4-MD2 signaling by antagonistic molecules.

It has been noticed that pathogen load in blood outstandingly contributes to both the severity of the disease and the mortality in patients with sepsis. Since the removal of the disease-causing agent (i.e., bacterial LPS) from blood could be understood as the most direct cure, the use of affinity sorbents for extracorporeal LPS sequestration represents a promising approach for treating sepsis [58,59]. In this regard, Toraymyxin® (Toray Industries, Tokyo Kapan), a polymyxin B (PMB)-based extracorporeal hemoperfusion cartridge, is presumably one of the most widely known systems based on affinity sorbents for extracorporeal blood cleansing. It contains polystyrene-derivative fibers (PMX-F) where PMB is covalently immobilized. Thereby, PMB binds with the lipid A constituent of LPS, which results in the adsorption and subsequent removal of endotoxin from blood. Toraymixyn® was developed in Japan, where it has been widely used for treating sepsis or septic shock since 1994 [57,60–62]. Despite the potential of this device, the use of PMB poses several health hazards due to its high nephro- and neurotoxicity. This fact, along with other possible side effects, supports the limited use of Toraymixyn® outside Japan [16,61,63]. In light of these drawbacks, developing systems for blood detoxification based on

affinity sorbents, capable of efficiently removing endotoxins from blood while ensuring a safe operation, is of paramount importance. The use of functionalized magnetic beads as LPS sequestration agents offers outstanding possibilities for developing extracorporeal blood cleansing systems that fulfil these challenges, viz. efficient endotoxin sequestration and reduced adverse side effects [64,65].

Extracorporeal blood detoxification using functionalized magnetic beads consists of a two-stage process, as it has been illustrated in Figure 1.4. In the first stage, the beads are contacted with the poisoned blood taken from the patient. Thereby, the functionalization molecule that decorates the beads surface captures the target endotoxin with high affinity and selectivity, which results in the formation of LPS-bead complexes. Then, these LPS-bead complexes are magnetically recovered from the blood in the second stage. Subsequently, the consequential endotoxin- and beads-free blood solution is returned to the circulatory system of the patient. Thereby, this strategy enables the recovery of non-magnetic substances, as bacterial LPS, through magnetic means [58,64,65].

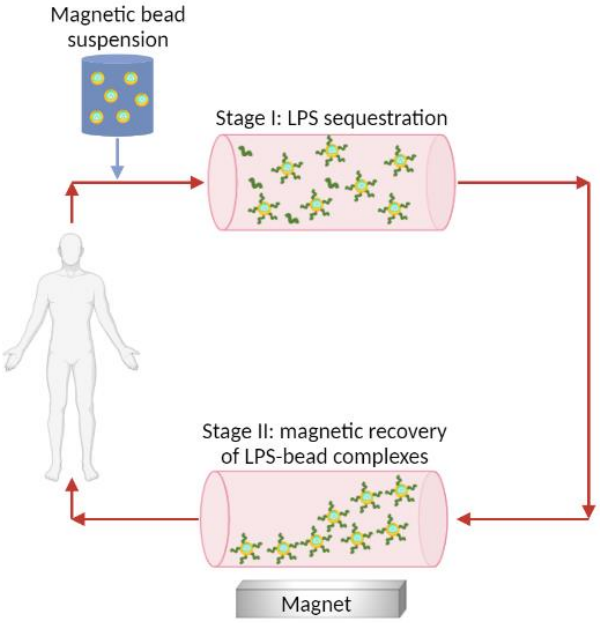

Figure 1.4. Extracorporeal blood detoxification using functionalized magnetic beads for selective endotoxin capture.

From all the available technologies to carry out the capture of endotoxins from blood, microfluidics is considered a promising alternative due to its inherent benefits. Hence, progress in the design of microfluidic systems for isolating toxic substances from blood has been made. For example, Kang et al. [58] and Yung et al. [66] have developed different blood-cleansing microdevices that use functionalized magnetic beads to selectively remove pathogens and toxins from blood.

The coupling of the unique advantages of both functionalized magnetic beads and microfluidics in order to fulfil the incubation and magnetic recovery stages previously described, gives rise to the development of magnetic cleansing microdevices (MCMDs). To avoid confusion with the terminology, in the present work microfluidic incubator refers to the device where the capture of LPS by the beads is addressed, and microfluidic micro-separator denotes the device where the magnetic recovery of the LPS-bead complexes is fulfilled, while MCMDs stands for devices that integrate both the incubation and magnetic recovery stages. In the following section, the benefits of microfluidics and magnetophoresis (i.e., particle manipulation under the influence of magnetic fields) are discussed, which supports the idea that MCMDs are attractive systems for LPS sequestration from blood.

1.3. Magnetophoretic microfluidic devices for blood detoxification

1.3.1. Overview

Microfluidics is a state-of-the-art technology that processes or manipulates small volumes of fluids (10^{-9} to 10^{-18} liters) using channels with dimensions of tens to hundreds of micrometers, which are also called microchannels [67,68]. The unique features derived from such reduced dimensions make microchannels suitable candidates for blood detoxification purposes. Thereby, scaling down the dimensions of fluidic channels to the microscale increases the surface-to-volume ratio of the fluids, which in turn leads to enhanced mass transfer rate. Furthermore, the laminar flow developed in microstructures allows for a precise control of the fluid flow. The small dimensions of microchannels also involve low-sample consumptions, thus reducing the risk of managing hazardous materials and the use of expensive reagents; accordingly, the decrease of the amount of waste that is generated and a considerable cost saving are accomplished. The use of small volumes also facilitates the control of process parameters, such as temperature, pressure, residence time, etc. On the other hand, the increasing interests that microfluidic devices have received can be also attributed to the fact that they are portable and can conveniently integrate several steps within the same device (e.g., in the blood detoxification process herein described, the incubation and magnetic recovery stages). Collectively, microfluidics meets process intensification through miniaturization [69–72].

Microfluidic devices have associated low fabrication cost due to the use of inexpensive materials and cost-effective manufacturing processes. Glass and polymers are materials commonly used in the manufacture of these devices [68,72]. The advantages of glass are its optical transparency, high chemical resistance, and outstanding mechanical and thermal stability. Conversely, microfluidic devices made of polymers are less expensive than those made of glass. Additionally, the benefits of using polymer materials are the existence of simple and cost-effective replication methods and the availability of a broad range of materials, such as, poly (methyl methacrylate) (PMMA), polycarbonate, or polystyrene, which allows the choice of the most suitable material for the specific application based on its properties. However, polymer materials have reduced thermal stability and stability

against organic solvents, acids, and bases [68,71,72].

The use of magnetic separation for retrieving magnetic beads arises from the advantages it offers in comparison to other separation technologies. Hence, magnetic separation is energetically more efficient, easier to operate, and commonly much faster; additionally, another attractive feature of magnetic separations relies on the fact that the separation performance is not affected by factors, such as, temperature, pH or the ionic concentration, which enables the operation in a wide range of these parameters. Therefore, many magnetophoretic microseparators have been developed for addressing the recovery of magnetic beads. These devices differ in their operation mode (namely, batch or continuous), in the magnetic source (i.e., permanent magnets, electromagnets or superconducting magnets) or in the magnetic source combinations (i.e., active or passive configurations) [73–75]. From all these alternatives, the capability of separating the beads in continuous mode (namely continuous-flow magnetophoresis) as well as the use of permanent magnets as a power-free magnetic field source have received special attention [69]. This fact arises from the advantages of continuous-flow magnetophoretic microseparators compared to batch systems. Thereby, in continuous-flow microchannels, the application of a magnetic gradient perpendicular to the flow direction enables bead deflection through multiple parallel streams. Conversely, in batch microchannels, beads are trapped at the regions where the gradient is the highest (typically the channel walls); as a result, beads tend to accumulate in these regions which involves the restriction of the fluid flow. Since in continuous-flow channels beads leave the device within a flowing phase, these systems can minimize such flow restriction, thus enhancing the overall efficiency and capacity of the microseparator. Additionally, batch microseparators may entail the non-specific entrapment of sample components (in this particular case blood components) in the capturing regions, which degrades the quality of the treated solution [73,74]. On the other hand, the prospect of using permanent magnets that do not require power or maintenance for generating the magnetic force that drives bead recovery makes this technology attractive for the implementation of small scale separations in low-resource areas [69,73].

It is worth mentioning that the reduced dimensions of microchannels not only confer them attractive characteristics, as previously mentioned, but also one of their main drawbacks, that is, the capability of only processing

small flow rates. This fact could limit the use of microfluidic devices to certain analytical, biological, chemical, or medical applications [69,73]. Therefore, to keep the unique features of microfluidics and overcome the impossibility of treating high flow rates, optimizing the system parameters and variables is required [69].

Functionalized magnetic micron- or nanosized particles, also referred to as beads, offer promising possibilities for the capture of the target compound from complex media; thus, magnetic beads have received special attention to be used as LPS sequestration agents for blood detoxification purposes [65,74]. This fact stems from their interesting properties. Specifically, they exhibit high surface-to-volume ratios and loading capacities, as well as chemical stability and biocompatibility after being submitted to several surface treatments. Such enhanced features lead to the reduction of both the costs and the generated contamination, and to the increase of the process selectivity when using magnetic beads in comparison to conventional materials. Additionally, the recovery of the magnetic beads from the media can be easily accomplished through the application of magnetic fields since their superparamagnetic behavior enables their manipulation with simple permanent magnets [65,69,70,74].

Magnetic beads for endotoxin capture are typically based on composites, where several materials are combined to maximize LPS removal while ensuring blood quality and functionality (Figure 1.5) [65,76]. The inner core of the beads consists of magnetic elements, including iron, nickel, cobalt, and their oxides, such as magnetite (Fe_3O_4) or maghemite (Fe_2O_3). This bare core can be further coated with different layers to enhance beads properties (e.g., stability against oxidation and spontaneous binding, physicochemical stability, biocompatibility, etc.) or provide a functionalizable surface. Since surface area inversely scales with size, the smaller the size of the core, the larger the surface area for functionalization; however, magnetic recovery is negatively affected by the reduction of the core size. Therefore, a trade-off between increasing the surface area and facilitating magnetic recovery must be achieved when designing functionalized magnetic beads. Collectively, the inner core harbors the magnetic features of the beads, whereas the functionalized shell carries the biotargeting agents that selectively capture LPS [64,65,76,77].

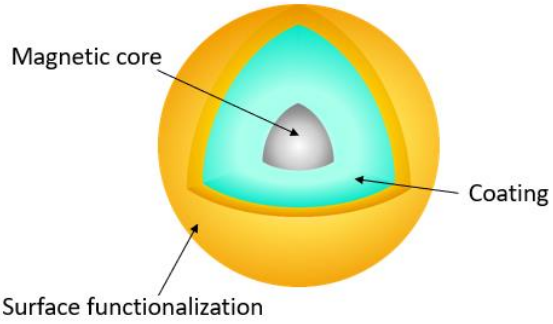

Figure 1.5. Magnetic bead based on composites for LPS sequestration.

1.3.2. LPS binding molecules

Functionalized magnetic beads for the capture of endotoxins from blood are tailored to recognize the target compound to be captured, in this case, bacterial LPS [65,77]. To this end, identifying the most suitable biotargeting agents, that is, molecules that bind to LPS with high affinity and selectivity, is required. Once such LPS binding molecules are found, modifications can be introduced to them in order to enhance the specificity and strength of their interaction with LPS [48]. Several LPS binding molecules with different origins have been reported in the literature, including but not limited to, bacterial proteins (FhuA, or OmpT), human proteins (CD14, LBP, MD2 and TLR4), or anti-LPS factors (ALFs) from crustaceans and marine chelicerates, such as, *Limulus polyphemus* ALF (LALF), *Tachypleus tridentatus* ALF, (TALF) or *Penaeus monodon* ALF (ALFPm3) [21,78].

From the different LPS binding molecules that have been recognized, ALFs have received special attention for designing molecules with therapeutic potential against sepsis [79,80]. ALFs are antimicrobial peptides (AMPs) exclusively found in marine chelicerates and crustaceans, and key immune effectors that bind and neutralize bacterial LPS [81–85]. Originally identified from the hemolymph of the horseshoe crabs *L. polyphemus* and *T. tridentatus*, ALFs were later found in several shrimp species, such as *P. monodon* [82,86,87]. They are amphipathic peptides (around 100 amino acids) that comprise two conserved cysteine residues forming a disulfide loop that delimits a β-hairpin [80,82,85,86,88]. Particularly, the three-dimensional structures of LALF and ALF-Pm3 have been solved by X-ray crystallography

and nuclear magnetic resonance (NMR), respectively; they are extremely similar and consist of three α-helices packed against a four-stranded β-sheet [79,85,86]. It is worth mentioning that the structure of ALFPm3 without any bound ligand is deposited in the Protein Data Bank (PDB) under the accession code 2JOB; however, the structure of LALF is not available in the PDB.

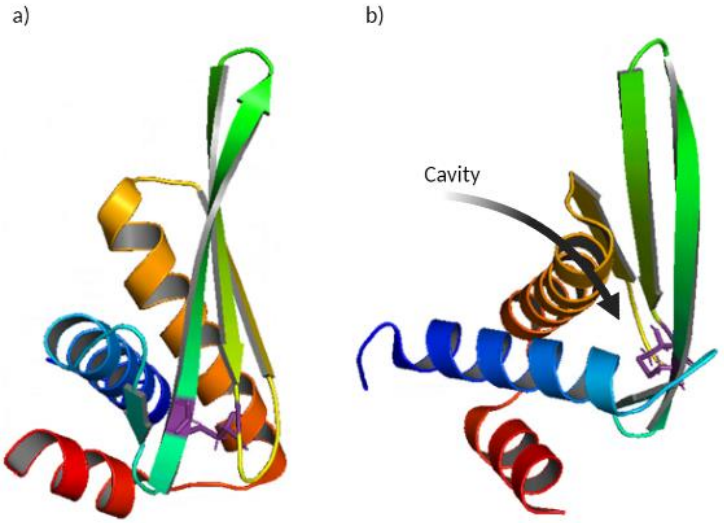

Figure 1.6. Cartoon model representation of ALFPm3 showing (a) the front and lateral sides and (b) the back side of the protein. Cysteine residues are represented in stick model and coloured in purple.

Understanding how LPS interacts with LALF or ALFPm3 is of paramount importance to advance in the design of biotargeting agents that exhibit an enhanced ability to sequestrate LPS, and thus to optimize the incubation stage of MCMDs. However, the interaction mechanism or the LPS binding site in the abovementioned ALFs have not been demonstrated yet to the best of the author's knowledge. Due to the availability of the ALFPm3 NMR structure in the PDB, its interaction with bacterial LPS is investigated in this dissertation.

Collectively, as it has been discussed throughout this chapter, the individual advantages of microfluidics and functionalized magnetic beads foster that their coupling in MCMDs has been understood as an attractive and

promising strategy for the capture of endotoxins from blood. Although important progress has been made in the development of these systems, there exist some design challenges that remain uncovered and need to be addressed in order to ensure the successful implementation of MCMDs. Addressing this issue through a trial-and-error experimental approach is impracticable due to the numerous variables that affect the design of both the LPS sequestration and magnetic bead recovery stages. Additionally, some detailed insights that are needed for the endotoxin capture stage cannot be experimentally accessed. Hence, the use of computational techniques proves valuable for surmounting the limitations of purely experimental approaches.

1.4. Scope and objectives of the thesis

This thesis contributes to the design of MCMDs that enable the successful and efficient sequestration of bacterial LPS from blood. Specifically, it is focused on the use of advanced simulation techniques, namely molecular dynamics (MD) and computational fluid dynamics (CFD), as predictive tools for the rational design of the incubation and magnetic recovery stages that comprise MCMDs. The methodology and results herein reported prove valuable to move forward on the design of MCMDs for blood detoxification purposes, thus, paving the way for the development of novel strategies for fighting against sepsis.

The first chapter provides an overall picture about both the antibiotic resistance threat and novel strategies to surmount such global challenge. Particularly, an exhaustive overview about the role of bacterial LPS in Gram-negative bacterial infections is provided in order to understand the crucial implications that LPS has on antibiotic resistance and on the pathogenesis of sepsis. Additionally, the existence of a global healthcare concern due to the emergence of antibiotic resistant bacteria is highlighted, thus demonstrating the need of moving forward in the design of alternatives for treating bacterial infections that could eventually be applied in sepsis treatments. Thereby, a magnetic-based microfluidic strategy for blood detoxification purposes is reported and described, and the benefits of microfluidics and magnetophoresis are also emphasised.

The second chapter focuses on advancing in the design of the LPS sequestration stage by combining MD simulations and wet-lab experiments. The importance of MD for being used as a predictive tool is highlighted and the fundamentals of MD simulations are introduced to establish the underlaying theoretical basis. In this chapter, the interaction between ALF-Pm3 and lipid A is investigated through MD simulations. The insights gained *in silico* are also confirmed *in vitro*.

The third chapter is focused on the computer-aided optimization of the magnetic recovery stage using CFD techniques. The principles of magnetic manipulation and fluid dynamics in microchannels are presented in order to introduce the underlying theoretical background. In this chapter, two approaches are followed to address the optimization of magnetophoretic microseparators, namely, (i) optimize the geometrical features of the

microchannels, and (ii) increase the driving force for the bead recovery (i.e., magnetic force). This methodology leads to the introduction and description of several magnetophoretic microdevices that have been widely used for bead isolation purposes.

Finally, based on the research analysis and results provided in the previous chapters, the main conclusions related to the methodological development and optimization of MCMDs for blood detoxification are proposed in the fourth chapter. With a special focus on the valuable knowledge that is gained by MD and CFD techniques, the role of these computational techniques for guiding experimental work is emphasized. Additionally, an overview of challenges for continuing this research is provided.

1.5. References of Chapter 1

[1] Z. Breijyeh, B. Jubeh, R. Karaman, Resistance of Gram-negative bacteria to current antibacterial agents and approaches to resolve it, Molecules. 25 (2020) 1340. https://doi.org/10.3390/molecules25061340.

[2] R.B. Moyes, J. Reynolds, D.P. Breakwell, Differential staining of bacteria: Gram stain, Curr. Protoc. Microbiol. (2009) 1–8. https://doi.org/10.1002/9780471729259.mca03cs15.

[3] K.P. Lundquist, J.C. Gumbart, Presence of substrate aids lateral gate separation in LptD, Biochim. Biophys. Acta. Biomembr. 1862 (2020) 183025. https://doi.org/10.1016/j.bbamem.2019.07.013.

[4] B. Bertani, N. Ruiz, Function and biogenesis of Lipopolysaccharides, EcoSal Plus. 8 (2018) 1–19. https://doi.org/10.1128/ecosalplus.esp-0001-2018.

[5] P. Sperandeo, A.M. Martorana, A. Polissi, Lipopolysaccharide biogenesis and transport at the outer membrane of Gram-negative bacteria, Biochim. Biophys. Acta - Mol. Cell Biol. Lipids. 1862 (2017) 1451–1460. https://doi.org/10.1016/j.bbalip.2016.10.006.

[6] P. Blasco, D.S. Patel, O. Engström, W. Im, G. Widmalm, Conformational Dynamics of the Lipopolysaccharide from *Escherichia coli* O91 Revealed by Nuclear Magnetic Resonance Spectroscopy and Molecular Simulations, Biochemistry. 56 (2017) 3826–3839. https://doi.org/10.1021/acs.biochem.7b00106.

[7] G. Klein, S. Raina, Regulated assembly of LPS, its structural alterations and cellular response to LPS defects, Int. J. Mol. Sci. 20 (2019) 356. https://doi.org/10.3390/ijms20020356.

[8] F.A. Baltoumas, S.J. Hamodrakas, V.A. Iconomidou, The Gram-negative outer membrane modeler: Automated building of lipopolysaccharide-rich bacterial outer membranes in four force fields, J. Comput. Chem. 40 (2019) 1727–1734. https://doi.org/10.1002/jcc.25823.

[9] D. Jefferies, J. Shearer, S. Khalid, Role of O-antigen in response to mechanical stress of the *E. coli* outer membrane: insights from coarse-grained MD simulations, J. Phys. Chem. B. 123 (2019) 3567–3575. https://doi.org/10.1021/acs.jpcb.8b12168.

[10] A. Kesireddy, K.R. Pothula, J. Lee, D.S. Patel, M. Pathania, B. Van Den Berg, W. Im, U. Kleinekathöfer, Modeling of specific

Lipopolysaccharide binding sites on a Gram-negative porin, J. Phys. Chem. B. 123 (2019) 5700–5708. https://doi.org/10.1021/acs.jpcb.9b03669.

[11] R. Domalaon, T. Idowu, G.G. Zhanel, F. Schweizer, Antibiotic hybrids: The next generation of agents and adjuvants against gram-negative pathogens?, Clin. Microbiol. Rev. 31 (2018) e00077-17. https://doi.org/10.1128/CMR.00077-17.

[12] T.J. Silhavy, D. Kahne, S. Walker, The bacterial cell envelope, Cold Spring Harb Perspect Biol. 2 (2010) a000414. https://www.ncbi.nlm.nih.gov/pmc/articles/PMC2857177/pdf/cshperspect-PRK-a000414.pdf.

[13] D. Artner, A. Oblak, S. Ittig, J.A. Garate, S. Horvat, C. Arrieumerlou, A. Hofinger, C. Oostenbrink, R. Jerala, P. Kosma, A. Zamyatina, Conformationally constrained lipid A mimetics for exploration of structural basis of TLR4/MD-2 activation by lipopolysaccharide, ACS Chem. Biol. 8 (2013) 2423–2432. https://doi.org/10.1021/cb4003199.

[14] Y. Gao, J. Lee, G. Widmalm, W. Im, Modeling and simulation of bacterial outer membranes with lipopolysaccharides and enterobacterial common antigen, J. Phys. Chem. B. 124 (2020) 5948–5956. https://doi.org/10.1021/acs.jpcb.0c03353.

[15] M.A. Knirel, Y. A. Valvano, Bacterial Lipopolysaccharides. Structure, Chemical Synthesis, Biogenesis and Interactions with Host Cells, Springer, New York, 2011.

[16] D. Petsch, F.B. Anspach, Endotoxin removal from protein solutions, J. Biotechnol. 76 (2000) 97–119. https://doi.org/10.1016/S0168-1656(99)00185-6.

[17] C. Laguri, A. Silipo, A.M. Martorana, P. Schanda, R. Marchetti, A. Polissi, A. Molinaro, J.P. Simorre, Solid state NMR studies of intact lipopolysaccharide endotoxin, ACS Chem. Biol. 13 (2018) 2106–2113. https://doi.org/10.1021/acschembio.8b00271.

[18] A. Rahnamoun, K. Kim, J.A. Pedersen, R. Hernandez, Ionic environment affects bacterial lipopolysaccharide packing and function, Langmuir. 36 (2020) 3149–3158. https://doi.org/10.1021/acs.langmuir.9b03162.

[19] J.A. Garate, C. Oostenbrink, Lipid A from lipopolysaccharide recognition: Structure, dynamics and cooperativity by molecular dynamics simulations, Proteins Struct. Funct. Bioinforma. 81 (2013)

658–674. https://doi.org/10.1002/prot.24223.

[20] V. Sampath, Bacterial endotoxin-lipopolysaccharide; structure, function and its role in immunity in vertebrates and invertebrates, Agric. Nat. Resour. 52 (2018) 115–120. https://doi.org/10.1016/j.anres.2018.08.002.

[21] A. Basauri, C. González-Fernández, M. Fallanza, E. Bringas, R. Fernandez-Lopez, L. Giner, G. Moncalián, F. de la Cruz, I. Ortiz, Biochemical interactions between LPS and LPS-binding molecules, Crit. Rev. Biotechnol. 40 (2020) 292–305. https://doi.org/10.1080/07388551.2019.1709797.

[22] M. Zheng, M. Zheng, S. Epstein, A.P. Harnagel, H. Kim, T.J. Lupoli, Chemical biology tools for modulating and visualizing Gram-negative bacterial surface polysaccharides, ACS Chem. Biol. 16 (2021) 1841–1865. https://doi.org/10.1021/acschembio.1c00341.

[23] A. Steimle, I.B. Autenrieth, J.S. Frick, Structure and function: Lipid A modifications in commensals and pathogens, Int. J. Med. Microbiol. 306 (2016) 290–301. https://doi.org/10.1016/j.ijmm.2016.03.001.

[24] R.G. Huber, N.A. Berglund, V. Kargas, J.K. Marzinek, D.A. Holdbrook, S. Khalid, T.J. Piggot, A. Schmidtchen, P.J. Bond, A thermodynamic funnel drives bacterial lipopolysaccharide transfer in the TLR4 pathway, Structure. 26 (2018) 1151–1161. https://doi.org/10.1016/j.str.2018.04.007.

[25] M. Vaara, M. Nurminen, Outer membrane permeability barrier in *Escherichia coli* mutants that are defective in the late acyltransferases of lipid A biosynthesis, Antimicrob. Agents Chemother. 43 (1999) 1459–1462. https://doi.org/10.1128/aac.43.6.1459.

[26] A. Rice, M. Rooney, A.I. Greenwood, M.L. Cotten, J. Wereszczynski, Lipopolysaccharide simulations are sensitive to phosphate charge and ion parameterization, J. Chem. Theory Comput. 16 (2020) 1806–1815. https://doi.org/10.1021/acs.jctc.9b00868.

[27] A. Borio, A. Holgado, J.A. Garate, R. Beyaert, H. Heine, A. Zamyatina, Disaccharide-based anionic amphiphiles as potent inhibitors of lipopolysaccharide-induced inflammation, ChemMedChem. 13 (2018) 2317–2331. https://doi.org/10.1002/cmdc.201800505.

[28] V. Kargas, J.K. Marzinek, D.A. Holdbrook, H. Yin, R.C. Ford, P.J. Bond, A polar SxxS motif drives assembly of the transmembrane domains of Toll-like receptor 4, Biochim. Biophys. Acta - Biomembr. 1859 (2017) 2086–2095. https://doi.org/10.1016/j.bbamem.2017.07.010.

[29] M. Molteni, S. Gemma, C. Rossetti, The role of Toll-Like Receptor 4 in infectious and noninfectious inflammation, Mediators Inflamm. 2016 (2016) 6978936. https://doi.org/10.1155/2016/6978936.

[30] K. Miyake, Innate recognition of lipopolysaccharide by Toll-like receptor 4-MD-2, Trends Microbiol. 12 (2004) 186–192. https://doi.org/10.1016/j.tim.2004.02.009.

[31] C. Cao, M. Yu, Y. Chai, Pathological alteration and therapeutic implications of sepsis-induced immune cell apoptosis, Cell Death Dis. 10 (2019) 782. https://doi.org/10.1038/s41419-019-2015-1.

[32] J.M. Cote, C.A. Ramirez-Mondragon, Z.S. Siegel, D.J. Czyzyk, J. Gao, Y.Y. Sham, I. Mukerji, E.A. Taylor, The stories tryptophans tell: exploring protein dynamics of heptosyltransferase I from *Escherichia coli*, Biochemistry. 56 (2017) 886–895. https://doi.org/10.1021/acs.biochem.6b00850.

[33] B. Li, T.J. Webster, Bacteria antibiotic resistance: New challenges and opportunities for implant-associated orthopedic infections, J. Orthop. Res. 36 (2018) 22–32. https://doi.org/10.1002/jor.23656.

[34] R.I. Aminov, A brief history of the antibiotic era: Lessons learned and challenges for the future, Front. Microbiol. 1 (2010) 1–7. https://doi.org/10.3389/fmicb.2010.00134.

[35] C.L. Ventola, The antibiotic resistance crisis: Part 1: Causes and Threats, Pharm. Ther. 40 (2015) 277–283. http://www.ncbi.nlm.nih.gov/pubmed/25859123%5Cnhttp://www.pubmedcentral.nih.gov/articlerender.fcgi?artid=PMC4378521.

[36] J. Davies, D. Davies, Origins and evolution of antibiotic resistance., Microbiol. Mol. Biol. Rev. 74 (2010) 417–433. https://doi.org/10.1128/mmbr.00016-10.

[37] M. Hutchings, A. Truman, B. Wilkinson, Antibiotics: past, present and future, Curr. Opin. Microbiol. 51 (2019) 72–80. https://doi.org/10.1016/j.mib.2019.10.008.

[38] Centers for Disease Control snd Prevention (CDC), Antibiotic/antimicrobial resistance (AR/AMR). Available online: https://www.cdc.gov/drugresistance/about.html. (Accessed on 4 December 2021).

[39] European Centre for Disease Prevention and Control (ECDC), Facsheet for the general public-Antimicrobial resistance. Available online: https://www.ecdc.europa.eu/en/antimicrobial-resistance/facts/factsheets/general-public. (Accessed on 4 December

2021)

[40] C.A. López, H. Zgurskaya, S. Gnanakaran, Molecular characterization of the outer membrane of *Pseudomonas aeruginosa*, Biochim. Biophys. Acta - Biomembr. 1862 (2020) 183151. https://doi.org/10.1016/j.bbamem.2019.183151.

[41] D.E.S. Santos, L. Pol-Fachin, R.D. Lins, T.A. Soares, Polymyxin binding to the bacterial outer membrane reveals cation displacement and increasing membrane curvature in susceptible but not in resistant lipopolysaccharide chemotypes, J. Chem. Inf. Model. 57 (2017) 2181–2193. https://doi.org/10.1021/acs.jcim.7b00271.

[42] A. Rice, J. Wereszczynski, Atomistic scale effects of lipopolysaccharide modifications on bacterial outer membrane defenses, Biophys. J. 114 (2018) 1389–1399. https://doi.org/10.1016/j.bpj.2018.02.006.

[43] M.W. Martynowycz, A. Rice, K. Andreev, T.M. Nobre, I. Kuzmenko, J. Wereszczynski, D. Gidalevitz, *Salmonella* membrane structural remodeling increases resistance to antimicrobial peptide LL-37, ACS Infect. Dis. 5 (2019) 1214–1222. https://doi.org/10.1021/acsinfecdis.9b00066.

[44] M. Arzanlou, W.C. Chai, H. Venter, Intrinsic, adaptive and acquired antimicrobial resistance in Gram-negative bacteria, Essays Biochem. 61 (2017) 49–59. https://doi.org/10.1042/EBC20160063.

[45] M. Kelly, S. Cambray, K.A. McCarthy, W. Wang, E. Geisinger, J. Ortiz-Marquez, T. Van Opijnen, J. Gao, Peptide probes of colistin resistance discovered via chemically enhanced phage display, ACS Infect. Dis. 6 (2020) 2410–2418. https://doi.org/10.1021/acsinfecdis.0c00206.

[46] A. Pandeya, I. Ojo, O. Alegun, Y. Wei, Periplasmic targets for the development of effective antimicrobials against Gram-negative bacteria, ACS Infect. Dis. 6 (2020) 2337–2354. https://doi.org/10.1021/acsinfecdis.0c00384.

[47] A. Boags, P.C. Hsu, F. Samsudin, P.J. Bond, S. Khalid, Progress in molecular dynamics simulations of Gram-negative bacterial cell envelopes, J. Phys. Chem. Lett. 8 (2017) 2513–2518. https://doi.org/10.1021/acs.jpclett.7b00473.

[48] C. González-Fernández, A. Basauri, M. Fallanza, E. Bringas, C. Oostenbrink, I. Ortiz, Fighting against bacterial lipopolysaccharide-caused infections through molecular dynamics simulations: A review, J. Chem. Inf. Model. 61 (2021) 4839–4851. https://doi.org/10.1021/acs.jcim.1c00613.

[49] Centers for Disease Control snd Prevention (CDC), Antibiotic resistance threats in the United States, 2019. Atlanta, GA: U.S. Department of Health and Human Servaces, CDC.

[50] F. Prestinaci, P. Pezzotti, A. Pantosti, Antimicrobial resistance: A global multifaceted phenomenon, Pathog. Glob. Health. 109 (2015) 309–318. https://doi.org/10.1179/2047773215Y.0000000030.

[51] European Centre for Disease Prevention and Control (ECDC), Antimicrobial resistance in the EU/EEA (EARS-Net) Annual Epidemiological Report 2019, Stockholm: ECDC, 2020.

[52] World Health Organization (WHO), Antimicrobial resistance: Global repost in surveillance, 2014, Switzerland.

[53] R.E.W. Hancock, A. Nijnik, D.J. Philpott, Modulating immunity as a therapy for bacterial infections, Nat. Rev. Microbiol. 10 (2012) 243–254. https://doi.org/10.1038/nrmicro2745.

[54] T. Gulistan, S. Ahmad, S.S. Azam, Conformational transition of Acinetobacter baumannii KdsC enzyme and the role of magnesium in binding: An insight from comparative molecular dynamics simulation and its implications in novel antibiotics design, J. Mol. Graph. Model. 99 (2020) 107625. https://doi.org/10.1016/j.jmgm.2020.107625.

[55] S.K. Panda, S. Saxena, L. Guruprasad, Homology modeling, docking and structure-based virtual screening for new inhibitor identification of Klebsiella pneumoniae heptosyltransferase-III, J. Biomol. Struct. Dyn. 38 (2020) 1887–1902. https://doi.org/10.1080/07391102.2019.1624296.

[56] F.B. Anspach, O. Hilbeck, Removal of endotoxins by affinity sorbents, J. Chromatogr. A. 711 (1995) 81–92. https://doi.org/10.1016/0021-9673(95)00126-8.

[57] S. Harm, D. Falkenhagen, J. Hartmann, Endotoxin adsorbents in extracorporeal blood purification: Do they fulfill expectations?, Int. J. Artif. Organs. 37 (2014) 222–232. https://doi.org/10.5301/ijao.5000304.

[58] J.H. Kang, M. Super, C.W. Yung, R.M. Cooper, K. Domansky, A.R. Graveline, T. Mammoto, J.B. Berthet, H. Tobin, M.J. Cartwright, A.L. Watters, M. Rottman, A. Waterhouse, A. Mammoto, N. Gamini, M.J. Rodas, A. Kole, A. Jiang, T.M. Valentin, A. Diaz, K. Takahashi, D.E. Ingber, An extracorporeal blood-cleansing device for sepsis therapy, Nat. Med. 20 (2014) 1211–1216. https://doi.org/10.1038/nm.3640.

[59] I.K. Herrmann, A. Schlegel, R. Graf, C.M. Schumacher, N. Senn, M.

Hasler, S. Gschwind, A.M. Hirt, D. Günther, P.A. Clavien, W.J. Stark, B. Beck-Schimmer, Nanomagnet-based removal of lead and digoxin from living rats, Nanoscale. 5 (2013) 8718–8723. https://doi.org/10.1039/c3nr02468g.

[60] C. Yamashita, K. Moriyama, D. Hasegawa, Y. Kato, T. Sakai, T. Kawaji, Y. Shimomura, Y. Kurimoto, M. Nagata, O. Nishida, *In vitro* study of endotoxin adsorption by a polymyxin b-immobilized fiber column, Blood Purif. 46 (2018) 269–273. https://doi.org/10.1159/000489920.

[61] B. Davies, J. Cohen, Endotoxin removal devices for the treatment of sepsis and septic shock, Lancet Infect. Dis. 11 (2011) 65–71. https://doi.org/10.1016/S1473-3099(10)70220-6.

[62] J. Cohen, Non-antibiotic strategies for sepsis, Clin. Microbiol. Infect. 15 (2009) 302–307. https://doi.org/10.1111/j.1469-0691.2009.02753.x.

[63] P. Jagtap, R. Mishra, S. Khanna, P. Kumari, B. Mittal, H.K. Kashyap, S. Gupta, Mechanistic evaluation of lipopolysaccharide-alexidine interaction using spectroscopic and *in silico* approaches, ACS Infect. Dis. 4 (2018) 1546–1552. https://doi.org/10.1021/acsinfecdis.8b00087.

[64] J. Gómez-Pastora, C. González-Fernández, E. Real, A. Iles, E. Bringas, E.P. Furlani, I. Ortiz, Computational modeling and fluorescence microscopy characterization of a two-phase magnetophoretic microsystem for continuous-flow blood detoxification, Lab Chip. 18 (2018) 1593–1606. https://doi.org/10.1039/c8lc00396c.

[65] J. Gómez-Pastora, E. Bringas, M. Lázaro-Díez, J. Ramos-Vivas, I. Ortiz, The reverse of controlled release: Controlled sequestration of species and biotoxins into nanoparticles (NPs), in: P. Stroeve, M. Mahmoudi (Eds.), Drug Deliv. Syst., World Scientific, New Jersey, 2018: pp. 207–243. https://doi.org/10.1142/9789813201057_0006.

[66] C.W. Yung, J. Fiering, A.J. Mueller, D.E. Ingber, Micromagnetic-microfluidic blood cleansing device, Lab Chip. 9 (2009) 1171–1177. https://doi.org/10.1039/b816986a.

[67] G.M. Whitesides, The origins and the future of microfluidics, Nature. 442 (2006) 368–373. https://doi.org/10.1038/nature05058.

[68] R. Monošík, L. Angnes, Utilisation of micro- and nanoscaled materials in microfluidic analytical devices, Microchem. J. 119 (2015) 159–168. https://doi.org/10.1016/j.microc.2014.12.003.

[69] C. González Fernández, J. Gómez Pastora, A. Basauri, M. Fallanza, E. Bringas, J.J. Chalmers, I. Ortiz, Continuous-flow separation of magnetic particles from biofluids: How does the microdevice geometry determine the separation performance?, Sensors. 20 (2020) 3030. https://doi.org/10.3390/s20113030.

[70] C. González-Fernández, J. Gómez-Pastora, E. Bringas, M. Zborowski, J.J. Chalmers, I. Ortiz, Recovery of magnetic catalysts: advanced design for process intensification, Ind. Eng. Chem. Res. 60 (2021) 16780–16790. https://doi.org/10.1021/acs.iecr.1c03474.

[71] C.M. Niemeyer, C.A. Mirkin, eds., Nanobiotechnology; Concepts, Applications and Perspectives, Wiley-VCH, Germany, 2004.

[72] W.K. Tomazelli Coltro, C.M. Cheng, E. Carrilho, D.P. de Jesus, Recent advances in low-cost microfluidic platforms for diagnostic applications, Electrophoresis. 35 (2014) 2309–2324. https://doi.org/10.1002/elps.201400006.

[73] J. Gómez-Pastora, On the design of lab-on-a-chip devices for magnetophoretic separations (doctoral dissertation), University of Cantabria (Spain), (2018).

[74] J. Gómez-Pastora, X. Xue, I.H. Karampelas, E. Bringas, E.P. Furlani, I. Ortiz, Analysis of separators for magnetic beads recovery: From large systems to multifunctional microdevices, Sep. Purif. Technol. 172 (2017) 16–31. https://doi.org/10.1016/j.seppur.2016.07.050.

[75] J. Gómez-Pastora, I.H. Karampelas, E. Bringas, E.P. Furlani, I. Ortiz, Numerical analysis of bead magnetophoresis from flowing blood in a continuous-flow microchannel: implications to the bead-fluid interactions, Sci. Rep. 9 (2019) 7265. https://doi.org/10.1038/s41598-019-43827-x.

[76] L. Borlido, A.M. Azevedo, A.C.A. Roque, M.R. Aires-Barros, Magnetic separations in biotechnology, Biotechnol. Adv. 31 (2013) 1374–1385. https://doi.org/10.1016/j.biotechadv.2013.05.009.

[77] L. Bromberg, E.P. Chang, T.A. Hatton, A. Concheiro, B. Magariños, C. Alvarez-Lorenzo, Bactericidal core-shell paramagnetic nanoparticles functionalized with poly(hexamethylene biguanide), Langmuir. 27 (2011) 420–429. https://doi.org/10.1021/la1039909.

[78] R. Chaby, Lipopolysaccharide-binding molecules: Transporters, blockers and sensors, Cell. Mol. Life Sci. 61 (2004) 1697–1713. https://doi.org/10.1007/s00018-004-4020-4.

[79] A. Hoess, S. Watson, G.R. Siber, R. Liddington, E. Schulz, Crystal

structure of an endotoxin-neutralizing protein from the horseshoe crab, *Limulus* anti-LPS factor, at 1.5 A resolution, EMBO J. 12 (1993) 3351–3356. https://www.ncbi.nlm.nih.gov/pmc/articles/PMC413608/pdf/emboj00081-0013.pdf.

[80] K. Somboonwiwat, M. Marcos, A. Tassanakajon, S. Klinbunga, A. Aumelas, B. Romestand, Y. Gueguen, H. Boze, G. Moulin, E. Bachère, Recombinant expression and anti-microbial activity of anti-lipopolysaccharide factor (ALF) from the black tiger shrimp *Penaeus monodon*, Dev. Comp. Immunol. 29 (2005) 841–851. https://doi.org/10.1016/j.dci.2005.02.004.

[81] W. Sun, W. Wan, S. Zhu, S. Wang, S. Wang, X. Wen, H. Zheng, Y. Zhang, S. Li, Characterization of a novel anti-lipopolysaccharide factor isoform (*Sp*ALF5) in mud crab, *Scylla paramamosain*, Mol. Immunol. 64 (2015) 262–275. https://doi.org/10.1016/j.molimm.2014.12.006.

[82] R.D. Rosa, A. Vergnes, J. de Lorgeril, P. Goncalves, L.M. Perazzolo, L. Sauné, B. Romestand, J. Fievet, Y. Gueguen, E. Bachère, D. Destoumieux-Garzón, Functional Divergence in Shrimp Anti-Lipopolysaccharide Factors (ALFs): From Recognition of Cell Wall Components to Antimicrobial Activity, PLoS One. 8 (2013) e67937. https://doi.org/10.1371/journal.pone.0067937.

[83] T. Kadowaki, H. Inagawa, C. Kohchi, T. Nishizawa, Y. Takahashi, G.I. Soma, Anti-lipopolysaccharide factor evokes indirect killing of virulent bacteria in Kuruma Prawn, In Vivo. 25 (2011) 741–744.

[84] Z.G. Hou, Y. Wang, K. Hui, W.H. Fang, S. Zhao, J.X. Zhang, H. Ma, X.C. Li, A novel anti-lipopolysaccharide factor *Sp*ALF6 in mud crab *Scylla paramamosain* exhibiting different antimicrobial activity from its single amino acid mutant, Dev. Comp. Immunol. 72 (2017) 44–56. https://doi.org/10.1016/j.dci.2017.02.009.

[85] P. Schmitt, R.D. Rosa, D. Destoumieux-Garzón, An intimate link between antimicrobial peptide sequence diversity and binding to essential components of bacterial membranes, Biochim. Biophys. Acta - Biomembr. 1858 (2016) 958–970. https://doi.org/10.1016/j.bbamem.2015.10.011.

[86] Y. Yang, H. Boze, P. Chemardin, A. Padilla, G. Moulin, A. Tassanakajon, M. Pugnière, F. Roquet, D. Destoumieux-Garzón, Y. Gueguen, E. Bachère, A. Aumelas, NMR structure of rALF-Pm3, an anti-lipopolysaccharide factor from shrimp: Model of the possible lipid A-binding site, Biopolymers. 91 (2009) 207–220.

https://doi.org/10.1002/bip.21119.

[87] K. Somboonwiwat, E. Bachère, V. Rimphanitchayakit, A. Tassanakajon, Localization of anti-lipopolysaccharide factor (ALF*Pm3*) in tissues of the black tiger shrimp, *Penaeus monodon*, and characterization of its binding properties, Dev. Comp. Immunol. 32 (2008) 1170–1176. https://doi.org/10.1016/j.dci.2008.03.008.

[88] A. Tassanakajon, K. Somboonwiwat, P. Supungul, S. Tang, Discovery of immune molecules and their crucial functions in shrimp immunity, Fish Shellfish Immunol. 34 (2013) 954–967. https://doi.org/10.1016/j.fsi.2012.09.021.

CHAPTER 2

Design of tailor-made lipopolysaccharide capture agents

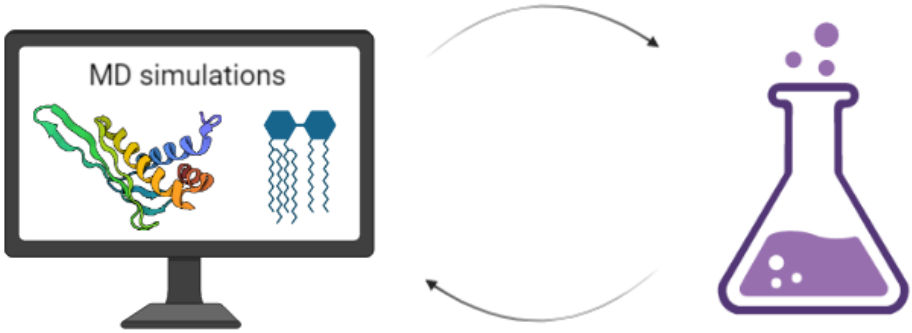

2.1. Framework

As discussed in Chapter 1, ALFs have been understood as potential candidates in the design of novel strategies to bind and capture bacterial lipopolysaccharide; thus, special interest has been devoted to the elucidation of the interaction mechanism between LPS and LALF or ALFPm3 [1,2]. In this regard, the LPS binding site in LALF and ALFPm3 has been hypothesized. For example, Hoess et al. [2] suggested that the LPS-binding motif in LALF probably entails an amphipathic loop. They proposed that such LPS binding site was also shared by two mammalian proteins, namely lipopolysaccharide-binding protein (LBP) and bactericidal/permeability-increasing protein (BPI). Similarly, Yang and coworkers [1] tried to study experimentally the interaction of ALFPm3 with LPS, lipid A and a lipid A analogue. However, the size of LPS and the lipid A analogue hampered the experimental elucidation of their binding site in ALFPm3. Therefore, hypothesizing that LPS-binding molecules have a similar lipid A binding site, they performed a structural comparison of the ALFPm3 and FhuA-LPS complex structures and proposed several amino acids that could belong to the lipid A binding site. Despite the important knowledge derived from the works of Hoess et al. [2] and Yang et al. [1], the LPS binding site that they have suggested has not been neither *in silico* nor experimentally demonstrated. Nevertheless, proving the binding pose of LPS with LALF or ALFPm3 is key for moving a step forward in the design of LPS sequestration agents. More specifically, identifying the residues of LALF or ALFPm3 that interact with LPS could serve to design novel molecules with considerably enhanced ability for LPS capture, which in turn involves the design of more efficient endotoxin sequestration agents. For addressing this investigation, understanding microscopic details of the LALF-LPS or ALFPm3-LPS interactions is imperative. Gaining such detailed knowledge is beyond the possibilities of wet-lab experiments. Therefore, MD will be used as a computational microscope to shed light into the abovementioned interactions, which significantly contributes to advance in the design of LPS sequestration molecules.

2.2. *In silico* elucidation of the ALFPm3-lipid A interaction

2.2.1. Overview of MD simulations

Classical MD simulations have proven valuable for elucidating and understanding the structure, function, and dynamics of biomolecules, as well as their interplay with other molecules at the atomic level. Since MD provides incredibly detailed insights into the molecular process of interest that often goes beyond the reach of sophisticated wet-lab experiments, this *in silico* method facilitates the interpretation of experimental data, and can be used as a prior stage to experiments, thus leading to time and cost savings due to the significant minimization of the number of experiments that need to be carried out [3–9]. As such, MD procedures have been widely employed for investigating phenomena related to bacterial LPS since the late 1990's, when this *in silico* method was used, for instance, to build a model of the PMB-lipid A complex, thus paving the way to design LPS antagonists [10]. Additionally, the great significance of MD for moving a step forward in the LPS research is supported by the exponential increase of the number of published studies that make use of MD to simulate LPS systems since the late 1990s, as noticed from Figure 2.1. Such increase has been fueled by the feasibility of accessing to biologically meaningful time and length scales, despite the complexity of LPS-related systems, which can be accomplished by combining different computational methods with MD simulations [4–6,11–14]. Prior to explaining the basics about these methods, the fundamentals of MD need to be introduced, which is addressed in the following section.

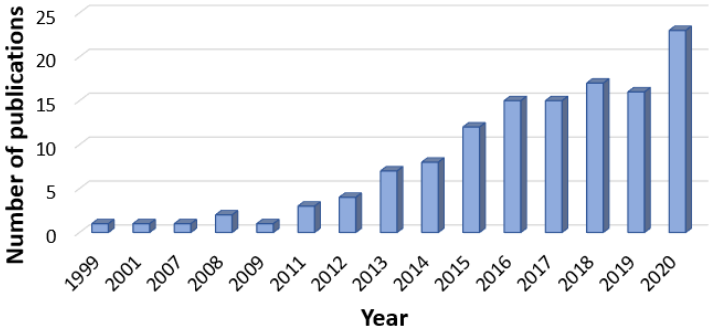

Figure 2.1. Number of publications in the last 21 years related to the use of MD simulations in LPS research and found in the Scopus database using the restrictive keywords "molecular dynamics simulation*" and "LPS".

2.2.2. Fundamentals of MD

MD simulations predict how every particle in a molecular system evolves with time according to the laws of classical physics. In the context of biomolecular simulations, "particles" typically stands for single atoms or the grouping of a few atoms in a single particle [8,13]. Thereby, MD simulations generate a series of conformations (namely, a trajectory) of the system under investigation, which enable exploring different movements in microscopic systems [15,16]. The general protocol for performing MD simulations has been schematized in Figure 2.2 and involves the steps that are described below.

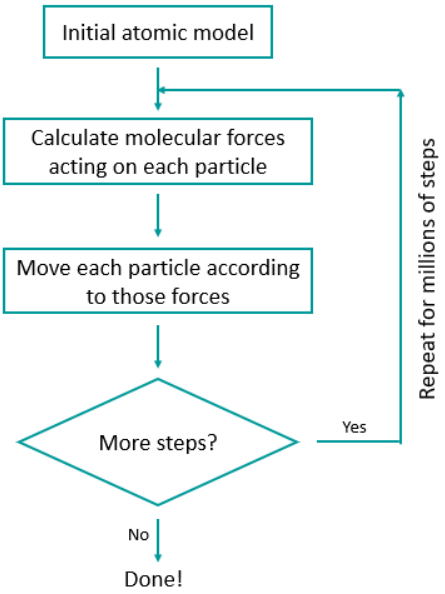

Figure 2.2. Simplified schematic of the procedure of a typical MD simulation.

Firstly, a model of the molecules to be investigated is prepared from structural data derived from X-ray crystallography, NMR or homology-modelling [8,17]. Accurate MD simulations rely on the availability of accurate experimental structures or reliable homology models. Therefore, the increasing number of structurally characterized molecules, which are stored in the PDB, represents the cornerstone for performing MD simulations [8,18]. Once the system has been built, the forces acting on every particle of the

system are estimated using a model known as a force field. Finally, from these forces, the classical Newton's equation of motion (Eq. 2.1) is used to compute accelerations and velocities and to update the atom positions [12,13,17,19].

$$\mathbf{F}_i = m_i \mathbf{a}_i = -\frac{\partial U(\mathbf{r}^N)}{\partial \mathbf{r}_i} \tag{2.1}$$

where m_i, and $\mathbf{a}_i$ stand for the mass and acceleration of particle i. $\mathbf{F}_i$ represents the force acting on particle i by the reminder of the particles of a system involving N particles, and is given by the negative partial spatial derivative of the potential energy function U, which is a function of the positions $\mathbf{r}^N = (\mathbf{r}_1, \mathbf{r}_2, \ldots, \mathbf{r}_N)$ of all N particles in the system [12,15].

The potential energy function of a molecular system, denoted as the "force field" (FF), describes the interactions that are established between particles. The FF consists of so-called bonded and non-bonded terms, thus accounting for the intramolecular and intermolecular interactions between particles, respectively. Thereby, the bonded terms are associated with bonds, angles, and torsions, whereas the non-bonded terms describe the electrostatic and van der Waals interactions, as it has been schematized in Figure 2.3 [12,15,20]. An example of a potential energy function is given by the following equation:

$$\begin{aligned} U(\mathbf{r}) = & \sum_{\text{bonds}} \frac{1}{4} K_b (b^2 - b_0^2)^2 \\ & + \sum_{\text{angles}} \frac{1}{2} K_\theta (\cos\theta - \cos\theta_0)^2 \\ & + \sum_{\text{impropers}} \frac{1}{2} K_\xi (\xi - \xi_0)^2 \\ & + \sum_{\text{dihedrals}} K_\phi [1 + \cos(\delta)\cos(m\phi)]^2 \\ & + \sum_{\text{pairs}} \left(\frac{C12_{ij}}{\mathbf{r}_{ij}^{12}} - \frac{C6_{ij}}{\mathbf{r}_{ij}^{6}} \right) + \sum_{\text{pairs}} \frac{q_i q_j}{4\pi\varepsilon_0\varepsilon_1} \frac{1}{\mathbf{r}_{ij}} \end{aligned} \tag{2.2}$$

where K_b represents the bond force constant, b the bond length, and b_0 the bond length at equilibrium; K_θ denotes the bond angle force constant, θ the bond angle, and θ_0 the bond angle at equilibrium; ξ is the improper dihedral angle, ξ_0 the improper dihedral angle at equilibrium, and K_ξ the improper dihedral force constant; ϕ represents the dihedral angle, δ the phase shift, m the multiplicity, and K_ϕ the force constant for torsional dihedral interactions; r_{ij} is the distance between particles i and j, $C12$ and $C6$ are the repulsive and attractive Lennard-Jones parameters respectively; ε_0 is the vacuum dielectric permittivity, ε_1 is the relative permittivity of the medium in which the particles are located, and q_i and q_j are the charges of particles i and j, respectively [17,21].

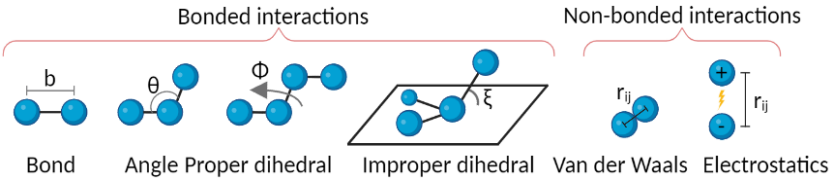

Figure 2.3. Types of interactions that are considered in the FF.

FFs are parametrized to fit quantum-mechanical calculations and/or experimental data [12,17,21]. The most commonly used FFs for MD simulations of biomolecular systems, such as, GROMOS, CHARMM, AMBER, and OPLS, have been constantly improved and tested over the years [12,15].

Different algorithms can be employed for numerically integrating the Newton's equation of motion, such as, leap-frog, Verlet or velocity Verlet. A simple and efficient algorithm is the leap-frog scheme. According to this algorithm, the leaf-frog velocity (**v**) and position (**r**) of particle i are given by [22,23]:

$$\mathbf{v}_i(t + \Delta t/2) = \frac{\mathbf{F}_i(t)}{m_i} \cdot \Delta t + \mathbf{v}_i(t - \Delta t/2) \tag{2.3}$$

$$\mathbf{r}_i(t + \Delta t) = \mathbf{v}_i(t + \Delta t/2) \cdot \Delta t + \mathbf{r}_i(t) \tag{2.4}$$

In these equations, t is the time and Δt denotes the simulation time step. This time step must be small enough so that the fastest vibrations are properly integrated. For example, including bond vibrations, which involve one of the fastest motions, requires the use of considerably small time steps (0.5 fs). The need of using small time steps in order to ensure numerical

stability represents the major bottleneck of MD simulations, as it makes simulations computationally demanding. To address this limitation, bond lengths can be constrained, since bond vibrations are commonly not of interest in MD simulations. In this regard, algorithms to constraint bond length, such as SHAKE, are routinely employed, which results in the possibility of using considerably higher time steps (2 fs) [8,19,22,23].

Biomolecular experiments are usually carried out at constant number of particles N, pressure P and temperature T (i.e., in the NPT ensemble). To ensure compatibility with experiments, MD simulations are performed in the isothermal-isobaric ensemble, that is, at constant temperature and pressure [24]. Pressure can be controlled by scaling the simulation volume, and the temperature by scaling the velocities. For that purpose, thermostat and barostat algorithms are used to keep the temperature and the pressure constant, respectively. Thermostat and barostat algorithms used in MD simulations include, but are not limited to, Berendsen, Nosé-Hoover, and Nosé-Hoover chain [22,23].

On the other hand, MD simulations of biomolecular systems not only involve the molecules of interest (e.g., a protein), but the solvent (typically water) also plays a pivotal role since biomolecules typically experience a hydrated environment. However, water is very dense, and thus, many water molecules are needed for hydrating a solute molecule, which is computationally very expensive due to the vast number of particles to be simulated. To circumvent this problem, several approaches have been developed, such as, implicit, explicit solvent models or coarse-grained water models. However, MD simulations are generally performed using explicit water models, for instance, the simple point charge (SPC) or the transferable intermolecular potential 4P (TIP4P). When simulating the solvent explicitly, the system boundaries must be treated in a special way [23,25]. For instance, if a shell of solvent molecules is placed around the solute, the solvent would evaporate. To circumvent this issue, periodic boundary conditions (PBC) are used. According to this approach, when particles cross the limits of the simulation box, they re-enter at the opposite site of the box, thus, creating infinite copies of the box. The concept of PBC for a two-dimensional system is illustrated in Figure 2.4. Additionally, there exist several shapes for space-filling boxes, such as, rectangular, triclinic, or truncated octahedron [23,26].

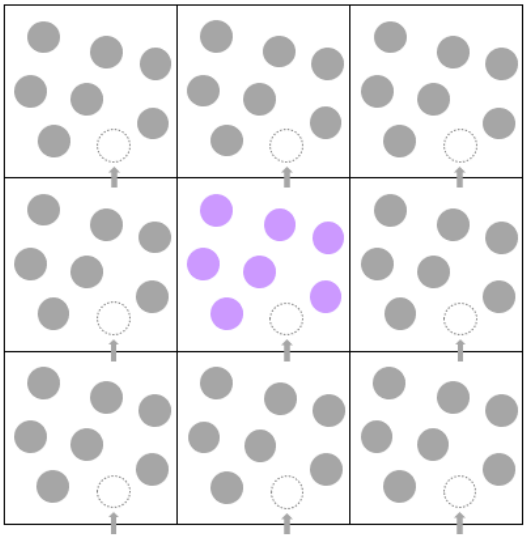

Figure 2.4. Graphic representation in two dimensions of the PBC. The simulation box is highlighted at the centre and is surrounded by periodic images of itself.

Collectively, an overview of the input parameters of MD simulations is depicted in Figure 2.5. It should be pointed out that for details about the equations that are involved in the aforementioned algorithms, the reader is directed to the following references (Ref. [22,27]).

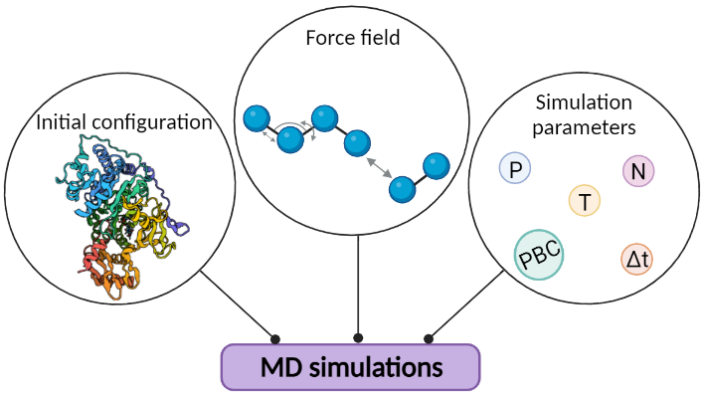

Figure 2.5. Ingredients of MD simulations.

Once the fundamentals of MD have been introduced, different model resolutions, enhanced sampling and free energy calculation methods that have been applied to investigate various LPS phenomena (e.g., the shield role of LPS in bacterial OMs, the TLR4 signalling pathway, etc.) are reported and discussed (subsections 2.2.2.1 and 2.2.2.2). Thereby, an overall picture of these computational methods is provided instead of purely focusing on those that have been used for designing LPS sequestration agents.

2.2.2.1. Model resolution and enhanced sampling methods: application to LPS research

As demonstrated from Figure 2.1, MD simulations have been used over the years to investigate phenomena related to bacterial LPS, which has significantly contributed to make progress on the development of different strategies (e.g., novel antibiotics, LPS sequestration agents, vaccines, etc.) to surmount LPS-caused infections [28]. With the pace of advances in the development of algorithms and in the computing power, the investigation of more complex LPS systems as well as the access to biologically meaningful time scales have been made possible [8,11,29]. Therefore, important progress on the elucidation of the mechanisms underlaying the bacterial resistance to different agents, key steps of the immune system activation and the interaction of LPS with bio-affinity ligands has been achieved by combining MD and different computational methods. These methods range from conventional atomistic to enhanced sampling methods. Recognizing such methods is crucial for moving a step forward on the elucidation of different events related to LPS, and thus, on the development of strategies to fight against bacterial infections. In this subsection, the MD methods that have been employed in the last four years for exploring LPS-related systems are briefly described. A more detailed description of these methods can be found elsewhere [6,30–37].

Depending on the definition of the elementary particles considered in the model, molecules can be represented at various levels of resolution, as schematized in Figure 2.6a. All-atom molecular dynamics (AA-MD) simulations, which rely on describing the molecules at atomistic resolution, represent the common approach to reproduce the motion of biomolecular systems [11–13]. According to this simulation method, the positions and velocities of every atom in the system are determined by solving Newton's

equations [12,13,15]. Thereby, AA-MD enables the simulation of biological processes of interest with considerable accuracy and high level of detail [31,38]. Due to the short time steps of AA-MD simulations (1-2 fs) that are required for ensuring the numerical stability, millions or billions of time steps are typically involved in AA-MD; this fact, along with the millions of interatomic interactions that are commonly evaluated during each time step, makes atomistic simulations greatly computationally demanding [8,11,39,40]. Therefore, despite enabling the capture of the biomolecules behaviour at atomic detail, the time (typically from nanoseconds to microseconds) and length scales that can be achieved by AA-MD simulations are insufficient to explore several biological processes of interest that take place on microsecond to second time scales [8,12,13,38].

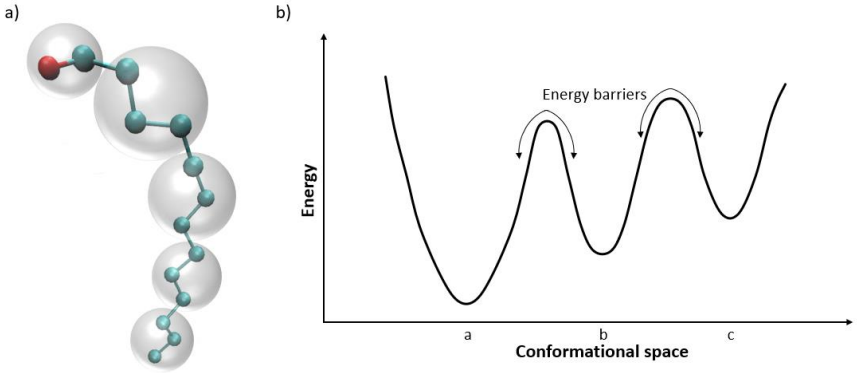

Figure 2.6. Schematics of (a) all-atom (balls and sticks) and coarse-grained (shaded spheres) representations and (b) the rugged energy landscape of a biomolecule.

A popular alternative to overcome the limitations of AA-MD is based on simplifying the representation of the biomolecules by using coarse-grained models [11,12,31]. As such, the modelling of individual atoms, characteristic of AA-MD, is replaced by describing groups of atoms as a single bead, which reduces the number of particle-particle interactions to be computed [11,12,33,38,41]. Therefore, coarse-grained molecular dynamics (CG-MD) enables the simulation of more complex and larger systems (hundreds of nanometers) and longer timescales (on the order of seconds) since the number of simulated particles is lower [11,12,33,40,42]. Consequently, as a result of the decrease in the number of degrees of freedom, the potential

energy surface is smoother. This fact, along with the absence of high frequency bonds, allows the use of longer integration time steps (10-30 fs) than typical time steps of AA-MD, which in turn implies longer simulations. Besides, smoothing the energy function also leads to faster sampling the conformational states of the system under investigation using CG-MD in comparison to AA-MD over similar timescales [11,33,39,40].

Although coarse-grained modelling enables the investigation of biomolecular processes beyond the time and length barriers of AA-MD, dismissing atomic details in the models of biomolecules may lead to inaccuracies on the properties to be predicted, as well as to the impossibility of examining other properties. Therefore, coupling the accuracy of all-atom models and the efficiency of coarse-grained ones is desirable [12,31,33,43]. In this regard, atomic resolution and time-size scalability can be accomplished by following different strategies, such as: (i) reconstructing all-atom structures from coarse-grained simulations (known as backmapping or reverse mapping), and (ii) using hybrid all-atom/coarse-grained (AA/CG) models for the simulations [31,42,44,45]. Backmapping entails the conversion of coarse-grained models to all-atom structures in order to recover atomic information from CG simulations [42,45]; conversely, hybrid multiscale AA/CG models combine different levels of resolution at once, providing an atomistic description of the regions of interest, while enhancing the sampling speed by using coarse-grained resolution in the remaining regions [11,36,41,44–46].

Additionally, when performing MD simulations, sufficient sampling of the conformational space of the system under investigation is of paramount importance, so that all physically relevant conformational states can be considered [47,48]. However, complex biomolecular systems are characterized by rugged energy landscapes, and the crossing of energy barriers between metastable states can be difficult. This fact leads to the trapping of such systems in energy wells of the conformational space, thus hindering the exploration of new states (Figure 2.6b) [30,35,48,49]. In order to surmount this limitation and widen the sampling time scales that are typically accessed by MD, several enhanced sampling approaches have been developed [30,49]. Furthermore, appropriate sampling enables the calculation of the free energy of the processes under study [11]. Therefore, in the following, the fundamentals of several enhanced sampling methods used

in LPS-research are briefly described. Prior to such explanation, it should be pointed out that enhanced sampling methods can be applied with both atomistic and coarse-grained molecular representations in order to successfully explore the system of interest [50]. Additionally, coarse-graining is also an enhanced sampling method since by coarse-graining the system the number of degrees of freedom is reduced and the potential energy surface is smoothened [11,12].

Umbrella sampling (US) is one of the most commonly used methods for enhancing sampling. In practice, this method introduces a bias potential (termed as umbrella potential) to guide the system from one state to another (e.g., from being free in solution to be bound to a membrane). The pathway between these states is covered by performing independent MD simulations (so-called windows) using umbrella potentials. Subsequently, individual umbrella windows can be combined using different methods, being the most commonly used the weighted histogram analysis method (WHAM). It should be pointed out that the choice of the parameters of the umbrella potentials is of paramount importance; for example, the selection of the force constant is key, since the bias potentials are typically harmonic [32,35,51–53]. Additionally, Hamiltonian replica-exchange with solute tempering (HREST) has also been used for enhancing the sampling efficiency. Particularly, in the HREST2 method the temperature is the same for all replicas, whereas the potential energy for each of them is scaled differently [54,55].

On the other hand, in steered MD (SMD) simulations conformational sampling is facilitated by applying a time-dependent external force to lead the motion of the selected atoms [30,32,37]. Typically, one end of the molecule is kept fixed, whereas the opposing one is subject to the external force (for instance harmonic), which can be applied following several protocols, including, pulling at constant velocity or force. It is worth mentioning that such force could be exerted to any atom or group of atoms, thus it is not restricted to be applied to the ends of the molecule [30,37,56,57]. For this simulation method the restraint stiffness and the pulling velocity are of paramount importance for the derived results [30,37].

Another approach for increasing the sampling is the adaptive biasing force (ABF) method, which is based on calculating and averaging the instantaneous force exerted along the coordinate of interest; then, an external biasing force with the same magnitude as the average force but in

opposing direction is adaptively applied [32,50,58]. Finally, the simulated annealing (SA) method relies on firstly heating the system to a high temperature (higher than the physiological temperature), and then cooling it down gradually. These heating-cooling cycles are typically repeated several times (10-100) [59–61].

2.2.2.2. Free energy calculations: application to LPS research

Gaining insights into LPS phenomena not only calls for the access to biologically meaningful length and time scales, but also could require the calculation of the free energy since it enables the understanding of thermodynamics aspects of the event under investigation [62–65]. Specifically, computing the free energy of the binding of LPS with other molecules (Figure 2.7) is of paramount importance to assess the ability of these molecules to bind to the endotoxin.

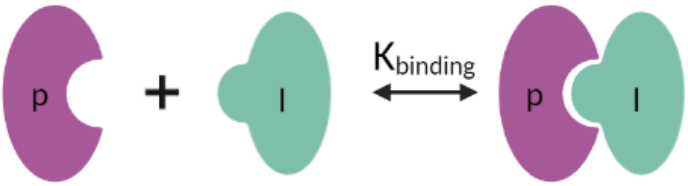

Figure 2.7. Schematic representation of protein(p)-ligand (l) binding.

Thereby, the affinity of a ligand to its target protein is determined by the change in the Gibbs free energy (ΔG_{bind}) of the system before and after the binding event [66,67].

$$\text{Protein} + \text{Ligand} \leftrightarrow \text{Protein} - \text{Ligand} \tag{2.5}$$

This equilibrium is characterized by the binding constant $K_{binding}$ (M^{-1}),

$$K_{binding} = \frac{[\text{Protein}-\text{Ligand}]}{[\text{Protein}][\text{Ligand}]} \tag{2.6}$$

where square brackets denote the equilibrium concentration of the protein-ligand complex ([Protein-Ligand]), the free protein ([Protein]) and free ligand ([Ligand]).

$K_{binding}$ is related to the binding free energy ΔG_{bind} by the following equation:

$$\Delta G_{bind} = -R_g T \ln K_{binding} \quad (2.7)$$

where R_g is the ideal gas constant and T the absolute temperature.

Since $K_{binding}$ or their corresponding ΔG_{bind} measures the ligand-receptor affinity, computational methods have been developed for determining ΔG_{bind}. Particularly, the LPS-molecule binding free energy can be computed *in silico* using several methods, which differ in accuracy and computational cost [11,68,69]. The linear interaction energy (LIE), solvated interaction energy (SIE), molecular mechanics Poisson−Boltzmann surface area (MM-PBSA) and molecular mechanics generalized Born surface area (MM-GBSA) methods are frequently used for free energy calculations since they exhibit an intermediate performance in terms of efficiency and accuracy [68,70,71]. These methods evaluate solely the initial and final states of the system, and thus they are called end-point methods [68,70,72].

The LIE method involves performing only two MD simulations: one of the ligand complexed with the receptor, and the other of the ligand in solution. Thereby, according to the LIE approach, the binding free energy is linearly proportional to the difference between energy averages of electrostatic and van der Waals interactions of the ligand with its surroundings in the bound and free states; these differences are scaled by two empirical parameters [32,58–60,68,71].

In the MM-PBSA and MM-GBSA methods, the free energy could be computed from three separate simulations (i.e. ligand-receptor complex, free receptor and free ligand); however, simulating only the complex is more commonly done due to stability issues [32,61,68,71]. Hence, the free energy is calculated from the vacuum molecular mechanics (MM) energies, the polar and non-polar solvation free energies and the conformational entropy change upon ligand-receptor binding. The polar contribution to the solvation free energy is calculated using the Poisson-Boltzman equation (MM-PBSA method) or a Generalized-Born model (MM-GBSA method) [70,71,73,74].

Finally, the SIE approach estimates the binding free energy from the intermolecular interaction energy in the bound state and the desolvation free energy, which represents the energy change between the bound and free

states. Both the interaction and desolvation contributions include a nonpolar and an electrostatic component [63,75].

2.2.2.3. Trajectory analysis

In this subsection, various methods that are typically used to analyze trajectories are introduced. It is worth mentioning that except DSSP (Dictionary of Secondary Structures of Proteins), which monitors the secondary structure elements of proteins, these methods can be applied to other (bio)molecules [22,23].

DSSP

DSSP is an analysis tool that identifies secondary structures of proteins via the analysis of backbone hydrogen bonds. Seven different secondary structures can be recognized, namely, bend, turn, β-strand, β-bridge, 3_{10}-helix, α-helix, π-helix.

Nuclear Overhauser Effect distances

The intermolecular nuclear Overhauser effect (NOE) is of paramount importance for determining the structure of proteins in solution NMR. The intensity of a NOE depends on the distance between spins I and S. The effective distance as sensed by the NOE in slow tumbling molecules, such as proteins from a MD trajectory is given by:

$$\mathrm{r_{NOE}}(\mathrm{i,j}) = \langle \mathrm{r_{i,j}^{-3}} \rangle^{-1/3} \tag{2.8}$$

However, $\mathrm{r_{NOE}}$ is generally not examined during simulation analysis but is used to compute the NOE distance violation in a protein simulation (i.e., $\mathrm{r_{NOE}^{exp}} - \mathrm{r_{NOE}^{sim}}$). Hence, by quantifying these violations, the fulfillment of the NOE distance restrains during the simulation can be checked.

Positional RMSD

The positional root mean square deviation (RMSD) is a measurement of how much the structures of two given conformation differ. For calculating the RMSD, the two structures are aligned, which is commonly addressed by least-squares fitting a set of atoms onto the reference structure; then, the square deviation between the position of every atom i ($\mathbf{r}_\mathrm{i}$) with respect to its

position in the reference structure $\mathbf{r}_i^{\mathrm{ref}}$ is computed:

$$\mathrm{RMSD}\left(\mathbf{r}, \mathbf{r}^{\mathrm{ref}}\right) = \sqrt{\frac{1}{N}\sum_{i=1}^{N}\left(\mathbf{r}_i - \mathbf{r}_i^{\mathrm{ref}}\right)^2} \tag{2.9}$$

RMSF

The root mean square fluctuation (RMSF) reflects the fluctuations of an atom coordinate ($\mathbf{r}_i$) around its mean ($\bar{\mathbf{r}}_i$) over the simulation time t_{total}. As for the calculation of the RMSD, the individual frames are commonly least-squares fitted to a reference structure before calculation.

$$\mathrm{RMSF}(\mathbf{r}_i) = \sqrt{\frac{1}{t_{total}}\sum_{t}^{t_{total}}[\mathbf{r}_i(t) - \bar{\mathbf{r}}_i]^2} \tag{2.10}$$

SASA

The solvent accessible surface area (SASA) is defined as the van der Waals surface of the molecule that is accessible to the solvent. It is calculated by rolling a solvent sphere with a defined van der Waals radius (0.14 nm for water) over the van der Waals surface of the solute molecule.

SASA enables determining, for instance, if residues on the protein surface tend to interact with water or with the protein itself. Hence, a decrease in the SASA denotes an unfavorable water-protein interaction.

Hydrogen bonds

Hydrogen bonding occurs between an electronegative atom and an electropositive hydrogen atom bonded to a second electronegative atom. In biomolecules, nitrogen and oxygen are typically the electronegative atoms. Hydrogen bonds are identified through two geometrical criteria, namely, the hydrogen-acceptor distance and the angle between the donor, hydrogen, and acceptor atoms. Typically, the hydrogen-acceptor distance should be around 0.25 nm and the angle above 135°.

Salt bridges

A salt bridge can be defined as an interaction between a pair of oppositely charged groups where at least one pair of heavy atoms lie within a hydrogen bond distance. In proteins, the side-chain carboxyl oxygen atom

of aspartic acid or glutamic acid and the side-chain nitrogen atom of arginine, lysine or histidine could be involved in salt bridges.

2.2.3. Modeling approach

Once a brief overview about the basic theoretical descriptions of the computational methods that have been used for investigating different phenomena of bacterial LPS has been provided, the *in silico* elucidation of the ALFPm3-LPS interaction mechanism is addressed. In this regard, the lipid A constituent, instead of the whole LPS molecule, was considered for the MD simulations. This choice, which considerably reduces the complexity of the system, arises from several observations. Firstly, lipid A harbors the ability of LPS for activating the immune system response, and thus it plays a crucial role in the development of sepsis. On the other hand, the lipid A moiety of LPS is key for several LPS-molecule binding events, and is the most toxic constituent of LPS [76–78]. Hence, in this work, *Escherichia coli* lipid A, whose structure has been represented in Figure 2.8, was selected to study its interaction with ALFPm3. In *E. coli* lipid A the glucosamines (GlcN I and GlcN II) that compose the β(1→6)-linked glucosamine disaccharide backbone are phosphorylated at position O1 of GlcN I and O4' of GlcN II. *E. coli* lipid A is hexaacetylated, thus six acyl chains of variable lengths are esterified with the disaccharide backbone. More specifically, the glucosamine disaccharide is N-acylated at positions 2 and 2' and O-acylated at positions 3 and 3' of GlcN I and GlcN II with 3-hydroxymyristatic [14:0(3-OH)] acid. These primary acyl chains in GlcN II are esterified at their 3-hydroxy group with so-called secondary acyl chains; thereby, the ester-linked acid carries a myristoyl group (14:0), and the amide-linked acid a lauroyl group (12:0). [78–80]

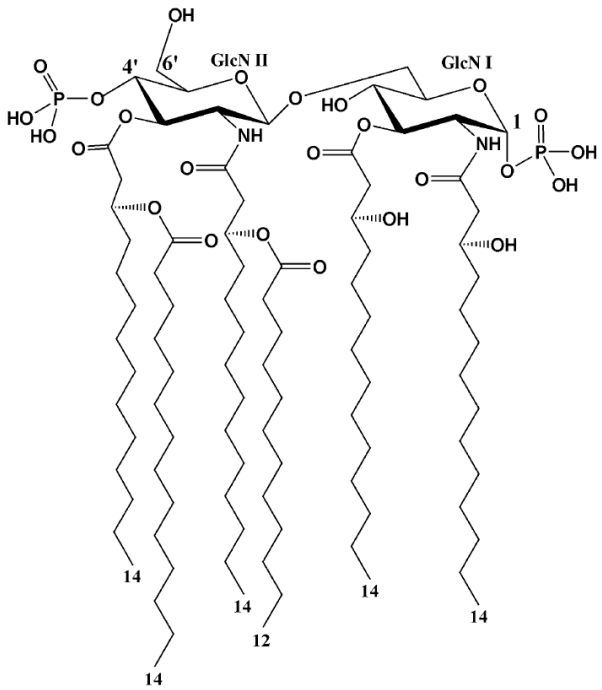

Figure 2.8. Chemical structure of *E. coli* lipid A. [78]

2.2.3.1. Biomolecular models

Deriving the structural model of the system to be investigated is of paramount importance for subsequently performing MD simulations. As mentioned in Chapter 1, the complex structure of ALFPm3 either with lipid A or LPS has not been resolved experimentally, which implies that any structure stored in the PDB can be directly used for the simulations. In view of the unavailability of the ALFPm3-lipid A complex structure, it was build using several computational approaches. To this end, the NMR derived structure of ALFPm3 was retrieved from the PDB (PDB entry: 2JOB). From the 15 conformers of the NMR structural ensemble, the atomic coordinates of the first conformer were used since according to Yang et al. [1] it was the best representative conformer. The ALFPm3-lipid A complex was built following the hypothesis of Yang et al. [1], Hoess et al. [2], and Ferguson et al. [79], who hypothesized that LPS binding molecules share a similar lipid A binding domain. Particularly, the procedure followed by Yang et al. [1] for proposing a possible lipid A binding site in ALFPm3 was applied. Thereby, the structure

of ALFPm3 was superimposed with that of a protein in complex with LPS, since the protein residues that are key for the binding with LPS should have their counterparts in ALFPm3 according to the hypothesis of Yang et al. [1] More specifically, the S1-S4 β-strands of ALFPm3 were superimposed to the 7-10 β-strands of FhuA (an *E. coli* ferric hydroxamate uptake receptor), whose structure in complex with LPS is available in the PDB under the accession code 1QFG. The β-strands of FhuA for the superimposition were selected on the basis that most of positively charged and several hydrophobic residues of this protein involved in the interaction with lipid A have their counterpart in the ALFPm3 structure. An almost perfect match between the amino acids of FhuA and ALFPm3 that Yang et al. [1] proposed as counterparts was obtained (see Figure A1.1 of Annexe A1). Subsequently, the FhuA and the constituents of LPS different from lipid A were removed. Given that the lipid A component of LPS that is in complex with FhuA (PDB ID: 1QFG) was incomplete since it lacked some acyls chains, the software MOE (Molecular Operating Environment) was used to add the atoms to the lipid A molecule that were absent. As a result, the ALFPm3-lipid A complex to be used as initial structure for the simulations was obtained (Figure 2.9).

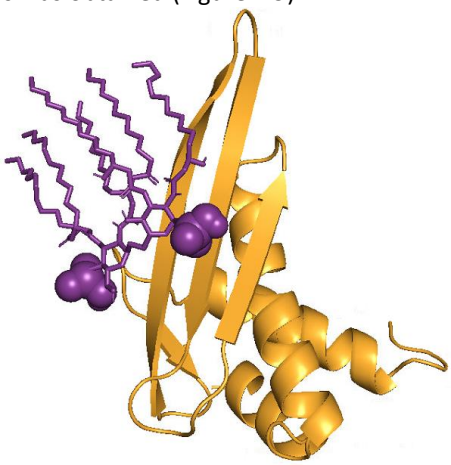

Figure 2.9. Initial structure of ALFPm3-lipid A complex for the MD simulations. Lipid A and ALFPm3 are coloured in purple and orange respectively.

AA-MD simulations were performed in water and in NaCl buffers (~ 50 and 150 mM NaCl) to investigate the influence of the ionic strength (NaCl concentration) on the ALFPm3-lipid A binding. Particularly, the 150 mM NaCl buffer was used to mimic the physiological ion concentration [81,82], whereas the 50 mM NaCl buffer was considered to test the effect of an intermediate ionic strength. On the other hand, MD simulations with and without applying restrictions to the protein structure were run to determine the conditions that ensure an appropriate ALFPm3 structure upon lipid A binding. These restraints derive from the NOE distances that are also stored in the PDB apart from the ALFPm3 NMR structure.

2.2.3.2. Simulation setup

Simulations were performed with the GROMOS11 simulation package on nVIDIA graphic processing units (GPUs). Running production MD simulations requires the previous preparation of the molecular system to be studied. More specifically, such system preparation entails several steps, namely, the generation of both the atomic coordinates and molecular topologies of all molecules involved in the system to be simulated, solvating the system, establishing the simulation box, relaxing the steric clashes, and the thermalization and equilibration of the system.

The GROMOS 54A8 force field was used for the protein. The topology of the protein was built assuming pH 7.0 for protonation states; the protonation state of all histidines was chosen to be neutral with the proton positioned on N_{δ}. On the other hand, the force field parameters of the lipid A were kindly provided by Prof. Chris Oostenbrink, who had optimized these parameters to study the interaction of lipid A with other biomolecules. The SPC water model was used to solvate the system. All systems were simulated in rectangular periodic boxes with a minimum solute-to-wall distance of 1.2 nm. Na^+ and Cl^- ions were added to neutralize the system and maintain the target NaCl concentrations (~ 50 and 150 mM NaCl).

Energy minimization of the systems was performed twice, that is, before and after the solvation, using the steepest descent algorithm. Thereby, undesirable steric clashes resulting from both the generation of the atomic Cartesian coordinates of the ALFPm3-lipid A complex, and the system solvation were relaxed. Prior to production runs, each system was thermalized and equilibrated. In this step, velocities were sampled from a

Maxwell-Boltzmann distribution at a low temperature (60 K) and the system was gradually heated up to the final production simulation temperature (300 K) for 20 ps with 2.0 fs time step. In this stage, the atoms of ALFPm3 and lipid A are positionally restrained to avoid an excessive disruption of the initial conformation due to the initial random velocities; these restraints were loosened while the system is heating up. Unconstrained production simulations were carried out in the NPT ensemble at 300 K and 1 bar. The weak coupling scheme was used for both temperature and pressure fluctuation control, with a coupling time of 0.1 and 0.5 ps respectively; an isothermal compressibility of $4.575 \cdot 10^{-4}$ $mol \cdot nm^3 \cdot kJ^{-1} \cdot mol$ was used for pressure coupling. The SHAKE algorithm was considered to constraint bond lengths of solute and solvent. Nonbonded interactions up to a short range of 0.8 nm were calculated at every time step from a pair-list that was updated every five steps. Interactions up to a long-range cutoff of 1.4 nm were computed at pair-list updates and kept constant in between. A reaction-field contribution was added to the electrostatic interactions and forces to account for a homogeneous medium with a dielectric permittivity of 61 outside the cutoff sphere. When the NOE distance restraints were applied to the protein in the production simulations, the force constant for distance restraining and the coupling time were set to 1000 $kJ \cdot mol^{-1} \cdot nm^{-1}$ and 1 ps, respectively. Three independent replicas with different random seed numbers for generating initial velocities were performed to allow scrutiny of the reproducibility of the results; each replica was run for 50 ns with a time step of 2.0 fs. Apart from GROMOS11 for conducting the simulations, VMD (Visual Molecular Dynamics), PyMol, and and Grace (GRaphing, Advanced Computation and Exploration of data) packages were used for visualization and graphical representation purposes.

Analysis of the trajectories was performed using GROMOS toolkit and in-house scripts. This analysis involves both examining the maintenance of the protein structure upon ligand binding and investigating the ALFPm3-lipid A interactions and binding mode. The maintenance of the protein structure during the simulations was verified through the determination of the protein secondary structure, the fulfillment of the NOE distances, and its stability. For that purpose, the dssp, prep_noe, noe, post_noe, rmsd and rmsf programs of GROMOS++ were used. In this work, the RMSD of the ALFPm3 backbone atoms (C-α, N, C) was derived and the RMSF of the protein backbone atoms was computed from the C-α protein atoms. Additionally, the RMSD of the

whole lipid A structure was calculated from the protein backbone atoms. The last frame of the equilibration trajectory was used as reference structure for these calculations (namely, protein RMSF and protein and lipid RMSD). The RMSD of the protein backbone atoms was also employed for verifying the convergence of the simulations. On the other hand, the elucidation of the ALFPm3-lipid A interaction mechanism and their binding mode were addressed by computing the hydrogen bonds and salt bridges that are established between these molecules, as well as by calculating the complex interface area and the ligand-binding free energy according to the LIE method. The use of this method arises from the fact that it has already been applied for estimating the binding free energy of lipid A and similar ligands with another biomolecule (namely, MD2) [83,84].

Hydrogen bonds were computed using the hbond program of GROMOS++. Particularly, a donor-acceptor pair was considered to be hydrogen bonded if the acceptor-hydrogen distance was lower than 0.25 nm and the donor-hydrogen-acceptor angle was higher than 135°. On the other hand, to determine the salt bridges that are formed between the negatively charged phosphates of lipid A and the positively charged residues of ALFPm3, in-house Bash and Python scripts were written. In line with the hydrogen bond analysis, a geometric criterion was also considered for determining if two oppositely charged atoms form a salt bridge. Accordingly, a cut-off of 0.7 nm between the central phosphorous atoms and the CZ, NZ, CG or CE1 of arginine, lysine, glutamic acid, or histidine was considered, respectively. This cut-off value was also used by Garate et al. [83] to compute the salt bridges that lipid A forms with other biomolecules. The conservation in other ALFs of the ALFPm3 amino acids that were identified to be key for the interaction with lipid A through hydrogen bond and salt bridge analysis was assessed by aligning the sequences of ALFPm3 with other ALFs. To this end, the multiple sequence alignment program "Clustal Omega" (European Bioinformatics Institute, EBI) (https://www.ebi.ac.uk/Tools/msa/clustalo/) was employed.

The interface area (IA) between ALFPm3 and lipid A was computed from the SASA of the protein ($SASA_{protein}$), the lipid ($SASA_{lipid}$), and the protein-lipid complex ($SASA_{complex}$). Specifically, since the complex interface area is not accessed to the solvent, it was calculated according to the following equation:

$$\mathrm{IA}_{\mathrm{protein-lipid}} = \frac{\mathrm{SASA}_{\mathrm{protein}} + \mathrm{SASA}_{\mathrm{lipid}} - \mathrm{SASA}_{\mathrm{complex}}}{2} \quad (2.11)$$

Finally, the binding free energy was determined according to the LIE method. This approach states that the interaction energy of the lipid with its surroundings when it is free in solution and when it is bound to the receptor need to be computed. Thereby, according to the LIE method, the binding free energy (ΔG_{bind}) is given by:

$$\Delta G_{bind} = \alpha \Delta \langle U_{l-s}^{vdW} \rangle + \beta \Delta \langle U_{l-s}^{el} \rangle \quad (2.12)$$

Where $\langle\ \rangle$ represents the MD energy averages of the nonbonded electrostatic (el) and van der Waals (vdW) of the ligand with its surrounding environment (l-s). The Δ stands for the difference between such averages in the bound (i.e., ligand in the binding site of the solvated receptor) and free (ligand in solution) states. The parameters α and β are scaling factors for these energy terms [58–60]. In this work, for computing the free energy of the ALFPm3 (receptor)-lipid A (ligand) binding, the electrostatic and van der Waals components of the interaction energy were weighted considering α = 0.18 and β = 0.09 as stated in the literature for calculating the binding free energy of lipid A with other proteins [83,84]. For computing ΔG_{bind}, the ene_ana tool of GROMOS++ was employed and the first two nanoseconds were discharged so that ΔG_{bind} could be calculated from the equilibrated part of the simulation. To compute the electrostatic and van der Waals energies of the ligand with its surroundings in the free state, simulations of lipid A in the absence of ALFPm3 were performed; specifically, three independent MD simulations with different random seed numbers were run in order to improve sampling and ensure the validity of the results.

2.2.4. Results

2.2.4.1. Influence of the ionic strength of the contact medium

Protein-ligand binding is highly dependent on the ionic strength of the medium where such contact takes place. Depending on the nature of both the ligand and the binding pocket, the ionic strength could enhance or hamper such binding as demonstrated by Papaneophytou et al. [85]. In light of this different influence, the impact of ionic strength on the ALFPm3-lipid A binding was *in silico* determined although the ALFPm3-lipid A binding for addressing the sequestration of bacterial endotoxin as potential sepsis

treatment would be performed at the blood ionic strength (∼ 150 mM). However, understanding how the ionic strength influences such binding could prove valuable for applications where biofluids are not involved, such as endotoxin removal from food industry, thus broadening the usefulness of the present study beyond the biomedical application.

As explained section 2.2.3.2, analysing the trajectories from the simulations not only entail the calculations that enable gaining insights into the ALFPm3-lipid A interaction mechanism, but also those about the maintenance of the protein structure upon ligand binding. Hence, the trajectory analysis described below begins with the verification of the protein structure and continues with the calculations that determine how ALFPm3 and lipid A interact. For the sake of simplicity, the most representative replica from the three performed at each NaCl concentration (∼ 0, 50 and 150 mM) has been selected for comparing the calculations that enable addressing the abovementioned issues.

Firstly, the DSSP analysis was performed to investigate the alterations in the ALFPm3 secondary structure upon lipid A binding. Hence, the DSSP analysis demonstrated the number of amino acids involved in different structures (α-helix, β-strand, turn, and bend) of ALFPm3. Figure 2.10a shows that regardless of the ionic strength of the contact media, the secondary structure of ALFPm3 comprises three α-helices (first α-helix: ∼ G6-L21; second α-helix: ∼ Q70-K88; third α-helix: ∼ Q93-S100) and four β-strands (first β-strand: ∼ K26-L29, second β-strand: ∼ H32-K43, third β-strand: ∼ Q46-C55, fourth β-strand: ∼ R62-T67), as it was determined in the work of Yang et al. [1], where the NMR structure of this protein was derived. Thereby, changes in the secondary structure of ALFPm3 as a result of the interaction with lipid A are hardly noticeable, thus, the secondary structure of ALFPm3 is preserved during the simulation time. The reader is directed to Figure A1.2 of Annexe A1 where the amino acids name and the single-letter amino acids code are included.

Additionally, the maintenance of the protein structure was also verified by computing the violations of the NOE distances. According to Figure 2.10b where the number of times that the NOE distances are violated are counted, low number of distance violations occurs. Specifically, the higher number of violations involves a distance of 0.025 nm for the three contact media, which is small enough to be neglected. Moreover, it is worth

mentioning that the NOE distance restraints were derived for the ALFPm3 without any bound ligand. However, in these simulations, both the protein and the lipid are involved; thus, the strict fulfilment of the NOE distances may not be addressed. This fact, along with the low violation distance, leads to the consideration that NOE distances are satisfied during the simulation for the three tested ionic strengths.

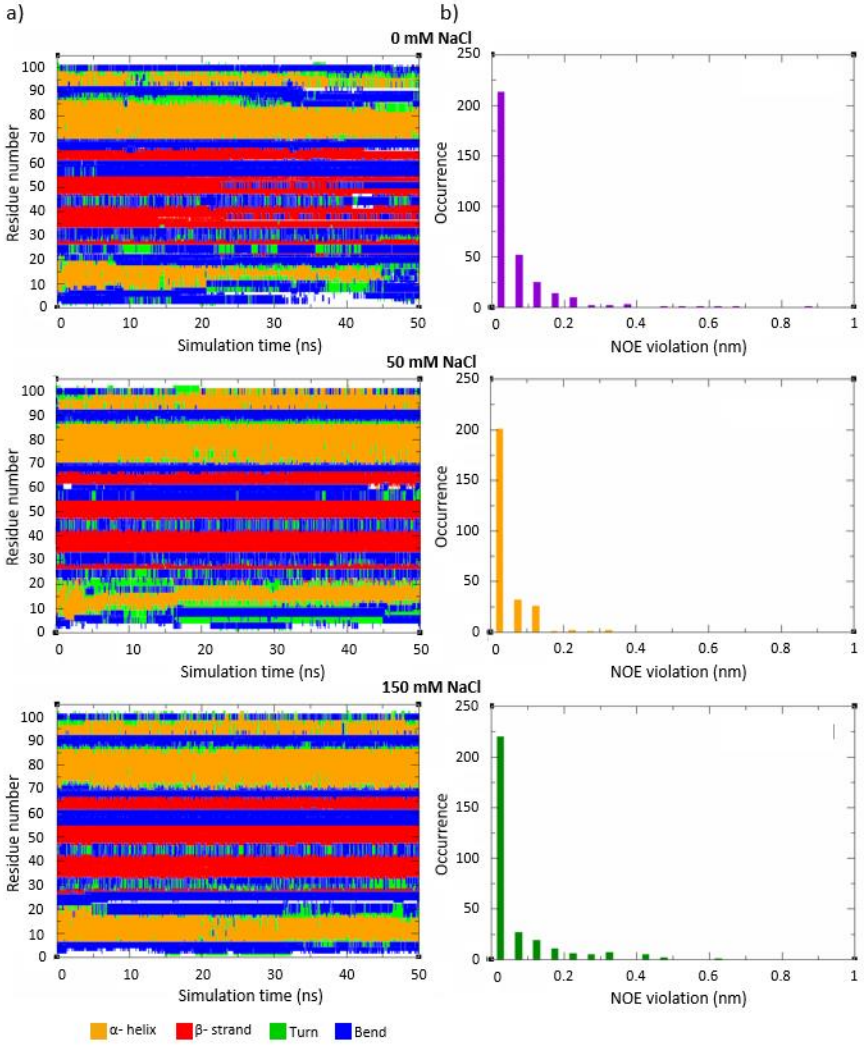

Figure 2.10. (a) Secondary structure and (b) NOE violations of ALFPm3 in different contact media.

Finally, protein stability was examined through the RMSF analysis of the ALFPm3 backbone atoms. As illustrated in Figure 2.11, a similar behaviour is observed for the three contact media. Hence, the highest RMSF values involved the backbone atoms of the residues that compose the first and second α-helices (which correspond to the atom numbers represented in the x axis of Figure 2.11 ~ 1-35 and 259-306 respectively), and the backbone atoms of the turn that connect the strands of the β-hairpin (atom number ~ 127-139). For the simulations where NaCl is used as contact medium (either 50 or 150 mM NaCl) the highest RMSFs involved the first α-helix; conversely, considerably lower RMSF values are obtained for the other α-helices and β-strands. Since the highest RMSFs entail the first amino acids of ALFPm3, which could not be completely derived by NMR, instead of the protein body, it can be substantiated that ALFPm3 did not exhibit high fluctuations along the MD simulations. However, when the simulations are performed exclusively in water, higher RMSF values are obtained in the protein body (second α-helices and the turn that links the strands in the β-hairpin), which could indicate that ionic strength impacts protein flexibility affecting either protein structure itself or the protein-lipid binding. In view of the protein structure analysis, it can be deduced that the ALFPm3 structure is maintained during its interaction with lipid A over the simulation time regardless of the ionic strength, since important changes in the amino acids that compose the secondary structure, fluctuations or violations of NOE distances were not noticed.

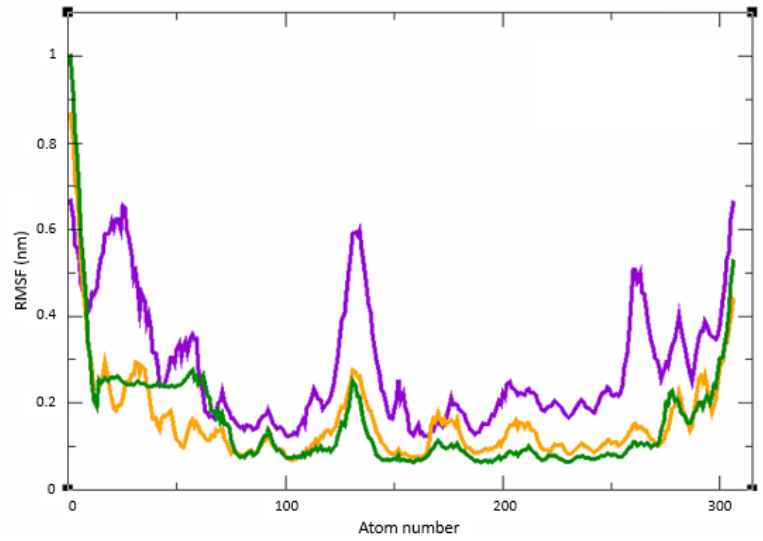

Figure 2.11. RMSF plot showing the residual fluctuation of ALFPm3 backbone atoms in different contact media: 0 mM NaCl (purple), 50 mM NaCl (yellow), 150 mM NaCl (green). Note that x axis represents the number of ALFPm3 backbone atoms (C-α, N, C).

Once the maintenance of the protein structure upon ligand binding has been verified, the next step involves investigating how the ionic strength affects ALFPm3-lipid A binding. For that purpose, the RMSD of the protein and the lipid, the interface area between the protein and the lipid and their binding affinity have been analysed. Figure 2.12a displays the protein RMSD from its initial structure for the production simulations. These results highlight the higher stability of the ALFPm3 when the binding is performed in NaCl buffer compared to the use of pure water as contact media. It can be noticed that an increase in the ionic strength leads to enhancing the protein stability. Thereby, when exclusively water is used for the environment of the ALFPm3-lipid A contact, higher protein RMSD values are observed, which denotes that the protein structure undergoes a significant change. In this case, the protein RMSD takes almost 40 ns to stabilize. Since the total simulation time is 50 ns, and according to the tendency of the RMSD graph, it cannot be ensured that ALFPm3 has reached a stable conformation throughout the simulation or that MD simulation converges. Conversely, the protein RMSD when NaCl (either 50 or 150 mM) is used for the contact

medium shows a stable tendency around low RMSDs values along the 50 ns long MD simulations, which demonstrates the stability of the protein conformation and the convergence of the MD simulations. Therefore, protein flexibility and stability revealed by RMSD of its backbone atoms show that NaCl stabilizes ALFPm3, which support the use of NaCl buffers for the endotoxin capture by ALFPm3.

Regarding the lipid A RMSD (Figure 2.12b), it exhibits a similar behaviour to that of the protein. Thereby, when NaCl is used as buffer lipid A reaches faster a stable conformation and the convergence of the simulation could be ensured. On the other hand, the high RMSD values reveal a high dynamic nature and flexibility, which arises from the aliphatic tails of the ligand. The dynamic behaviour of the lipid implies that during the simulation it covers different locations of the conformational space to find an energetically comfortable conformation. Thus, the stable position of the lipid respect to the protein that results from the simulation could considerably differ from that at the beginning of the simulation according to the high RMSD values.

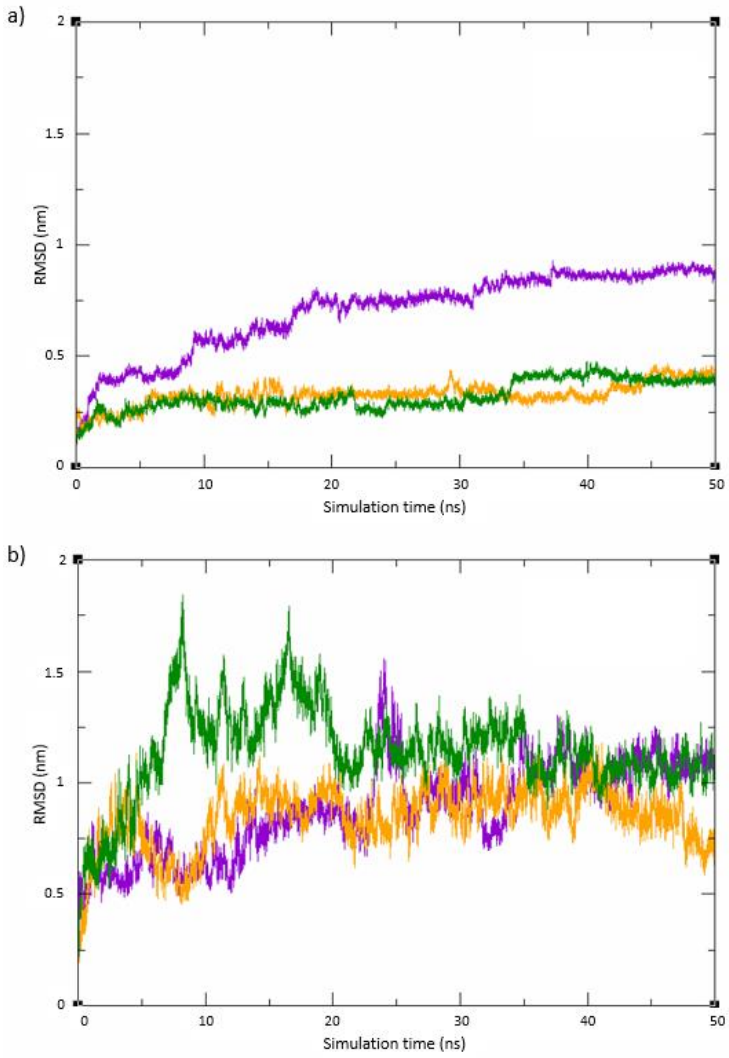

Figure 2.12. Time-series of the RMSD of (a) ALFPm3 backbone atoms, and (b) lipid A structure in different contact media: 0 mM NaCl (purple), 50 mM NaCl (yellow) and 150 mM NaCl (green).

To verify the abovementioned result, snapshots at both the beginning and end of the simulation were taken for the 50 and 150 mM NaCl systems (Figure 2.13). The comparison of these snapshots reveals that a considerably different binding pose is observed. More specifically, the binding mode at the

beginning of the production simulation is similar to that of the complex system used as initial structure for the simulations (i.e., the one derived from the superimposition of ALFPm3 with FhuA, see Figure 2.9). In that pose, lipid A is oriented downwards and faces the external side of the protein β-hairpin. However, when the system is allowed to freely move and interact during the production of MD simulations, the lipid A changes its orientation and tends to move towards the back side of the β-hairpin, that its, to the ALFPm3 cavity. This indicates that the structure derived according to the procedure of Yang et al. [1] (Figure 2.9) differs from the stable ALFPm3-lipid A binding mode. Additionally, taking into account the highly hydrophobic content of lipid A and the binding pose discovered from the simulations, where this ligand tends to move towards the back side of the β-hairpin, the lipid A binding site in ALFPm3 could be located in the protein cleft.

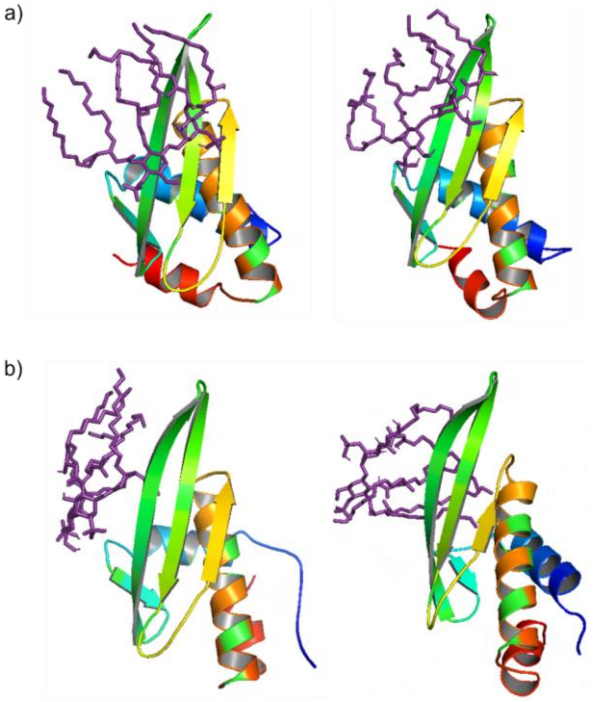

Figure 2.13. Snapshots showing the ALFPm3-lipid A binding mode at (a) the beginning, (b) the end of the MD simulations for the 50 mM NaCl (left) and 150 mM NaCl (right) systems. Lipid A is coloured in purple and ALFPm3 in rainbow colours.

To further assess the stability of the ALFPm3-lipid A binding the interface area of the contact between these molecules was calculated. A stable binding involves an interface area that oscillates around a constant value, since it implies that the protein and the lipid are bound along the entire simulation. Conversely, when the binding is unstable, the lipid and the protein are not constantly in contact, but at certain times water molecules and/or Na^+, Cl^- ions exist between them, and thus the interface area value drops to zero. According to Figure 2.14, the interface area does not remain stable along the simulation time regardless of the ionic strength of the media. Hence, the ALFPm3-lipid A binding mode that has been found with the simulations is unstable.

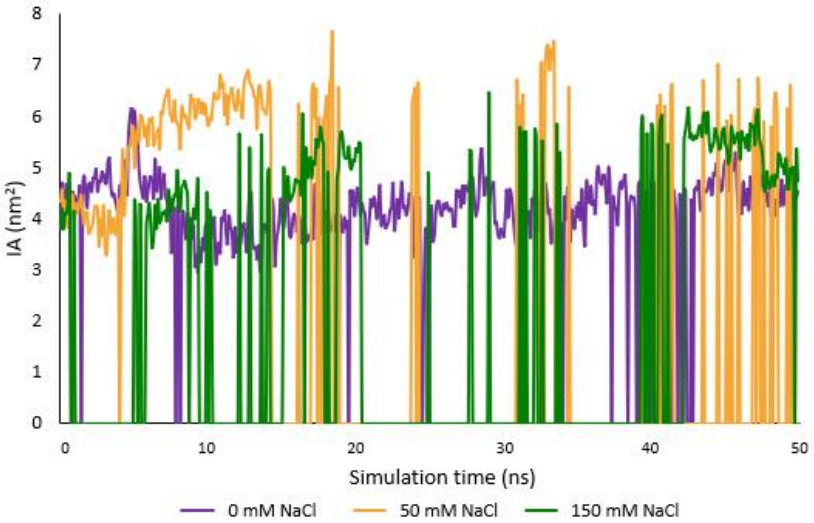

Figure 2.14. Time evolution of the ALFPm3-lipid A complex interface area in different contact media.

Finally, the binding affinity of ALFPm3 and lipid A in different contact media was determined according to the LIE method. Particularly, the binding free energy computed with this approach was used to determine the binding constants, as detailed in section 2.2.3.2. Additionally, the total binding free energy (ΔG_{bind}) has been decomposed into the van der Waals (ΔG_{bind}^{vdw}) and electrostatic (ΔG_{bind}^{elec}) contributions, being $\Delta G_{bind}^{vdw} = \alpha\Delta\langle V_{l-s}^{vdW}\rangle$ and $\Delta G_{bind}^{elec} = \beta\Delta\langle V_{l-s}^{el}\rangle$ (see Eq. 2.12). According to the free energy and affinity constant of the ALFPm3-lipid A binding in different media that have been included in

Table 2.1, more favourable binding free energies, and thus, binding constants are obtained when NaCl (either 50 or 150 mM) is used as contact media. Thereby, the binding constant increases one order of magnitude when the NaCl buffer is used compared to the simulations where exclusively water was used as contact media. On the other hand, according to (ΔG_{bind}^{vdw}) and (ΔG_{bind}^{elec}), increasing the ionic strength of the medium positively affects the hydrophobic interactions but negatively impacts the electrostatic ones between ALFPm3 and lipid A; this result agrees with the lipid movement from the protein front side to its cavity, where several hydrophobic amino acids are located as previously discussed.

Table 2.1. ALFPm3-lipid A binding free energies and binding constant in different contact media.

	0 mM NaCl	**50 mM NaCl**	**150 mMNaCl**
ΔG_{bind}^{vdw} (kJ·mol^{-1})	-9.51 ± 2.20	-13.85 ± 2.36	-22.25 ± 2.62
ΔG_{bind}^{elec} (kJ·mol^{-1})	-5.11 ± 2.47	-5.36 ± 2.05	4.28 ± 2.12
ΔG_{bind} (kJ·mol^{-1})	-14.61 ± 4.68	-19.21 ± 4.41	-17.97 ± 4.74
$K_{binding}$ (M^{-1})	3.51·10^{2}	2.22·10^{3}	1.35·10^{3}

Understanding the effect of the ionic strength of the contact medium on protein-ligand binding has received special attention, and the scientific community has devoted important efforts on studying protein-ligand interactions at varying salt concentrations [85–90]. As it was previously mentioned, depending on the nature of both the ligand and the binding pocket, increasing salt concentration has a different effect on the binding constant. Thus, Papaneophytou et al. [85] demonstrated that when both the ligand and the binding site were hydrophilic the increase of the ionic strength hampered the protein-ligand interaction. Conversely, when the ligand and the binding site were amphipathic, the ionic strength enhances the protein-ligand binding constant. Lipid A is an amphipathic molecule according to its constituents, which were described in in Chapter 1. However, the hydrophobic, hydrophilic, or amphipathic nature of the putative lipid A binding site in ALFPm3 has not been unveiled in the literature. In this work, the hydrophobic, hydrophilic or amphipathic nature of ALFPm3 was provided by Prof. Chris Oostenbrink as a result of a fruitful collaboration; it was calculated according to the spatial aggregation propensity (SAP) method [91,92]. It can be seen from Figure 2.15 that the back side of the protein cavity

involves both hydrophobic and hydrophilic patches, thus, this possible binding site has an amphipathic character. According to Papaneophytou et al. [85], when both the ligand and the binding pocket are amphipathic the increase of the ionic strength positively impacts the protein-ligand binding. Therefore, higher binding constants of ALFPm3-lipid A are obtained with using the 50 or 150 mM NaCl buffer than when the contact medium purely consists of water.

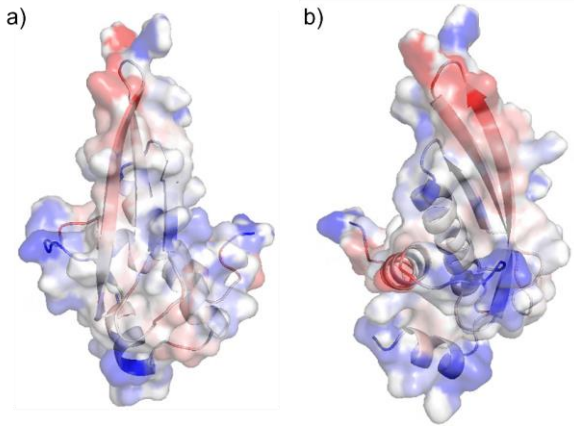

Figure 2.15. Visualization of the hydrophobic (red) and hydrophilic (blue) patches in the (a) front side and (b) back side of ALFPm3.

To sum up, the ionic strength of the contact medium does not influence the maintenance of the ALFPm3 structure as a result of its interaction with lipid A. On the other hand, the NaCl concentration positively affects the binding affinity of ALFPm3 and lipid A and promotes the reach of a stable conformation for both the protein and the lipid. Additionally, the lipid A binding site in ALFPm3 found as a result of the MD simulations agrees with the conclusion of Yang and coworkers [1], who stated that such binding site involves positively charged and several hydrophobic amino acids located in the back side of the protein. However, this binding pose notably differs from the one derived following the alignment procedure of Yang et al. [1], which mainly involved amino acids located in the external side of the β-hairpin. Despite the enhancement of ALFPm3-lipid A interaction when NaCl buffers are used, an unstable binding has been elucidated, since the protein and the lipid do not remain bound during the whole simulation but the molecules that compose the medium (water and/or Na^+, Cl^- ions) interpose between them.

Let's consider that lipid A binds to ALFPm3 in the protein cavity. To make this happen, the protein has to open up and adjust so that lipid A acyl chains could became buried in the protein core with the phosphates oriented towards water. However, applying the NOE distance restraints the protein is forced to satisfy such distances, which could hamper that it adopts a more open conformation, and ultimately the access of the lipid to the back side of the β-hairpin. In the following section, the ALFPm3-lipid A binding will be assessed in the absence of NOE distance restraints.

2.2.4.2. Effect of NOE distance restraints

In order to promote the completely free dynamics of the protein, and thus facilitate the access of lipid A to the back side of the protein β-hairpin, simulations of the ALFPm3-lipid A complex without applying NOE distance restraints to the protein were performed. Due to the positive impact of ionic strength on ALFPm3-lipid A binding and to mimic the physiological conditions, these simulations were conducted in 150 mM NaCl buffer. As with the previous set of simulations, the analysis of the trajectories involves both verifying the maintenance of the protein structure and shedding light into the ALFPm3-lipid A binding.

The DSSP analysis reveals that the secondary structure of ALFPm3, comprising three α-helices (first α-helix: ~ G6-L21; second α-helix: ~ Q70-K88; third α-helix: ~ Q93-S100) and four β-strands (first β-strand: ~ K26-L29, second β-strand: ~ H32-K43, third β-strand: ~ Q46-W54, fourth β-strand: ~ R62-T67), is maintained despite not applying NOE distance restraints as it has been illustrated in Figure 2.16a. On the other hand, as it could be expected, the absence of NOE distance restraints leads to an increase of the upper bound violations of the NOE distances since the protein is completely free to move (Figure 2.16b). Nevertheless, the violation distances with the highest occurrence (distances of 0.025 nm) are the same as those the simulations where NOE distances restraints were applied. Thus, the violations of the distances when the restrictions are not applied are low enough to be considered negligible. Collectively, ALFPm3 structure upon ligand interaction is maintained even if NOE distances restraints are not applied.

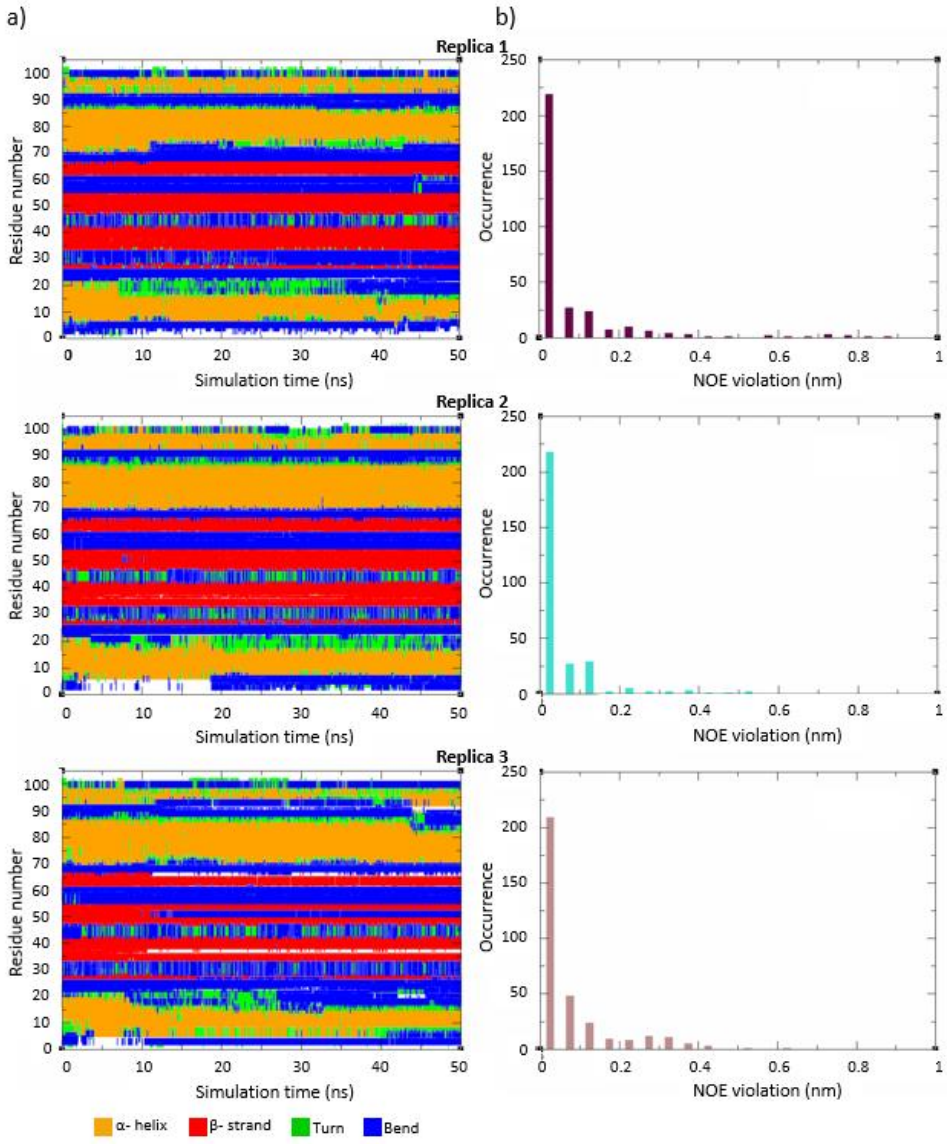

Figure 2.16. (a) Secondary structure and (b) NOE violations of ALFPm3 for the three independent replicas when the contact medium consists of 150 mM NaCl, and NOE distance restrains are not applied.

On the basis of the analysis of the protein RMSD during the three MD simulations (Figure 2.17a), it was confirmed that the protein reaches a stable conformation, and the convergence of the simulation is accomplished. The lipid RMSD (Figure 2.17b) reveals that the initial lipid conformation considerably changes during the first 20-30 ns of the simulation. Then, the lipid adopts a stable conformation, since from that time on, the RMSD remains oscillating around a constant value.

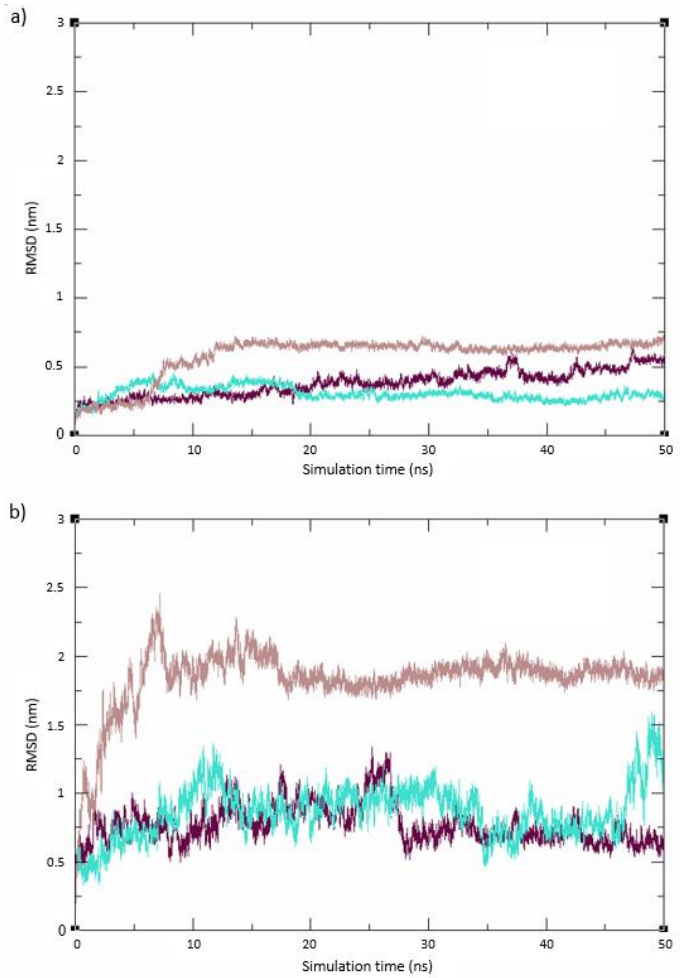

Figure 2.17. Time-series of the RMSD of (a) ALFPm3 backbone atoms, and (b) lipid A structure for the three independent replicas (first replica: maroon; second replica: turquoise; third replica: brown) when the contact medium consists of 150 mM NaCl, and NOE distance restrains are not applied.

The high lipid RMSD leads to the extraction of snapshoots at the end of the three simulations, in order to determine the ALFPm3-lipid A binding pose when NOE distance restraints are not applied. According to Figure 2.18, the lipid tries to reach the back side of the β-hairpin and to bury its aliphatic tails in the cavity of ALFPm3. Once again, this binding site seems reasonable given the highly hydrophobic nature of the lipid. Despite observing this tendency in all three simulations, the energy barriers of the conformational space could hinder the access of lipid A to the protein core, since the lipid has to cover a wide region of the conformational space to move from the initial conformation, where it is downwards and facing the external side of the protein, to the protein core, where it is upwards with the aliphatic tails buried in the protein and the phosphates facing water. Therefore, the complete insertion of lipid A in the cavity of ALFPm3 is only attained in one out of the three simulations that is, in the third replica.

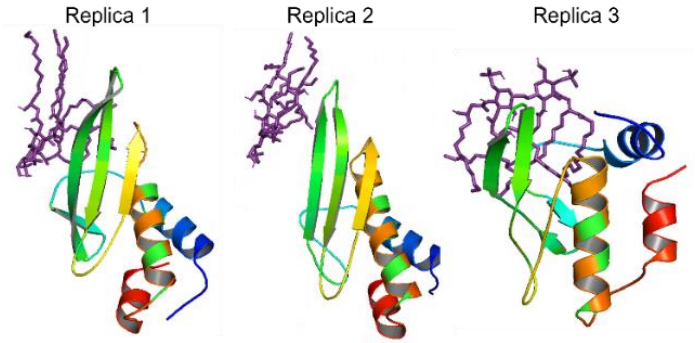

Figure 2.18. Snapshots at the end of the three independent simulations showing the ALFPm3-lipid A binding mode when the contact medium consists of 150 mM NaCl, and NOE distance restrains are not applied.

The change in the lipid conformation and location is also revealed by the salt bridges and hydrogen bonds analysis (Figure 2.19). More specifically, in the simulation where the lipid reaches the protein cavity (third replica), stable salt bridges along the simulation are not observed. However, when the lipid is not able to reach such protein cavity (first and second replicas), it establishes long-lived salt bridges with residues located in the external side of ALFPm3, namely, glutamic acid 25, E25, (salt bridge ID: 5), lysine 35, K35, (salt bridge ID: 9) and lysine 39, K39, (salt bridge ID: 11 and 12 since both phosphates of the lipid are involved in the salt bridges). These amino acids

have also been proposed by Yang et al. [1] to interact with lipid A. Particularly, the salt bridges that involve K39 and the lipid phosphates are highly stable and observed in the two simulations where the lipid does not reach the protein cavity.

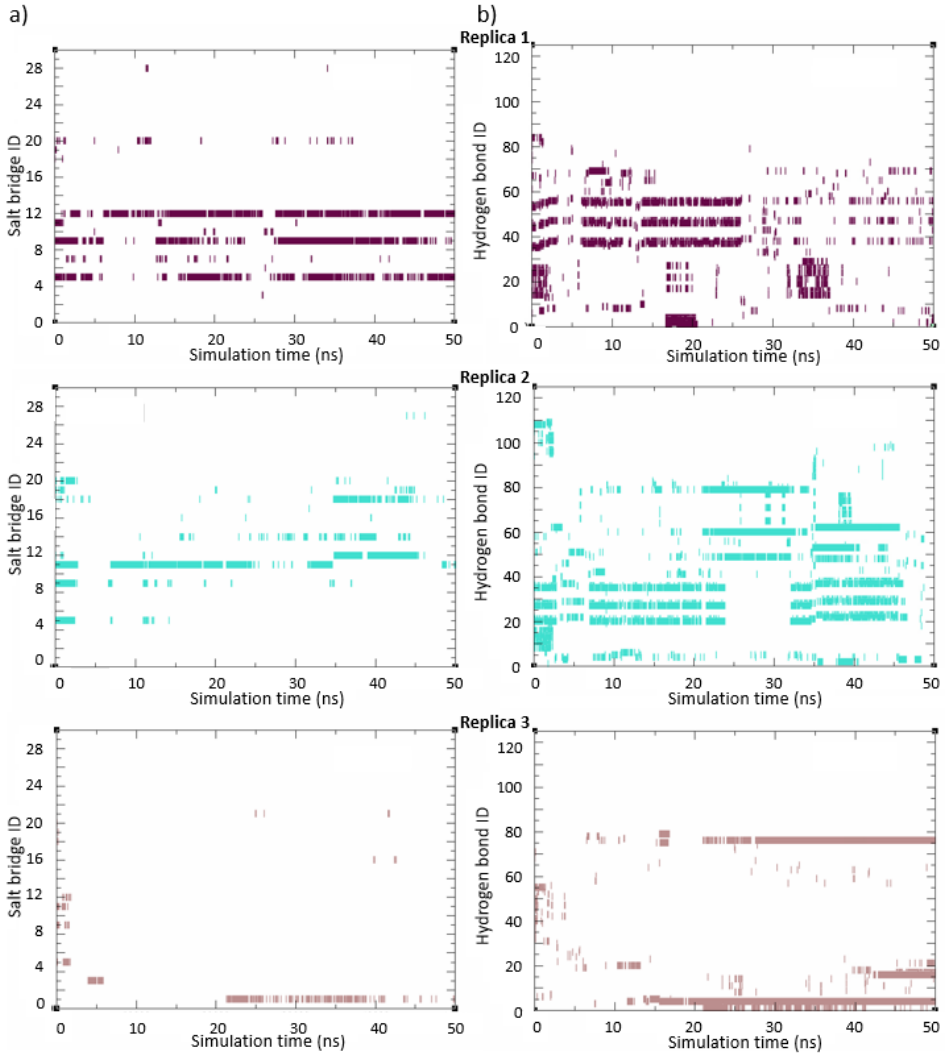

Figure 2.19. Occurrence of (a) salt bridges and (b) hydrogen bonds between ALFPm3 and lipid A for the three independent replicas when the contact medium consists of 150 mM NaCl, and NOE distance restraints are not applied.

Regarding the hydrogen bond analysis, it can be noticed from Figure 2.19b that when the lipid is anchored in the protein cavity (third replica) it binds through stable hydrogen bonds to ALFPm3 residues located in the protein cleft. Specifically, tyrosine 49, Y49, (hydrogen bond ID: 4) and glutamine 70, Q70, (hydrogen bond ID: 76), which are located in the protein cavity, establish hydrogen bonds with a percentage of occurrence higher than 40% with the lipid in the third replica. The importance of these residues in the ALFPm3-lipid A binding is reflected by the fact that the hydrogen bonds with the lipid where they are involved appear as long as lipid A tries to reach the back side of the protein. Conversely, in the simulations where the lipid does not reach the protein cavity (first and second replicas) short-lived hydrogen bonds are observed, being the occurrence percentage of them lower than 21%; additionally, Y49 and Q70 do not take part in them since these amino acids are located in the back side of ALFPm3.

Following the analysis of the ALFPm3-lipid A binding through the calculation of the interface area between the protein and the lipid (Figure 2.20), it can be observed that a stable binding is obtained for the third replica since the interface area oscillates around the same value ($\sim$ 7 nm^2); this simulation is the one that involves the complete burial of the lipid tails in the protein core. Conversely, the first and second replicas, where the lipid does not completely reach the back side of the β-hairpin, exhibit an unstable binding, since the protein and the lipid are not bound during the whole simulation as revealed by the drop to zero of the interface area value. The fact that stable interface areas are derived when the lipid is fully inserted in the protein core supports the suggestion that the lipid A binding site in ALFPm3 is located in the back side of the protein and that the stable binding pose entails the burial of the lipid acyl chains whereas the phosphates are exposed to the media.

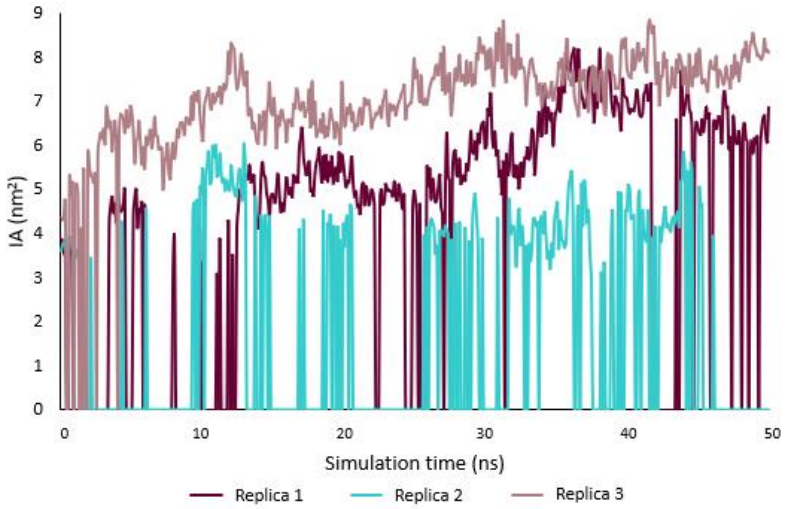

Figure 2.20. Time evolution of the ALFPm3-lipid A complex interface area for the three independent replicas when the contact medium consists of 150 mM NaCl buffer and NOE distance restraints are not applied.

The ALFPm3-lipid A free energy of binding determined according to the LIE method, which has been included in Table 2.2, also supports the stronger binding in the third replica (ΔG_{bind}= -24.24 kJ·mol^{-1}) than in the first and second ones. Therefore, the highest binding constant is obtained for the third replica ($K_{binding}$= 1.67·10^4 M^{-1}) which is two orders of magnitude higher than for the other simulations. By decomposing the binding free energy of the three simulations into its electrostatic and van der Waals contributions it can be demonstrated that the binding is dominated by hydrophobic interactions, since the van der Waals component of the binding free energies ($\Delta G_{bind}^{vdw} = \alpha\Delta\langle V_{l-s}^{vdW}\rangle$) is more favourable than the electrostatic component ($\Delta G_{bind}^{elec} = \beta\Delta\langle V_{l-s}^{el}\rangle$), which is near 0 or even positive for the second and first replicas respectively. The dominant role of hydrophobic interactions for the ALFPm3-lipid A binding arises from the nature of the ligand. The global and decomposed binding free energies as well as the binding constants have been included in Table 2.2.

Table 2.2. ALFPm3-lipid A binding free energies and binding constant for the three independent replicas when the contact medium consists of 150 mM NaCl, and NOE distance restraints are not applied.

	Replica 1	**Replica 2**	**Replica 3**
$\Delta \mathbf{G}_{\mathbf{bind}}^{\mathbf{vdw}}$ (kJ·mol^{-1})	-20.64 ± 4.09	-11.50 ± 2.33	-20.86 ± 2.29
$\Delta \mathbf{G}_{\mathbf{bind}}^{\mathbf{elec}}$ (kJ·mol^{-1})	5.68 ± 3.65	-0.92 ± 2.09	-3.38 ± 2.34
$\Delta \mathbf{G}_{\mathbf{bind}}$ (kJ·mol^{-1})	-14.96 ± 7.74	-12.42 ± 4.43	-24.24 ± 4.63
$\mathbf{K}_{\mathbf{binding}}$ (M^{-1})	$4.04 \cdot 10^{2}$	$1.46 \cdot 10^{2}$	$1.67 \cdot 10^{4}$

Given the high hydrophobic content of the lipid and the results of the simulations, it is reasonable to assume that the lipid tries to bury itself in the protein cavity where hydrophobic amino acids are located. However, this performance is not observed in all the simulations, although the lipid always leaves the conformation where it is facing the external side of the β-hairpin and moves toward the back side of the protein. A stable binding pose in the back side of the protein implies that the lipid remains buried in the protein cavity along the simulation time. Thus, to assess the stability of the binding pose derived from the third replica, simulations were run considering as initial structure one from this simulation.

2.2.4.3. Assessing ALFPm3-lipid A binding stability

To further confirm that the lipid A binding site in ALFPm3 is completely located in the back side of the β-hairpin instead of in both the front and back sides (i.e., lipid surrounding the protein) as hypothesised by Yang et al. [1], simulations using as initial structure one from the third replica of the simulations where NOE distance restraints were not applied are run. Thereby, the location of the lipid A binding site in the back side of ALFPm3 entails that the lipid does not leave the protein cavity during the simulation; otherwise, the binding site is not located in the protein cavity since the lipid tires to search for another binding site more energetically comfortable. As previously discussed, the ALFPm3-lipid A binding is driven by hydrophobic interactions. Hence, the complex structure with the most favourable van der Waals interaction energy was extracted from the trajectory of the third replica to be used as the initial structure for this new set of simulations; NOE distance restraints were not applied and 150 mM NaCl buffer was used as contact media. Since the maintenance of the ALFPm3 structure upon ligand binding in 150 mM NaCl when NOE distance restraints are not applied has been

already confirmed in the previous section, the analysis of the ALFPm3-lipid A binding was performed by computing the protein and ligand RMSD, the hydrogen bonds they form and their interface area and binding free energy.

The RMSD of the protein reveals that it maintains almost the same stable value along the 50 ns of the simulations for the three replicas as it has been depicted in Figure 2.21a. Additionally, the RMSD of the lipid (Figure 2.21b) oscillates around the same value during the simulation, which in turn implies that its insertion in the protein cavity gives rise to an energetically comfortable binding.

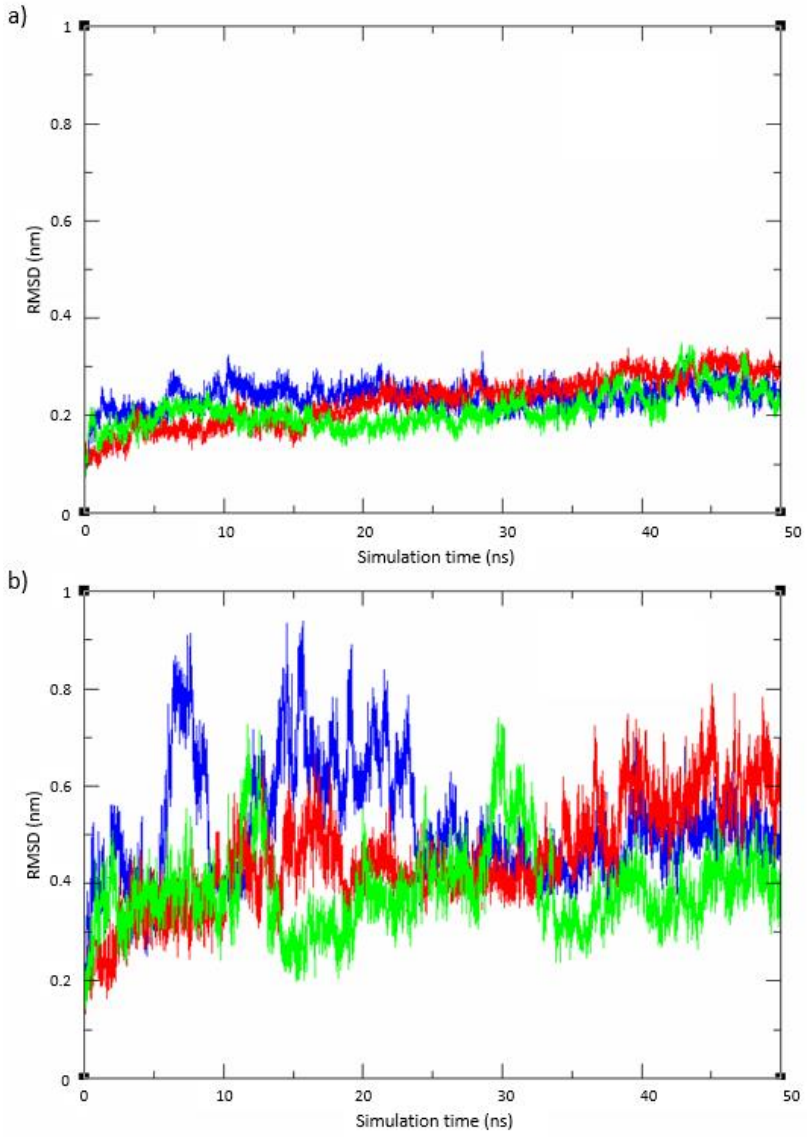

Figure 2.21. Time-series of the RMSD of (a) ALFPm3 backbone atoms, (b) lipid A structure, for the three independent replicas (first replica: blue; second replica: red; third replica: green) when the contact medium consists of 150 mM NaCl buffer, NOE distance restraints are not applied, and the initial complex structure involves the lipid buried in the protein cavity.

The comfortable binding site in the protein back side is also supported by the interface area. Hence, in contrast to previous simulations where the interface area drops to zero, in these simulations it remains stable oscillating around a constant value of ~ 8 nm^2 during the simulation as noticed from Figure 2.22.

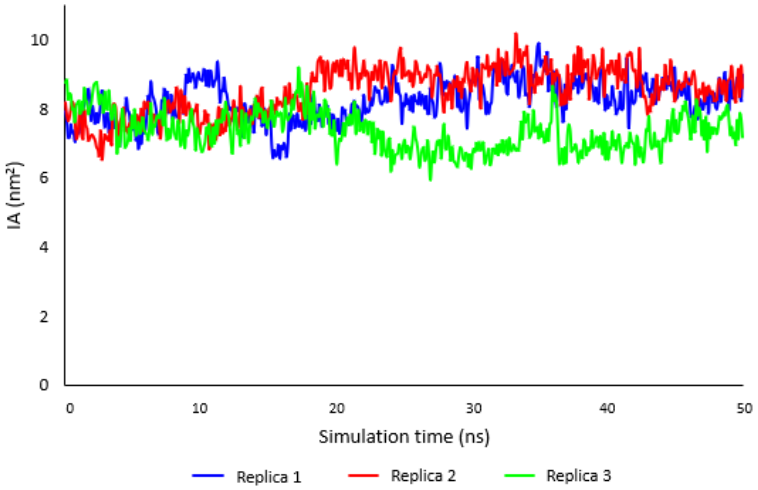

Figure 2.22. Time evolution of the ALFPm3-lipid A complex interface area for the three independent replicas when the contact medium consists of 150 mM NaCl buffer, NOE distance restraints are not applied, and the initial complex structure involves the lipid buried in the protein cavity.

The stable binding in the protein cavity is also revealed by the long-lived hydrogen bonds that lipid A establishes with amino acids located in that part of the protein. As noticed from Figure 2.23, Y49 (hydrogen bond ID: 2 in the first and second replicas, and 3 in the third replica) and Q70 (hydrogen bond ID: 29, 41, 37 in the first, second and third replicas, respectively) are the most stable hydrogen bonds along the simulation for the three replicas. Therefore, it can be considered that these amino acids are key for interacting with the lipid.

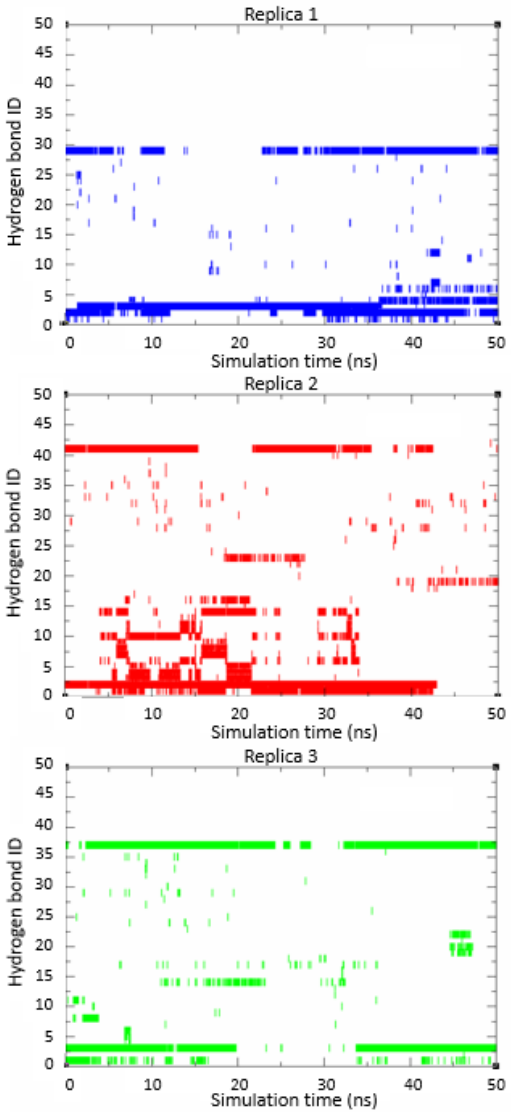

Figure 2.23. Occurrence of hydrogen bonds between ALFPm3 and lipid A for the three independent replicas when the contact medium consists of 150 mM NaCl buffer, NOE distance restraints are not applied, and the initial complex structure involves the lipid buried in the protein cavity.

The location of the lipid A biding site in the cavity of ALFPm3 was also confirmed by the binding free energies, its van der Waals and electrostatic contributions and the binding constants, which were included in Table 2.3. The binding free energy further confirms the binding of lipid A in the ALFPm3 cavity since its value is considerably more favourable for any of the three replicas than for the simulations reported in the previous sections. The lipid binding in ALFPm3 core involves the burial of its aliphatic tails into the protein cavity, which implies that hydrophobic interactions between these acyl chains and hydrophobic residues play a pivotal role in the binding. This fact is revealed by the van der Waals contribution to the binding free energy, which is not only more favourable than the electrostatic contributions for this set of simulations, but also than the van der Waals contributions of the simulations included in previous sections. Finally, the free energy yields an average binding constant ($K_{binding}$= $6.80 \cdot 10^4$ M^{-1}) of the same order of magnitude as that for the binding of LPS with other biomolecules [93].

Table 2.3. ALFPm3-lipid A binding free energies and binding constant for the three independent replicas when the contact medium consists of 150 mM NaCl, NOE distance restraints are not applied, and the initial complex structure involves the lipid buried in the protein cavity.

	Replica 1	**Replica 2**	**Replica 3**
ΔG_{bind}^{vdw} (kJ·mol^{-1})	-26.80 ± 2.35	-25.21 ± 2.77	-20.83 ± 2.17
ΔG_{bind}^{elec} (kJ·mol^{-1})	-0.08 ± 1.86	-4.50 ± 2.05	-0.63 ± 2.00
ΔG_{bind} (kJ·mol^{-1})	-26.88 ± 4.21	-29.72 ± 4.82	-21.46 ± 4.17
$K_{binding}$ (M^{-1})	$4.81 \cdot 10^4$	$1.50 \cdot 10^5$	$5.48 \cdot 10^3$

Collectively, the stability of the binding pose located in the back side of the β-hairpin, revealed by the protein and lipid RMSD and the interface area, along with the binding constant, has been confirmed. As it was previously discussed, the binding mode in the back side of ALFPm3 requires that the protein opens up and adjusts so that the lipid could be inserted. However, as a result of such structural change, the protein could not be able to recover its original structure if the lipid leaves the binding site due to the reversibility of the binding equilibrium. Thereby, if protein unfolds when the lipid is removed from the protein cavity, it implies that the binding site is not located in that part of the protein, since the protein-lipid interaction is reversible, and thus, the protein should recover its original conformation. To

assess the reversibility of the ALFPm3-lipid A binding despite the significant opening of the protein cavity, an ALFPm3-lipid A structure where the lipid is fully inserted in the protein cavity was extracted from these last simulations, and the lipid was removed. The resulting apo-ALFPm3 structure was used as the initial one for performing MD simulations. The superimposition of such apo-ALFPm3 and the ALFPm3 structure stored in the PDB (ID: 2JOB), which is illustrated in Figure 2.24, shows the considerably higher opening of the protein cavity in apo-ALFPm3.

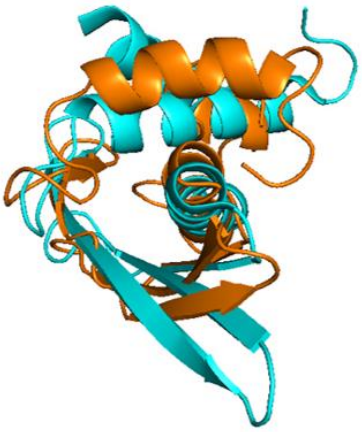

Figure 2.24. Superimposition of ALFPm3 structures: the one stored in the PDB (blue) and the one obtained from the MD simulations of the protein-lipid complex after lipid removal (orange).

The analysis of these simulations involves examining the elements that compose the secondary structure of the protein. Thus, the DSSP was computed. According to the DSSP analysis showed in Figure 2.25, the structure of apo-ALFPm3 after removing the lipid from its binding cavity comprises three α-helices (first α-helix: ~ G6-K17; second α-helix: ~ Q70-K84; third α-helix: ~ Q93-S100) and four β-strands (first β-strand: ~ K26-L29, second β-strand: ~ H32-K43, third β-strand: ~ Q46-W54, fourth β-strand: ~ G63-T67) as initially derived by Yang et al. [1]. Consequently, the reversibility of the protein-ligand binding has been *in silico* assessed, and thus, the location of the lipid binding site in the protein cavity has been verified.

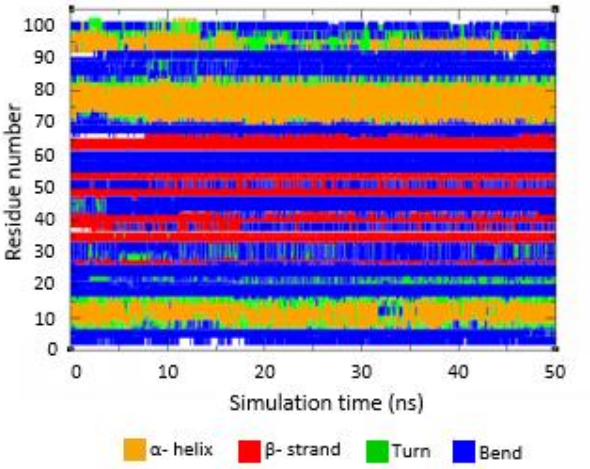

Figure 2.25. Secondary structure of apo-ALFPm3 derived after lipid removal from the protein-lipid complex.

From all *in silico* results provided through this chapter the interaction mechanism between ALFPm3 and lipid A can be proposed. Thus, MD simulations revealed that the lipid A binding site in ALFPm3 was located in the protein cavity and that the binding pose involves the burial of the lipid acyl chains in such cavity. Due to the high hydrophobic content of lipid A, it seems reasonable that the stable ALFPm3-lipid A binding is dominated by hydrophobic interactions. However, interactions between the phosphates and the positively charged residues of the outer face of ALFPm3 β-hairpin have been also observed in MD simulations. Taking into account that the interaction of LPS with other molecules, such as PMB, FhuA or lysozyme, comprises both electrostatic and hydrophobic interactions [94], it can be concluded that the ALFPm3-lipid A interaction consists of a two-stage process. More specifically, the positively charged residues that are located in the external side of ALFPm3 firstly recognise the phosphate groups of lipid A through electrostatic interactions. These electrostatic interactions are followed by hydrophobic interactions that drive the lipid movement towards the back side of the protein, where it buries its aliphatic tails in the protein cleft (Figure 2.26 a). Thus, a stable binding with the acyl chains inserted in the protein cavity and the phosphates exposed to the medium is achieved. In this interaction mechanism, three residues have been found to play a pivotal role, which have been depicted in Figure 2.26b. One of them (K39) is positively

charged and is located in the front side of the β-hairpin; it forms stable salt bridges with both lipid phosphates. On the other hand, Y49 and Q70, which are polar and neutral residues, are located in the protein cavity and establish hydrogen bonds with the lipid. Finally, it is worth mentioning that the binding mode herein elucidated resembles that of lipid A with MD2, a protein involved in the human immune system response against bacterial infection (see Figure A1.3 of Annexe A1), which also supports the stable ALFPm3-lipid A binding mode that has been elucidated through MD simulations.

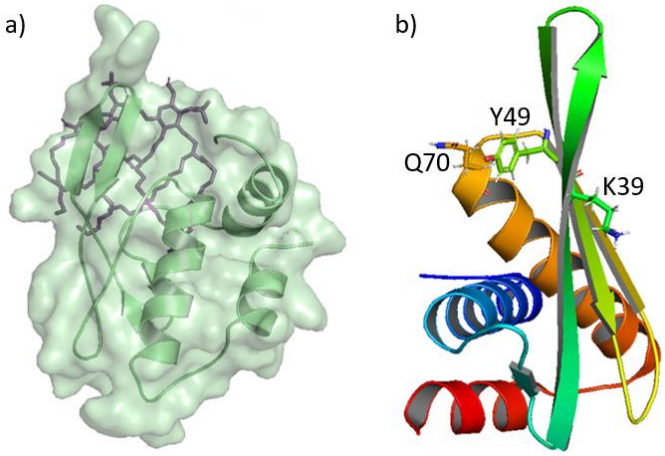

Figure 2.26. (a) ALFPm3-lipid A binding pose with the aliphatic tails inserted in the protein cavity (surface and cartoon representation of ALFPm3 in green and stick representation of lipid A in purple), and (b) representation of key amino acids of ALFPm3 for the interaction with lipid A.

2.2.4.4. Lipid A binding site in ALFs

In the literature it has been widely suggested that LPS binding molecules share a common LPS-binding epitope [1,2,79]. This fact, along with the similar secondary structure of ALFPm3 and LALF, which consists of three α-helices packed against a four stranded β-sheet, could lead to the conservation of the ALFPm3 amino acids that have been identified to play a pivotal role in the binding with lipid A (K39, Y49 and Q70) in LALF. If these amino acids were conserved in LALF, their importance in the binding with LPS/lipid A would be substantiated and the findings of this work would be broadened to other ALFs. To test this suggestion, the sequences of ALFPm3

and LALF were aligned (Figure 2.27). It was found that from the three residues (K39, Y49 and Q70) of ALFPm3 that were key to interact with lipid A, two of them (K39 and Y49) were conserved in LALF. More specifically, the counterparts of K39, Y49 and Q70 in ALFPm3 are K40, Y50 and R71 in LALF, respectively. While the nature of the amino acid is maintained in both proteins for K40-K39 (positively charged) and Y50-Y49 (polar and neutral), the type of the amino acid changes in Q70 (ALFPm3) and R71 (LALF). Thereby, Q70 of ALFPm3, which is polar and neutral, is aligned with R71 of LALF, which is positively charged. As a result of the alignment, it can be concluded that the ALFPm3 residues that are outstandingly crucial in the interaction with lipid A, are K39 and Y49 since they are conserved among several ALFs.

```
                  11          21          31          41          51
ALFPm3    EAYV-QGWEAVAAAVASKIVGLWRNEKTELLGHECKFTVKPYLKRFQVYYKGRMWCPGWT
LALF      EAEADGIWTQLIFTLVKNLATLWQSGDFQFLDHECHYRIKPTFRRLKWKYKGKFWCPSWT

           61          71          81          91          101
ALFPm3    AIRGEASTRSQSGVAGKTAKDFVRKAFQKGLISQQEANQWLSS--
LALF      SITGRATKSSRSGAVEHSVRNFVGQAKSSGLITQRQAEQFISQYN
```

Figure 2.27. Alignment of ALFPm3, and LALF amino acid sequences. Amino acids in the 39th, 49th and 70th positions of ALFPm3 are highlighted in blue.

2.3. *In vitro* validation of *in silico* predictions

2.3.1. Framework

Despite the important insights about the ALFPm3-lipid A binding that have been gained through MD simulations, the comprehensive determination of their interaction mechanism requires that *in silico* predictions match what happens experimentally. Hence, the *in vitro* validation of the *in silico* findings is addressed and described throughout the following sections. Particularly, the crucial role for binding to lipid A of the ALFPm3 residues identified by MD simulations (K39 and Y49) is assessed by quantifying the change in the binding affinity when these amino acids are substituted by others with opposite charge or polarity. Accordingly, if the predicted amino acids were key for interacting with lipid A, ALFPm3 would lose its ability to bind lipid A when they are substituted. Therefore, this methodology requires determining the binding affinity of both the original and substituted ALFPm3 towards LPS in order to decipher the effect of amino acid replacement. For that purpose, ALFPm3 with and without substituted amino acids need to be firstly synthesised, and then, contacted with LPS in order to quantify their binding ability.

As concluded from the MD simulations, the interaction of ALFPm3 and lipid A entails the initial recognition of the ligand by electrostatic interactions, and afterwards, a stable binding in the protein cleft driven my hydrophobic interactions. Hence, the validation of the interaction mechanism requires the individual substitution of residues involved in both steps. According to *in silico* results, the residue K39 plays a pivotal role in the lipid A recognition, whereas the hydrophobic residue Y49 is involved in the stable binding pose. Despite the possibility of individually substituting these two residues, special attention must be devoted to their role in ensuring the protein structure [20,95,96]. More specifically, if residues that are crucial for ALFPm3 folding are substituted, the protein would fall apart, which prevents the determination of its capacity to bind lipid A. Hydrophobic interactions are widely accepted to be key for the formation and stabilization of the protein's secondary structure [95]. Therefore, K39, which is positively charged and located in the external side of the protein facing water, does not play a pivotal role in the ALFPm3 folding. Conversely, Y49 is located in the protein cleft, and it can be engaged in polar interactions due to the polar groups of its structure

and in hydrophobic interactions through its aromatic ring [97]. Hence, it could be essential for protein folding. While there is the possibility of ALFPm3 unfolding as a result of the Y49 replacement, both substitutions (i.e., K39 and Y49) will be performed.

To demonstrate the role of K39 in the interaction of ALFPm3 with lipid A, it could be substituted by a residue with negative charge since lysine (K) is positively charged. Due to the length of the lysine side chain, glutamic acid (E) can be chosen instead of aspartic acid (D), which is shorter, for replacing lysine. Additionally, Y49 is a polar and neutral residue; thus, it can be substituted by a nonpolar residue, such as alanine (A) or phenylalanine (F). Tyrosine is an aromatic amino acid; thus, selecting another aromatic amino acid (i.e., phenylalanine) for the substitution could be beneficial since the aromatic ring could be involved in interaction with other side chain to maintain protein stability (for comparing the structures of alanine and phenylalanine see Figure A1.2 of Annexe A1).

Once glutamic acid and phenylalanine have been selected to substitute lysine and tyrosine respectively, the next step comprises the synthesis of two proteins, such that the sequence of one of them contains a glutamic acid in the 39^{th} position instead of a lysine, and the sequence of the other protein a phenylalanine in the 49^{th} position, instead of a tyrosine. The synthesis of two proteins, each of them having a different substitution, arises from the need of introducing individual amino acid changes so that the impact of these amino acids on LPS binding can be assessed independently. Additionally, as previously stated, the wild-type (WT) protein (i.e., the protein without the substituted amino acids) must be also synthesized to assess the impact of replacing these amino acids. For that purpose, a deoxyribonucleic acid (DNA) able to produce the WT protein is required so that a DNA that produces the protein with the substitutions could be obtained. Members of the Advanced Separation Processes (ASP) research group, where the present thesis is developed, have already obtained recombinant WT-LALF using genetic engineering techniques, and have also experimentally quantified the capacity of WT-LALF to bind LPS [98]. It is worth mentioning that protein synthesis is a tough task that involves tedious protocols; thus, obtaining a soluble protein is challenging. More specifically, the successful synthesis of WT-LALF involved the test of a vast number of experimental conditions until the most appropriate ones (i.e., those that enable the synthesis of soluble

WT-LALF) were found. Additionally, as discussed in section 2.2.4.4, a similar interaction mechanism of both LALF and ALFPm3 with LPS is expected due to the similarity of their 3D structures. These facts have motivated the use of the DNA of WT-LALF, which have already been obtained, instead of the DNA of ALFPm3, which is not available yet, to assess the importance of the *in silico* predicted residues in the interaction with lipid A. Therefore, the DNA coding for WT-LALF will be modified to enable the synthesis of LALF with the desired substitutions. On the other hand, the results of the WT-LALF-LPS binding, which have been previously obtained in the ASP research group, will be taken for comparing the ability of WT and substituted LALF to bind LPS.

The WT-LALF obtained in the ASP research group is a recombinant protein that apart from the LALF amino acid sequence, also comprises a maltose binding protein (MBP) stability tag in order to enhance the protein solubility, and a histidine tail composed of six histidines for facilitating the protein purification. For further information about the synthesis and structure of the WT-LALF, the reader is directed to the following work [98]. The alignment of such WT-LALF and ALFPm3 (see Figure A1.4 of Annexe A1) shows that the residues K39 and Y49 of ALFPm3 correspond to K37 and Y47 in WT-LALF, respectively. Thus, K37 and Y47 are the amino acids to be substituted in WT-LALF in order to assess their role in the interaction of WT-LALF with LPS.

To replace K37 and Y47, the nucleotide sequence of the DNA that produces the WT protein is altered, thus obtaining a DNA that makes the protein with the abovementioned substitutions (hereafter mutated protein). This methodology is called mutagenesis, which can randomly modify the WT-DNA sequence or generate at a specific change in a predefined way (namely, site-directed mutagenesis) [99]. Since for substituting K37 and Y47 with glutamic acid and phenylalanine, respectively, point mutations need to be generated, the site-directed mutagenesis (SDM) is performed. From the different approaches for SDM that have been developed, in this work the QuikChange™ method, which was developed by Stratagene (La Jolla, USA), is used since it is one of the most reliable and fastest strategies. It is worth mentioning that the protocol detailed below to obtain the two LALFs with the individual substitutions is carried out twice, so that two LALFs, one with the K37E substitution and the other with the Y47F substitution could be independently synthesised (hereafter K37E-LALF and Y47F-LALF).

The QuikChange™ method for SDM, which has been schematized in Figure 2.28, employs a pair of complementary oligonucleotide primers with the desired mutation and a DNA vector with an insert of interest (namely plasmid). In this particular case, the plasmid corresponds to that used in the ASP research group for synthetizing WT-LALF (see details in Ref. [98]). During a polymerase chain reaction (PCR), the DNA template, which contains the parental gene that encodes the protein, is firstly denaturalized; then, the mutagenic oligonucleotide primers are annealed to the template DNA and extended with a DNA polymerase. Subsequently, parental DNA is removed by enzymatic digestion with *Dpn* I endonuclease, which is a restriction enzyme that digests methylated and hemimethylated DNA. The product of this step is transformed into competent cells, which perform nick repair. Transformants are grown in Luria-Bertani (LB) agar plates containing the appropriate antibiotic for the plasmid vector, thus ensuring the survival of cells that take up the plasmid, while those without the plasmid will die [99–102].

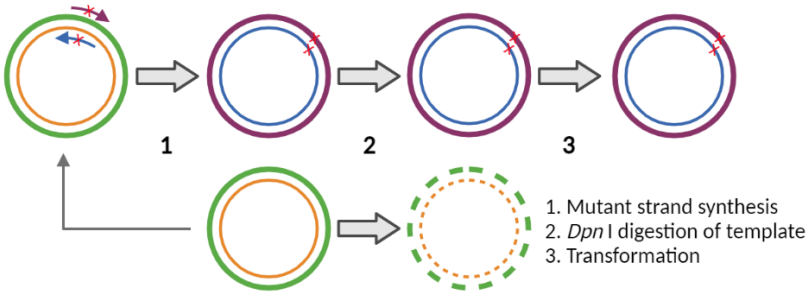

Figure 2.28. Overview of the QuikChange II SDM method. Adapted from Agilent Technologies, Inc [100].

Once the mutated DNAs (mDNAs), namely K37E-DNA and Y47F-DNA, have been obtained, they are transformed in a *E. coli* bacteria in order to express the mutated LALFs (mLALFs), that is, K37E-LALF and Y47F-LALF. Thereby, bacteria cells that contain mDNA reproduce, thus replicating the plasmid and passing it to their offspring. Then, bacterial cells containing mDNA are cultured so that they can be induced to transcribe and translate mLALF. Since the protein is synthesized inside the cells, they are lysed so that the target mLALF (K37E-LALF or Y47F-LALF), along with other proteins and macromolecules, is excreted. For isolating mLALF, the product of the cell lysis is subjected to purification protocols, in order to remove the molecules

released during lysis. Finally, the purified mLALF can be used for experimentally assessing its ability to bind to LPS. This procedure has been illustrated in Figure 2.29.

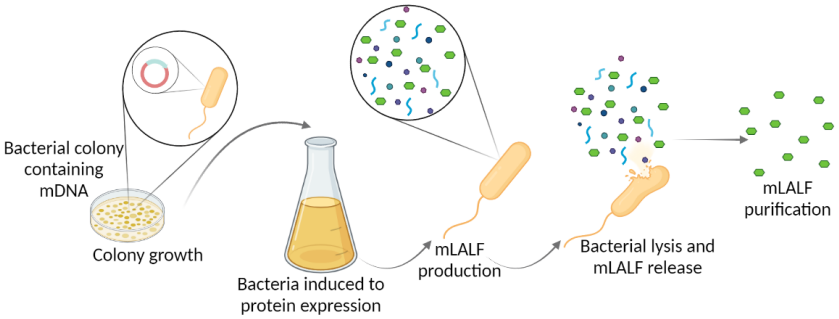

Figure 2.29. General procedure for K37E-LALF and Y47F-LALF synthesis.

Once K37E-LALF and Y47F-LALF are synthesised, the experiments for quantifying their capacity for capturing LPS are performed. These experiments comprise two steps. Firstly, the functionalization of the beads with the synthesized mLALF, that is K37E-LALF and Y47F-LALF (one at a time), is performed. Herein, agarose beads are used as a particle model system to anchor the mLALFs. Subsequently, the functionalized beads are incubated with LPS and their capacity for capturing LPS is determined.

2.3.2. Materials

Oligonucleotides for obtaining mDNA were designed and purchased to StabVida; additionally, oligonucleotides for Sanger sequencing were obtained from Integrated DNA Technologies (IDT) (Leuven, Belgium). Annexe A1 contains the oligonucleotide sequences for plasmid construction and for Sanger sequencing (Table A1.1). The QuikChange II SDM Kit was purchased from Agilent Technologies, Inc. Antibiotics, namely, kanamycin (Kn), and gentamycin (Gn) were obtained from Apollo Scientific. Isopropyl β-D-1-thiogalactopyranoside (IPTG) and PageRuler^{TM} Plus Prestained Protein Ladder were purchased to Thermo Scientific. Phenylmethylsulfonyl fluoride (PMSF), lysozyme from chicken egg white, and imidazole were from Sigma Aldrich. Dithiothreitol (DTT), sodium dodecyl-sulphate (SDS), and the GeneJET plasmid miniprep kit were obtained from Fisher Scientific, and acrylamide:bis-acrylamide from BioRad. Tris-HCl, NaCl, LB medium and LB agar medium were

acquired from Scharlab, S. L. HisTrap HP histidine-tagged protein purification columns (5 mL) and agarose beads were purchased to GE Healthcare, and BlueSafe protein stain to Nzytech. Fluorescein isothiocyanate-(FITC) labelled *E. coli* O111:B4 LPS (FITC-LPS) was purchased from Merck. Membrane MF-Millipone (0.45 µm pore size) and 30 kDa Centricon® centrifugal filters (Amicon ® Ultra) were obtained from Merck Millipore. Solutions were prepared with MilliQ® water.

C1000 TouchTM Thermal Cycler (Biorad) was used for the PCR reactions. Optical density (OD) and protein and DNA concentration measurements were carried out in a Nanodrop 2000c spectrophotometer (Thermo Scientific). A microPulser electroporator (Biorad) and 2 mm electroporation cuvettes (Molecular BioProducts) were used for mDNA transformation. Avanti J-30I centrifuge (Beckman Coulter, USA), Sorvall WX Ultra Series Centrifuge (Thermo Scientific) and Centrifuge 5810R (Eppendorf) were used for different centrifugation requirements. Electrophoresis was performed using the mini-protean system (BioRad). A MiniPlus 3 peristaltic pump (Gilson) was used to equilibrate and load the HisTrap HP histidine-tagged protein purification columns, and the fast protein liquid chromatography (FPLC) system ÄKTA type (GE Healthcare) for target protein elution from these columns. The concentration of FITC-LPS on supernatant was determined using the SPARK® multimode microplate reader (Tecan) in multiwell cell culture plates (96 wells) purchased to VWR.

Finally, the solutions and buffers employed for the experimental validation of the ALFPm3-LPS interaction mechanism has been listed in Table 2.4. The composition of each of them has also been specified.

Table 2.4. Solutions and buffers used for the experimental validation of the ALFPm3-LPS interaction.

Solution/buffer	Composition
SDS sample loading buffer 2x	50 mM Tris-HCl pH=6.8, 2% SDS, 10% glycerol, 0.1% bromophenol, 100 mM β-mercaptoethanol
1x SDS-PAGE buffer	25 mM Tris-HCl, 192 mM glycine, 1% SDS, pH= 8.4
Lysis buffer	100 mM Tris-HCl, 500 mM NaCl, 1% Triton X-100, 5 mM DTT, pH=7.5. Supplemented when used with 100 $\mu g \cdot mL^{-1}$ lysozyme, PMSF
Buffer A	100 mM Tris-HCl, 500 mM NaCl, 50 mM imidazole, pH=7.5
Buffer B	100 mM Tris-HCl, 500 mM NaCl, imidazole 500 mM, pH=7.5
Buffer C	50 mM Tris-HCl, 150 mM NaCl, 5 mM DTT, pH=7.5
Buffer D	50 mM Tris-HCl, 150 mM NaCl, pH=7.5

2.3.3. Experimental procedure

2.3.3.1. Mutagenesis

SDM

SDM was used to generate point mutants in expression vectors. For that purpose, the QuikChange II SDM Kit with *Pfu*Ultra high-fidelity (HF) DNA polymerase was employed. The mutant strand synthesis reaction was performed with the PCR conditions described in Table 2.5 and Table 2.6.

Table 2.5. PCR reaction mixture for SDM with QuikChange® II SDM kit.

Component	Volume
10x reaction buffer	5 µL
10 mM forward primer	1.1 µL
10 mM reverse primer	1.1 µL
dNTP mix	1 µL
Template DNA	0.5 µL
PfuUltra HF DNA polymerase	1 µL
H_2O	Up to 50 µL

Table 2.6. PCR program used for SDM with QuikChange® II SDM kit.

Time	Temperature (°C)	Cycles
30 s	95	1
30 s	95	12
1 min	55	
1 min/kb of plasmid length	68	
∞	4	1

An overview of the experimental procedure of SDM is depicted in Figure 2.30. The PCR product is treated with 1 µL of *Dpn* I restriction enzyme at 37°C for 1 hour to digest parental DNA template. *Dpn* I was inactivated by incubating *Dpn* I-treated DNA at 85°C during 5 minutes. Then, 1 µL *Dpn* I-treaded DNA was transformed into XL1-Blue supercompetent cells using heat pulses and plated onto LB agar plates containing the appropriate antibiotic for the plasmid vector (i.e., Kn). Finally, the existence of the desired mutations on mDNA was verified by extracting plasmid DNA from some colonies and sequencing.

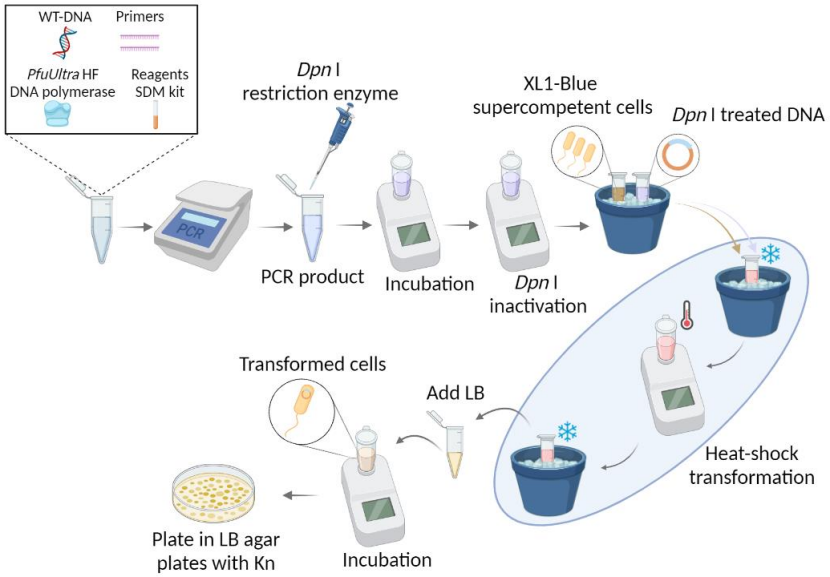

Figure 2.30. Procedure for SDM to generate point mutations in WT-DNA.

DNA extraction, nucleic acids quantification and Sanger sequencing

mDNA (K37E-DNA and Y47F-DNA) extraction was carried out using the GeneJET plasmid miniprerp kit following the manufacture's protocol. Once mDNA was extracted, its concentration was measured with Nanodrop 2000c spectrophotometer at a wavelength of 260 nm and using 2 µL of each sample. The purity of the extracted mDNA was confirmed considering that the 260/280 nm ratio was approximately 1.8.

Subsequently, mDNA was sequenced by the Sanger method through the "YouTube It" service provided by StabVida (Madan Parque, Portugal). Their recommendations were followed to prepare the samples (mDNA + primer). Finally, the nucleotide sequences provided by StabVida were converted into amino acid sequence using the online tool "Expasy" (Swiss Institute of Bioinformatics, SIB) (https://web.expasy.org/translate/). Then, the amino acid sequences of both K37E-LALF and Y47F-LALF were aligned to that of WT-LALF using the multiple sequence alignment program "Clustal Omega" (European Bioinformatics Institude, EBI) (https://www.ebi.ac.uk/Tools/msa/clustalo/).

2.3.3.2. Protein expression

Culture medium and bacterial growth measures

Once it has been verified that the obtained mDNAs include individually the desired mutations (one of them included the K37E substitution and the other the Y47F substitution) K37E-LALF and Y47F-LALF can be synthesised. LB supplemented with 50 $\mu g \cdot mL^{-1}$ Kn sterilized by filtration (0.22 µm) was employed for the cultures. Cultures growth was determined through OD at a wavelength of 600 nm (OD_{600}) using a Nanodrop 2000c spectrophotometer; a sample volume of 1 mL was used for the measurements.

DNA transformation

For mDNA transformation, *E. coli* ArcticExpress competent cells were transformed with mDNA by electroporation, which consists of the application of a high-voltage current to the cells that renders permeable the plasma membrane, thus enabling the entry of DNA to the cells [103]. For that purpose, Arctic Express competent cells were obtained through the following

protocol. Cultures were grown in LB with the appropriate antibiotic (Gn) until a OD_{600} of 0.5-0.7 was reached. Then, the culture was poured into a previously cooled falcon tube and centrifuged at 4°C for 15-20 minutes. The supernatant was discharged, and the pellet was resuspended following this order of washing: two washes with 10 mL of cold distilled water and subsequently, one wash with 10 mL of 10% cold sterile glycerol. The centrifugation conditions were the same as the abovementioned ones for these three washing steps. Then, the pellet of the last rinsing was resuspended in 200 µL of glycerol and centrifuged at 4°C during 15 minutes. Finally, the *E. coli* competent cells were aliquoted in 100 µL Eppendorf tubes (50 µL/tube) and frozen using dry ice and ethanol for achieving a fast freezing and then preserved at -80°C.

The transformation process itself (see Figure 2.31) was carried out by mixing 50 µL of *E.coli* ArcticExpress competent cells and 1 µL of mDNA (K37E-DNA or Y47F-DNA). This mixture was performed in a 2 mm electroporation cuvette that was previously cooled in ice. A microPulser electroporator was used to apply an electric pulse (2.5 $kV \cdot cm^{-1}$,25 µF capacitance and 200 Ω). Then, the pulsed cells were resuspended in 1 mL of LB preheated to 37°C and transferred to a 2 mL Eppendorf tube for being incubated at 37°C during 1 hour. Finally, 150 µL of the culture were spread on LB agar plates supplemented with the required antibiotics (i.e., Kn and Gn) to select the transformed cells.

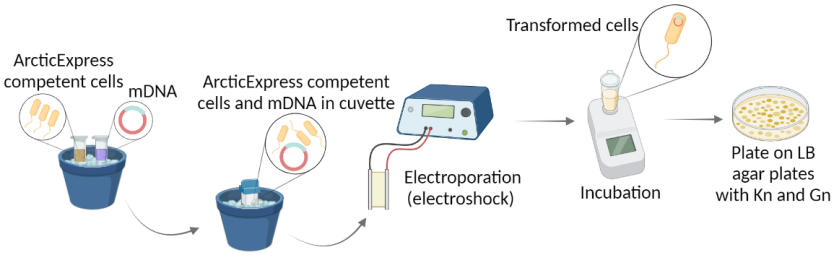

Figure 2.31. mDNA transformation process by electroporation.

Protein overexpression

For the overexpression of K37E-LALF and Y47F-LALF (Figure 2.32), an initial 50 mL culture of the transformed *E. coli* ArcticExpress was grown at 37°C overnight in LB medium supplemented with Kn and Gn. Then, the 50 mL culture were transferred to a 1 L flask preheated at 37°C, where Kn and Gn

were also added. This culture was grown with shaking at 37°C until the OD_{600} was 0.4-0.6. At this point, the induction was carried out by adding IPTG to the culture to a final concentration of 1 mM. The overexpression was done at 18°C overnight.

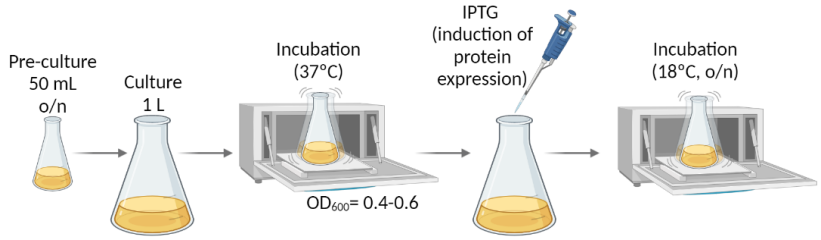

Figure 2.32. Schematics of the main steps for performing protein overexpression.

2.3.3.3. Protein purification

Cell lysate

The purification of the overexpressed K37E-LALF and Y47-LALF were addressed; the protocol for purifying these proteins, which has been schematized in Figure 2.33, is performed at 4°C in order to minimize their degradation. Thereby, the induced cell culture was harvested by centrifugation at 4000 rpm for 20 minutes using the Avanti J-30I centrifuge, and the resultant cellular pellet was frozen at -80°C. Then, pellets were thawed and resuspended in 50 mL of lysis buffer (see Table 2.4) supplemented with 10 µg/mL of lysozyme and 1:1000 PMSF (a protease inhibitor) and incubated during 30 minutes. Cell lysis was performed by sonicating the previous mixture during 3 cycles, which consisted of alternating 1 minute of sonication and 1 minute rest to avoid the sample being overheated. Subsequently, the cell lysate was ultracentrifuged at 40000 rpm during 15 minutes using the Sorvall WX Ultra Series Centrifuge. To verify protein expression, samples were taken, and the synthesised proteins were observed by electrophoresis under denaturalizing conditions.

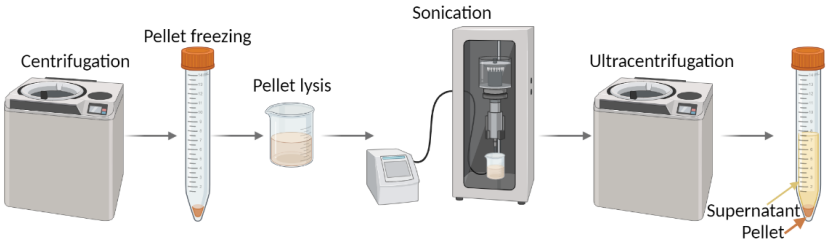

Figure 2.33. Procedure for obtaining soluble target protein (K37E-LALF and Y47F-LALF).

Protein electrophoresis under denaturalizing conditions

The successful expression of K37E-LALF and Y47F-LALF were analysed by sodium dodecyl-sulphate polyacrylamide gel electrophoresis (SDS-PAGE). The procedure for SDS-PAGE has been depicted in Figure 2.34. Gels containing 15% of acrylamide were used due to the size of the proteins, and prepared with 0.1% SDS and acrylamide:bis-acylamide (29:1). Pellets were resuspended in 150 µL of 2x loading buffer (see Table 2.4), and supernatant samples were mixed in a 1:1 volume ratio with this buffer. These samples were boiled for 5 minutes before loading 15 µL of them into acrylamide gel wells. 5 µL of PageRuler^{TM} Plus Prestained Protein Ladder were used as molecular weight marker. Electrophoresis was performed using a Mini-protean system at 180 V during 45 minutes in 1x SDS-PAGE buffer (see Table 2.4). Finally, protein fractions in acrylamide gels were observed using BlueSafe protein stain.

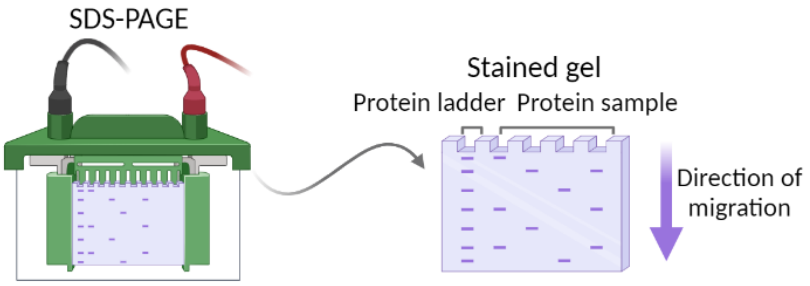

Figure 2.34. SDS-PAGE and target protein detection.

Immobilized Metal Affinity Chromatography (IMAC)

Protein purification was carried out using a 5 mL HisTrap HP histidine-tagged protein purification column (Figure 2.35). These columns are packed with Ni-NTA (nickel nitriloacetic acid) agarose resins; thereby, the nickel anchored on the resins binds to the 6x histidine tag that was included in the protein sequence [98]. The supernatant obtained from the ultracentrifugation of the cell lysate was loaded onto the column, that was previously washed with 5 column volumes (CV) of filtered and sterile MilliQ® water and equilibrated with 5 CV of buffer A (see Table 2.4) using a MiniPlus 3 peristaltic pump. Afterwards, the flow through was saved and the column was once again equilibrated with 5 CV of buffer A prior to being connected to the FPLC system ÄKTA type. The ÄKTA equipment was used to elute the proteins bound to the column through a buffer B (see Table 2.4) gradient following this procedure: initial wash with 5 mL of buffer A, 0-100% gradient of buffer B in 15 fractions, rinse with 15 mL of buffer B and final wash with 15 mL of buffer A. Samples of elution fractions were analysed by SDS-PAGE to confirm the presence of the 58 kDa band belonging to LALF proteins. All buffers employed for protein purification were previously filtered using Membrane MF-Millipore (0.45 µm pore size) in order to remove particles that could lead to damage the HisTrap column.

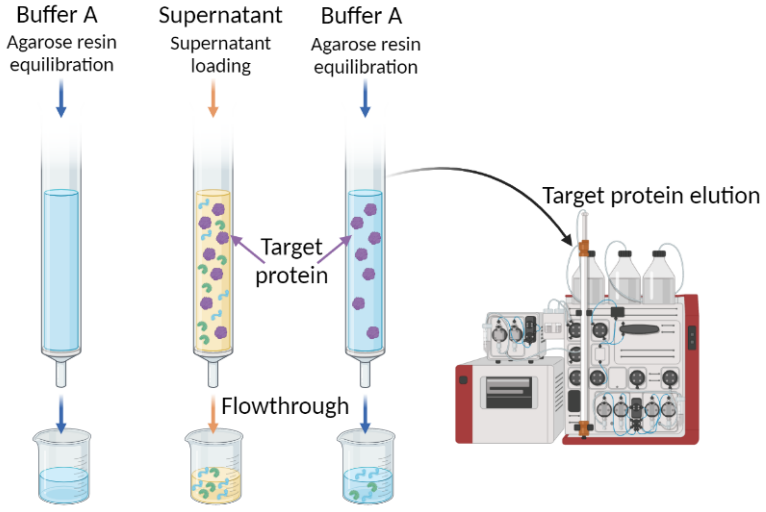

Figure 2.35. Protein purification procedure.

Protein concentration and buffer exchange

Protein solutions that are obtained from the purification step contain a high concentration of salts (NaCl, imidazole) and low protein concentration. In order to decrease the salt content and concentrate the target protein, 30 kDa Centricon® centrifugal filters were used. This filtration system enables the passage of small molecules while retaining the target protein. Thereby, the product of the purification was mixed with buffer C (see Table 2.4) in Centricons and centrifuged at 42000 rpm and 4°C using the Centrifuge 5810R. This procedure, which has been schematized in Figure 2.36, was repeated until an appropriate protein concentration was reached. Protein concentration was determined by measuring the absorbance at 280 nm using the Nanodrop 2000c spectrophotometer, where the extinction coefficient ($\varepsilon = 104.5\ \mathrm{mol} \cdot \mathrm{L}^{-1}$) and the molecular weight (57.9 kDa) of the LALF proteins were introduced. Finally, the pure and high concentrated protein solution that was obtained was aliquoted in 2 mL Eppendorf tubes, and ultra-frozen with ethanol and dry ice to be conserved at -80°C.

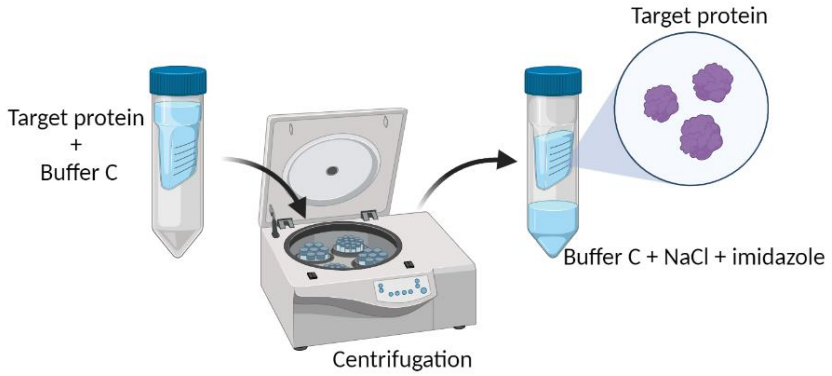

Figure 2.36. Overview of protein concentration and buffer exchange process.

2.3.3.4. LPS sequestration by agarose beads

Once K37E-LALF has been synthesised, its ability to sequestrate LPS was assessed. This assay comprises two steps, namely, (i) bead functionalization with the biotargeting agent (i.e., K37E-LALF), (ii) LPS capture by the biotargeting agent anchored to the beads.

Firstly, 500 µL of agarose beads were centrifuged to remove the ethanol where they are initially suspended and resuspended in 500 µL of buffer D (see Table 2.4). Then, beads were rinsed for 3 times; in each rinse cycle, beads were centrifuged and resuspended in the previous buffer. Subsequently, beads were incubated with the protein under gentle shaking, so that they became functionalized by the biotargeting agent due to the strong affinity of the histidine-tag of K37E-LALF to Ni^{2+} by chelation. Beads functionalization was monitored from the initial protein concentration (in the absence of beads) and protein concentration in the supernatant (in the presence of beads) at different times. Thereby, the difference between these protein concentrations (i.e., initial and in the supernatant) represents the amount of protein that is anchored on the beads surface. Once the bead-protein equilibrium was reached, which implies that beads were unable to continue capturing the protein, beads were washed 3 times following the same procedure as that previously mentioned in order to remove the unbound protein in the beads surface. Thus, protein concentration was also measured in the washing solution in order to verify that protein remained anchored. All mentioned protein concentrations were measured in a Nanodrop 2000c spectrophotometer at 280 nm and specifying the protein size (57.9 kDa) and the molar extinction coefficient (ε=104.5 mol·L^{-1}).

Subsequently, K37E-LALF functionalized beads were contacted with FITC-LPS solution and the LPS removal was quantified. Following the procedure of Basauri et al. [104] different LPS-protein ratios ($\phi_{\mathrm{protein/LPS}}$), were tested in order to verify the worsening of the LALF ability to sequestrate LPS when it is mutated even when considerably favourable binding conditions (protein mass significantly higher than LPS mass) were used. More specifically, 75 µL of a FITC-LPS solution with a concentration of 100-125 µg·mL^{-1} were incubated with the functionalized beads under gently shaking during different times. Afterwards, the LPS-beads mixture was centrifuged, and samples of the supernatant were pipetted into a 96 well plate in order to measure the LPS concentration in the supernatant by fluorometric techniques, since LPS contained fluorescence conjugates and thus LPS concentration correlated with intensity of fluorescence. Measurements were carried out in a Spark® multimode microplate reader using an excitation/emission wavelength of 495 nm and 525 nm, respectively. This procedure has been depicted in Figure 2.37.

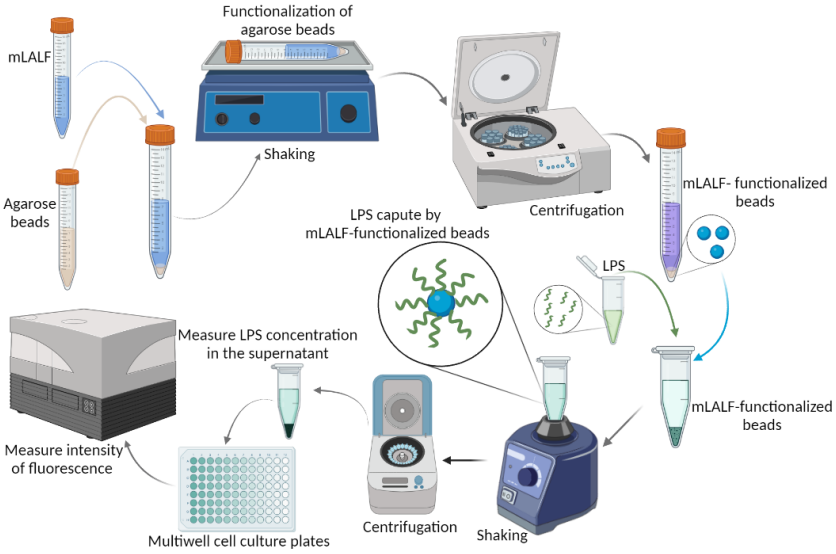

Figure 2.37. Overview of the LPS sequestration procedure including beads functionalization and LPS capture by the functionalized beads.

Additionally, FITC-LPS was contacted with beads without being functionalized by K37E-LALF following the same procedure as the previously detailed, regarding the initial beads washing and the contact of FITC-LPS with the beads. In this way, the ability of bare beads to capture LPS was assessed. A summary of all experimental conditions has been included in Table 2.7.

Table 2.7. Experimental design to assess the ability of K37E-LALF-functionalized and bare agarose beads to capture LPS.

Beads	$\phi_{protein/LPS}$ (-)	Contact time (min)
K37E-LALF functionalized beads	~ 300	20
	~ 400	60
Bare agarose beads	-	20
	-	60

2.3.4. Results

2.3.4.1. Protein synthesis

Sanger sequencing

Prior to protein synthesis, the mDNA sequences that result from the SDM must be checked in order to verify the presence of the desired amino acid substitutions. According to the alignment results (Figure 2.38), the mDNAs have the proper amino acid substitution. Hence, it can be easily noticed that the lysine (K) of the 37th position in WT-LALF has been replaced by a glutamic acid (E) in K37E-LALF, while the remainder sequence is unchanged. Similarly, Figure 2.38b also shows that the tyrosine (Y) of the 47th position in WT-LALF has been changed by a phenylalanine (F) and that it is the only amino acid that has been substituted in Y47F-LALF. Collectively, the mDNAs contain the desired point mutation, thus, they are suitable to be used for synthesizing K37E-LALF and Y47F-LALF. It should be pointed out that the complete amino acid sequences of WT-LALF, K37E-LALF and Y47F-LALF have not been included in Figure 2.38, but rather the part of the sequences where the presence of the amino acid substitutions is shown.

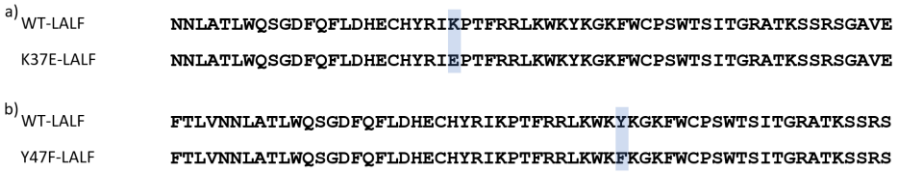

Figure 2.38. Alignment of the amino acid sequences of WT-LALF with (a) K37E-LALF, (b) Y47F-LALF. Residues that are not conserved are highlighted in blue.

Protein overexpression

Protein overexpression represents a challenging step in the whole process of the obtention of the target protein. Thereby, there exists a wide variety of options that could be selected, such as, the most appropriate host cell, the introduction of stability tags, the temperature, etc., that may have a great influence on the successful production of the target protein. Improper selection of these conditions could result, for instance, in the failure of the protein obtention or in the production of misfolded proteins, that typically

aggregate and forms inclusion bodies, thus, preventing their further use [105,106]. Taking advantage of the previously derived work in the ASP research group, the conditions for obtaining K37E-LALF and Y47F-LALF were the same as the most advantageous ones for obtaining WT-LALF. Hence, the expression of both K37E-LALF and Y47F-LALF, which include a MBP stability tag in their sequence, were carried out in ArcticExpress at 18°C. The overexpression of these proteins was analysed by SDS-PAGE. Electrophoresis gel results are illustrated in Figure 2.39 for K37E-LALF and Y47F-LALF overexpressions. It can be easily noticed that a band markedly appear in each SDS-PAGE gel and that they correspond to molecule size of ~58 kDa. Therefore, these results support the successful overexpression of both K37E-LALF and Y47F-LALF.

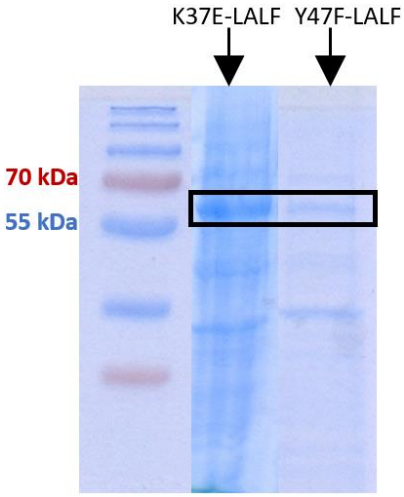

Figure 2.39. SDS-PAGE gel showing the overexpression of K37E-LALF and Y47F-LALF. Page Ruler protein ladder sizes are indicated on the left.

Protein purification

As seen in Figure 2.39, the product of the overexpression not only contains the target protein (i.e., K37E-LALF or Y47F-LALF), but also other proteins, since apart from the target band at ~58 kDa, other bands appear. In order to obtain a solution almost exclusively composed of the target protein, a purification step is required. The procedure for performing the purification of the protein has been detailed in Section 2.3.3.3. As explained in such section, protein purification was accomplished by using HisTrap HP

histidine-tagged protein purification columns, which are packed with highly cross-linked agarose beads that have immobilized Ni^{2+} ions. Protein purification using these columns is based on the different binding strength of the proteins that compose the initial sample with the beads. More specifically, the six histidines that compose the affinity tag of both K37E-LALF and Y47F-LALF strongly bind to the Ni^{2+} ions of the beads, which results in the protein entrapment in the column [107,108]. Conversely, the proteins present in the initial sample that lack such affinity tag do not interact with the Ni^{2+} ions (or their interaction is weak) and thus they are not retained but leave the column in the flowthrough. Due to the strong interaction between the his-tagged proteins and the beads divalent ions, the proteins are eluted from the column by an imidazole concentration gradient of buffer B (from 20 mM to 500 mM).

Figure 2.40 illustrates the chromatograms obtained during the purification process of K37E-LALF and Y47F-LALF. The elution profile exhibits an increase in the absorbance when the target protein leaves the column, since the target proteins absorb UV radiation at 280 nm. According to the chromatograms, K37E-LALF is contained in fractions 7^{th} to 9^{th}, and Y47F-LALF is contained in fractions 7^{th} and 8^{th}. The peak area of K37E-LALF is higher than that of Y47F-LALF, which indicates that the amount of purified protein is higher for K37E-LALF than for Y47F-LALF.

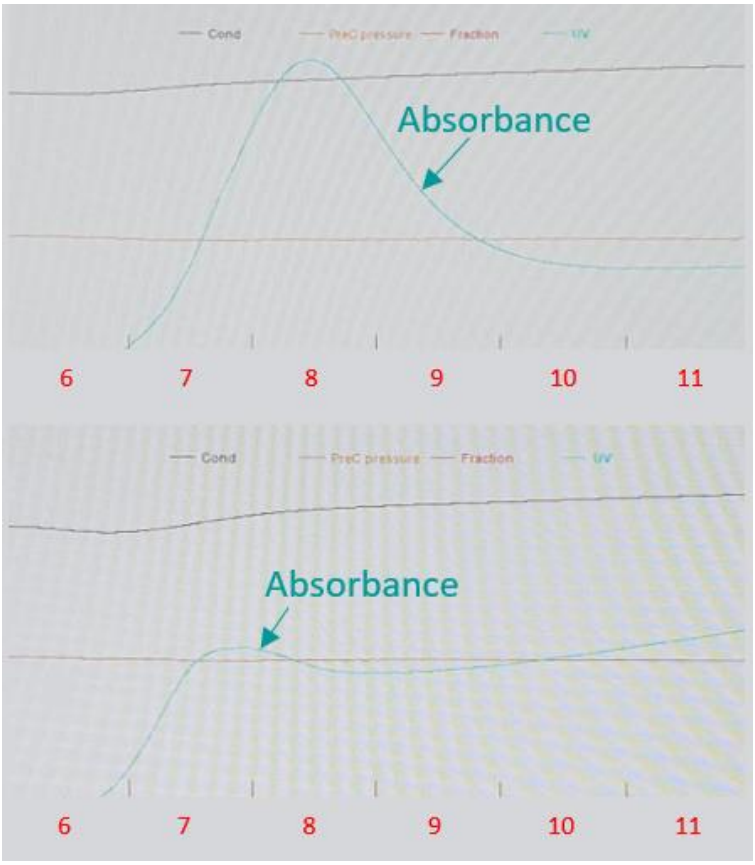

Figure 2.40. FPLC chromatogram of the elution from HisTrap HP columns of K37E-LALF (upper), and Y47F-LALF (lower).

In order to verify the obtention of these purified proteins, the fractions (from 7th to 9th for K37E-LALF and 7th and 8th for Y47F-LALF) that were obtained during the purification of the proteins were mixed with SDS sample loading buffer (see Table 2.4) and loaded onto an SDS-PAGE acrylamide gel. As noticed from Figure 2.41a, and according to the absorbance peaks of the chromatogram, fractions from 7th to 9th contain K37E-LALF. Similarly, the smaller area of the Y47F-LALF chromatogram peak (Figure 2.40) matches with the slightly appearance of the protein in these fractions, which indicates that Y47F-LALF could not be appropriately purified. This result denotes that although the protein has been successfully overexpressed, as concluded from Figure 2.39, it could not be purified through IMAC.

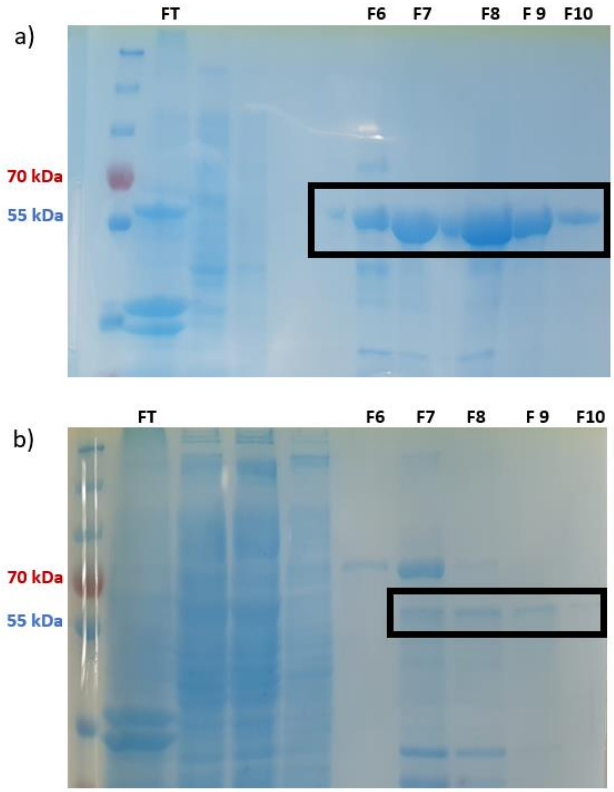

Figure 2.41. SDS-PAGE gel showing the purification fractions of (a) K37E-LALF and (b) Y47F-LALF.

As previously discussed, IMAC relies on the interaction of the six histidines tail of the protein with the Ni^{2+} ions of the beads that were packed in the column. If these interactions are absent or weak, the protein is not retained in the beads, and thus it is not subsequently eluted by the imidazole gradient, but it leaves the column in the flowthrough. The chromatogram and SDS-PAGE gel results suggest that the histidine tail of Y47F-LALF is not binding as expected with the Ni^{2+} ions. This fact may arise from the protein misfolding during synthesis due to the substitution of a hydrophobic amino acid (Y47) that could be involved in key interactions for ensuring protein structure. More specifically, an appropriate interaction involves that the histidines are exposed on the protein surface; otherwise, these histidines could not form a complex with Ni^{2+}. Hence, the Y47F substitution could affect protein folding

such that histidines are buried or insufficiently exposed, and thus, they are not accessed to the Ni^{2+} ions. It has been reported that due to its hydrophobic nature, tyrosine tends to pack tightly within the hydrophobic protein interior, and is key for driving rapid protein folding and scaffold stability [109]. Therefore, the important role of Y47 in the maintenance of the protein structure causes that its replacement prevents the appropriate protein folding and thus the protein purification through IMAC.

The impossibility of purifying Y47F-LALF prevents analysing the effect of this amino acid substitution on the ability of the protein to bind LPS. Therefore, LPS binding assays were only performed with K37E-LALF as biotargeting agent. For that purpose, the purified K37E-LALF fractions were concentrated and buffer exchanged to buffer C (see Table 2.4) in order to concentrate the protein and remove salts as detailed in section 2.3.3.3.

2.3.4.2. Agarose beads functionalization

Once K37E-LALF has been synthesized and purified, the functionalization of agarose beads is addressed. In order to compare the LPS binding affinity of K37E-LALF with WT-LALF at different protein/LPS ratios ($\phi_{\mathrm{protein/LPS}}$), two beads' batches (500 µl of beads in each of them) were functionalized. The monitoring of the functionalization step was performed by measuring the protein concentration in the supernatant, as depicted in Figure 2.42. The concentration of the initial protein solution contacted with the first and second bathes of beads was 4.4 $mg{\cdot}mL^{-1}$ and 2.87 $mg{\cdot}mL^{-1}$ respectively. It can be easily noticed that protein concentration in the supernatant decreases with time since it has been captured by the beads due to the interaction of the protein histidine tail and the Ni^{2+} ions immobilized in the beads surface. After being contacted during 20 hours approximately, the protein-bead equilibrium has already been reached, which implies that beads are no longer able to continue capturing K37E-LALF, thus, the beads functionalization has been completed. Subsequently, beads were rinsed with buffer D in order to remove the unbounded protein, as explained in section 2.3.3.3.

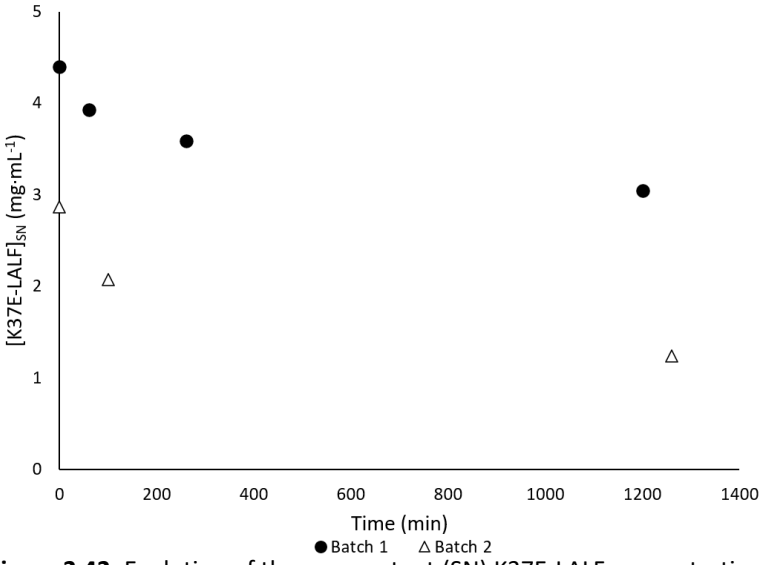

Figure 2.42. Evolution of the supernatant (SN) K37E-LALF concentration during the functionalization of agarose beads.

2.3.4.3. LPS sequestration assay

Once beads have been functionalized, they are incubated with FITC-LPS in order to assess the binding ability of the protein. Two $\phi_{\mathrm{protein/LPS}}$ values and contact times were tested. Particularly, for a $\phi_{\mathrm{protein/LPS}}$ value around 300 and a contact time of 20 minutes, a percentage of LPS capture of 26% is achieved when K37E-LALF functionalized beads are used. The worse LPS capture ability of K37E-LALF in comparison to WT-LALF is demonstrated by the fact that obtaining a similar performance with both proteins requires the use of $\phi_{\mathrm{protein/LPS}}$ values one order of magnitude lower for WT-LALF than for K37E-LALF; in other words, the mass of K37E-LALF must be one order of magnitude higher than that of WT-LALF for attaining a similar endotoxin capture since the same LPS mass was contacted with the proteins. Hence, when WT-LALF/LPS ratios around 35.6 are accomplished and the contact time is 20 minutes the percentage of LPS capture is $\sim$ 30% [104]. Additionally, for comparable protein/LPS concentration ratios ($\phi_{\mathrm{protein/LPS}} \approx 400$) the percentage of LPS capture using K37E-LALF functionalized beads is approximately half of that when WT-LALF functionalized beads are used. Thereby, WT-LALF functionalized beads enable the 85% capture of LPS in 10

minutes [104], whereas K37E-LALF functionalized beads are only able to provide the 42 % of LPS sequestration despite increasing the contact time to 60 minutes. Collectively, substituting the lysine of the 37th position in WT-LALF by glutamic acid leads to a considerably decrease in the protein ability to bind LPS, which demonstrated the key role of K37 in the interaction of LPS, thus verifying the *in silico* prediction.

It is worth mentioning that the use of ALFs as LPS capturing agents enables the selective sequestration of the endotoxin since not only are electrostatic interactions involved but also hydrophobic interactions, which play a key role in the stable binding given the hydrophobic nature of LPS as discussed in sections 2.2.4.2 and 2.2.4.3. However, since LPS is negatively charged, positively charged molecules could also be used to sequestrate LPS despite the fact they merely interact electrostatically. In this sense, agarose beads, which have anchored to their surface Ni^{2+} ions could also be used to capture LPS through electrostatic interactions [110,111]. Thus, the ability of bare agarose beads (i.e., beads without being functionalized with either WT-LALF or K37E-LALF) to capture LPS was examined following the same protocol as for the functionalized beads. Results revealed that bare agarose beads yield a percentage of LPS capture of around 55% when contact times of 20 and 60 minutes are considered. From this result, it can be easily noticed that bare beads harbour a higher LPS binding ability than K37E-LALF functionalized beads.

In an effort to compare the apparent equilibrium constant of bare beads and WT-LALF functionalized beads, the Ni^{2+} content of the bare beads was measured so that this binding constant could be calculated. The apparent binding constant of the bare beads and LPS was computed following the methodology of Basauri et al. [104], and the derived graph has been illustrated in Figure 2.43. The slope of the graph represents the apparent equilibrium constant, which for the bare beads is $8.41 \cdot 10^{1}$ M^{-1}. This value is two orders of magnitude lower than for WT-LALF ($2.8 \cdot 10^{3}$ M^{-1} [104]) which substantiates the use of WT-LALF for developing LPS biotargeting agents. Collectively, the LPS binding molecules herein tested could be ranked according to their ability to capture the endotoxin as: WT-LALF > Ni^{2+} > K37E-LALF.

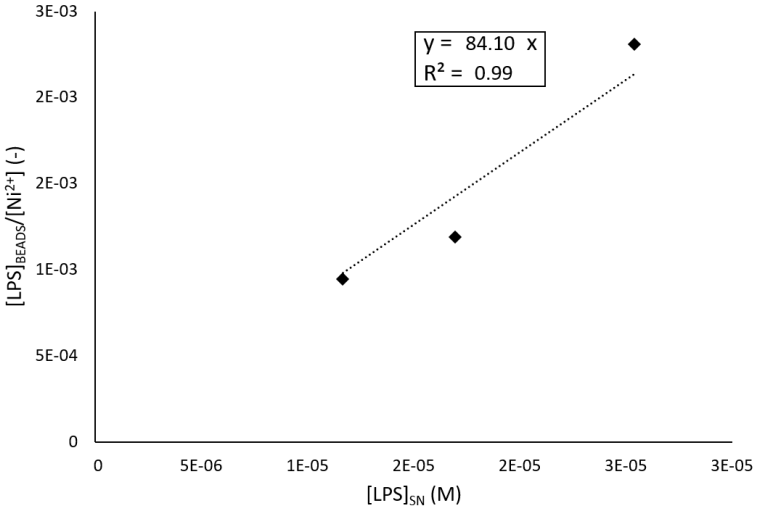

Figure 2.43. Adsorption isotherm of the LPS-Ni^{2+} agarose beads interaction.

2.4. Conclusions

The development of MCMDs for endotoxin removal from blood requires the design of magnetic-based LPS sequestration agents. For that purpose, selecting a biotargeting agent able to capture LPS with high affinity and selectivity is of paramount importance. Several LPS binding molecules have been reported in the literature. From all of them, ALFs have been recognised as potential candidates to develop therapeutics against sepsis. Hence, gaining insight into the interaction mechanism between LPS and several ALFs, such as LALF or ALFPm3, has received special attention. Despite these efforts, the binding mode of LPS and ALFs has not been elucidated yet. However, understanding how these molecules interact and bind is key for advancing in the design of LPS sequestration agents. More specifically, molecules with outstandingly enhanced ability for capturing LPS could be designed once the binding site of LPS in LALF or ALFPm3 and the residues of these ALFs that are key for the interaction with the endotoxin are elucidated. Addressing this investigation calls for exploring the LALF/ALFPm3-LPS interaction at microscopic detail. To this end, MD, which is understood as a computational microscope, can provide the atomic level details required for making progress on the elucidation of the LALF/ALFPm3-LPS interaction.

In this work, the interaction mechanism between ALFPm3 and the lipid A constituent of LPS is investigated through AA-MD simulations. Such protein-ligand interaction was investigated in media with different ionic strengths; moreover, the effect of applying NOE distance restraints to the protein structure to promote their maintenance upon ligand binding was also assessed. A thorough analysis of the trajectories derived from the MD simulations reveals that the ionic strength has a positive effect on the ALFPm3-lipid A binding, which is supported by the amphipathic character of both the ligand and the ALFPm3 cavity, which was found to be the lipid A binding site. In this regard, since the binding site is located in the internal side of the protein instead of in the external side, the application of NOE distance restraints hampers that the protein could open up its structure to accommodate the lipid. According to the salt bridges analysis, the residue K39 is involved in salt bridges with both phosphates of the lipid, which agrees with the hypothesis of Yang et al. [1]; additionally, the hydrogen bond analysis revealed that Y49 and Q70 form hydrogen bonds with the lipid. However, these hydrogen bonds and salt bridges are not involved in all the simulations.

Thus, in the simulations where the lipid is able to bury itself in the protein cavity, the salt bridges are not observed but the hydrogen bonds are formed. On the contrary, in the simulation where the lipid is not able to reach the protein cleft, salt bridges are formed at the beginning of the simulation and as the lipid tries to move to the back side of the β-hairpin the hydrogen bonds appear. The location of the lipid A binding site in the protein cavity was also assessed by performing simulations considering as initial structure one where the lipid was fully inserted in such cavity. Additionally, the reversibility of the ALFPm3-lipid A binding was further confirmed by running simulations of the apo-protein with an opened conformation as a result of the lipid binding. Collectively, the ALFPm3-lipid A interaction mechanism involves two steps; thus, the lipid is firstly recognised by the protein through electrostatic interactions, and then, a stable binding driven by hydrophobic interactions is formed which involves the protein cavity, where the lipid acyl chains are buried into such cavity with the phosphates upwards facing the media.

The *in silico* derived results were validated *in vitro* in order to further confirm the abovementioned interaction mechanism. In this case, LALF instead of ALFPm3 was used for the experimental validation since the LALF-LPS contact had already been investigated in the ASP research group. SDM was used to introduce point mutations in the DNA sequence of WT-LALF. Once mDNAs with the desired mutation (one amino acid substitution in each of them) were obtained, K37E-LALF and Y47F-LALF were overexpressed and purified. Although both proteins were successfully overexpressed, the purification of Y47F-LALF failed, probably due to the protein misfolding as a result of the substitution of an amino acid involved in the protein core. Thus, the ability to capture LPS could only be assessed for K37E-LALF. For that purpose, agarose beads were functionalized with K37E-LALF and K37E-LALF-LPS contacts were performed considering different K37E-LALF/LPS ratios and contact times. The results revealed that the substitution of lysine by glutamic acid in the 37^{th} position of LALF led to a considerably loosening of the capacity to bind LPS in comparison to WT-LALF. On the other hand, since bare agarose beads (beads without being functionalized with K37E-LALF or WT-LALF) have Ni^{2+} in their surface, their ability to capture LPS through electrostatic interactions was also investigated. It was found that bare agarose beads were able to capture more LPS that K37E-LALF, although their performance was worse than that of WT-LALF.

Overall, this chapter contributes to the design of an important aspect of the incubation stage in MCMDs, namely, the biotargeting agents for LPS capture. Thereby, valuable findings about the ALFPm3-lpid A/LPS interaction have been derived throughout this chapter, which can be used to design novel molecules with enhanced LPS binding capacity. The methodology followed for that purpose could be extended to the investigation of the interaction of endotoxin with other (bio)molecules. Once an appropriate molecule for functionalizing the beads has been identified and verified, the recovery of the LPS-bead complexes should be investigated. Hence, in the next chapter the design and optimization of magnetic microseparators for particle retrieval after LPS sequestration are addressed.

2.5. References of Chapter 2

[1] Y. Yang, H. Boze, P. Chemardin, A. Padilla, G. Moulin, A. Tassanakajon, M. Pugnière, F. Roquet, D. Destoumieux-Garzón, Y. Gueguen, E. Bachère, A. Aumelas, NMR structure of rALF-Pm3, an anti-lipopolysaccharide factor from shrimp: Model of the possible lipid A-binding site, Biopolymers. 91 (2009) 207–220. https://doi.org/10.1002/bip.21119.

[2] A. Hoess, S. Watson, G.R. Siber, R. Liddington, E. Schulz, Crystal structure of an endotoxin-neutralizing protein from the horseshoe crab, *Limulus* anti-LPS factor, at 1.5 A resolution, EMBO J. 12 (1993) 3351–3356. https://www.ncbi.nlm.nih.gov/pmc/articles/PMC413608/pdf/emboj00081-0013.pdf.

[3] D.L. Mobley, M.K. Gilson, Predicting binding free energies: Frontiers and benchmarks, Annu. Rev. Biophys. 46 (2017) 531–558. https://doi.org/10.1146/annurev-biophys-070816-033654.

[4] A. Boags, P.C. Hsu, F. Samsudin, P.J. Bond, S. Khalid, Progress in molecular dynamics simulations of Gram-negative bacterial cell envelopes, J. Phys. Chem. Lett. 8 (2017) 2513–2518. https://doi.org/10.1021/acs.jpclett.7b00473.

[5] S. Khalid, T.J. Piggot, F. Samsudin, Atomistic and coarse grain simulations of the cell envelope of Gram-negative bacteria: What have we learned?, Acc. Chem. Res. 52 (2019) 180–188. https://doi.org/10.1021/acs.accounts.8b00377.

[6] R.S. Katiyar, P.K. Jha, Molecular simulations in drug delivery: Opportunities and challenges, Wiley Interdiscip. Rev. Comput. Mol. Sci. 8 (2018) e1358. https://doi.org/10.1002/wcms.1358.

[7] A.A.T. Naqvi, T. Mohammad, G.M. Hasan, M.I. Hassan, Advancements in docking and molecular dynamics simulations towards ligand-receptor interactions and structure-function relationships, Curr. Top. Med. Chem. 18 (2018) 1755–1768. https://doi.org/10.2174/1568026618666181025114157.

[8] S.A. Hollingsworth, R.O. Dror, Molecular dynamics simulation for all, Neuron. 99 (2018) 1129–1143. https://doi.org/10.1016/j.neuron.2018.08.011.

[9] W.F. van Gunsteren, J. Dolenc, A.E. Mark, Molecular simulation as an aid to experimentalists, Curr. Opin. Struct. Biol. 18 (2008) 149–153.

https://doi.org/10.1016/j.sbi.2007.12.007.

[10] S. Bhattacharjya, S. A. David, V.L. Mathan, P. Balaram, Polymyxin B nonapeptide: conformations in water and in the lipopolysaccharide-bound state determined by two- dimensional NMR and molecular dynamics, Biopolymers. 41 (1997) 251–265.

[11] L.K. Ladefoged, T. Zeppelin, B. Schiøtt, Molecular modeling of neurological membrane proteins − from binding sites to synapses, Neurosci. Lett. 700 (2019) 38–49. https://doi.org/10.1016/j.neulet.2018.05.034.

[12] J. Mortier, C. Rakers, M. Bermudez, M.S. Murgueitio, S. Riniker, G. Wolber, The impact of molecular dynamics on drug design: Applications for the characterization of ligand-macromolecule complexes, Drug Discov. Today. 20 (2015) 686–702. https://doi.org/10.1016/j.drudis.2015.01.003.

[13] R.O. Dror, R.M. Dirks, J.P. Grossman, H. Xu, D.E. Shaw, Biomolecular simulation: A computational microscope for molecular biology, Annu. Rev. Biophys. 41 (2012) 429–452. https://doi.org/10.1146/annurev-biophys-042910-155245.

[14] J. Lee, D.S. Patel, J. Ståhle, S.J. Park, N.R. Kern, S. Kim, J. Lee, X. Cheng, M.A. Valvano, O. Holst, Y.A. Knirel, Y. Qi, S. Jo, J.B. Klauda, G. Widmalm, W. Im, CHARMM-GUI Membrane Builder for Complex Biological Membrane Simulations with Glycolipids and Lipoglycans, J. Chem. Theory Comput. 15 (2019) 775–786. https://doi.org/10.1021/acs.jctc.8b01066.

[15] M. Zheng, J. Zhao, C. Cui, Z. Fu, X. Li, X. Liu, X. Ding, X. Tan, F. Li, X. Luo, K. Chen, H. Jiang, Computational chemical biology and drug design: Facilitating protein structure, function, and modulation studies, Med. Res. Rev. 38 (2018) 914–950. https://doi.org/10.1002/med.21483.

[16] T. Casalini, Not only in silico drug discovery: Molecular modeling towards in silico drug delivery formulations, J. Control. Release. 332 (2021) 390–417. https://doi.org/10.1016/j.jconrel.2021.03.005.

[17] J.D. Durrant, M.J. Andrew, Molecular dynamics simulations and novel drug discovery, BMC Biol. 9 (2011) 71. https://doi.org/doi:10.1186/1741-7007-9-71.

[18] H. Gohlke, G. Klebe, Approaches to the description and prediction of the binding affinity of small-molecule ligands to macromolecular receptors, Angew. Chemie - Int. Ed. 41 (2002) 2644–2676. https://doi.org/10.1002/1521-3773(20020802)41:15<2644::AID-

ANIE2644>3.0.CO;2-O.

[19] A. Hospital, J.R. Goñi, M. Orozco, J.L. Gelpí, Molecular dynamics simulations: Advances and applications, Adv. Appl. Bioinforma. Chem. 8 (2015) 37–47. https://doi.org/10.2147/AABC.S70333.

[20] S.B. Hwang, C.J. Lee, S. Lee, S. Ma, Y.M. Kang, K.H. Cho, S.Y. Kim, O.Y. Kwon, C.N. Yoon, Y.K. Kang, J.H. Yoon, K.Y. Nam, S.G. Kim, Y. In, H.H. Chai, W.E. Acree, J.A. Grant, K.D. Gibson, M.S. Jhon, H.A. Scheraga, K.T. No, PMFF: Development of a physics-based molecular force field for protein simulation and ligand docking, J. Phys. Chem. B. 124 (2020) 974–989. https://doi.org/10.1021/acs.jpcb.9b10339.

[21] P.C. Nair, J.O. Miners, Molecular dynamics simulations: from structure function relationships to drug discovery, Silico Pharmacol. 2 (2014) 4. https://doi.org/10.1186/s40203-014-0004-8.

[22] W. F. van Gunsteren, S. R. Billeter, A. A. Eising, P. H. Hünenberger, P. Krüger, A. E. Mark, W. R. P. Scott, and I. G. Tironi, The GROMOS software for (bio)molecular simulation (manual and user guide) (2019).

[23] M. Setz, Molecular dynamics simulations of biomolecules: From validation to application (doctoral dissertation), University of Natural Resources and Life Sciences (Vienna), (2018).

[24] P.E.M. Lopes, O. Guvench, A.D. MacKerell Jr., Current status of protein force fields for molecular dynamics, in: Kikol A. (Ed), Molecular Modeling of Proteins. Methods Mol Biol., Humana Press, New York, 2015: pp. 47–71. https://doi.org/10.1007/978-1-4939-1465-4_3.

[25] P. Mark, L. Nilsson, Structure and dynamics of the TIP3P, SPC, and SPC/E water models at 298 K, J. Phys. Chem. A. 105 (2001) 9954–9960. https://doi.org/10.1021/jp003020w.

[26] S. Sharma, P. Kumar, R. Chandra, Introduction to molecular dynamics, in: S. Sharma (Ed.), Molecular Dynamics Simulation of Nanocomposites Using BIOVIA Materials Studio, Lammps and Gromacs, Elsevier Inc., 2019. https://doi.org/10.1016/B978-0-12-816954-4.00001-2.

[27] D. van der Spoel, E. Lindahl, B. Hess, A. R. van Buuren, E. Apol, P. J. Meulenhoff, D. P. Tieleman, A. L. T. M. Sijbers, K. A. Feenstra, R. van Drunen, H. J. C. Berendsen, GROMACS user manual version 3.3, (2005).

[28] C. González-Fernández, A. Basauri, M. Fallanza, E. Bringas, C.

Oostenbrink, I. Ortiz, Fighting against bacterial lipopolysaccharide-caused infections through molecular dynamics simulations: A review, J. Chem. Inf. Model. 61 (2021) 4839–4851. https://doi.org/10.1021/acs.jcim.1c00613.

[29] M. Karplus, J.A. McCammon, Molecular dynamics simulations of biomolecules, Nat. Struct. Biol. 9 (2002) 646–652. https://doi.org/10.1038/nsb0902-646.

[30] A.H. Wang, Z.C. Zhang, G.H. Li, Advances in enhanced sampling molecular dynamics simulations for biomolecules, Chinese J. Chem. Phys. 32 (2019) 277–286. https://doi.org/10.1063/1674-0068/cjcp1905091.

[31] N. Singh, W. Li, Recent advances in coarse-grained models for biomolecules and their applications, Int. J. Mol. Sci. 20 (2019) 3774. https://doi.org/10.3390/ijms20153774.

[32] V. Limongelli, Ligand binding free energy and kinetics calculation in 2020, Wiley Interdiscip. Rev. Comput. Mol. Sci. 10 (2020) e1455. https://doi.org/10.1002/wcms.1455.

[33] C. Lorenz, N.L. Doltsinis, Molecular dynamics simulation: From “ab initio” to “coarse grained”, in: Handb. Comput. Chem., Springer, Switzerland, 2012: 195–238. https://doi.org/10.1007/978-94-007-0711-5_7.

[34] S. Takada, Coarse-grained molecular simulations of large biomolecules, Curr. Opin. Struct. Biol. 22 (2012) 130–137. https://doi.org/10.1016/j.sbi.2012.01.010.

[35] T. Mori, N. Miyashita, W. Im, M. Feig, Y. Sugita, Molecular dynamics simulations of biological membranes and membrane proteins using enhanced conformational sampling algorithms, Biochim. Biophys. Acta - Biomembr. 1858 (2016) 1635–1651. https://doi.org/10.1016/j.bbamem.2015.12.032.

[36] J. Barnoud, L. Monticelli, A. Kukol, Coarse-grained force fields for molecular simulations, in: Molecular modeling of proteins: Methods in Molecular Biology, Humana Press, 2015: pp. 125-149. https://doi.org/10.1007/978-1-4939-1465-4.

[37] P. Deuflhard, J. Hermans, B. Leimkuhler, A. E. Mark, S. Reich, R. D. Skeel, Computational Molecular Dynamics: Challenges, Methods, Ideas, Springer Science+Bussines Media, 1999. https://doi.org/10.1007/978-3-642-58360-5.

[38] E.A. Oprzeska-Zingrebe, J. Smiatek, Some notes on the thermodynamic accuracy of coarse-grained Models, Front. Mol. Biosci. 6 (2019) 87. https://doi.org/10.3389/fmolb.2019.00087.

[39] M. Kar, P., Feig, Recent advances in transferable coarse-grained modeling of proteins, Adv. Protein Chem. Struct. Biol. 96 (2014) 143–180. https://doi.org/10.1016/bs.apcsb.2014.06.005.

[40] F.L. Gervasio, V. Spiwok, Biomolecular simulations in structure-based drug discovery, Wiley VCH, 2018.

[41] A.J. Rzepiela, M. Louhivuori, C. Peter, S.J. Marrink, Hybrid simulations: Combining atomistic and coarse-grained force fields using virtual sites, Phys. Chem. Chem. Phys. 13 (2011) 10437–10448. https://doi.org/10.1039/c0cp02981e.

[42] J. Peng, C. Yuan, R. Ma, Z. Zhang, Backmapping from multiresolution coarse-grained models to atomic structures of large biomolecules by restrained molecular dynamics simulations using bayesian inference, J. Chem. Theory Comput. 15 (2019) 3344–3353. https://doi.org/10.1021/acs.jctc.9b00062.

[43] A.J. Rzepiela, L. V. Schäfer, N. Goga, H.J. Risselada, A.H. de Vries, S.J. Marrink, Reconstruction of atomistic details from coarse-grained structures, J. Comput. Chem. 31 (2010) 1333–1343. https://doi.org/10.1002/jcc.21415.

[44] S.O. Nielsen, R.E. Bulo, P.B. Moore, B. Ensing, Recent progress in adaptive multiscale molecular dynamics simulations of soft matter, Phys. Chem. Chem. Phys. 12 (2010) 12401–12414. https://doi.org/10.1039/c004111d.

[45] M.R. Machado, P.D. Dans, S. Pantano, A hybrid all-atom/coarse grain model for multiscale simulations of DNA, Phys. Chem. Chem. Phys. 13 (2011) 18134–18144. https://doi.org/10.1039/c1cp21248f.

[46] S. Riniker, A.P. Eichenberger, W.F. Van Gunsteren, Structural effects of an atomic-level layer of water molecules around proteins solvated in supra-molecular coarse-grained water, J. Phys. Chem. B. 116 (2012) 8873–8879. https://doi.org/10.1021/jp304188z.

[47] D.R. Roe, C. Bergonzo, T.E. Cheatham, Evaluation of enhanced sampling provided by accelerated molecular dynamics with hamiltonian replica exchange methods, J. Phys. Chem. B. 118 (2014) 3543–3552. https://doi.org/10.1021/jp4125099.

[48] J. Comer, J.C. Gumbart, J. Hénin, T. Lelievre, A. Pohorille, C. Chipot, The adaptive biasing force method: Everything you always wanted to

know but were afraid to ask, J. Phys. Chem. B. 119 (2015) 1129–1151. https://doi.org/10.1021/jp506633n.

[49] M. Meli, G. Colombo, A hamiltonian replica exchange molecular dynamics (MD) method for the study of folding, based on the analysis of the stabilization determinants of proteins, Int. J. Mol. Sci. 14 (2013) 12157–12169. https://doi.org/10.3390/ijms140612157.

[50] B.R. Jagger, S.E. Kochanek, S. Haldar, R.E. Amaro, A.J. Mulholland, Multiscale simulation approaches to modeling drug–protein binding, Curr. Opin. Struct. Biol. 61 (2020) 213–221. https://doi.org/10.1016/j.sbi.2020.01.014.

[51] J. Ikebe, K. Umezawa, J. Higo, Enhanced sampling simulations to construct free-energy landscape of protein–partner substrate interaction, Biophys. Rev. 8 (2016) 45–62. https://doi.org/10.1007/s12551-015-0189-z.

[52] C. Martinotti, L. Ruiz-Perez, E. Deplazes, R.L. Mancera, Molecular dynamics simulation of small molecules interacting with biological membranes, ChemPhysChem. 21 (2020) 1486–1514. https://doi.org/10.1002/cphc.202000219.

[53] Y. Meng, B. Roux, Efficient determination of free energy landscapes in multiple dimensions from biased umbrella sampling simulations using linear regression, J. Chem. Theory Comput. 11 (2015) 3523–3529. https://doi.org/10.1021/ct501130r.

[54] M. Yang, J. Huang, A.D. MacKerell, Enhanced conformational sampling using replica exchange with concurrent solute scaling and Hamiltonian biasing realized in one dimension, J. Chem. Theory Comput. 11 (2015) 2855–2867. https://doi.org/10.1021/acs.jctc.5b00243.

[55] S. Jo, W. Jiang, A generic implementation of replica exchange with solute tempering (REST2) algorithm in NAMD for complex biophysical simulations, Comput. Phys. Commun. 197 (2015) 304–311. https://doi.org/10.1016/j.cpc.2015.08.030.

[56] G.Z. Genchev, M. Källberg, G. Gürsoy, A. Mittal, L. Dubey, O. Perisic, G. Feng, R. Langlois, H. Lu, Mechanical signaling on the single protein level studied using steered molecular dynamics, Cell Biochem. Biophys. 55 (2009) 141–152. https://doi.org/10.1007/s12013-009-9064-5.

[57] P.C. Do, E.H. Lee, L. Le, Steered molecular dynamics simulation in rational drug design, J. Chem. Inf. Model. 58 (2018) 1473–1482.

https://doi.org/10.1021/acs.jcim.8b00261.

[58] W.E. Miranda, S.Y. Noskov, P.A. Valiente, Improving the LIE method for binding free energy calculations of protein-ligand complexes, J. Chem. Inf. Model. 55 (2015) 1867–1877. https://doi.org/10.1021/acs.jcim.5b00012.

[59] M.K. Gilson, H.X. Zhou, Calculation of protein-ligand binding affinities, Annu. Rev. Biophys. Biomol. Struct. 36 (2007) 21–42. https://doi.org/10.1146/annurev.biophys.36.040306.132550.

[60] K.B. Ljungberg, J. Marelius, D. Musil, P. Svensson, B. Norden, J. Åqvist, Computational modelling of inhibitor binding to human thrombin, Eur. J. Pharm. Sci. 12 (2001) 441–446. https://doi.org/10.1016/S0928-0987(00)00185-8.

[61] M.S. Lee, M.A. Olson, Calculation of absolute protein-ligand binding affinity using path and endpoint approaches, Biophys. J. 90 (2006) 864–877. https://doi.org/10.1529/biophysj.105.071589.

[62] F. Fogolari, A. Corazza, G. Esposito, Free energy, enthalpy and entropy from implicit solvent end-point simulations, Front. Mol. Biosci. 5 (2018) 11. https://doi.org/10.3389/fmolb.2018.00011.

[63] M. Naïm, S. Bhat, K.N. Rankin, S. Dennis, S.F. Chowdhury, I. Siddiqi, P. Drabik, T. Sulea, C.I. Bayly, A. Jakalian, E.O. Purisima, Solvated Interaction Energy (SIE) for scoring protein-ligand binding affinities. 1. Exploring the parameter space, J. Chem. Inf. Model. 47 (2007) 122–133. https://doi.org/10.1021/ci600406v.

[64] R. Hall, T. Dixon, A. Dickson, On Calculating Free Energy Differences Using Ensembles of Transition Paths, Front. Mol. Biosci. 7 (2020) 106. https://doi.org/10.3389/fmolb.2020.00106.

[65] W. F. van Gunsteren, X. Daura, A. E. Mark, Computation of free energy, Helv. Chim. Acta. 85 (2002) 3113–3129.

[66] S.G. Krimmer, G. Klebe, Thermodynamics of protein-ligand interactions as a reference for computational analysis: How to assess accuracy, reliability and relevance of experimental data, J. Comput. Aided. Mol. Des. 29 (2015) 867–883. https://doi.org/10.1007/s10822-015-9867-y.

[67] V. Horňák, R. Dvorský, E. Šturdík, Receptor-Ligand Interaction and Molecular Modelling, Gen Physiol Biophys. 18 (1999) 231–248.

[68] S. Genheden, U. Ryde, Comparison of the efficiency of the LIE and MM/GBSA methods to calculate ligand-binding energies, J. Chem.

Theory Comput. 7 (2011) 3768–3778. https://doi.org/10.1021/ct200163c.

[69] H. Guitiérrez-de-Terán, J. Aqvist, Linear interaction energy: method and applications in drug design, in: R. Baron (Ed.) Computational Drug Discovery and Design, Methods Mol. Biol., Springer Science+Bussines Media, 819 2012: pp. 305–323. https://doi.org/10.1007/978-1-61779-465-0_20.

[70] E. Wang, H. Sun, J. Wang, Z. Wang, H. Liu, J.Z.H. Zhang, T. Hou, End-Point Binding Free Energy Calculation with MM/PBSA and MM/GBSA: Strategies and Applications in Drug Design, Chem. Rev. 119 (2019) 9478–9508. https://doi.org/10.1021/acs.chemrev.9b00055.

[71] E.A. Rifai, M. Van Dijk, N.P.E. Vermeulen, A. Yanuar, D.P. Geerke, A comparative linear interaction energy and MM/PBSA study on SIRT1-ligand binding free energy calculation, J. Chem. Inf. Model. 59 (2019) 4018–4033. https://doi.org/10.1021/acs.jcim.9b00609.

[72] J.M.J. Swanson, R.H. Henchman, J.A. McCammon, Revisiting free energy calculations: A theoretical connection to MM/PBSA and direct calculation of the association free energy, Biophys. J. 86 (2004) 67–74. https://doi.org/10.1016/S0006-3495(04)74084-9.

[73] S. Genheden, U. Ryde, The MM/PBSA and MM/GBSA methods to estimate ligand-binding affinities, Expert Opin. Drug Discov. 10 (2015) 449–461. https://doi.org/10.1517/17460441.2015.1032936.

[74] H. Sun, L. Duan, F. Chen, H. Liu, Z. Wang, P. Pan, F. Zhu, J.Z.H. Zhang, T. Hou, Assessing the performance of MM/PBSA and MM/GBSA methods. 7. Entropy effects on the performance of end-point binding free energy calculation approaches, Phys. Chem. Chem. Phys. 20 (2018) 14450–14460. https://doi.org/10.1039/c7cp07623a.

[75] T. Sulea, E.O. Purisima, The solvated interaction energy method for scoring binding affinities, in: R. Baron (Ed.) Computational Drug Discovery and Design, Methods Mol. Biol., Springer Science+Bussines Media, 819 (2012) 295–303. https://doi.org/10.1007/978-1-61779-465-0_19.

[76] A. Farrotti, P. Conflitti, S. Srivastava, J.K. Ghosh, A. Palleschi, L. Stella, G. Bocchinfuso, Molecular dynamics simulations of the host defense peptide temporin L and Its Q3K Derivative: An atomic level view from aggregation in water to bilayer perturbation, Molecules. 22 (2017) 1235. https://doi.org/10.3390/molecules22071235.

[77] P. Jagtap, R. Mishra, S. Khanna, P. Kumari, B. Mittal, H.K. Kashyap, S.

Gupta, Mechanistic evaluation of lipopolysaccharide-alexidine interaction using spectroscopic and in silico approaches, ACS Infect. Dis. 4 (2018) 1546–1552. https://doi.org/10.1021/acsinfecdis.8b00087.

[78] M.A. Knirel, Y. A. Valvano, Bacterial Lipopolysaccharides. Structure, Chemical Synthesis, Biogenesis and Interactions with Host Cells, Springer, New York, 2011.

[79] A.D. Ferguson, W. Welte, E. Hofmann, B. Lindner, O. Holst, J.W. Coulton, K. Diederichs, A conserved structural motif for lipopolysaccharide recognition by procaryotic and eucaryotic proteins, Structure. 8 (2000) 585–592. https://doi.org/10.1016/S0969-2126(00)00143-X.

[80] A. Steimle, I.B. Autenrieth, J.S. Frick, Structure and function: Lipid A modifications in commensals and pathogens, Int. J. Med. Microbiol. 306 (2016) 290–301. https://doi.org/10.1016/j.ijmm.2016.03.001.

[81] J. Lee, K.R. Pothula, U. Kleinekathöfer, W. Im, Simulation study of Occk5 functional properties in *Pseudomonas aeruginosa* outer membranes, J. Phys. Chem. B. 122 (2018) 8185–8192. https://doi.org/10.1021/acs.jpcb.8b07109.

[82] J. Lee, D.S. Patel, I. Kucharska, L.K. Tamm, W. Im, Refinement of OprH-LPS interactions by molecular simulations, Biophys. J. 112 (2017) 346–355. https://doi.org/10.1016/j.bpj.2016.12.006.

[83] J.A. Garate, C. Oostenbrink, Lipid A from lipopolysaccharide recognition: Structure, dynamics and cooperativity by molecular dynamics simulations, Proteins Struct. Funct. Bioinforma. 81 (2013) 658–674. https://doi.org/10.1002/prot.24223.

[84] A. Borio, A. Holgado, J.A. Garate, R. Beyaert, H. Heine, A. Zamyatina, Disaccharide-based anionic amphiphiles as potent inhibitors of lipopolysaccharide-induced inflammation, ChemMedChem. 13 (2018) 2317–2331. https://doi.org/10.1002/cmdc.201800505.

[85] C.P. Papaneophytou, A.I. Grigoroudis, C. McInnes, G. Kontopidis, Quantification of the effects of ionic strength, viscosity, and hydrophobicity on protein-ligand binding affinity, ACS Med. Chem. Lett. 5 (2014) 931–936. https://doi.org/10.1021/ml500204e.

[86] M.A.D. Neves, S. Slavkovic, Z.R. Churcher, P.E. Johnson, Salt-mediated two-site ligand binding by the cocaine-binding aptamer, Nucleic Acids Res. 45 (2017) 1041–1048. https://doi.org/10.1093/nar/gkw1294.

[87] M.T. Agasid, L. Sørensen, L.H. Urner, J. Yan, C. V. Robinson, The effects

of sodium ions on ligand binding and conformational states of G protein-coupled receptors-insights from mass spectrometry, J. Am. Chem. Soc. 143 (2021) 4085–4089. https://doi.org/10.1021/jacs.0c11837.

[88] T.T. Waldron, G.L. Schrift, K.P. Murphy, The salt-dependence of a protein-ligand interaction: Ion-protein binding energetics, J. Mol. Biol. 346 (2005) 895–905. https://doi.org/10.1016/j.jmb.2004.12.018.

[89] K.A. Sharp, R.A. Friedman, J. Hecht, Salt effects on polyelectrolyte-ligand binding : comparison of limiting law / counterion binding models, Biopolymers. 36 (1995) 245–262. https://onlinelibrary.wiley.com/doi/pdf/10.1002/bip.360360211.

[90] S. Damodaran, J.E. Kinsella, The effects of neutral salts on the stability of macromolecules. A new approach using a protein-ligand binding system, J. Biol. Chem. 256 (1981) 3394–3398. https://doi.org/10.1016/s0021-9258(19)69621-3.

[91] V. Voynov, N. Chennamsetty, V. Kayser, B. Helk, B.L. Trout, Predictive tools for stabilization of therapeutic proteins, MAbs. 1 (2009) 580–582. https://doi.org/10.4161/mabs.1.6.9773.

[92] N. Chennamsetty, V. Voynov, V. Kayser, B. Helk, B.L. Trout, Design of therapeutic proteins with enhanced stability, Pnas. 106 (2009) 11937–11942. http://www.pnas.org/content/106/29/11937.full.pdf?with-ds=yes.

[93] A. Basauri, C. González-Fernández, M. Fallanza, E. Bringas, R. Fernandez-Lopez, L. Giner, G. Moncalián, F. de la Cruz, I. Ortiz, Biochemical interactions between LPS and LPS-binding molecules, Crit. Rev. Biotechnol. 40 (2020) 292–305. https://doi.org/10.1080/07388551.2019.1709797.

[94] R. Chaby, Lipopolysaccharide-binding molecules: Transporters, blockers and sensors, Cell. Mol. Life Sci. 61 (2004) 1697–1713. https://doi.org/10.1007/s00018-004-4020-4.

[95] V.V. Khrustalev, E.V. Barkovsky, Stabilization of secondary structure elements by specific combinations of hydrophilic and hydrophobic amino acid residues is more important for proteins encoded by GC-poor genes, Biochimie. 94 (2012) 2706–2715. https://doi.org/10.1016/j.biochi.2012.08.008.

[96] S. Malleshappa Gowder, J. Chatterjee, T. Chaudhuri, K. Paul, Prediction and analysis of surface hydrophobic residues in tertiary structure of proteins, Sci. World J. 2014 (2014) 971258.

https://doi.org/10.1155/2014/971258.

[97] M.H. Al Mughram, C. Catalano, J.P. Bowry, M.K. Safo, J.N. Scarsdale, G.E. Kellogg, 3D Interaction homology: hydropathic analyses of the "π-cation" and "π-π" interaction motifs in phenylalanine, tyrosine, and tryptophan residues, J. Chem. Inf. Model. 61 (2021) 2937–2956. https://doi.org/10.1021/acs.jcim.1c00235.

[98] A. Basauri, Advanced methodology for LPS capture from biofluids (dostoral dissertation), University of Cantabria (Spain), (2021).

[99] P. E. Carrigan, P. Ballar, S. Tuzmen, Site-directed mutagenesis, in: J. K. DiStefano (Ed.) Disease Gene Identification: Methods in Molecular Biology (Methods and Protocols), Humana Press, Totowa, 700, 2011: pp. 107–124. https://doi.org/10.1007/978-1-61737-954-3_8.

[100] Agilent Technologies, QuikChange ® II XL Site-Directed Mutagenesis Kit (instruction manual), (2015).

[101] A. Karnik, R. Karnik, C. Grefen, SDM-Assist software to design site-directed mutagenesis primers introducing " silent" restriction sites, BMC Bioinformatics. 14 (2013) 105. https://doi.org/10.1186/1471-2105-14-105.

[102] H. Liu, J.H. Naismith, An efficient one-step site-directed deletion, insertion, single and multiple-site plasmid mutagenesis protocol., BMC Biotechnol. 8 (2008) 91. https://doi.org/10.1186/1472-6750-8-91.

[103] J.C. Lessard, Transformation of *E. coli* via electroporation, in: J. Lorsch (Ed.) Methods in Enzymology, Elsevier Inc., Amsterdam, The Netherlands, 2013: pp. 321-327. https://doi.org/10.1016/B978-0-12-418687-3.00027-6.

[104] A. Basauri, M. Fallanza, L. Giner-Robles, R. Fernandez-Lopez, G. Moncalián, F. de la Cruz, I. Ortiz, Integrated strategy for the separation of endotoxins from biofluids. LPS capture on newly synthesized protein, Sep. Purif. Technol. 255 (2021) 117689. https://doi.org/10.1016/j.seppur.2020.117689.

[105] G.L. Rosano, E.A. Ceccarelli, Recombinant protein expression in *Escherichia coli*: Advances and challenges, Front. Microbiol. 5 (2014) 1–17. https://doi.org/10.3389/fmicb.2014.00172.

[106] K. Mathieu, W. Javed, S. Vallet, C. Lesterlin, M.P. Candusso, F. Ding, X.N. Xu, C. Ebel, J.M. Jault, C. Orelle, Functionality of membrane proteins overexpressed and purified from *E. coli* is highly dependent upon the strain, Sci. Rep. 9 (2019) 2654.

https://doi.org/10.1038/s41598-019-39382-0.

[107] GE Healthcare, HisTrap affinity columns intructions (instructions), (2006).

[108] GE Healthcare, HiTrap Chelating HP (instructions), (2003).

[109] K.M. Makwana, R. Mahalakshmi, Implications of aromatic-aromatic interactions: From protein structures to peptide models, Protein Sci. 24 (2015) 1920–1933. https://doi.org/10.1002/pro.2814.

[110] H. Chang, K. Gnanasekaran, N.C. Gianneschi, F.M. Geiger, Bacterial model membranes deform (resp. persist) upon Ni^{2+} binding to inner core (*resp*. O-antigen) of lipopolysaccharides, J. Phys. Chem. B. 123 (2019) 4258–4270. https://doi.org/10.1021/acs.jpcb.9b02762.

[111] C.M. Ongkudon, J.H. Chew, B. Liu, M.K. Danquah, Chromatographic removal of endotoxins: A bioprocess engineer's perspective, ISRN Chromatogr. 2012 (2012) 649746. https://doi.org/10.5402/2012/649746.

CHAPTER 3

Optimizing magnetic bead recovery from flowing blood in microchannels

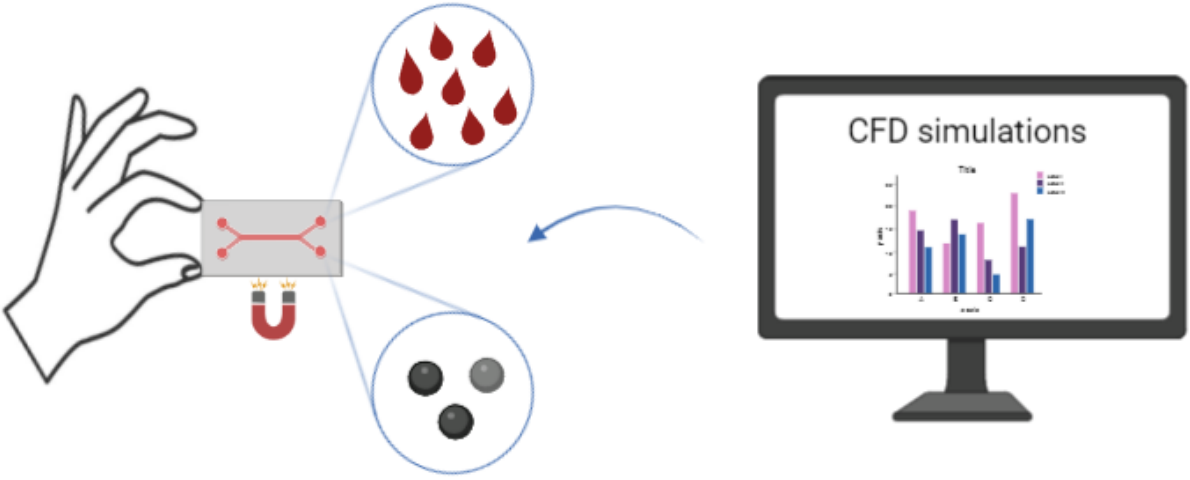

3.1. Microfluidic systems for magnetic bead recovery

Within the last decade, the use of continuous-flow magnetophoretic microseparators (CMMSs) for recovering magnetically-labelled compounds from complex media has attracted great attention inside the scientific community; this fact arises from the unique benefits that the coupling of magnetophoresis and microfluidics offers, as reported in Chapter 1. Thereby, the design of such CMMSs has been the focus of intense research in order to develop systems that enable the efficient retrieval of the target compounds. In this regard, microchannels with different geometries, for example, linear straight configuration or L/T-shaped microchannels, have been developed. From the variety of microchannel geometries, the linear straight-shaped channel has been more widely used due to its simplicity and ease of process modelling [1,2]. Regardless of the specific geometry of the microchannel, CMMSs are typically based on the collection of the particles into a coflowing buffer stream as a result of their deflection from the phase where they are initially, by the application of a magnetic gradient perpendicular to the flow direction [3]. The concept of bead retrieval in Y-Y (input-output) shaped linear straight CMMSs (hereafter Y-Y shaped CMMSs) that use a permanent magnet to generate the magnetic field has been schematized in Figure 3.1.

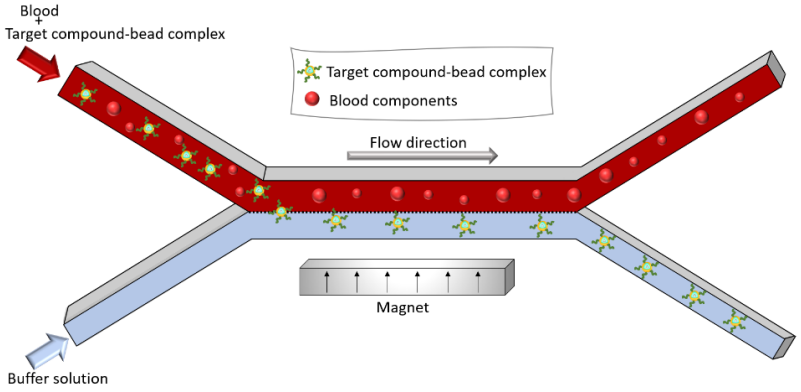

Figure 3.1. Schematic diagram of magnetic bead recovery in Y-Y shaped CMMSs.

The successful implementation of CMMSs for addressing the recovery of endotoxin-bead complexes in blood detoxification processes requires the simultaneous fulfilment of two technological challenges. More specifically, complete bead recovery at the CMMSs outlet must be attained while ensuring

the quality and functionality of blood [4]. Hence, important efforts have been devoted to the determination of the operating conditions that enable the accomplishment of these requirements. In this regard, a large number of scientific reports have addressed the separation of magnetic materials (either particles or droplets) in continuous-flow channels, both theoretically and experimentally [5–9]. These studies have analyzed the influence of multiple variables and parameters on the separator performance, such as particle size, flow rates, magnet dimensions and positions, fluid properties, etc [2,10–13]. Particularly, the ASP research group has already made important progress on the characterization of key performance metrics in Y-Y shaped CMMSs, namely, flow patterns, mass transfer between co-flowing fluids, and magnetic particle recovery; for that purpose, they introduced a CFD-based computational model that was experimentally validated [12,14,15].

Once the characterization of CMMSs has been addressed, and thus, the operating conditions for ensuring blood quality and functionality have been determined, the next step involves the optimization of magnetic bead retrieval so that complete recoveries could be accomplished at relatively high flow rates, thus minimising the time required for particle retrieval. The necessity of performing such optimization arises from the huge gap between the volumetric throughputs (i.e., flow rate of the sample to be processed) that are required for blood detoxification (i.e., processing patient blood within reasonable time) and those provided by microdevices [16]. However, prior to addressing the optimization of the magnetic recovery in microchannels, it is important to bear in mind the conditions that enable the maintenance of blood quality and functionality, since they are the cornerstone for the suitable performance of CMMSs. Therefore, the main findings about flow patterns and mass transfer in Y-Y shaped CMMSs that have been previously elucidated by the ASP research group will be briefly reported.

Ensuring blood quality and functionality imply that blood loss, dilution or biomolecule diffusion between co-flowing streams are avoided among other factors [12,17]. In order to achieve this requirement for the real application of CMMSs, Gómez-Pastora et al. [14] analyzed the flow patterns of miscible fluids and mass transfer between co-flowing fluids in Y-Y shaped CMMSs, since phase mixing or the transport of blood components could lead to a considerable degradation of the blood quality and functionality. They found that phase separation in these devices can be accomplished when the

ratio between the flow rates of the phases that are introduced in the Y-Y shaped CMMSs yields the same pressure drop for both phases (e.g., blood and water) along the channel length. Additionally, avoiding the interdiffusion between steams of blood components can be achieved by ensuring a residence time in the microchannel lower than the diffusion time of the biomolecules. Particularly, they stated that residence/diffusion time ratios lower than 0.1 should be attained. Apart from determining the operation conditions that enable keeping blood quality and functionality, Gómez-Pastora et al. [12] investigated how magnetic bead recovery is affected by several variables and parameters (namely, flow rates, particle size, rheological properties of the fluids, and magnet size). Despite the results they obtained that substantiated the promising performance of Y-Y shaped CMMSs, considerably low fluid flow rates (approximately 0.005 $\mu L \cdot s^{-1}$) were needed for attaining complete bead retrieval from blood, which reveals the low efficiency of these systems. However, the feasible application of CMMSs for blood detoxification purposes calls for the development of systems that allow the processing of poisoned blood in an acceptable time period so that the chance of survival of septic patients could be increased if these devices were eventually applied in clinical treatments. In order to address this challenge, enhancing the efficiency of these systems is computationally addressed throughout this chapter. For that purpose, two strategies are followed, that is, optimizing the geometrical features of the channel and increasing the magnetic gradient exerted on the particles by selecting a more appropriate magnet arrangement.

To tackle the first tactic, the impact of several geometrical features of Y-Y shaped CMMSs that use a single permanent magnet to generate the magnetic field (namely cross section shape, thickness, length, and volume) on the particle recovery has been investigated. It is worth mentioning that despite the important insights that have been gained about the influence of several variables on the CMMSs performance, as previously stated, a realistic analysis of the geometrical features of microdevices is missing, and literature data on the effect of the geometry of microfluidic channels on particle magnetophoresis are scarce. For instance, Nandy and coworkers [18] identified analytically the relationship between the efficiency of magnetic particle capture in a straight microchannel, that uses a line dipole as magnetic source, and several physical parameters, including the channel width. Plouffe

et al. [19]assessed the influence of the width of their sheath microfluidic-magnetophoretic device for MCF-7 carcinoma cells separation and concluded that the increase in the channel width negatively affected the capture efficiency[19]. Hale and Darabi [20] reported a computational study for the optimization of a microfluidic-magnetophoretic device for DNA isolation. In their study, the influence of the channel height and the substrate thickness on the magnetic field generated in the device was analyzed. They found that by reducing the substrate thickness and the channel height, a higher magnetic flux was obtained, which contributed to the optimization of the DNA isolation. Nevertheless, these analyses are not realistic, as the channel height, width, and thickness are determined by the employed fabrication methods, and it should be noted that one may influence another, and the cross-sectional area affects the volumetric throughput of the system. Additionally, how the cross-sectional shape of CMMSs could influence particle magnetophoresis has not been elucidated, and it is worth mentioning that this is also determined by the fabrication method employed.

In fact, the available fabrication methods have limitations regarding the chip dimensions that could be achieved, the materials that may be employed and/or the geometrical characteristics of the cross section; thus, these factors can impact the performance of the system. For example, the etching process utilized for producing glass chips has several limitations regarding the geometrical design due to the isotropicity of the technique, which allows only shallow, semicircular channel cross sections in the glass substrates [21–23]. As such, the non-symmetrical, U-shaped (U) chip sections derived from wet etching might influence the system performance when compared to channels with the strictly rectangular (R) sections that arise from lithography techniques [24–27]. Indeed, Gómez-Pastora et al.[12] addressed the separation of magnetic beads from blood solutions in both glass and SU-8 microchannels fabricated with different techniques, and they observed that, even when the same inlet velocities and magnets were applied, the systems rendered different particle recovery. This was attributed to the distinct chips cross sections as well as to the different channel thicknesses (as a result of applying different bonding techniques). Such geometric differences could affect the hydrodynamic and magnetic features of these systems respectively. However, they did not quantify these effects on the particle recovery or the flow rates that could be effectively employed, since the information regarding the hydrodynamic and magnetic conditions inside the

separators was not yet available. Since the goal of a CMMS for bead recovery is to produce a high particle recovery at high throughputs (i.e., at high flow rates of the sample to be treated [28]), the analysis of the performance reported by channels fabricated with different methods and having different cross section shapes, dimensions and thicknesses is an important step in process optimization.

Nevertheless, optimizing the geometrical features of the microchannel may not be sufficient for considerably increasing the treated flow rate while providing complete particle capture [16]. In this regard, further optimization of the performance of CMMSs relies on increasing the driving force for the isolation of the particles, i.e., the magnetic force exerted on the beads. Generating regions with high magnetic field gradients has become a potential strategy for enhancing the efficiency of these systems. To this end, the use of several permanent magnets arranged in a quadrupolar orientation, which gives rise to a quadrupole magnetic sorter (QMS), represents an outstanding alternative since field gradients higher than those typically reached by a single permanent magnet could be obtained with QMSs [29–33]. Thereby, several QMSs have been designed and tested over the years for carrying out the magnetic isolation of both not labelled and labelled cells with magnetic beads. In order to quantify the impact of the magnet arrangement on the performance of CMMSs, two different designs of typical CMMSs were tested: (i) a Y-Y shaped CMMS with a single permanent magnet and, (ii) a CMMS with a quadrupolar magnet configuration (which will be referred to as micro-QMS).

Once the tactics pursued in this dissertation for optimizing the performance of CMMSs have been explained in detail, the numerical model employed for the computer aided optimization of CMMSs is introduced in the following sections. This model will be used for addressing both tactics for CMMSs optimization. The use of a numerical model for addressing this investigation arises from the powerful platform it provides to further explain, understand, and design CMMSs in advance of the actual, physical fabrication.

3.2. Particle magnetophoresis in microchannels

3.2.1. CFD-based computational model

The optimization of magnetic bead recovery in CMMSs requires the prediction of magnetophoretic particle transport in the device. To this end, the CFD-based computational model introduced by Gómez-Pastora et al. [17] has been adapted and applied. In this section, the theoretical basis of this model is briefly described; for a deepen explanation the reader is directed to the following work [17].

Broadly speaking, two approaches are typically used to model particle magnetophoresis in microchannels, namely, the Eulerian and Lagrangian approaches. The Eulerian approach, which models particles collectively, accounts for Brownian motion by solving a drift-diffusion equation. In the Lagrangian approach, which models particles as discrete units, Brownian motion is neglected, and the motion of the individual particles is predicted by the classical Newton physics [1,34,35]. Gerber et al. develop a criterion to apply the Eulerian approach [36]:

$$|F_{ext}|D_p \leq kT \tag{3.1}$$

where $|F_{ext}|$ is the magnitude of the total force acting on the particle and D_p is the particle size, and k and T denote the Boltzmann's constant, and the absolute temperature, respectively.

The Eulerian approach is used to study the behaviour of nanosized particles when the Brownian diffusion becomes the dominant factor; this fact occurs when the magnetic force exerted on the beads is weak or the particle size is sufficiently small. Conversely, bigger particles, (e.g., with a diameter of hundreds of nanometers or beyond) are modelled according to the Lagrangian approach [17,34,35]. The approaches for modelling bead magnetophoresis and the criterion for their application have been illustrated in Figure 3.2.

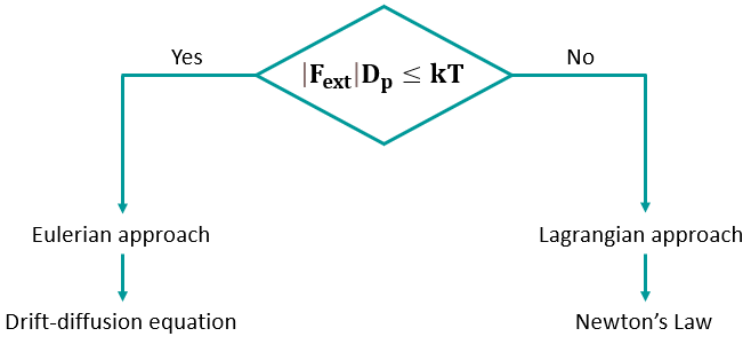

Figure 3.2. Approaches used to model magnetic particle transport.

Due to the particle sizes and the magnitude of the dominant forces acting on them, in this thesis the Lagrangian approach is used to model bead dynamics, whereas fluid transport is computed with an Eulerian approach. Thus, the model considered in this dissertation, based on the one developed by Gómez-Pastora et al. [17], involves an Eulerian-Lagrangian approach to predict the bead movement under the influence of a magnetic field. In this regard, as abovementioned, the trajectory of each particle is predicted by applying the classical Newtonian dynamics:

$$m_p \frac{d\mathbf{v_p}}{dt} = \sum \mathbf{F_{ext}} \tag{3.2}$$

where m_p and $\mathbf{v_p}/dt$ are the bead mass and acceleration, and $\mathbf{F_{ext}}$ is the resultant force vector exerted on each bead.

The inertia term on the left-hand side of Eq. 3.2 can be neglected since the particle mass is small. Hence, the particle motion is commonly estimated by setting the external forces equal to zero. In this regard, expressions for the forces acting on the beads must be derived so that the Newton's law could be solved. To this end, recognizing such forces is required.

The magnetophoretic particle motion in a carrier fluid is governed by various factors that facilitate or hinder the process. These factors include (a) magnetic force, (b) viscous drag, (c) gravity, (d) buoyancy, (e) inertia, (f) particle-fluid interactions (perturbations to the flow field), (g) thermal kinetics (Brownian motion), and (h) interparticle effects (magnetic dipole-dipole

interaction, electric double layer interaction, van der Waals force) [1,37]. The development of a comprehensive model that takes all these factors into account is highly complex and often unnecessary for practical applications [35]. Therefore, Gómez-Pastora et al. [17] introduced a model that only considers the dominant forces acting on the beads, that is, the magnetic and viscous drag forces.

The magnetic force ($\mathbf{F_m}$) is predicted with the "effective" dipole moment method as discussed in the work of Gómez-Pastora et al. [1], and can be expressed as:

$$\mathbf{F_m} = \mu_0 V_p f(H_a)(\mathbf{H_a} \cdot \nabla)\mathbf{H_a} \tag{3.3}$$

$$f(H_a) = \chi_{p,e} \qquad \forall \qquad |H_a| < \left(\frac{(x_p - x_f)+3}{3(x_p - x_f)}\right) M_{s,p} \tag{3.4}$$

$$f(H_a) = \frac{M_{s,p}}{|H_a|} \qquad \forall \qquad |H_a| \geq \left(\frac{(x_p - x_f)+3}{3(x_p - x_f)}\right) M_{s,p} \tag{3.5}$$

where μ_0 is the permeability of the free space ($4\pi \cdot 10^{-7}$ H·m^{-1}), V_p is the particle volume, $\mathbf{H_a}$ is the applied magnetic field at the bead center, χ_p and χ_f represent the magnetic susceptibilities of the bead and the fluid, respectively. $\chi_{p,e}$ and $M_{s,p}$ are the effective susceptibility of the bead (that can be related to the intrinsic susceptibility, χ_p) [38] and the particle saturation magnetization. Hence, the expression for $\mathbf{F_m}$ takes into account the conditions below and above the saturation of the particle as a function of the external applied field [15].

The components of the magnetic force (using Cartesian coordinates) are given by:

$$F_{m,x} = \mu_0 V_p f(H_a)\left(H_{a,x}\frac{\partial H_{a,x}}{\partial x} + H_{a,y}\frac{\partial H_{a,x}}{\partial y} + H_{a,z}\frac{\partial H_{a,x}}{\partial z}\right) \tag{3.6}$$

$$F_{m,y} = \mu_0 V_p f(H_a)\left(H_{a,x}\frac{\partial H_{a,y}}{\partial x} + H_{a,y}\frac{\partial H_{a,y}}{\partial y} + H_{a,z}\frac{\partial H_{a,y}}{\partial z}\right) \tag{3.7}$$

$$F_{m,z} = \mu_0 V_p f(H_a)\left(H_{a,x}\frac{\partial H_{a,z}}{\partial x} + H_{a,y}\frac{\partial H_{a,z}}{\partial y} + H_{a,z}\frac{\partial H_{a,z}}{\partial z}\right) \tag{3.8}$$

Finally, the hydrodynamic force $\mathbf{F_{hd}}$ is numerically predicted in this work using the following expression:

$$\mathbf{F}_{\mathrm{hd}} = -\mathrm{V_p}\nabla \mathrm{P} + \mathrm{M}_{\mathrm{added}}\left(\frac{\partial \mathbf{v}}{\partial \mathrm{t}} - \frac{\partial \mathbf{v}_{\mathrm{p}}}{\partial \mathrm{t}}\right) + \mathbf{F}_{\mathrm{drag}} \tag{3.9}$$

where

$$\mathbf{F_{drag}} = \frac{1}{2}\rho\left(\mathbf{v} - \mathbf{v}_{\mathrm{p}}\right)\left|\mathbf{v} - \mathbf{v}_{\mathrm{p}}\right|\mathrm{A_p C_d} \tag{3.10}$$

and

$$\mathrm{C_D} = \frac{24}{\mathrm{Re_p}} + \frac{6}{1+\sqrt{\mathrm{Re_p}}} + 0.4 \tag{3.11}$$

where P is the pressure and $\mathrm{M_{added}}$ is the added mass equal to $0.5\rho V_p$, being ρ the fluid density [7]. $\mathbf{v}$ is the fluid velocity, $\mathbf{F_{drag}}$ is the drag force and A_P is the bead cross sectional area, which can be written as $A_P = \pi r_p^2$, being r_p the particle radius. C_D is the drag coefficient for steady-state flow around a sphere [39] and Re_p is the particle Reynolds number [12,40].

As for the fluid velocity field, the Navier Stokes and continuity equations for incompressible flows were employed, accounting for the effect of the bead motion on the fluid flow through a two-way coupling model:

$$\frac{\mathrm{d}(\rho \mathbf{v})}{\mathrm{dt}} = -\nabla \mathrm{P} + \mathrm{div}(\boldsymbol{\tau}) + \frac{1}{\mathrm{V}}\mathbf{F}_{\mathrm{P}} \tag{3.12}$$

$$\nabla \cdot (\mathbf{v}) = 0 \tag{3.13}$$

where the div($\boldsymbol{\tau}$) term denotes the contribution of shear stress on the fluid velocity.

The last term in Equation (3.12) represents particle induced fluid accelerations, and $\mathbf{F_P}$ can be written as:

$$\mathbf{F}_{\mathrm{P}} = -\sum\left[\mathbf{F}_{\mathrm{drag}} + \mathrm{M}_{\mathrm{added}}\left(\frac{\mathrm{d}\mathbf{v}}{\mathrm{dt}} - \frac{\mathrm{d}\mathbf{v}_{\mathrm{p}}}{\mathrm{dt}}\right)\right] \tag{3.14}$$

This model has been used for the tactics, namely, optimizing the geometrical features of the microchannel (first tactic), and increasing the magnetic gradient exerted on the beads (second tactic), that have been pursued to enhance the performance of CMMSs. However, since the number and arrangement of the magnets, as well as the channel geometry are different for these tactics, the distribution of the magnetic field inside the microchannels is also different; thus, two strategies have been followed to calculate the magnetic field and force acting on the particles depending on whether non-homogeneous or homogeneous magnetic gradients are generated.

3.2.1.1. Non-homogeneous magnetic gradients

For devices that use a single permanent magnet (first tactic), which leads to the generation of non-homogeneous magnetic gradients, the analytical model developed by Furlani [41] has been solved in order to calculate the magnetic field distribution inside the microdevices. More specifically, the magnetic field components of the magnet used to address the first tactic for optimizing the performance of CMMSs are:

$$B_x(x,y,z) = \frac{\mu_0 \mathbf{M_{m,s}}}{4\pi} \sum_{k=1}^{2} \sum_{m=1}^{2} (-1)^{k+m} \ln\left(\frac{(y-y_1)+[(x-x_m)^2+(y-y_1)^2+(z-z_k)^2]^{\frac{1}{2}}}{(y-y_2)+[(x-x_m)^2+(y-y_2)^2+(z-z_k)^2]^{\frac{1}{2}}} \right) \quad (3.15)$$

$$B_y(x,y,z) = \frac{\mu_0 \mathbf{M_{m,s}}}{4\pi} \sum_{k=1}^{2} \sum_{m=1}^{2} (-1)^{k+m} \ln\left(\frac{(x-x_1)+[(x-x_1)^2+(y-y_m)^2+(z-z_k)^2]^{\frac{1}{2}}}{(x-x_2)+[(x-x_2)^2+(y-y_m)^2+(z-z_k)^2]^{\frac{1}{2}}} \right) \quad (3.16)$$

$$B_z(x,y,z) = \frac{\mu_0 \mathbf{M_{m,s}}}{4\pi} \sum_{k=1}^{2} \sum_{n=1}^{2} \sum_{m=1}^{2} (-1)^{k+n+m} \times \tan^{-1}\left[\frac{(x-x_n)(y-y_m)}{(z-z_k)[(x-x_n)^2+(y-y_m)^2+(z-z_k)^2]^{\frac{1}{2}}} \right] \quad (3.17)$$

where $\mathbf{M_{m,s}}$ is the magnetization of the element, (x_1, x_2), (y_1, y_2) and (z_1, z_2) are the locations of the corners of the magnet.

In order to calculate the magnetic force, the partial derivatives of the field components, which can be expressed according to the following equations, have to be computed.

$$\frac{\partial B_x}{\partial x} = \frac{\mu_0 \mathbf{M_{m,s}}}{4\pi} \sum_{k=1}^{2} \sum_{m=1}^{2} (-1)^{k+m} (x - x_m) \left[\frac{[F_1 - (y-y_1)]^{-1}}{F_1} - \frac{[F_2 - (y-y_2)]^{-1}}{F_2} \right] \quad (3.18)$$

$$\frac{\partial B_x}{\partial y} = \frac{\mu_0 \mathbf{M_{m,s}}}{4\pi} \sum_{k=1}^{2} \sum_{m=1}^{2} (-1)^{k+m}$$

$$x \left[\frac{1 + (y-y_1)[F_1 - (y-y_1)]^{-1}}{F_1} - \frac{1 + (y-y_2)[F_2 - (y-y_2)]^{-1}}{F_2} \right] \quad (3.19)$$

$$\frac{\partial B_x}{\partial z} = \frac{\mu_0 \mathbf{M_{m,s}}}{4\pi} \sum_{k=1}^{2} \sum_{m=1}^{2} (-1)^{k+m} (z - z_k) \left[\frac{[F_1 - (y-y_1)]^{-1}}{F_1} - \frac{[F_2 - (y-y_2)]^{-1}}{F_2} \right] \quad (3.20)$$

where:

$$F_1(x, y, z, x_m, y_1, z_k) = (y - y_1) + [(x - x_m)^2 + (y - y_1)^2 + (z - z_k)^2]^{\frac{1}{2}} \quad (3.21)$$

$$F_2(x, y, z, x_m, y_2, z_k) = (y - y_2) + [(x - x_m)^2 + (y - y_2)^2 + (z - z_k)^2]^{\frac{1}{2}} \quad (3.22)$$

and:

$$\frac{\partial B_y}{\partial x} = \frac{\mu_0 \mathbf{M_{m,s}}}{4\pi} \sum_{k=1}^{2} \sum_{m=1}^{2} (-1)^{k+m}$$

$$x \left[\frac{1 + (x-x_1)[H_1 - (x-x_1)]^{-1}}{H_1} - \frac{1 + (x-x_2)[H_2 - (x-x_2)]^{-1}}{H_2} \right] \quad (3.23)$$

$$\frac{\partial B_y}{\partial y} = \frac{\mu_0 \mathbf{M_{m,s}}}{4\pi} \sum_{k=1}^{2} \sum_{m=1}^{2} (-1)^{k+m} (y - y_m) \left[\frac{[H_1 - (x-x_1)]^{-1}}{H_1} - \frac{[H_2 - (x-x_2)]^{-1}}{H_2} \right] \quad (3.24)$$

$$\frac{\partial B_y}{\partial z} = \frac{\mu_0 \mathbf{M_{m,s}}}{4\pi} \sum_{k=1}^{2} \sum_{m=1}^{2} (-1)^{k+m} (z - z_k) \left[\frac{[H_1 - (x-x_1)]^{-1}}{H_1} - \frac{[H_2 - (x-x_2)]^{-1}}{H_2} \right] \quad (3.25)$$

where:

$$H_1(x, y, z, x_1, y_m, z_k) = (x - x_1) + [(x - x_1)^2 + (y - y_m)^2 + (z - z_k)^2]^{\frac{1}{2}} \quad (3.26)$$

$$H_2(x, y, z, x_1, y_m, z_k) = (x - x_2) + [(x - x_2)^2 + (y - y_m)^2 + (z - z_k)^2]^{\frac{1}{2}} \quad (3.27)$$

and finally:

$$\frac{\partial B_z}{\partial x} = \frac{\mu_0 \mathbf{M_{m,s}}}{4\pi} \sum_{k=1}^{2} \sum_{n=1}^{2} \sum_{m=1}^{2} (-1)^{k+n+m} \frac{(y-y_m)(z-z_k)[(y-y_m)^2 + (z-z_k)^2] g^3}{(x-x_n)^2 (y-y_m)^2 g^2 + (z-z_k)^2} \quad (3.28)$$

$$\frac{\partial B_z}{\partial y} = \frac{\mu_0 \mathbf{M_{m,s}}}{4\pi} \sum_{k=1}^{2} \sum_{n=1}^{2} \sum_{m=1}^{2} (-1)^{k+n+m} \frac{(x-x_n)(z-z_k)[(x-x_n)^2+(z-z_k)^2]g^3}{(x-x_n)^2(y-y_m)^2 g^2+(z-z_k)^2} \quad (3.29)$$

$$\frac{\partial B_z}{\partial z} = \frac{\mu_0 \mathbf{M_{m,s}}}{4\pi} \sum_{k=1}^{2} \sum_{n=1}^{2} \sum_{m=1}^{2} (-1)^{k+n+m} \frac{(x-x_n)(y-y_m)[g^{-2}+(z-z_k)^2]g^3}{(x-x_n)^2(y-y_m)^2 g^2+(z-z_k)^2} \quad (3.30)$$

where:

$$g(x, y, z, x_n, y_m, z_k) \frac{1}{[(x-x_n)^2+(y-y_m)^2+(z-z_k)^2]^{\frac{1}{2}}} \quad (3.31)$$

Once the field components, and the partial derivatives are determined, and from the relationship between magnetic field **B** and the field strength **H**, $\mathbf{H}=\mathbf{B}/\mu_0$, the magnetic force field can be estimated. It should be pointed out that the CFD-based model described in section 3.2.1 with the previously detailed equations for calculating the magnetic field and force was validated via application to a prototype device which was experimentally characterized using fluorescence microscopy [12,14].

3.2.1.2. Homogeneous magnetic gradients

For devices with homogeneous magnetic gradients (second tactic), which results from the arrangement of four permanent magnets in quadrupolar orientation (so-called QMSs), the partial derivatives of the field components are constant. Therefore, when beads are magnetically saturated the magnetic force is almost constant along the microchannel length. Hence, the calculation of the magnetic force, according to Eq. 3.32, is easier than for non-homogenous magnetic gradients.

$$\mathbf{F}_m = \mu_0 V_p M_p \nabla \mathbf{H}_a \quad (3.32)$$

The theoretical model herein employed for the QMS has been validated by simulating a QMS system reported in the literature [33], that had been experimentally employed for recovering a paramagnetic material (deoxygenated red blood cells, with a size similar to the magnetic beads used in this work, and with a known magnetization and size/volume distribution, which have been widely reported in the literature) [42,43]. The model results resulted to be in good agreement with the experimental data for several flow

rate values, as can be observed in Figure A2.1 of Annexe A2.

3.2.2. Simulation setup

After introducing the model for the computer aided optimization of CMMSs, in this section important features of the microdevices to be analyzed are described and the simulation setup to address the tactics for optimizing these systems (i.e., optimization of the channel geometry and increasing the magnetic gradient exerted on the beads) are explained. Furthermore, dimensionless parameters were developed and introduced to properly compare the different CMMSs and working conditions. It is worth mentioning that these parameters can also be extrapolated to compare other systems different from the ones reported here.

Firstly, the simulation setup, which is similar for both tactics, is described. Hence, to predict bead motion in the different tested CMMSs, the magnetic and fluidic models introduced in the previous sections have been solved using the commercial CFD software *FLOW-3D* (version 11.2, Flow Science, Inc.). More specifically, the magnetic field distribution (for devices with non-homogeneous magnetic gradients) and the magnetic force (for devices with non-homogeneous or homogeneous magnetic gradients) were calculated in a customized FORTRAN subroutine compiled in *Visual Studio* 2013 (Microsoft), which was linked to the *FLOW-3D* hydrodynamics solver during running. The customized magnetic force and field subroutine send the components of the magnetic force to *FLOW-3D* at each time step so that they were incorporated into the total force within the particle analysis model. MATLAB (version 2015, The MathWorks, Inc) was also employed for the visualization of the magnetic field and force distributions inside the different channels. The simulations were performed on a 48-core workstation with 128 GB of RAM.

The beads motion depends on their properties and the magnetic characteristics of the surrounding fluid. In this work, investigating particle magnetophoresis is simplified by considering that the particles comprise both the LPS bound to the biotargeting agent and the magnetic bead, thus the presence of the endotoxin and functionalization is contemplated in the bead size; future studies will take into account the morphological and structural variations of LPS-bound biotargeting beads. Thereby, spherical, micron-sized beads with different diameters (4.9, 2.45, 2.22 and 2 μm) have been

considered. Regardless of the particle size, beads are assumed to have the same density, which is equal to 2000 $kg \cdot m^{-3}$. The magnetization of the particles is estimated by using saturation magnetization and susceptibility values of $M_{s,p} = 1.5 \cdot 10^4$ $A \cdot m^{-1}$ and $\chi_{p,e} = 0.25$, respectively, which fall within the range of commercially available beads [12,44]. Regarding the magnetic properties of the surrounding fluids, they are considered non-magnetic, since their susceptibilities are considerably lower than that of the particles. To evaluate $\mathbf{F_{hd}}$, the properties of the fluids as well as the velocity profile are needed. One of the fluids in this analysis, blood, presents a non-Newtonian rheology. However, it is modelled as a Newtonian fluid and its viscosity was quantified with an analytical, empirical expression, and has a value of 3.5 cP [45,46]. It should be noted that it has been demonstrated in previous work [47] that blood follows a Newtonian rheology when the shear rate exceeds about 100 s^{-1}, and it has also been experimentally validated [12]. On the other hand, the aqueous buffer solution was modelled as water with a constant viscosity equal to 1 cP.

Once the general aspects of the simulation setup have been introduced, the systems that are analyzed in order to optimize of CMMSs are described in detail. Firstly, enhancing the CMMSs performance by optimizing the geometrical features of the microchannels is addressed. Subsequently, a further improvement in the CMMSs performance is tackled by increasing the magnetic gradient that is exerted on the particles.

3.2.2.1. Y-Y shaped CMMSs description and simulation setup for enhancing CMMSs performance by optimizing the channel geometry

Following the work of Gómez-Pastora et al. [12,14] the geometry of the Y-Y shaped CMMSs previously characterized by them has been optimized. Particularly, the effect of the cross-sectional shape and channel length/thickness on the device performance (i.e., bead capture and volumetric throughput of the system) was analyzed, by studying two different cross sections with different thicknesses and depths and three channel lengths. All the devices have two inlets and two outlets with a Y-Y shape, as presented in Figure 3.3a. The length (L) of the devices was varied from 2 to 10 mm. The cross sections are displayed in Figure 3.3b, where H represents the depth of the channel while W is the width, which is similar for all tested

geometries. As seen, channels with rectangular and U-shaped cross sections have been considered, as these are the typically derived from the most popular fabrication methods [12,14,48,49]. Furthermore, these Y-Y shaped CMMSs comprise a single permanent magnet to generate the magnetic field. More specifically, a permanent magnet of dimensions 10 x 5 x 3 mm^3 is modeled as the magnetic field source, which is commercially available. This magnet generates a magnetic field of approximately 500 mT in its pole surface. The magnet location relative to the channel for all of the studied systems is illustrated in Figure 3.3c.

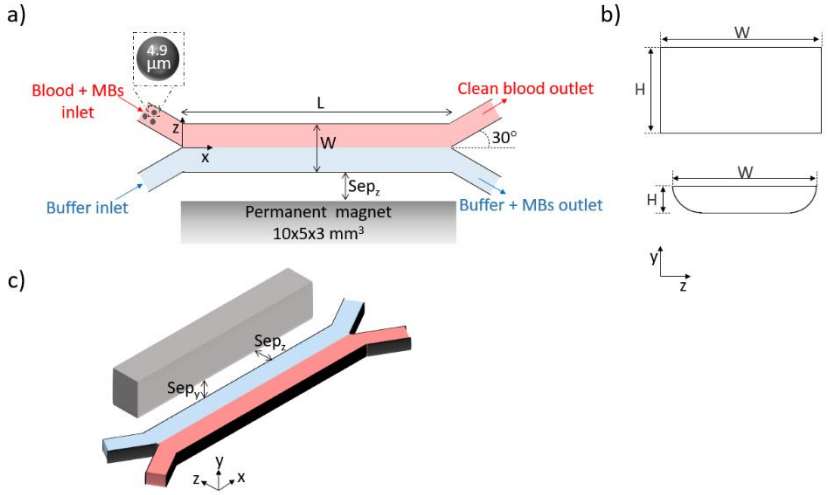

Figure 3.3. (a) Top view of the Y-Y shaped CMMS, (b) Schematic representation of the channel cross-sections studied in this work, and (c) the magnet position relative to the channel location (Sep_y and Sep_z are the magnet separation distances in y and z, respectively).

In Table 3.1, the dimensions of the microchannels under study are listed. It should be noted that, when wet etching techniques are employed for fabrication, microchannels with U shapes are obtained and the minimum channel width (W_{min}) determines H, according to the following expression [50,51]:

$$W_{min} = x + 2\,H \tag{3.33}$$

where x denotes the etching mask opening width, usually 20 µm.

For the devices herein analyzed, the width of the inlets/outlets is the narrowest (approximately half of the main channel width), and these inlets/outlets determine the H value that can be achieved by wet etching, which in this case is only 60 µm as seen in Table 3.1. On the other hand, the depth of rectangular channels is limited by the thickness of the SU-8 layer that can be produced, since thick films could lead to difficulties in the fabrication process and subsequently to faults in the final microchannels. Common SU-8 layer thickness ranges from 2 to 260 µm, depending on the SU-8 type and on several fabrication variables [52–55]. Since in the work of Gómez-Pastora [12] 200 µm depth R devices were used to experimentally validate the CFD model, and this depth is within the range of feasible SU-8 film thicknesses, in this work the depth of rectangular channels was set in 200 µm as well. All of these limitations are important as they affect the hydraulic diameter (D_h) and the chip volume. In order to suitably compare rectangular and U-shaped cross sections, the D_h as well as the chip volume were also calculated by using the appropriate equations for each type of devices [56,57], which are detailed in Table 3.1. Rectangular and U-shaped devices were further characterized and compared by estimating the fluidic resistance (R_f) of the channels according to Eq. 3.34 [58–60]:

$$R_f = \frac{8\,\eta\,L}{\pi\,R_h^4} \tag{3.34}$$

where η is the fluid viscosity and R_h the hydraulic radius of the channel.

The R_f value for each of the studied geometries is listed in Table 3.1. By taking all of the previously described parameters into account, a realistic analysis of the geometrical features of the chip can be performed.

Table 3.1. Dimensions and geometric features of the Y-Y shaped CMMSs under study.

	Rectangular shape (R)			**U shape (U)**		
L (mm)	2	5	10	2	5	10
W (μm)	300	300	300	280	280	280
H (μm)	200	200	200	60	60	60
D_h (μm)	240	240	240	97	97	97
L/D_h	8	21	42	21	51	103
Volume (mm^3)	0.12	0.3	0.6	0.03	0.08	0.15
R_f (10^{12} $Pa{\cdot}s{\cdot}m^{-3}$)	0.33	0.83	1.65	6.46	16.14	32.29

The technique and the material selected for the device fabrication not only influence the channel geometry but also determine the thickness of the total chip. During the fabrication process, a bonding step is necessary, where a slide is placed on top of the channel sealing the device. As such, the thickness of the cover bonded to the channel affects the channel-magnet distance, and thus, the magnitude of the magnetic force acting on the beads. For glass channel configurations, 1 mm thick microscope slides are generally employed as covers, whereas polymer devices can be sealed with submillimeter cover plates [52,55,61–63]. In the works of Gómez-Pastora et al. [12,14], devices with cover thicknesses of 80 μm and 1 mm for polymer and glass channels, respectively, were experimentally employed. Since these values are in agreement with the cover slide thicknesses considered in the literature for fabricating polymer and glass channels, the same dimensions are considered in this work. In Figure 3.4a, the magnet position relative to each device is depicted. For all of the systems, the magnet-channel distance in z-direction (Sep_z) is 190 μm. Correspondingly, Sep_y, is defined as the separation between the magnet and the surface of the device (i.e., surface of the channel slide) in y-direction. This dimension was set to 1 mm for both types of devices. However, the total magnet-channel separation in y-direction should also account for the thickness of the cover slide, which was different for each configuration, as previously mentioned. In this case, the cover dimension in y is greater for the U device, as presented in Figure 3.4a. Although Sep_z and Sep_y take the same values in this work for the two cross section shapes studied, the cover thickness affects the magnetic field generated inside the device, and thus, the magnetic force acting on the beads. Therefore, in Figure 3.4b-d, the magnetic force distribution in x and y

directions inside both channels have been also presented for the three tested lengths. To plot this distribution, the force acting on the particles that are located at the channel midplane, z=0, were simulated. Inspection of this plot indicated that, although the chip-magnet separation remains the same for both devices (same Sep_z and Sep_y), the thickness of the cover materials relative to, and combined with the depth of the channel, affects the magnitude of the magnetic force developed across the channel, impacting the performance of the separation. Thus, thick cover slides are not desirable when they are placed between the magnet and the particles to be separated.

In this case, the average magnetic force in z direction (the direction of the magnetic field gradient) is estimated to be 0.038 nN for R devices, whereas it decreases to approximately 0.013 nN for U devices. While there is this difference between the R and U devices, Figure 3.4b-d indicates that the average magnetic force acting on the particles does not dramatically change for each cross section shape; both the magnetic field and the magnetic field gradient are similar along L for this channel-magnet configuration. It should be noted that relatively thin slides (polymer devices) are not appropriate for processes where high pressures or temperatures are required; for these cases, the mechanical stability of the device (influenced by the hardness and thickness of the cover as well as the bonding method) is paramount.

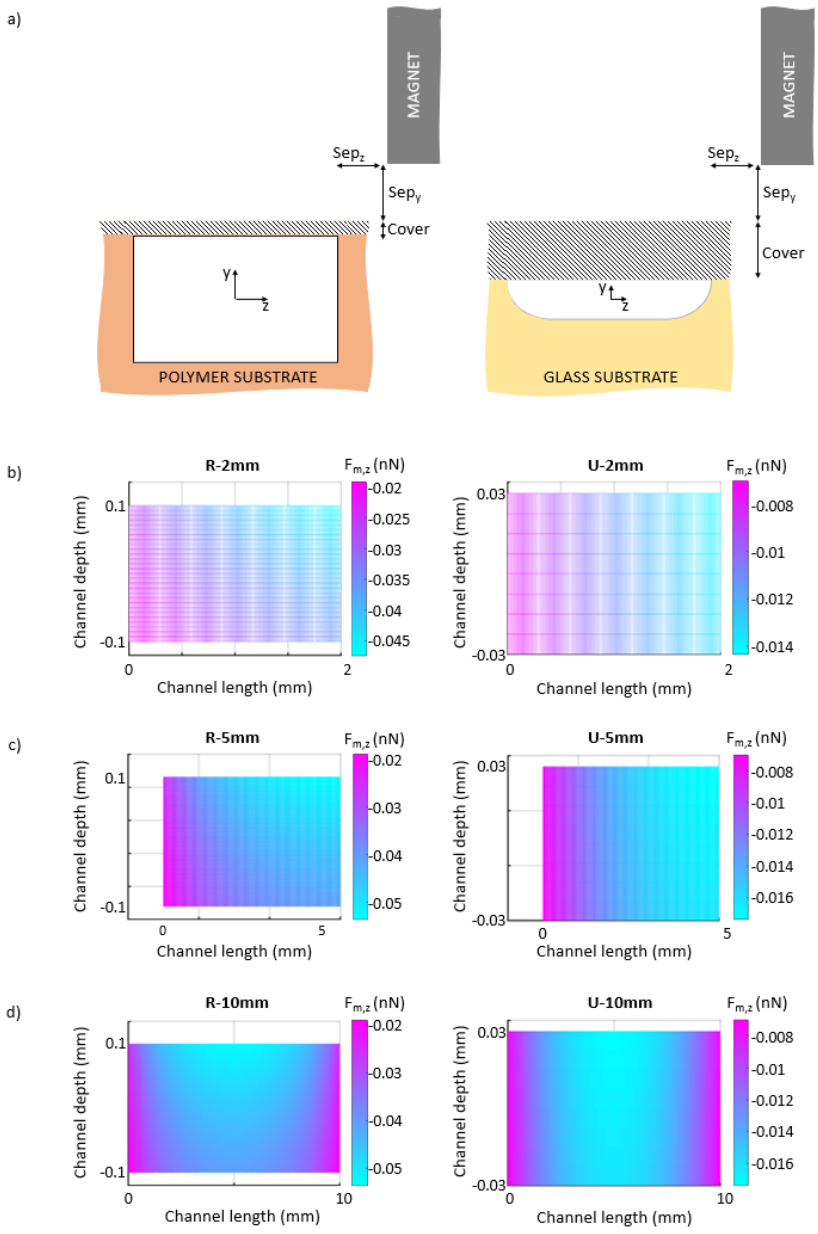

Figure 3.4. (a) Channel-magnet configuration and (b-d) magnetic force distribution in the channel midplane for 2 mm, 5 mm, and 10 mm long rectangular (left) and U-shaped (right) devices.

In summary, to elucidate the effect of the geometry on the Y-Y shaped CMMSs performance, channels with different cross section shapes were analyzed. The width and the three tested lengths of these channels, as well as the channel-magnet position were similar for both types of cross section devices, whereas the depth (and thus the volume) and the cover thickness, which are highly fabrication-dependent variables, change with the cross section shape. These differences create different hydrodynamic and magnetic conditions inside the channels, which are demonstrated below to ultimately determine the device performance.

Regarding the simulation conditions, the flow field and particle magnetophoresis were initially solved using a 3D model to evaluate the influence of the cross section on the velocity distribution and on the particle locations across the cross section, but due to the increased computational cost of these simulations, the influence of the channel dimensions on the magnetophoresis studies was simulated in 2D (although the magnetic force was calculated analytically in 3D). A uniform grid was employed for all the simulations; the mesh was composed of approximately 400,000 cells.

For studying the magnetophoresis process under different flow conditions, the inlet blood flow rate was varied between 0.005 and 3 $\mu L \cdot s^{-1}$ depending on the geometry. These hydrodynamic conditions ensure medium shear rates in the channels, under which blood can be treated as a Newtonian fluid. Nevertheless, shear stresses are still too low to observe hemolysis [64,65]. The calculated average velocity for every flow rate was used as an initial condition. As for the boundary conditions, a no slip condition (zero velocity) was applied along the microchannel walls while at the outlet, a calculated outflow boundary was used. Beads were introduced into the domain at a constant concentration of 0.1 $g \cdot L^{-1}$, which corresponds to a flow of 10-2500 $particles \cdot s^{-1}$, depending on the fluid flow rate; they were randomly injected through the cross section of the blood inlet as seen in Figure 3.3a, with a velocity equal to the blood stream. The simulation time was kept below 15 s for all the cases, which enabled tracking the path of 100-400 beads.

3.2.2.2. QMS description and simulation setup for enhancing CMMSs performance by increasing the magnetic gradient

The micro-QMS comprises essentially two components, namely, the flow channel and the magnets [33,66]. The flow channel, where the recovery of the magnetic beads takes place, consists of an annular channel; specifically, it is composed of a cylindrical shell in the external side that is concentric with a cylindrical rod located at the center, as it is illustrated in Figure 3.5a. As it has been represented in Figure 3.5b, the flow channel has inlet and outlet manifolds that allow for the injection of the magnetic particles suspended in the blood and the buffer solution at the system inlet, as well as the collection of the magnetic beads free blood and the magnetic beads enriched buffer solution at the outlet [33,66]. Once injected, the blood and the buffer flow through the annular channel; particularly, the blood flows through the half of the annular channel that is closest to the rod, whereas the buffer solution co-flows through the other half of the annular channel (closest to the magnet poles). Magnetic beads, which are injected through the same inlet as the blood, migrate radially between r_{rod} and rout (see Figure 3.5b and c) and are collected in the coflowing buffer stream by applying a magnetic field [33,66].

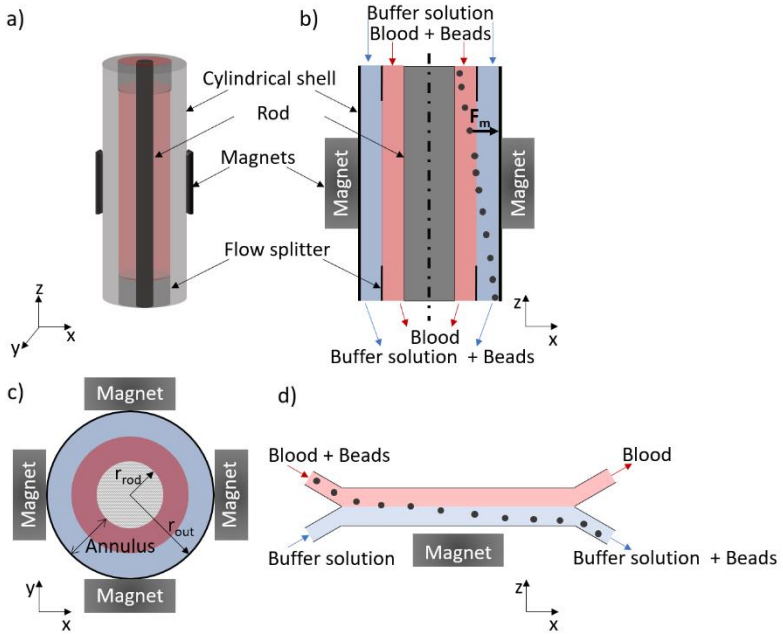

Figure 3.5. (a) Perspective view, (b) longitudinal section, and (c) cross-section of the micro-QMS; (d) longitudinal section of the conventional micro-recovery system.

The dimensions of the annular channel under investigation are listed in Table 3.2. These geometrical features correlated well with those of other QMSs reported in the literature [31–33,66–68]. It is worth mentioning that the dead volume of the flow channel (V_{dead}) has been calculated using r_{rod}. The r_{rod} value should be carefully selected in order to design systems with a V_{dead}/V_{total} high enough to work at magnetic field values that maximize the particle magnetization (i.e., saturate the particles). Thus, the V_{dead}/V_{total} value needs to be optimized to ensure both the beads saturation and the processing of relatively high flow rates (see Figure A2.2 of Annexe A2). Additionally, in order to effectively compare the performance of the micro-QMS and the Y-Y shaped CMMSs with rectangular cross-section with a single permanent magnet, which were described in section 3.2.2.1, (Figure 3.3a and Figure 3.5d), the channel length and annulus of the micro-QMS were chosen to be the same as in the Y-Y shaped CMMSs (see Ref. [4]). It is worth mentioning that Y-Y shaped CMMSs with rectangular cross section (hereafter, conventional micro-recovery system) were chosen for comparing their

performance with that of the QMS since they prove to be more efficient than U-shaped cross section channels as it will be discussed in section 3.3.1. Additionally, 10 mm long channels (QMS and conventional micro-recovery system) have been considered herein since from the different geometries tested for optimizing the geometry of Y-Y shaped CMMSs (section 3.2.2.1) conventional systems with that length provided the best performance.

Table 3.2. Channel and magnet parameters of the micro-QMS system.

Parameter	Value
Rod radius, r_{rod}, (mm)	2.54
Outer QMS radius, r_{out}, (mm)	2.84
Annulus (μm)	300
QMS length, L, (mm)	10
V_{dead}/V_{total} (-)	0.8
Magnet dimensions (Length x Height x Width) (mm^3)	10x5x3
Maximum field, B_0, (mT)	530.7
Magnetic field gradient, ∇B, ($T \cdot m^{-1}$)	186
Maximum energy product of permanent magnets, $(BxH)_{max}$, ($kJ \cdot m^{-3}$)	350

On the other hand, the magnetic field that drives the particle recovery is provided by four permanent magnets arranged in quadrupolar orientation that surround the annular channel [33,66]. Magnets with the same dimensions as the one employed in the conventional micro-recovery system (10x5x3 mm^3), which is commercially available, have been considered. These magnets produce a quadrupole field with a maximum field (B_0) at the pole tips (B_0= 530.7 mT) and a constant field gradient equal to $1.5 \cdot 10^8$ $A \cdot m^{-2}$ (or 186 $T \cdot m^{-1}$) through the QMS axial section. Since the maximum field in the micro-QMS matches the magnetic field on the pole surface of the permanent magnet considered in the conventional system, comparing the performance of both systems can be suitably addressed. Additionally, the maximum energy product of each magnet (see Table 3.2) has been provided by the commercial vendor.

Regarding the simulation setup, the force balance acting on each particle was solved using a 3D analysis, since the magnetic force was computed in x, y, and z directions. However, the governing equations that describe the flow were solved in 2D (only the radial and axial components were computed). A mesh independence study was performed in order to

optimize the number of cells considered in the simulations; hence, a tradeoff between the accuracy of the results and the computational cost of the simulations was achieved by using a mesh that comprises approximately 1,000,000 cells.

For investigating the particle magnetophoresis in the micro-QMS system under different flow conditions, the blood was injected at velocities varying between 1.6 and 70.3 cm·s^{-1}, which results in a flow rate range of 2.5-104 mL·min^{-1}. These velocities for each flow rate were used as initial conditions. With respect to the boundary conditions, a no slip condition (zero velocity) along the walls of the micro-QMS was applied, and at the outlet, the outflow boundary was used. Depending on the inlet velocity value of the blood, a particle flow rate between 2000 and 8000 particles·s^{-1} was considered, which corresponds to a concentration value between 0.6 and 1.48 mg·L^{-1}. Beads were randomly introduced into the cross section of the blood inlet, as depicted in Figure 3.5, with the same velocity as the blood. A simulation time lower than 2.5 s was kept for all cases.

3.2.3. Dimensionless analysis

Two dimensionless parameters were introduced to elucidate the effect of (i) the channel geometry, and (ii) the force balance acting on the beads, on the system performance and to efficiently compare across the broad set of geometries and CMMSs (namely, QMS and conventional micro-recovery system). The first parameter, J, relates the magnetic and the drag forces that are exerted on the beads in z and x directions, respectively (for the Y-Y shaped CMMSs), and in the radial and axial dimensions, respectively (for the QMS). With this parameter, the fluidic and magnetic variables and parameters that influence the bead trajectory (particle volume, magnetization, magnetic field strength and gradient inside the channel, viscosity of the fluids and inlet mean velocities) are considered. The J parameter can be described as [15]:

$$J = \frac{\overline{F_m}}{\overline{F_{drag}}} = \frac{\overline{F_m}}{6\pi r_p \eta_b \bar{v}_b} \tag{3.35}$$

To calculate J, the magnetic force was estimated at the midplane of the channel for Y-Y shaped CMMSs considering Eqs. 3.15-3.31. For the micro-

QMS, the magnetic force was calculated from Eq. 3.32. To determine the drag force, the viscosity (η_b) and average velocity ($\bar{v}_b$) of the blood phase were considered, since successful particle recovery entails the migration of the beads from the blood, where they are initially, to the buffer stream.

The second parameter θ balances both the residence time of the particles in the microdevice (t_{res}) and the time they require to travel from the blood to the buffer solution considering that they move completely perpendicular to the flow direction (t_m) [48,69]. Apart from the variables and parameters included in J, θ also includes the channel length (L)/characteristic length (CL) ratio, defined as the aspect ratio. Hence, this design parameter can be written as:

$$\theta = \frac{t_{res}}{t_m} = \frac{L}{CL} \cdot J \tag{3.36}$$

It is worth mentioning that for optimizing the geometrical features of Y-Y shaped CMMSs the D_h will be considered as characteristic length. Additionally, when comparing the performance of the conventional micro-recovery system and the micro-QMS, the channel width will be considered for the former and the annulus for the later as characteristic lengths for calculating θ.

In this way, J can be used for studying the performance of a single device through the analysis of the fluidic and magnetic conditions developed inside the chip, accounting for the overall magnet-channel distance, and hence including the effect of the different cover thicknesses considered. Conversely, θ takes into account the geometrical characteristics of the device (width, depth, length, and thus, volume), which allows comparing the performance of channels with different size and shape.

On the other hand, the system performance is assessed by calculating the bead recovery that can be accomplished. Specifically, the bead recovery is defined as the percentage of particles that leave the system through the buffer outlet compared to the total number that leaves the system (i.e., bead recovery is normalized to the outlet):

$$\text{Bead recovery } (\%) = \frac{\text{Particles}_{\text{buffer}}}{\text{Particles}_{\text{blood}} + \text{Particles}_{\text{buffer}}} \cdot 100 \tag{3.37}$$

Finally, in order to compare the performance of the QMS and the conventional micro-recovery system, the exploitation of the magnetic energy for obtaining complete bead recoveries (ϕ) was also computed. Specifically, ϕ, in units of $m \cdot s^{-1} \cdot kJ^{-1}$, is a measure of the velocity at which fluids can be injected in the microchannel for achieving complete particle retrieval, per unit of energy generated by the magnet arrangement. Such energy is computed as the product of the maximum energy product of the magnet, $(BxH)_{max}$, and the volume of the magnet arrangement, V_{magnet}.

$$\varphi\ (\mathrm{m} \cdot \mathrm{s}^{-1} \cdot \mathrm{kJ}^{-1}) = \frac{\mathrm{Velocity}_{\mathrm{Bead\ recovery=100\%}}}{(\mathrm{BxH})_{\mathrm{max}} \cdot \mathrm{V}_{\mathrm{magnet}}} \tag{3.38}$$

3.3. Results

3.3.1. Enhancing CMMSs performance by optimizing channel geometry

In this subsection, the effect of the microchannel geometry on both particle recovery and volumetric throughput of the system (i.e., blood treated flow rate) is explored. First, the cross section shape (keeping the same width, W) and the channel length will be evaluated, while the global analysis of the system taking into account the dimensionless parameters will be presented subsequently.

3.3.1.1. Influence of microchannel cross section shape

As mentioned before, the cross section shape may impact the velocity profile developed inside the microfluidic channel, and thus, the flow rates that could be employed to obtain complete recoveries. In order to assess the cross section effect, the velocity field achieved inside different channels was simulated. In Figure 3.6, the velocity distribution developed in a section perpendicular to the flow and the resulting bead positions in the channel cross section (for all x coordinates) are presented for devices with U-shape and rectangular cross sections when the same average velocity (0.86 $cm \cdot s^{-1}$) is applied at the inlets.

It can be perceived that, although the magnitude of the maximum velocity is lower for the U channel, the area over which this maximum velocity expands is higher in comparison to the rectangular channel. In fact, for the rectangular geometry, the area where the velocity achieves the highest value is lower and only located at the center of the cross section. Consequently, beads are exposed to the maximum velocity to a greater extent in U channels than in rectangular ones, as readily observed in Figure 3.6a. Nevertheless, since the maximum velocity achieved inside U channels is lower than the maximum velocity value in R channels, similar drag forces could be expected when applying the same inlet velocity to both channels. This different velocity distribution along with a different magnetic force field obtained inside the channels could give rise to a dissimilarity in the force balance acting on the particles. The particle locations across the cross sections of the channels for this working condition have been simulated; the results are presented in

Figure 3.6b. It can be observed that the particles move from the blood phase (left) to the right (buffer), and from the bottom wall to the top of the channel (where the magnet is placed) for both devices. However, the qualitative z component of the particle velocity vector $\mathbf{v_p}$ (flow into the figures) has a greater magnitude for the R channel, implying that, higher recoveries can be achieved within the R device. Thus, in rectangular channels the operating conditions acting on the beads seem to be more favorable for particle magnetophoresis than in U-shaped devices. In other words, for obtaining the same particle capture, the inlet flow rate in U-shaped channels must be reduced.

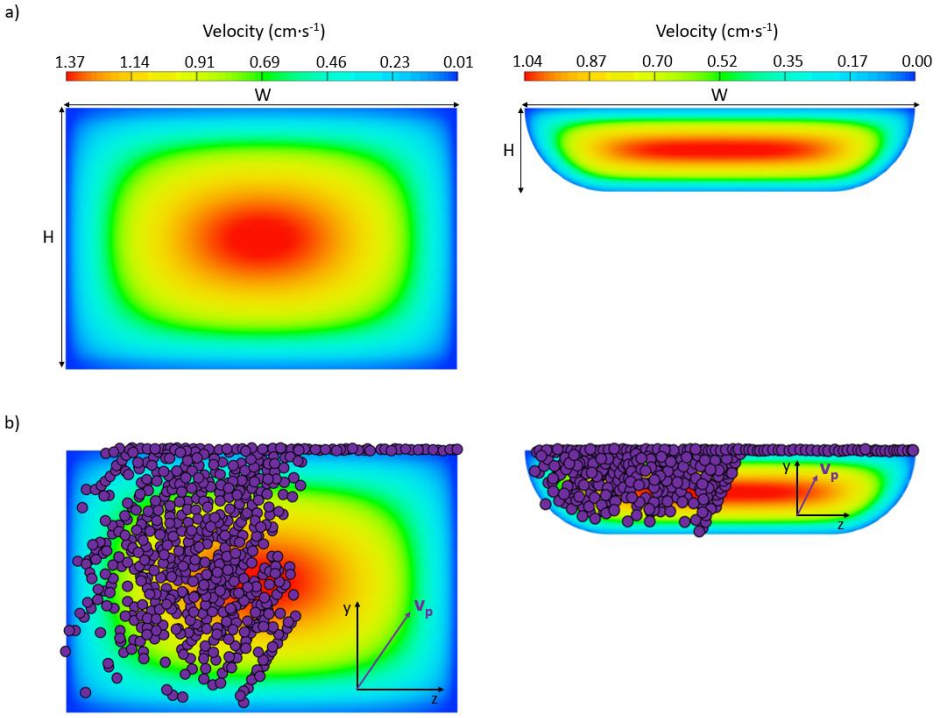

Figure 3.6. (a) Velocity distribution in a section perpendicular to the flow for rectangular (left) and U-shaped (right) cross section channels, and (b) particle location in these cross sections.

The bead recovery as a function of the fluid flow rate for both channels has been calculated. The results are presented in Figure 3.7a, where the equations of the least square curve fitting are specified; BR corresponding to the percentage of bead recovery and FR corresponding to the flow rate. It

can be observed that, for attaining comparable recoveries, the flow rate needs to be reduced at least one order of magnitude for the U channel in comparison to the rectangular one, which results in an undesirable decrease of the system throughput, and thus in an increase of the time required for the separation and concentration of the target compounds. This is attributed to the lower cross sectional area of the U device in comparison to the R device when comparable widths are employed (i.e. the cross sectional area of U channels is limited by the width as shown in Eq. 3.33), and also to the presence of a thicker cover slide, which affects the magnitude of the magnetic force.

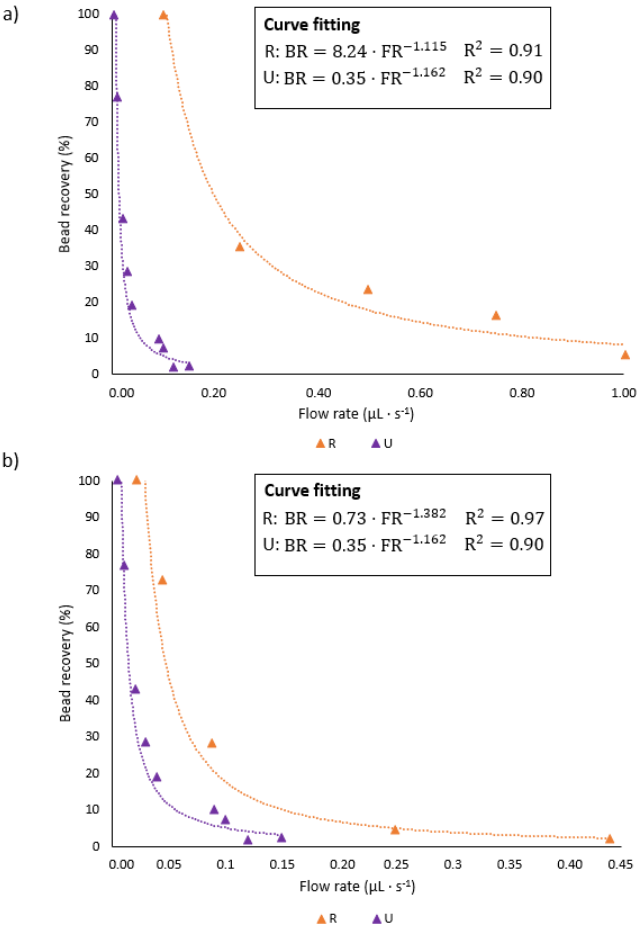

Figure 3.7. Influence of fluid flow rate on particle recovery when the applied magnetic force is (a) different and (b) equal in U-shaped and rectangular cross section microdevices.

In order to elucidate the effect of the cross section shape on the device performance, simulations applying the same magnetic field and inlet fluid velocity were carried out for rectangular and U-shaped channels. For achieving comparable magnetic forces, the same cover thickness (1 mm) was considered in both devices. Figure 3.7b displays the dependence of the particle capture with the inlet flow rate when similar magnetic and drag forces are applied. It can be deduced that although comparable magnetic and fluidic conditions were ensured, rectangular channels enable the treatment of flow rates up to four times higher than U-shaped ones while fulfilling analogous recoveries. It is worth mentioning that for designing magnetophoretic microseparators, the required bead collection, as well as the sample volume to be processed during a specific time (i.e. flow rate) must be established. However, the influence of the fluid velocity on the particle capture was also determined (Figure A2.3 of Annexe A2); these results show that, when the particle recovery is presented as a function of the average inlet velocity, comparable bead collections are achieved in both devices, which is expected since similar J values are derived for both channels. This observation led to the conclusion that the hydrodynamic conditions inside the channels are not highly affected by the cross section shape. Thereby, the weaken performance of U-shaped channels are expected to be due to their lower cross section area derived from the limitations to fabricate deeper glass channels. Nevertheless, there are some situations where glass channels might be preferred over SU-8 or polymeric devices on account of their strength, durability, chemical and heat resistance and optical transparency [22,23,70,71]. In this regard, optimizing their performance in order to enhance the volumetric throughput of the system while maintaining complete bead collection is imperative so as to microfluidic-magnetophoretic devices could be effectively employed. Therefore, in the following sections, the influence of the microchannel geometry (i.e., length and volume) and the process optimization are addressed.

3.3.1.2. Influence of microchannel length

The influence of microchannel length on the system performance was assessed by analyzing three channel lengths (L= 2, 5 and 10 mm) for both rectangular and U-shaped section channels. Specifically, only the channel length was modified for this study whereas the channel cross sectional dimensions were not modified (see Table 3.1). As previously demonstrated,

the average magnetic force exerted on the beads is not significantly influenced by the chip length for each cross section shape. Hence, the average Fm for the three tested lengths is approximately 0.013 nN in the U-shaped and 0.038 nN in rectangular devices.

Therefore, the range of flow rates that can be applied to achieve complete bead recovery was examined, by accounting for the effect of channel elongation. In Figure 3.8, the particle capture under variable fluid flow rates is depicted for the three lengths and the two cross sectional shapes examined. It can be seen that longer channels deliver greater residence time to the particles to go along the z-direction of the device for the same flow rate, promoting their collection at the buffer outlet (Figure A2.4 of Annexe A2). As such, for equal flow rates, a five-fold increase of channel length leads to an enhancement of the particle recovery of about 65% for rectangular and 44% for U-shaped section devices (Figure A2.5 of Annexe A2). This means that increasing the channel lengths by a factor of 5 did not result in equal recovery improvements between the R and U geometries. This disagreement between both systems is also attributed to the different cross sectional area as well as to the dissimilarity in the magnetic force achieved inside the chips. The improved performance of rectangular channels also stems from their lower R_f values, which are one or two orders of magnitude lower than those observed for U-shaped devices with the same length. Comparing channels with R_f values of the same order of magnitude, that is 10 mm long rectangular and 2 mm long U-shaped chips, it can be noticed that the R-10mm device allows the management of flow rates 100 times higher than U-2mm while attaining the entire bead recovery, which implies a significant enhancement in the volumetric throughput of the system.

Furthermore, Figure 3.8 reveals that the 10 mm long chip with rectangular section offers the best performance, since it provides the complete magnetic capture while treating sample flow rates one or two orders of magnitude higher than the other geometrical configurations, improving the volumetric throughput of the system.

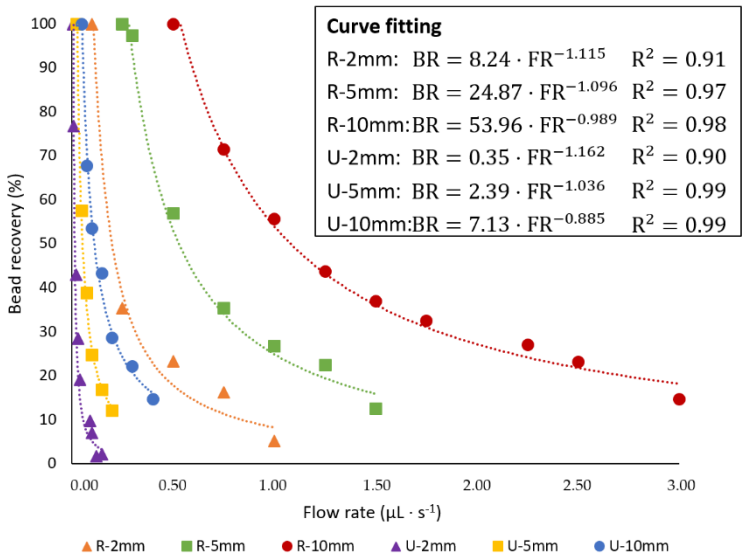

Figure 3.8. Magnetic bead capture as a function of fluid flow rate for all studied Y-Y shaped CMMS's geometries. Note that BR and FR stand for bead recovery and flow rate, respectively.

Once the cross section shape and channel length have been individually analyzed, in the next section the overall optimization of the system will be presented along with useful guidelines regarding the channel design.

3.3.1.3. Dimensionless channel design

In this subsection, the two dimensionless design parameters, J and θ introduced above, are applied to compare all the geometries under study and characterize their geometrical features. The J parameter is used to consider the operating regime of the microseparators into two regimes: hydrodynamic $J < 1$, and magnetic $J > 1$, as illustrated in Figure 3.9a. It can be easily deduced that for both devices, the particle recovery increases with J; in this case, J increases due to a decrease in the flow rate since the $\mathbf{F_m}$ is fixed for each cross section shape. Furthermore, complete particle capture is achieved working in hydrodynamic conditions (i.e., drag forces larger than magnetic ones) for all the systems ($J_2^R = 0.054$; $J_5^R = 0.022$; $J_{10}^R = 0.011$; $J_2^U = 0.084$; $J_5^U = 0.017$; $J_{10}^U = 0.008$). In addition, it was found that the J value that corresponds to complete particle recovery is similar for both devices; as seen in Figure 3.9,

the recovery as a function of J is dependent on L but independent on the cross sectional shape. Since the J parameter scales directly proportional to the magnetic and inversely to the drag force (Eq. 3.35), similar J values for each channel length stem from the compensation of the higher values of $\mathbf{F_m}$ and $\mathbf{F_{drag}}$ for rectangular channels in comparison to the U-shaped. Additionally, due to the similarity of the magnetic force exerted on the particles regardless the channel length for each cross section shape, the J parameter necessary to achieve complete recovery decreases as the channel length is increased. This is due to the fact that, by using longer devices, the applied flow rate can be also increased, and thus the fluid velocity inside the channels, which leads to higher drag forces (Figure A2.4 of Annexe A2). Therefore, optimum systems will be those that allow complete bead recovery at the smallest J, since the volumetric throughput could be enhanced up to 5 times by working with 10 mm R (J_{10}^R = 0.011) compared to 2 mm R (J_2^R = 0.054) channels, or 10 times when 10 mm U (J_{10}^U =0.008) devices are used instead of 2 mm U (J_2^U = 0.084).

Following the dimensionless analysis, to assess the overall influence of the channel geometry, the dimensionless parameter θ was exploited. In Figure 3.9b, the percentage of particle recovery as a function of θ for all the geometries is shown. As occurs with J, particle recovery is favored by increasing θ. However, contrary to what happened with J, the particle recovery as a function of θ is not dependent on the length of the channel, but slightly changes with the shape of the cross section. Accordingly, for the two types of cross sections considered in this study, the effect of increasing the L/D_h ratio is compensated with the decrease in the J parameter, due to the rise of the fluid drag force which results from the larger velocities that could be applied to obtain the same bead collection. For this reason, particle recovery as a function of θ does not change with the channel length. Thereby, regardless the aspect ratio, with rectangular section channels complete recoveries are accomplished approximately 2 times faster in comparison to U-shaped ones, as derived from the linear relationship ($R^2 \approx 0.98$) between the θ parameter and the percentage of particle capture for all the geometries except for the 2 mm long U device. This fact leads to lower θ values for rectangular channels (θ^R = 0.45) than for U-shaped ones (θ^U = 1.73) for attaining complete particle capture. Furthermore, for comparable aspect ratios, such as 5 mm long U (L/D_h = 51) and 10 mm long R (L/D_h = 42) or 2 mm long U (L/D_h = 21) and 5 mm long R (L/D_h = 21), the values of the J parameter

that yield entire capture are lower for rectangular channels (J_5^U = 0.017; J_{10}^R = 0.011; J_2^U =0.084; J_5^R = 0.022), and hence lower θ. It should be noted that because of the limitations for producing deeper glass devices, the cross section area of U is lower than for rectangular channels, since the limitations regarding the channel depth in R chips are less restrictive. Thus, similar aspect ratios entail longer R than U channels. Consequently, the higher magnetic forces and residence time combined with the different velocity distribution of rectangular channels make possible the use of higher velocities (i.e., higher drag forces) than in U-shaped, thus reinforcing the evidence that rectangular sections promote the improvement of the volumetric throughput of the system. As such, systems that bear complete recoveries with the lowest θ are preferred.

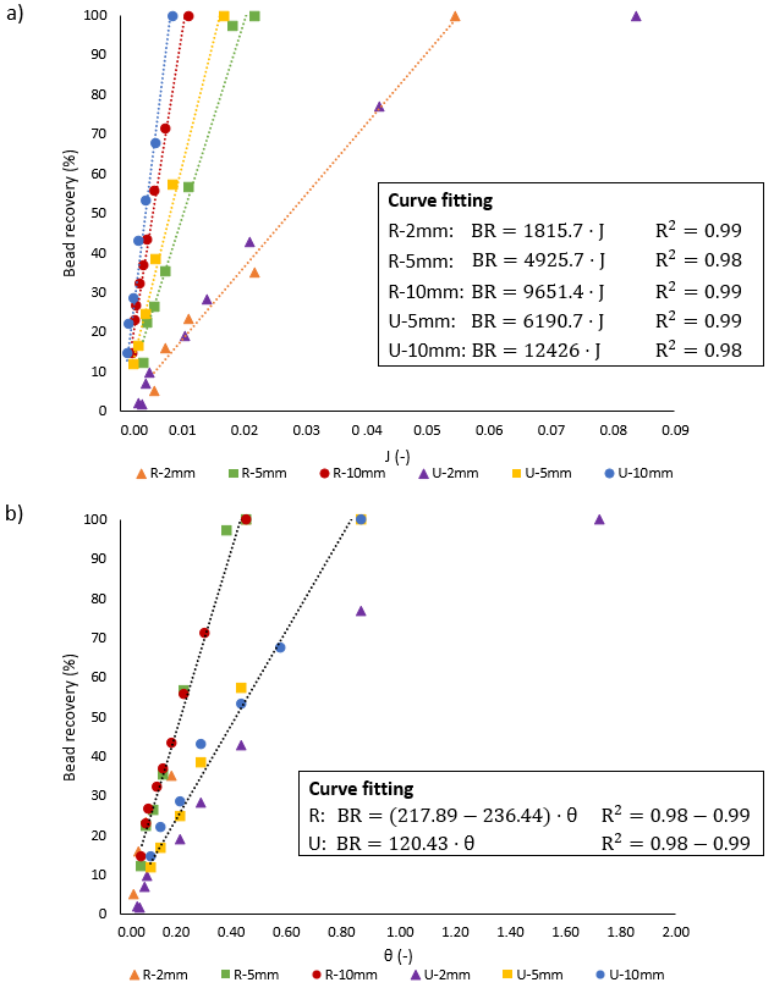

Figure 3.9. Influence of (a) magnetic and fluidic forces (J parameter) and (b) channel geometry (θ parameter) on particle recovery. Note that U-2mm does not accurately fit a line.

On the other hand, the comprehensive evaluation of the channel geometry has also been assessed by examining the impact of the channel volume on both the magnetic capture and the volumetric throughput of the system for each independent geometry. For that purpose, Figure 3.10a illustrates the bead recovery percentage as a function of the functional channel volume (without taking into account the substrate and cover volumes

presented in Figure 3.4a) when the same inlet velocity is considered (1.92 $cm \cdot s^{-1}$). It should be mentioned that the functional channel volume corresponds to the branch of the Y-Y shaped device whereby blood flows; since the microdevices considered in this study are symmetric in the z-direction (see Figure 3.3a), the total system volume is twice the channel volume. As presented in Figure 3.10a, by increasing the channel volume (microchannel lengthening), the particle residence time in the chip also increases, which promotes their collection at the buffer channel outlet (Figure A2.4 of Annexe A2). Furthermore, the analysis of the functional volume of the channels reveals that U devices are more efficient since they deliver higher recoveries than R devices when comparing the same volume. In this regard, for having comparable channel volumes, the length of U chips must be five times higher than for rectangular, due to the smaller cross section shape of U devices that arise from the weaknesses of the fabrication method as previously stated. Under these conditions, U-shaped chips provide higher residence time to the particles, which fosters their capture, thus leading to higher recoveries than in rectangular devices, although the magnetic force exerted in the rectangular channel is higher. This means that the effect of channel elongation has a greater impact than the application of higher magnetic forces. Similarly, for attaining comparable bead recoveries, the length of U channels should be approximately 2.5 times higher than the length of R channels. However, due to the lower deepness of U-shaped channels in comparison to rectangular, the volume of U is lower than of R devices, which demonstrates the more efficient performance of high aspect ratio (L/D_h) channels in terms of bead capture, given that they render similar recoveries with lower channel volumes.

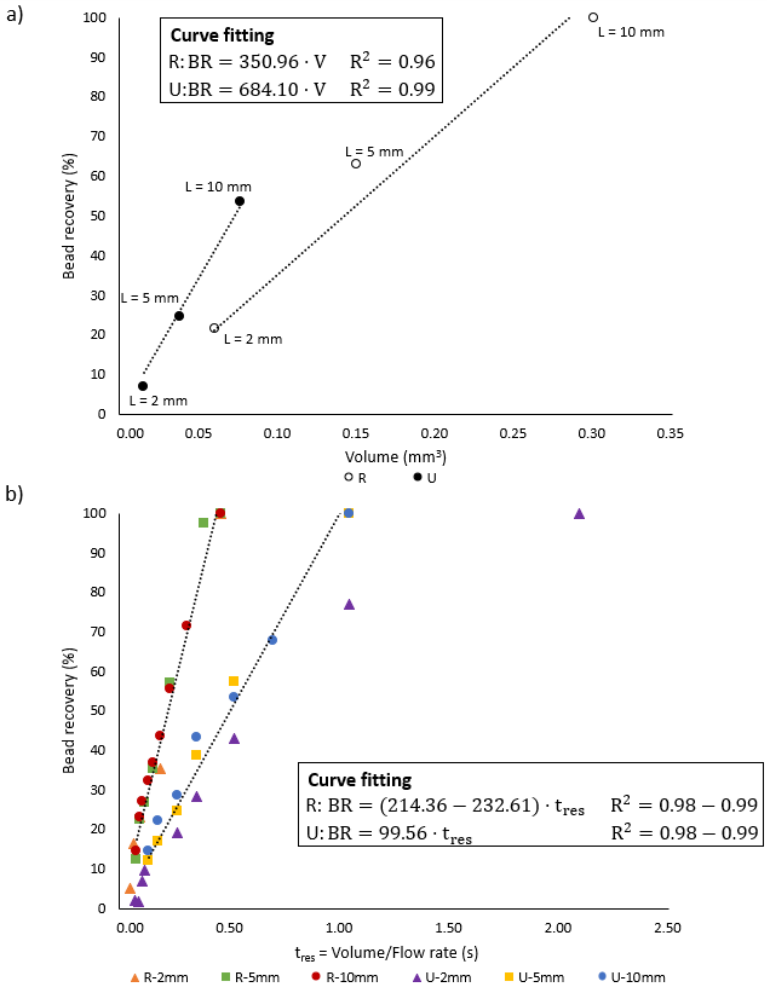

Figure 3.10. Dependence of bead capture on the (a) functional channel volume and (b) particle residence time (t_{res}). Note that in the curve fitting expressions V represents the functional channel volume and that U-2mm does not accurately fit a line.

Despite this efficient performance, the effect of the flow rate that can be treated has not been considered in Figure 3.10a. Since the fulfillment of the design requirements (i.e., treating relatively high blood flow rates while entirely capturing the beads) for a realistic application of these magnetophoretic microseparators is intrinsically related to the channel

geometry, and hence to the chip volume, in Figure 3.10b the dependence of the bead recovery with the ratio between the functional channel volume and the treated blood flow rate (namely residence time) is displayed. It can be noticed that such relationship is not influenced by the channel length for each cross section shape. Nevertheless, the residence time of the particles in the device required for attaining similar recoveries is lower in rectangular than in U-shaped channels; thus it is possible to achieve the complete bead capture by applying up to 5 times higher flow rates in R than in U, having both types of devices the same volume (Figure A2.4 of Annexe A2). Therefore, it can be concluded that while U-shaped chips are more efficient in terms of the lower volume they require for a desired recovery, rectangular channels allow higher sample flow rates to be subjected to magnetic forces for achieving the specified recovery with the same channel volume.

Overall, the results of the global analysis carried out in this work are presented in Table 3.3. As seen in this table, for the same fluidic conditions, the higher magnetic force acting on rectangular devices yields greater J values, which results in a higher bead collection in rectangular devices. Additionally, for similar θ values the recoveries obtained with rectangular channels can be approximately 3 times higher than with U-shaped, hence, displaying a faster raise in the percentage of particle capture with θ. This different dependency of the particle recovery on θ implies that particle capture attained by using rectangular in contrast to U-shaped section channels can be increased as much as 14 times. In this regard, with 10 mm long R channels obtaining complete recoveries is possible at inlet fluid velocities of 1.92 $cm \cdot s^{-1}$, whereas U-shaped devices must be elongated to a greater extent (or several channels in series must be used) in order to increase the residence time of the beads in the device and thus promote their entire recovery (Figure A2.4 of Annexe A2). In other words, the particle residence time in U channels should be approximately twice that in rectangular ones for achieving similar recoveries in both types of channels when applying the same inlet velocity; thus, rectangular devices allow attaining complete particle capture while treating blood flow rates 4.4 times higher than in U channels. Due to the higher residence time required by U-shaped chips, several devices have to be arranged in parallel for concurrently delivering comparable recoveries and volumetric throughputs to rectangular channels. Accordingly, for successfully treating a flow rate of 1 mL of blood per hour while capturing entirely the beads, one 10 mm long R device or six 10 mm long U devices,

operating in parallel, are required. However, it should be taken into account that the use of several microseparators either in series or in parallel, which is needed so that the performance of U devices is similar to that of rectangular ones, may lead to higher fabrication and operational costs, thus negatively affecting the system efficiency.

Table 3.3. Comparative analysis of all Y-Y shaped CMMSs configurations for the same inlet fluid velocity (1.92 $cm \cdot s^{-1}$).

	Particle recovery (%)	**Throughput ($\mu L \cdot s^{-1}$)**	**J (-)**	**θ (-)**	**t_{res} (s)**
U-2mm	7.09	0.1	0.004	0.086	0.1
U-5mm	24.78	0.1	0.004	0.216	0.26
U-10mm	53.5	0.1	0.004	0.432	0.52
R-2mm	21.57	0.44	0.012	0.103	0.11
R-5mm	63.02	0.44	0.012	0.258	0.26
R-10mm	100	0.44	0.012	0.516	0.53

3.3.2. Enhancing CMMSs performance by increasing the magnetic gradient

3.3.2.1. Influence of magnetic field gradient

In this section, the performance of the micro-QMS under investigation, whose geometrical features have been included in Table 3.2, is characterized and compared to a Y-Y shaped CMMS with rectangular cross section in which a single permanent magnet is used. As it has been previously mentioned, the arrangement of 4 permanent magnets in quadrupolar orientation leads to a considerable increase in the magnetic field gradient generated inside the QMS. Specifically, magnetic field gradients of about $1.5 \cdot 108\ A \cdot m^{-2}$ (or $186\ T \cdot m^{-1}$) are generated inside the micro-QMS, which results in magnetic forces acting on the beads of 0.17 nN. This magnetic force is one order to magnitude higher than the one generated in the conventional micro-recovery system operated with a single permanent magnet (around 0.038 nN). It is worth mentioning that although this difference in the magnetic force mainly stems from the higher magnetic field gradients in the micro-QMS, the distance between the magnet and the flow channel, which is higher for the conventional system (200 µm), should be also considered. Thereby, in the conventional system ensuring a channel-magnet distance is required

since otherwise the magnetic field gradient would be generated only around the magnet corners (at the channel inlet and outlet) with zero magnetic force along the channel length; moreover, the limitations of the methods employed for fabricating these systems hamper the magnet to be located next to the channel wall.

As a result of this high magnetic force, the fluids can also be injected in the micro-QMS at higher velocities while ensuring complete particle capture. In Figure 3.11a, the percentage of particle capture as a function of the blood inlet velocity is depicted. It can be seen that complete isolation of magnetic beads is fulfilled for fluid velocities of 7.44 $cm \cdot s^{-1}$. This velocity is approximately 4.5 times higher than the one that enables the complete particle capture in the conventional micro-recovery system that uses a single permanent magnet for generating the magnetic field. Therefore, for systems with the same cross-section area, the QMS allows the treatment of flow rates 4.5 times higher than conventional micro-separators, hence, leading to a significant enhancement of the system efficiency. Figure 3.11b illustrates the bead recovery as a function of the processed blood flow rate. As it can be easily noticed, complete recovery of magnetic beads in the micro-QMS is accomplished while treating blood flow rates as high as 11 $mL \cdot min^{-1}$, which is 367 times higher than the one processed in the conventional micro-recovery system (0.5 $\mu L \cdot s^{-1}$). Thus, the micro-QMS significantly enhances the blood flow rate that can be treated while providing complete bead capture; this high flow rate stems from both the larger cross section area of such system and the bigger magnetic field gradient achieved when 4 magnets are employed, which allows the processing of higher velocities in comparison to the conventional system. Therefore, increasing the magnetic field gradient entails a noteworthy enhancement of the system performance in comparison to lengthening of conventional micro-recovery systems, which represents another strategy fulfilled in the literature for improving the efficiency of particle retrieval [4]. Thereby, increasing the channel length of conventional systems from 2 mm to 10 mm involves only a five-fold increase of the blood flow rate that could be treated while entirely capturing the beads, which significantly contrasts with the ability of the QMS to treat 3 orders of magnitude higher flow rates in comparison to the conventional system. Thus, the micro-QMS exhibits an outstandingly improved efficiency, which substantiates its potential for being used for the recovery of magnetic beads when relatively high flow rates are required. These flow rates can be further

increased by using higher magnetic field gradients, such as the ones considered in several QMSs published in the literature, namely, 300 $T \cdot m^{-1}$ or 1750 $T \cdot m^{-1}$ [30,33]. Assuming that these magnetic gradients can be ensured in the micro-QMS presented here (or one with a similar cross sectional area) by employing permanent magnets with a higher maximum magnetic field at their pole tips, and keeping the magnetic field value high enough to saturate the particles, complete bead capture can be fulfilled at flow rates of 18 $mL \cdot min^{-1}$ and 104 $mL \cdot min^{-1}$; these values correspond to flow rates of approximately 1.6 (∇B= 300 $T \cdot m^{-1}$) and 9.5 (∇B= 1750 $T \cdot m^{-1}$) times higher than the ones than can be processed when using the 186 $T \cdot m^{-1}$ gradient employed in this study. However, increasing the magnetic field gradient by reducing the QMS radius (instead of increasing the maximum magnetic field) could entail an undesirable decrease of the flow rate that can be processed for providing entire bead capture. Indeed, the decrease of the QMS cross sectional area dominates the effect of increasing the magnetic field gradient exerted on the particles (see Figure A2.6 of Annexe A2). Collectively, the arrangement of magnets with high magnetic fields in their pole tips entails the application of higher magnetic field gradients, thus, enhancing the efficiency of the micro-QMS.

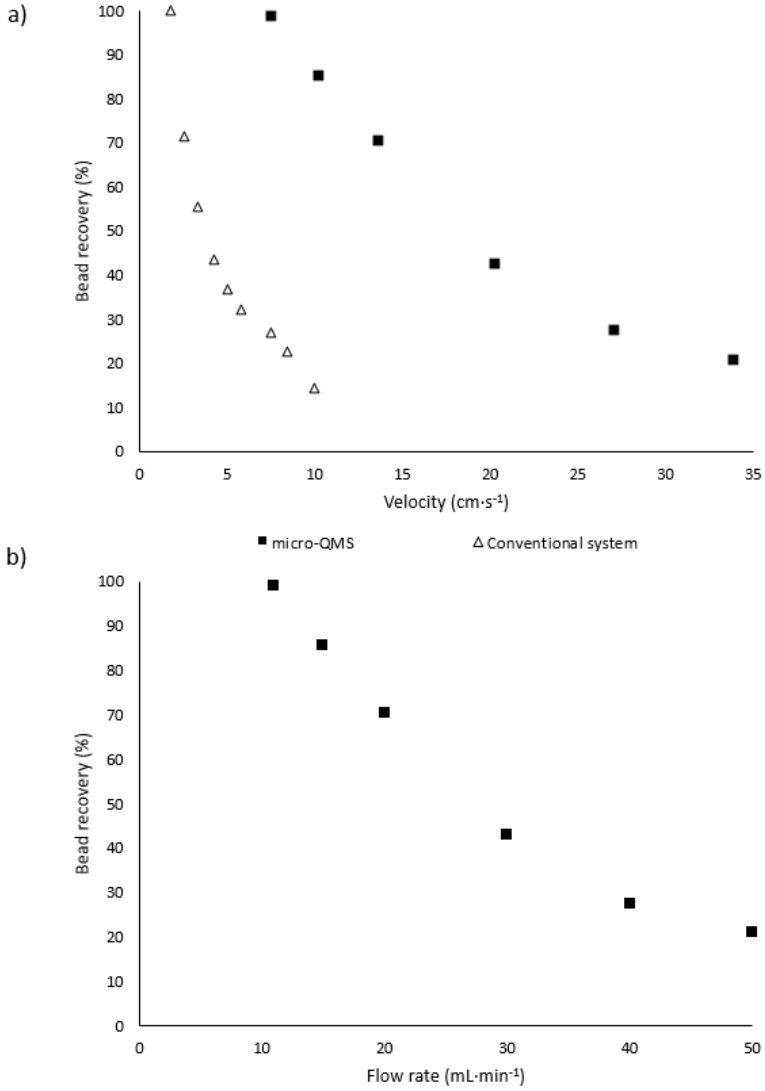

Figure 3.11. Dependence of particle recovery on blood a) velocity in the micro-QMS system and in the conventional system, and b) flow rate in the micro-QMS (the flow rates that can be processed by the conventional system are three orders of magnitude lower).

3.3.2.2. Effect of particle size

Reducing the dose of magnetic beads that is required for supporting the biotargeting agent to capture the target endotoxin seems promising in order to further fulfill the criteria of process intensification and to reduce the process costs. This fact could be addressed by decreasing the particle size, which leads to an increase of its specific surface area, and thus of the amount of biotargeting agent that can be adsorbed on the surface of the particles. Conversely, the magnetic bead recovery after the reaction process is favored by increasing the particle size, as it has been previously demonstrated [12]. Therefore, and by taking advantage of the improved performance of the micro-QMS, the reduction in particle size that can be accepted while achieving complete bead captures at relatively high fluid velocities in comparison to the use of particles with a diameter of 4.9 μm was assessed. To this end, the magnetophoresis of particles with different sizes when they are injected in the micro-QMS at the same velocity as the one that yields complete recoveries in the conventional system was investigated. As seen from Figure 3.12, the complete recovery is fulfilled in the QMS when 2.45 μm particles are used, whereas to achieve the same recovery with the conventional system 4.9 μm particles are required; thus, halving the particle size does not lead to worsen the micro-QMS performance. Further reduction of particle size (2 μm) results in an undesirable decrease of bead retrieval in the micro-QMS. Therefore, reducing bead diameter beyond 2.22 μm proves unaffordable, since particle recoveries lower than those obtained with the conventional systems are accomplished. The specific surface area of 2.22 μm and 4.9 μm particles is 1.35 $m2 \cdot g^{-1}$ and 0.61 $m2 \cdot g^{-1}$, respectively. Hence, as it was previously mentioned, smaller particles enable the adsorption on its surface of higher amounts of the biotargeting agent, thus favoring the sequestration of the target LPS. Additionally, the mass of particles required to achieve a surface area equal to 1 m^2 is 0.74 g for the 2.22 μm and 1.63 g for the 4.9 μm particles. Therefore, the use of 2.22 μm beads entails a 55% reduction of the particle mass for achieving the same surface area as 4.9 μm beads. Since complete retrieval of 2.22 μm beads can be accomplished in the micro-QMS, the improved performance, meeting the criteria for process intensification of the QMS over the conventional systems, is demonstrated.

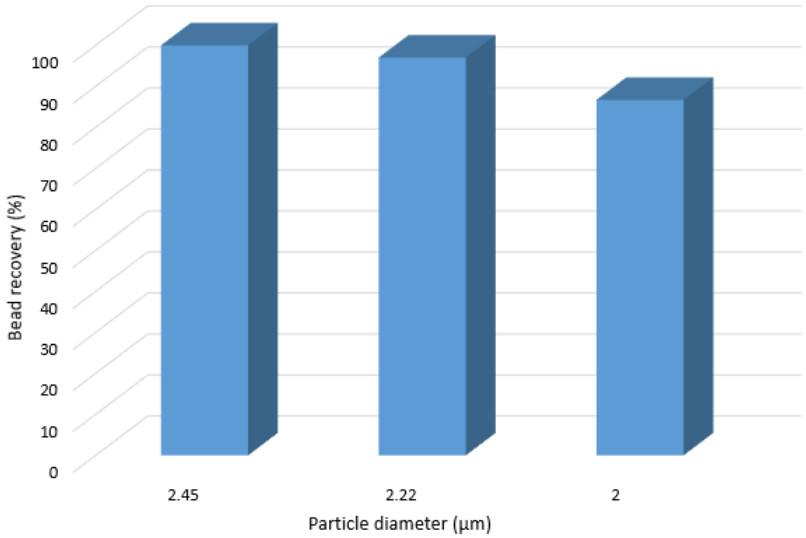

Figure 3.12. Effect of particle diameter on bead recovery in the micro-QMS.

3.3.2.3. Dimensionless micro-QMS characterization

In this subsection, the aforementioned parameters J, θ and ϕ will be applied to characterize the performance of the micro-QMS. The parameter J determines the ratio of forces, namely magnetic and drag, that should act on the beads in order to successfully achieve the desired particle recovery. When studying the influence of the fluid velocity on the micro-QMS performance, the magnetic force is the same in all scenarios, since the same magnetic field gradient and particle size held constant for all the simulations. Conversely, the drag force changes with the velocity at which the blood is injected in the micro-QMS. As it can be seen from Figure 3.13a, where the percentage of bead recovery has been represented as a function of J, the recovery of magnetic beads is favored by increasing J. This results from the decrease in the velocity, and thus the drag force, that is required for achieving complete particle capture. Regardless of the fluidic conditions, J-values lower than one are derived, which implies that higher drag forces than magnetic ones can be exerted on the beads while attaining entire recoveries. Particularly, the J-value that yields complete bead capture is 0.014, which is the same as the one for accomplishing the same recovery in the micro-QMS when different

magnetic field gradients (300 $T \cdot m^{-1}$ or 1750 $T \cdot m^{-1}$) are used, as well as in the conventional micro-recovery system. Since the J-parameter is directly proportional to the magnetic force and scales inversely to the drag force, these similar J-values regardless of the magnetic field gradient or the channel geometry system stems from the compensation of the magnetic and drag forces.

On the other hand, when investigating the effect of the particle size on the micro-QMS performance, the magnetic force changes with the size of the magnetic bead, although the same magnetic properties of the particles have been assumed for all the simulations. Moreover, particles with different diameters are subjected to different drag forces although the fluid velocity has been kept at the same value (1.67 $cm \cdot s^{-1}$). Thereby, reducing the particle size diameter leads to a decrease of the magnetic and drag forces exerted on these beads. It is worth mentioning that reducing the magnetic force negatively influences particle retrieval, whereas decreasing the drag force has a positive effect on it. According to equations 3.2, 3.3, and 3.9, particle size has a higher impact on the magnetic than on the drag force; hence, for the same fluidic conditions, lower J-values are expected when reducing the particle diameter. Thereby, the J parameter for 2.45 µm, 2.22 µm and 2 µm beads when the abovementioned fluid velocity is applied takes the values of $J_{2.45} = 0.016$, $J_{2.22} = 0.013$, $J_2 = 0.011$. Since it was previously demonstrated that reducing the particle diameter beyond 2.22 µm proves unaffordable due to the unacceptable recovery that could be accomplished, it can be concluded that bead size should be carefully chosen so that J-values around 0.013 could be obtained. Collectively, it can be rationalized that, regardless of the magnetic field gradient or the particle size, the improved performance of the micro-QMS over the conventional microrecovery system is maintained while ensuring J-values around 0.014.

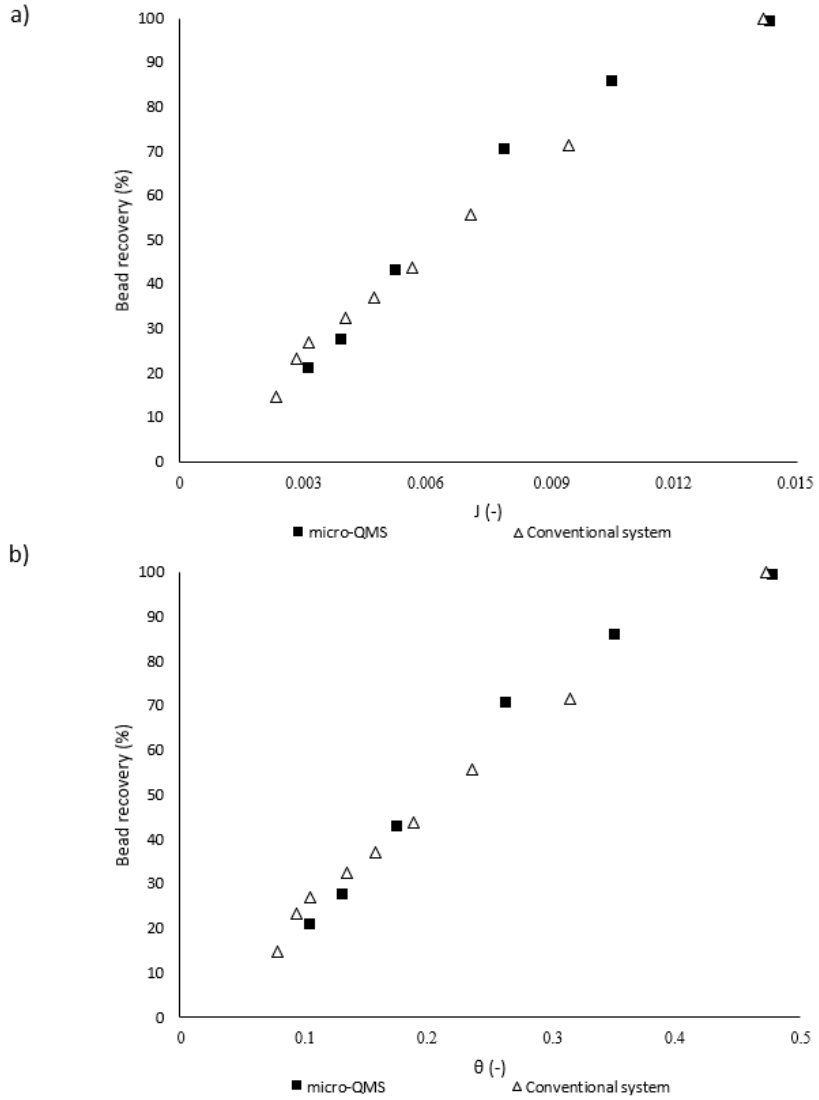

Figure 3.13. Magnetic bead retrieval as a function of the dimensionless parameters (a) J (balance of magnetic and drag forces), and (b) θ (coupling of magnetic and fluidic forces with the channel geometry).

Following the dimensionless analysis, the parameter θ was exploited to elucidate the simultaneous influence of the channel geometry and the magnetic and fluidic conditions inside the micro-QMS. The dependence of particle recovery with θ (Figure 3.13b) shows the same trend as with J; hence,

particle recovery increases with θ. Additionally, θ values lower than one are obtained for all the fluidic conditions that have been tested. Specifically, when θ is approximately 0.5 complete particle capture is fulfilled, regardless of the magnetic field gradient applied to the beads (186 $T \cdot m^{-1}$, 300 $T \cdot m^{-1}$ or 1750 $T \cdot m^{-1}$); according to the definition of the θ parameter (see equation 3.36), this θ-value denotes that magnetic beads can be entirely recovered by ensuring that the residence time of the particle in the device is one half of the time they need to go from the blood to the buffer stream considering that their movement is completely perpendicular to the flow direction. Given that the J parameter and the channel aspect ratio are the same for the micro-QMS and the conventional system, as it has been previously discussed, the same dependence of the percentage of bead recovery may be expected for these geometries.

Regarding the comparison of the θ parameter for beads with different sizes when an inlet fluid velocity of 1.67 $cm \cdot s^{-1}$ is used, it can be concluded that the θ-value for obtaining complete recoveries of 2.45 µm, 2.22 µm or 2 µm beads decreases with the particle diameter, $\theta_{2.45}$= 0.53, $\theta_{2.22}$ = 0.44, θ_2 = 0.36. Since smaller particles than 2.22 µm could not be entirely retrieved in the QMS while using the abovementioned inlet velocity, particle diameters that yield θ-values around 0.5 should be selected in order to ensure the outstanding performance of the micro-QMS in comparison to the conventional microrecovery system.

Finally, the efficacy of the exploitation of the energy generated by the magnet arrangement for attaining complete recoveries in the micro-QMS and in the conventional system was compared. To this end, the ϕ parameter is employed. As it was previously stated, the same magnets were used in both systems; thus, the maximum energy product and the volume of each magnet does not change for these systems (see Table 3.2). However, since the magnet arrangement in the QMS comprises 4 permanent magnets, the volume of the magnet arrangement in the QMS is 4 times higher than that in the conventional system, where solely a single magnet is used; therefore, the magnetic energy generated in the QMS is four times higher than in the conventional system. Due to this higher magnetic energy, fluids can be injected at considerably higher velocities (approximately 4 times higher) in the QMS than in the conventional system while fulfilling the entire particle retrieval, as it was previously discussed in section 3.3.2.1. However, if the fluid

velocity for fulfilling complete recoveries per unit of magnetic energy (ϕ parameter) is contrasted for the micro-QMS (ϕ_{QMS}= $3.54 \cdot 10^2$ $m \cdot s^{-1} \cdot kJ^{-1}$) and the conventional system ($\phi_{conventional}$= $3.17 \cdot 10^2$ $m \cdot s^{-1} \cdot kJ^{-1}$), it can be noted that both systems exhibit a similar efficiency in the exploitation of the magnetic energy, since the high fluid velocity in the QMS is compensated with its high magnetic energy, and the low fluid velocity in the conventional system counterbalances the low magnetic energy in this system. Collectively, assessing the performance of the micro-QMS and the conventional systems per unit of magnetic energy that they exploit, it can be concluded that both systems enable the injection of the fluids at the same velocity for fulfilling complete bead retrieval; however, the flow rate that can be processed in the micro-QMS while attaining such recovery is outstandingly higher, as stated in section 3.3.2.1. It should be also noted that the increase in the current magnetic field gradient in the QMS system is possible while using the same volume of magnet material. Indeed, this optimization could be accomplished by reducing the dead volume (V_{dead}) without modifying the device's width and length. Under this scenario, the efficiency in the exploitation of the magnetic energy would be considerably higher for the QMS system. Thus, the micro-QMS exhibits an outstandingly improved performance when compared to other separator designs, which substantiates its potential for recovering magnetic beads at relatively high flows.

3.4. Conclusions

The successful application of CMMSs for addressing the toxin-bead recovery in MCMDs calls for the development of systems that deliver complete particle retrieval at relatively high sample flow rates; this way the time required in the magnetic recovery stage is reduced, thus enhancing the chance of survival in septic patients, if these devices were eventually applied in clinical treatments. In this doctoral dissertation, two strategies have been investigated in order to design CMMSs that satisfy the abovementioned requirements.

1) On the one hand, the optimization of the geometry of Y-Y shaped CMMSs for carrying out the continuous-flow particle magnetophoresis from biofluids has been addressed. More specifically, for microdevices with the same width, the influence of the channel length/thickness and cross section shape on the system performance (i.e., particle recovery capacity and volumetric throughput expressed as residence time) was evaluated. To effectively compare all the systems under study, two dimensionless parameters, which account for the forces acting on the beads (J) and for the coupling of these forces and the geometrical features of the channels (θ), were used.

   According to the findings showed throughout this chapter, the lower magnetic force, due to the higher channel thickness, in addition to the lower cross sectional area as well as a different velocity distribution developed inside U channels lead to a notable reduction of the flow rates that can be treated for attaining complete particle recoveries in comparison to rectangular section channels, lessening the volumetric throughput of the system. Hence, for each specific cross section shape, the improvement of the microseparators performance was tackled by lengthening the channels. As expected, the resulting increase of the particles residence time in the device promotes their complete capture at higher flow rates, thus, significantly improving the system volumetric throughput. This means that channel elongation favors the system operation in a hydrodynamic regime, i.e. J parameter values considerably lower than 1. It has also been elucidated that the bead collection as a function of J only depends on the channel length, whereas the different relationship between particle recovery and θ for

the tested geometries is determined by the cross section shape. Thereby, rectangular channels accomplish complete recoveries faster than U-shaped section devices, being possible working with θ values approximately 4 times lower when rectangular channels are used. Finally, the effect of the system volume was analyzed, finding that for the same device volume, higher recoveries were obtained with U-shaped section channels. Nevertheless, a global analysis of all the geometries considered in this work allows one to conclude that the main weakness of U devices is their low volumetric throughput for achieving the desired capture in comparison to rectangular ones; hence, rectangular section channels are the best alternative since they need shorter residence times for a specific recovery than U devices. Despite the noteworthy differences in the performance between devices with these cross sectional shapes, U-shaped chips are imperative for applications where the use of glass channels is required due to the working conditions or the fluid nature.

2) On the other hand, the retrieval of magnetic particles has also been optimized by increasing the magnetic gradient exerted on the particles. For that purpose, four permanent magnets were arranged in quadrupolar orientation, which gives rise to a QMS. More specifically, the performance of such QMS has been assessed and it has been compared with the performance of a Y-Y shaped CMMS with rectangular cross section (conventional micro-recovery system) with similar geometrical features that operates with a single magnet. Different parameters, namely, the balance of forces acting on the particles (J), the coupling of such forces with the channel geometrical features (θ) and the exploitation of the magnetic energy for fulfilling entire recoveries (ϕ) have been used to characterize the micro-QMS.

   The findings discussed throughout this chapter revealed that the improved performance of the micro-QMS in comparison to the conventional micro-recovery system mainly stems from the outstandingly higher magnetic field gradients that are generated in the microchannel when a quadrupolar orientation of the magnets is taken. As a result of the high magnetic gradient, one order of magnitude higher magnetic forces are exerted on the beads. Hence, compared to the conventional system, the complete retrieval of either (a) particles

flowing at 4.5 times higher velocities or (b) 2.2 times smaller particles can be successfully fulfilled in the micro-QMS. Particularly, recovering beads at higher velocities entails the processing of ≈360 times higher flow rates that what can be treated by the conventional system, while the capture of smaller beads involves a 55% reduction of the particle dose for providing the same surface area. Regardless of the bead size or the magnetic field gradient, the dimensionless analysis reveals that complete particle retrieval is fulfilled when the balance of the magnetic and drag forces that act on the beads (J-parameter) is 0.014, and the coupling of magnetic and fluidic forces with the geometrical features of the channel (θ-parameter) is 0.5. Additionally, it was demonstrated through the ϕ parameter, which determines the highest fluid velocity for attaining entire particle capture, per unit of energy generated by the magnet arrangement, that the micro-QMS and the conventional system exhibit a similar efficiency in the exploitation of the magnetic energy for obtaining complete bead recovery ($\phi \approx 3.4 \cdot 10^{2}$ $m \cdot s^{-1} \cdot kJ^{-1}$).

Collectively, the design guidelines provided in this systematic study promote the understanding of the great importance of both the channel geometrical features and the magnet configuration on the CMMSs performance. These guidelines prove potentially valuable to tackle the rational design of any CMMSs, extending their exploitation beyond the geometries and magnet configurations considered in this work. Additionally, the efficient performance of the micro-QMS herein designed, which meets several criteria for process intensification, has been demonstrated, thus substantiating its potential for being exploited for blood detoxification purposes through the efficient capture and removal of endotoxins. Moreover, the basis for further optimization of QMS systems has also been provided.

3.5. References of Chapter 3

[1] J. Gómez-Pastora, X. Xue, I.H. Karampelas, E. Bringas, E.P. Furlani, I. Ortiz, Analysis of separators for magnetic beads recovery: From large systems to multifunctional microdevices, Sep. Purif. Technol. 172 (2017) 16–31. https://doi.org/10.1016/j.seppur.2016.07.050.

[2] X. Wu, H. Wu, Y. Hu, Enhancement of separation efficiency on continuous magnetophoresis by utilizing L/T-shaped microchannels, Microfluid. Nanofluidics. 11 (2011) 11–24. https://doi.org/10.1007/s10404-011-0768-7.

[3] J. Gómez-Pastora, E. Bringas, M. Lázaro-Díez, J. Ramos-Vivas, I. Ortiz, The reverse of controlled release: Controlled sequestration of species and biotoxins into nanoparticles (NPs), in: P. Stroeve, M. Mahmoudi (Eds.), Drug Deliv. Syst., World Scientific, New Jersey, 2018: pp. 207–243. https://doi.org/10.1142/9789813201057_0006.

[4] C. González Fernández, J. Gómez Pastora, A. Basauri, M. Fallanza, E. Bringas, J.J. Chalmers, I. Ortiz, Continuous-flow separation of magnetic particles from biofluids: How does the microdevice geometry determine the separation performance?, Sensors. 20 (2020) 3030. https://doi.org/10.3390/s20113030.

[5] N. Pamme, Magnetism and microfluidics, Lab Chip. 6 (2006) 24–38. https://doi.org/10.1039/b513005k.

[6] J. Gómez-Pastora, V. Amiri Roodan, I.H. Karampelas, A.Q. Alorabi, M.D. Tarn, A. Iles, E. Bringas, V.N. Paunov, N. Pamme, E.P. Furlani, I. Ortiz, Two-step numerical approach to predict ferrofluid droplet generation and manipulation inside multilaminar flow chambers, J. Phys. Chem. C. 123 (2019) 10065–10080. https://doi.org/10.1021/acs.jpcc.9b01393.

[7] J. Gómez-Pastora, I.H. Karampelas, E. Bringas, E.P. Furlani, I. Ortiz, Numerical analysis of bead magnetophoresis from flowing blood in a continuous-flow microchannel: implications to the bead-fluid interactions, Sci. Rep. 9 (2019) 7265. https://doi.org/10.1038/s41598-019-43827-x.

[8] M.D. Tarn, N. Pamme, On-Chip Magnetic Particle-Based Immunoassays Using Multilaminar Flow for Clinical Diagnostics, in: V. Taly, J.-L. Viovy, S. Descroix (Eds.), Microchip Diagnostics Methods and Protocols, Humana Press, New York, 2017: pp. 69–83. https://doi.org/10.1007/978-1-4939-6734-6_6.

[9] C. Phurimsak, M.D. Tarn, S.A. Peyman, J. Greenman, N. Pamme, On-chip determination of c-reactive protein using magnetic particles in continuous flow, Anal. Chem. 86 (2014) 10552–10559. https://doi.org/10.1021/ac5023265.

[10] S.A. Khashan, E.P. Furlani, Scalability analysis of magnetic bead separation in a microchannel with an array of soft magnetic elements in a uniform magnetic field, Sep. Purif. Technol. 125 (2014) 311–318. https://doi.org/10.1016/j.seppur.2014.02.007.

[11] M. Vojtíšek, M.D. Tarn, N. Hirota, N. Pamme, Microfluidic devices in superconducting magnets: On-chip free-flow diamagnetophoresis of polymer particles and bubbles, Microfluid. Nanofluidics. 13 (2012) 625–635. https://doi.org/10.1007/s10404-012-0979-6.

[12] J. Gómez-Pastora, C. González-Fernández, E. Real, A. Iles, E. Bringas, E.P. Furlani, I. Ortiz, Computational modeling and fluorescence microscopy characterization of a two-phase magnetophoretic microsystem for continuous-flow blood detoxification, Lab Chip. 18 (2018) 1593–1606. https://doi.org/10.1039/c8lc00396c.

[13] T.P. Forbes, S.P. Forry, Microfluidic magnetophoretic separations of immunomagnetically labeled rare mammalian cells, Lab Chip. 12 (2012) 1471–1479. https://doi.org/10.1039/c2lc40113d.

[14] J. Gómez-Pastora, C. González-Fernández, M. Fallanza, E. Bringas, I. Ortiz, Flow patterns and mass transfer performance of miscible liquid-liquid flows in various microchannels: Numerical and experimental studies, Chem. Eng. J. 344 (2018) 487–497. https://doi.org/10.1016/j.cej.2018.03.110.

[15] J. Gómez-Pastora, I.H. Karampelas, X. Xue, E. Bringas, E.P. Furlani, I. Ortiz, Magnetic bead separation from flowing blood in a two-phase continuous-flow magnetophoretic microdevice: theoretical analysis through computational fluid dynamics simulation, J. Phys. Chem. C. 121 (2017) 7466–7477. https://doi.org/10.1021/acs.jpcc.6b12835.

[16] C. González-Fernández, J. Gómez-Pastora, E. Bringas, M. Zborowski, J.J. Chalmers, I. Ortiz, Recovery of magnetic catalysts: Advanced design for process intensification, Ind. Eng. Chem. Res. 60 (2021) 16780–16790. https://doi.org/10.1021/acs.iecr.1c03474.

[17] J. Gómez-Pastora, On the design of lab-on-a-chip devices for magnetophoretic separations (doctoral dissertation), University of Cantabria (Spain), (2018).

[18] K. Nandy, S. Chaudhuri, R. Ganguly, I.K. Puri, Analytical model for the

magnetophoretic capture of magnetic microspheres in microfluidic devices, J. Magn. Magn. Mater. 320 (2008) 1398–1405. https://doi.org/10.1016/j.jmmm.2007.11.024.

[19] B.D. Plouffe, L.H. Lewis, S.K. Murthy, Computational design optimization for microfluidic magnetophoresis, Biomicrofluidics. 5 (2011) 013413. https://doi.org/10.1063/1.3553239.

[20] C. Hale, J. Darabi, Magnetophoretic-based microfluidic device for DNA isolation, Biomicrofluidics. 8 (2014) 044118. https://doi.org/10.1063/1.4893772.

[21] H. Becker, C. Gärtner, Polymer microfabrication methods for microfluidic analytical applications, Electrophoresis. 21 (2000) 12–26. https://doi.org/10.1002/(SICI)1522-2683(20000101)21:1<12::AID-ELPS12>3.0.CO;2-7.

[22] T. Wang, J. Chen, T. Zhou, L. Song, Fabricating microstructures on glass for microfluidic chips by glass molding process, Micromachines. 9 (2018) 269. https://doi.org/10.3390/mi9060269.

[23] M. Castaño-Álvarez, D.F. Pozo Ayuso, M. García Granda, M.T. Fernández-Abedul, J. Rodríguez García, A. Costa-García, Critical points in the fabrication of microfluidic devices on glass substrates, Sensors Actuators, B Chem. 130 (2008) 436–448. https://doi.org/10.1016/j.snb.2007.09.043.

[24] S. Prakash, S. Kumar, Fabrication of microchannels: A review, Proc. Inst. Mech. Eng. Part B J. Eng. Manuf. 229 (2015) 1273–1288. https://doi.org/10.1177/0954405414535581.

[25] M. Leester-Schädel, T. Lorenz, F. Jürgens, C. Ritcher, Fabrication of Microfluidic Devices, in: A. Dietzel (Ed.), Microsystems Pharmatechnology Manip. Fluids, Part. Droplets, Cells, Springer, Switzerland, 2016: pp. 23–57. https://doi.org/10.1007/978-3-319-26920-7_2.

[26] N.W. Bartlett, R.J. Wood, Comparative analysis of fabrication methods for achieving rounded microchannels in PDMS, J. Micromech. Microeng. 26 (2016) 115013. https://doi.org/10.1088/0960-1317/26/11/115013.

[27] P.F. Ng, K.I. Lee, M. Yang, B. Fei, Fabrication of 3D PDMS microchannels of adjustable cross-sections via versatile gel templates, Polymers. 11 (2019) 64. https://doi.org/10.3390/polym11010064.

[28] S.A. Khashan, S. Dagher, A. Alazzam, B. Mathew, A. Hilal-Alnaqbi,

Microdevice for continuous flow magnetic separation for bioengineering applications, J. Micromech. Microeng. 27 (2017) 055016. https://doi.org/10.1088/1361-6439/aa666d.

[29] M.A.M. Gijs, F. Lacharme, U. Lehmann, Microfluidic applications of magnetic particles for biological analysis and catalysis, Chem. Rev. 110 (2010) 1518–1563. https://doi.org/10.1021/cr9001929.

[30] J. Gómez-Pastora, X. Wu, N. Sundar, J. Alawi, G. Nabar, J.O. Winter, M. Zborowski, J.J. Chalmers, Self-assembly and sedimentation of 5 nm SPIONs using horizontal, high magnetic fields and gradients, Sep. Purif. Technol. 248 (2020) 117012. https://doi.org/10.1016/j.seppur.2020.117012.

[31] M. Nakamura, K. Decker, J. Chosy, K. Comella, K. Melnik, L. Moore, L.C. Lasky, M. Zborowski, J.J. Chalmers, Separation of a breast cancer cell line from human blood using a quadrupole magnetic flow sorter, Biotechnol. Prog. 17 (2001) 1145–1155. https://doi.org/10.1021/bp010109q.

[32] M. Hoyos, K.E. McCloskey, L.R. Moore, M. Nakamura, B.J. Bolwell, J.J. Chalmers, M. Zborowski, Pulse-injection studies of blood progenitor cells in a quadrupole magnet flow sorter, Sep. Sci. Technol. 37 (2002) 745–767. https://doi.org/10.1081/SS-120002215.

[33] L.R. Moore, D. Mizutani, T. Tanaka, A. Buck, M. Yazer, M. Zborowski, J.J. Chalmers, Continuous, intrinsic magnetic depletion of erythrocytes from whole blood with a quadrupole magnet and annular flow channel; pilot scale study, Biotechnol. Bioeng. 115 (2018) 1521–1530. https://doi.org/10.1002/bit.26581.

[34] E.P. Furlani, Magnetic biotransport: Analysis and applications, Materials. 3 (2010) 2412–2446. https://doi.org/10.3390/ma3042412.

[35] S.A. Khashan, E.P. Furlani, Effects of particle-fluid coupling on particle transport and capture in a magnetophoretic microsystem, Microfluid. Nanofluidics. 12 (2012) 565–580. https://doi.org/10.1007/s10404-011-0898-y.

[36] R. Gerbei, M. Takayasu, F.J. Friedlaender, Generalization of HGMS theory: The capture of ultra-fine particles, IEEE Trans. Magn. 19 (1983) 2115–2117. https://doi.org/10.1109/TMAG.1983.1062795.

[37] E.P. Furlani, Analysis of particle transport in a magnetophoretic microsystem, J. Appl. Phys. 99 (2006) 024912. https://doi.org/10.1063/1.2164531.

[38] E.P. Furlani, Y. Sahoo, K.C. Ng, J.C. Wortman, T.E. Monk, A model for predicting magnetic particle capture in a microfluidic bioseparator, Biomed. Microdevices. 9 (2007) 451–463. https://doi.org/10.1007/s10544-007-9050-x.

[39] F.M. White, Viscous Fluid Flow, McGraw-Hill, New York, 1974.

[40] B. Mathew, A. Alazzam, B. El-Khasawneh, M. Maalouf, G. Destgeer, H.J. Sung, Model for tracing the path of microparticles in continuous flow microfluidic devices for 2D focusing via standing acoustic waves, Sep. Purif. Technol. 153 (2015) 99–107. https://doi.org/10.1016/j.seppur.2015.08.026.

[41] E.P. Furlani, Permanent Magnet and Electromechanical Devices; Materials, Analysis and Applications, Academic Press, Waltham MA, 2001.

[42] J. Kim, J. Gómez-Pastora, C.J. Gilbert, M. Weigand, N.A. Walters, E. Reátegui, A.F. Palmer, M. Yazer, M. Zborowski, J.J. Chalmers, Quantification of the mean and distribution of hemoglobin content in normal human blood using cell tracking velocimetry, Anal. Chem. 92 (2020) 1956–1962. https://doi.org/10.1021/acs.analchem.9b04302.

[43] J. Kim, J. Gómez-Pastora, M. Weigand, M. Potgieter, N. A. Walters, E. Reátegui, A. F. Palmer, M. Yazer, M. Zborowski, J.J. Chalmers, A subpopulation of monocytes in normal human blood has significant magnetic susceptibility: quantification and potential implications, Cytom. Part A. 95 (2019) 478–487. https://doi.org/10.1002/cyto.a.23755.

[44] M.D. Tarn, S.A. Peyman, D. Robert, A. Iles, C. Wilhelm, N. Pamme, The importance of particle type selection and temperature control for on-chip free-flow magnetophoresis, J. Magn. Magn. Mater. 321 (2009) 4115–4122. https://doi.org/10.1016/j.jmmm.2009.08.016.

[45] E.J. Furlani, E.P. Furlani, A model for predicting magnetic targeting of multifunctional particles in the microvasculature, J. Magn. Magn. Mater. 312 (2007) 187–193. https://doi.org/10.1016/j.jmmm.2006.09.026.

[46] E.P. Furlani, K.C. Ng, Analytical model of magnetic nanoparticle transport and capture in the microvasculature, Phys. Rev. E. 73 (2006) 061919. https://doi.org/10.1103/PhysRevE.73.061919.

[47] R. Eibl, D. Eibl, R. Pörtner, G. Catapano, P. Czermak, Cell and Tissue Reaction Engineering, Springer, Berlin Heidelberg, 2009.

[48] N. Pamme, J.C.T. Eijkel, A. Manz, On-chip free-flow magnetophoresis:

Separation and detection of mixtures of magnetic particles in continuous flow, J. Magn. Magn. Mater. 307 (2006) 237–244. https://doi.org/10.1016/j.jmmm.2006.04.008.

[49] A.Q. Alorabi, M.D. Tarn, J. Gómez-Pastora, E. Bringas, I. Ortiz, V.N. Paunov, N. Pamme, On-chip polyelectrolyte coating onto magnetic droplets-Towards continuous flow assembly of drug delivery capsules, Lab Chip. 17 (2017) 3785–3795. https://doi.org/10.1039/c7lc00918f.

[50] H. Zhang, H. Guo, Z. Chen, G. Zhang, Z. Li, Application of PECVD SiC in glass micromachining, J. Micromech. Microeng. 17 (2007) 775–780. https://doi.org/10.1088/0960-1317/17/4/014.

[51] Y. Mourzina, A. Steffen, A. Offenhäusser, The evaporated metal masks for chemical glass etching for BioMEMS, Microsyst. Technol. 11 (2005) 135–140. https://doi.org/10.1007/s00542-004-0430-3.

[52] A. Mata, A.J. Fleischman, S. Roy, Fabrication of multi-layer SU-8 microstructures, J. Micromech. Microeng. 16 (2006) 276–284. https://doi.org/10.1088/0960-1317/16/2/012.

[53] NANO SU-8 2000 Negative Tone Photoresist Formulations 2002–2025. MicroChem Corporation: Newton, MA.

[54] NANO SU-8 2000 Negative Tone Photoresist Formulations 2035–2100. MicroChem Corporation: Newton, MA.

[55] C. Fu, C. Hung, H. Huang, A novel and simple fabrication method of embedded SU-8 micro channels by direct UV lithography, J. Phys. Conf. Ser. 34 (2006) 330–335. https://doi.org/10.1088/1742-6596/34/1/054.

[56] Y. Kazoe, I. Yamashiro, K. Mawatari, T. Kitamori, High-pressure acceleration of nanoliter droplets in the gas phase in a microchannel, Micromachines. 7 (2016) 142. https://doi.org/10.3390/mi7080142.

[57] K. V. Sharp, R.J. Adrian, J.G. Santiago, J.I. Molho, Liquid flows in microchannels, in: M. Gad-el-Hak (Ed.), MEMS Introd. Fundam., CRC Press, Boca Raton, 2006: pp. 10-1-10–46. ISBN 9781420036572.

[58] K.W. Oh, K. Lee, B. Ahn, E.P. Furlani, Design of pressure-driven microfluidic networks using electric circuit analogy, Lab Chip. 12 (2012) 515–545. https://doi.org/10.1039/c2lc20799k.

[59] H. Bruus, Theoretical Microfluidics, Oxford University Press:, New York, 2008. ISBN 9788578110796.

[60] D.J. Beebe, G.A. Mensing, G.M. Walker, Physics and Applications of Microfluidics in Biology, Annu. Rev. Biomed. Eng. 4 (2002) 261–286. https://doi.org/10.1146/annurev.bioeng.4.112601.125916.

[61] Y. Yalikun, Y. Tanaka, Large-scale integration of all-glass valves on a microfluidic device, Micromachines. 7 (2016) 83. https://doi.org/10.3390/mi7050083.

[62] H. Van Heeren, D. Verhoeven, T. Atkins, A. Tzannis, H. Becker, W. Beusink, P. Chen, Design Guideline for Microfluidic Device and Component Interfaces (Part 2) Ver. 3, (2017). Available online: http://www.makefluidics.com/en/design-guideline?id=7 (accessed on 9 March 2020).

[63] N. Scheuble, A. Iles, R.C.R. Wootton, E.J. Windhab, P. Fischer, K.S. Elvira, Microfluidic Technique for the Simultaneous Quantification of Emulsion Instabilities and Lipid Digestion Kinetics, Anal. Chem. 89 (2017) 9116–9123. https://doi.org/10.1021/acs.analchem.7b01853.

[64] E.C. Lynch, Red blood cell damage by shear stress. Biophys J 12 (1972) 257–273. https://www.ncbi.nlm.nih.gov/pmc/articles/PMC1484094/pdf/biophysj00725-0044.pdf.

[65] R. Paul, J. Apel, S. Klaus, F. Schügner, P. Schwindke, H. Reul, Shear stress related blood damage in laminar Couette flow, Artif. Organs. 27 (2003) 517–529. https://doi.org/10.1046/j.1525-1594.2003.07103.x.

[66] V.S.K. Sajja, D.J. Kennedy, P.W. Todd, T.R. Hanley, Computational fluid dynamics simulation of a quadrupole magnetic sorter flow channel: Effect of splitter position on nonspecific crossover, Can. J. Chem. Eng. 89 (2011) 1068–1075. https://doi.org/10.1002/cjce.20541.

[67] M. Zborowski, P.S. Williams, L. Sun, L.R. Moore, J.J. Chalmers, Cylindrical splitt and quadrupole magnetic field in application to continuous-flow magnetic cell sorting, J. Liq. Chromatogr. Relat. Technol. 20 (1997) 2887–2905. https://doi.org/10.1080/10826079708005599.

[68] M. Hoyos, L.R. Moore, K.E. McCloskey, S. Margel, M. Zuberi, J.J. Chalmers, M. Zborowski, Study of magnetic particles pulse-injected into an annular SPLITT-like channel inside a quadrupole magnetic field, J. Chromatogr. A. 903 (2000) 99–116. https://doi.org/10.1016/S0021-9673(00)00879-7.

[69] J. Lim, S.P. Yeap, C.H. Leow, P.Y. Toh, S.C. Low, Magnetophoresis of iron oxide nanoparticles at low field gradient: The role of shape

anisotropy, J. Colloid Interface Sci. 421 (2014) 170–177. https://doi.org/10.1016/j.jcis.2014.01.044.

[70] N. Pekas, Q. Zhang, M. Nannini, D. Juncker, Wet-etching of structures with straight facets and adjustable taper into glass substrates, Lab Chip. 10 (2010) 494–498. https://doi.org/10.1039/b912770d.

[71] C.T. Culbertson, J. Sibbitts, K. Sellens, S. Jia, Fabrication of Glass Microfluidic Devices, in: D. Dutta (Ed.), Microfluid. Electrophor. Methods Protoc., Humana Press, New York, 2019: pp. 1–12. ISBN 978-1-4939-8963-8.

CHAPTER 4

Conclusions and challenges for future research

4.1. Conclusions

This doctoral thesis contributes to the rational computer aided design of MCMDs to be applied for extracorporeal blood detoxification purposes based on the selective and efficient capture and removal of toxic agents (lipopolysaccharide) from bloodstream. This process comprises two stages: (i) LPS sequestration by the biotargeting agent that decorates the surface of the magnetic beads, and (ii) magnetic recovery of the LPS-bead complexes. Particularly, this dissertation addresses two important challenges for the development of these MCMDs. Hence, progress on the design of biotargeting agents able to capture LPS with high affinity has been made, and the optimization of the magnetic recovery of endotoxin-bead complexes has been tackled. On the basis of these challenges, two different parts can be undoubtedly distinguished in this thesis. Thus, apart from highlighting the need of developing novel strategies to fight against bacterial infections in Chapter 1, Chapter 2 is focused on shedding light on the interaction of lipid A with a potential biotargeting agent, namely ALFPm3, through MD simulations, and Chapter 3 deals with the enhancement of CMMSs efficiency by using CFD techniques.

On the in silico design of LPS biotargeting agents

ALFPm3 has been recognized as a promising molecule to develop therapeutics against sepsis. However, little was known about its binding with LPS/lipid A. Gaining insights into the ALFPm3-lipid A interaction paves the way for the design of the biotargeting agent based on ALFPm3 with an enhanced ability to capture lipid A. More specifically, once the interaction mechanism is unveiled and key residues are identified, modifications to ALFPm3 can be introduced in order to improve its interaction with lipid A. For addressing this investigation, MD simulations were performed, since MD is understood as a computational microscope that provides atomistic insights of the system under investigation, which is required to comprehensively elucidate the ALFPm3-lipid A interaction mechanism.

MD simulations demonstrated that the ionic strength of the medium where the contact takes place positively impacts the ALFPm3 stability when interacting with lipid A and the affinity between them, which substantiates the use of NaCl buffers that mimic the physiological conditions (~ 150 mM NaCl) for ALFPm3-lipid A binding. Additionally, the simulations of the ALFPm3-

lipid A complex in 150 mM NaCl revealed that the interaction between these molecules consists of a two-step process. Thus, ALFPm3 firstly recognizes lipid A through electrostatic interaction, and then, a stable binding driven by hydrophobic interactions is formed which involves the protein cleft, where the lipid acyl chains are buried into such cavity with the phosphates upwards facing the medium. Thus, the binding site of lipid A in ALFPm3 has been for the first time identified. Additionally, two residues of ALFPm3, namely, K39 and Y49 were found to play a pivotal role in the interaction with the lipid and also to be conserved in other ALFs.

On the in vitro validation of in silico predictions

In order to further confirm the *in silico* predicted ALFPm3-lipid A binding pose, an *in vitro* validation was performed. This experimental validation was based on quantifying the change in the ALFPm3-lipid A binding affinity when the ALFPm3 residues identified by MD simulations to be key for its interaction with the endotoxin (K39 and Y49) were individually substituted by others with opposite charge or polarity. Due to the similarity of ALFPm3 and LALF structures and the knowledge previously gained in the ASP research group about the experimental LALF-LPS binding, LALF, instead of ALFPm3, was used for the *in vitro* validation of *in silico* results. To this end, two LALFs were synthesized; in one of them the 37th lysine was substituted by a glutamic acid (K37E-LALF) and in the other, the 47th tyrosine was replaced by a phenylalanine (Y47F-LALF). K37E-LALF was overexpressed and purified; Y47F-LALF was successfully overexpressed, but it could not be purified since the Y47F substitution probably affected protein folding, and appropriate folding is required for the purification through IMAC. Therefore, only K37E-LALF functionalized agarose beads were contacted with LPS. Regardless of the K37E-LALF/LPS ratio ($\phi_{\mathrm{protein/LPS}} \sim 300$ and 400) and the contact time (20 or 60 minutes), considerably worsened capture ability of K37E-LALF in comparison to WT-LALF were found. This result supported the importance of the K37 residue in the interaction with LPS and thus conforms the *in silico* predictions. Additionally, bare agarose beads (which have Ni^{2+} ions in their surface) were also contacted with LPS and an intermediate LPS capture ability between WT-LALF and K37E-LALF was discovered.

On the optimization of CMMSs performance

Apart from the identification of a biotargeting agent that captures LPS with high affinity, the successful implementation of MCMDs also relies on the design of CMMSs that completely recover the LPS-bead complexes while processing high flow rates. To address the optimization of the CMMSs performance through CFD techniques, two strategies were pursued, namely, optimizing the geometrical features of the microchannels and increasing the magnetic gradient exerted on the particles by selecting a more appropriate magnet arrangement. Hence, following the work previously derived in the ASP research group, the geometry of Y-Y shaped CMMSs was performed. From the different channel lengths and cross sectional shapes it was found that rectangular 10 mm long channels deliver the best performance since they provide complete particle capture while treating one or two orders of magnitude higher blood flow rates than the other geometrical configurations; thereby, for 10 mm long channels, complete recoveries are accomplished for J (balance of forces acting on the particles) and θ (the coupling of such forces with the channel geometrical features) values equal to 0.011 and 0.45 respectively. However, channel lengthening was insufficient for considerably enhancing the CMMSs performance (i.e., increasing the processed flow rate while providing complete particle capture). Hence, once the microchannel geometry that yielded entire particle recovery and high volumetric throughput simultaneously has been identified, the increase of the magnetic gradient exerted on the particles, was tackled. To this end, a QMS, which has four permanent magnets arranged in a quadrupolar orientation, instead of a conventional Y-Y shaped CMMSs with a single permanent agent to generate the magnetic field was used for addressing magnetic particle recovery. The results demonstrated that the magnets configuration in the QMS involves the generation of considerably higher magnetic field gradients in the microchannel, and thus 1 order of magnitude higher magnetic forces are exerted on the beads in the QMS. Consequently, the micro-QMS provide complete retrieval of both (a) beads flowing at 4.5 times higher velocities, or (b) 2.2 times smaller particles. The dimensionless analysis reveals that in the QMS entire particle recovery is achieved when J is 0.014 and θ is 0.5; additionally, the ϕ (exploitation of the magnetic energy for fulfilling entire recoveries) value around $3.4 \cdot 10^2$ $m \cdot s^{-1} \cdot kJ^{-1}$ indicates that both the QMS and the Y-Y CMMSs exhibit a similar efficiency in the exploitation of the magnetic

energy for achieving complete bead recovery. The comparison of the performance of the QMS and the Y-Y shaped CMMSs confirmed the outstandingly enhanced performance of the QMS, compared to conventional Y-Y shaped CMMSs, and thus substantiated its use for carrying out the magnetic recovery stage in blood detoxification processes.

Overall, this doctoral dissertation provides methodological guidelines, combining different advanced simulation techniques, namely MD and CFD, for addressing the rational design of MCMDs. Although this work has been focused on the MCMDs to be applied for the capture of endotoxins from blood, these methodological guidelines can be also exploited for any MCMDs aiming at capturing different target compounds from complex media. Thus, the insights and methodologies provided in this work might be key for making progress on the design of these attractive MCMDs.

4.2. Challenges for future research

This thesis aims to make progress on the design of novel strategies for the capture of endotoxins from blood by combining microfluidics and the action of functionalized magnetic beads. Despite the achievements described throughout this work, there are still some challenges to be tackled so that the proposed MCMDs could be successfully applied in real case scenarios. Specifically, these challenges rely on (i) enhancing the LPS capture ability of the biotargeting agent, (ii) ensuring blood quality and functionality upon LPS sequestration by the biotargeting agent, (iii) designing a microfluidic incubator where the LPS sequestration by the functionzalized magnetic beads could be performed, (iv) integrating the incubation and magnetic recovery stages, and (v) parallelization of MCMDs to further enhance the efficiency of these systems.

Enhancing the ability of the biotargeting agents to capture LPS

On the basis of the interaction of lipid A with ALFPm3, biotargeting agents with enhanced ability to sequestrate LPS can be designed. Hence, the lipid A binding cleft in ALFPm3 could be used as scaffold for adding and/or replacing amino acids in order to yield high affinity binders of LPS. The use of these novel biotargeting agents for sequestrating the endotoxin would lead to a reduction of the time required for LPS capture from blood, thus improving the efficiency of MCMDs.

Ensure blood quality and functionality

Additionally, an important issue to be considered for designing affinity sorbents for biomedical applications entails the maintenance of the biofluid quality and functionality when they are used. Hence, apart from exhibiting an enhanced ability to capture LPS, the biotargeting agents must not pose any health hazard to the patient. In this regard, evaluating, for instance, the protein losses of blood due to their unspecific capture by the LPS sequestration agents is of paramount importance.

On the design of microfluidic incubators for LPS sequestration

Following the methodology developed in this work, the adsorption equilibrium between the novel biotargeting agent and LPS can be investigated in order to design a microfluidic incubator where the LPS capture form flood

could be accomplished. From the different geometries proposed in the literature for microfluidic incubators (e.g., S-shape, spiral, etc.), the one that enables the most efficient LPS capture while maintain blood properties must be selected.

On the integration of the incubation and magnetic recovery stages

Once the incubation stage is designed and optimized, it can be integrated with the micro-QMS (annular channel with quadrupole orientation of the permanent magnets) so that blood detoxification could be addressed in continuous mode. Thereby, the coupling of LPS sequestration and bead recovery stages will give rise to a MCMD.

Scaling out MCMDs

As it was discussed throughout this thesis, the reduced dimensions of microchannels lead to the treatment of low flow rates. Thus, in order to close the gap between the volumetric throughputs that deliver MCMDs with those required for treating the poised blood of the patient within an acceptable time period, the parallelization of MCMDs can be addressed. This strategy, so-called numbering-up or scale out, consists of the use of several MCMDs in parallel simultaneously, which will outstandingly improve the efficiency of the MCMDs, thus fostering their feasible implementation for the capture of endotoxins from blood.

4.3. Conclusiones

La presente tesis doctoral contribuye al diseño racional de MCMDs para llevar a cabo la detoxificación sanguínea extracorpórea basada en la captura y eliminación selectivas y eficientes de los agentes tóxicos (el lipopolisacárido) del torrente sanguíneo. Este proceso comprende dos etapas: (i) captura del LPS por la molécula que decora la superficie de las partículas magnéticas e (ii) recuperación magnética de los complejos LPS-partícula. Ambos retos de gran relevancia en el desarrollo de MCMDs. En concreto, se ha avanzado en el diseño de moléculas capaces de capturar con elevada afinidad el LPS y se ha abordado la optimización de la recuperación magnética de los complejos endotoxina-partícula. En base a esos retos, se pueden distinguir indudablemente dos partes en esta tesis. Así, además de resaltar la necesidad de desarrollar nuevas estrategias para hacer frente a las infecciones bacterianas en el Capítulo 1, el Capítulo 2 se centra en esclarecer la interacción del lípido A con ALFPm3 mediante simulaciones de MD, y el Capítulo 3 aborda la mejora de la eficiencia de los CMMSs mediante el uso de técnicas de CFD.

Diseño in silico de moléculas para capturar al LPS

Se ha reconocido al ALFPm3 como una molécula prometedora para desarrollar terapias contra la sepsis. Sin embargo, se tiene poca información acerca de su unión con el LPS/lípido A. Conocer la interacción de ALFPm3 con el lípido A facilita el diseño de moléculas basadas en ALFPm3 con una habilidad mejorada para capturar al lípido A. Concretamente, una vez que se determina el mecanismo de interacción y se identifican los aminoácidos clave en la interacción, se pueden introducir modificaciones en ALFPm3 a fin de mejorar su interacción con el lípido A. Para abordar esta investigación, se llevaron a cabo simulaciones MD, ya que MD es considerada un microscopio computacional que proporciona conocimiento a nivel atómico del sistema estudiado, lo cual es necesario para dilucidar exhaustivamente el mecanismo de interacción de ALFPm3 y el lípido A.

De acuerdo a las simulaciones MD, la fuerza iónica del medio donde tiene lugar el contacto favorece la estabilidad del ALFPm3 cuando interacciona con el lípido A y la afinidad entre ellos, lo que avala el uso de disoluciones de NaCl con una concentración similar a las condiciones fisiológicas ([NaCl]= ~ 150 mM) para la unión del ALFPm3 con el lípido A.

Asimismo, las simulaciones del complejo ALFPm3-lípido A en una disolución 150 mM de NaCl revelaron que el proceso de interacción entre esas moléculas consiste en dos etapas. En primer lugar, ALFPm3 reconoce al lípido A mediante interacciones electrostáticas y a continuación, se forma una unión estable en la cavidad de la proteína debido a las interacciones hidrofóbicas, donde las cadenas acilo del lípido están insertadas en la cavidad y los fosfatos están orientados hacia arriba y expuestos al medio. De esta forma, se ha identificado por primera vez el sitio de unión del lípido A en ALFPm3. Asimismo, se descubrió que dos aminoácidos de ALFPm3, concretamente K39 e Y49, juegan un papel importante en la interacción con el lípido y que se conservan en otras proteínas anti-LPS.

Validación experimental de las predicciones obtenidas in silico

A fin de confirmar el modo de unión de ALFPm3 y el lípido A determinado *in silico*, se llevó a cabo la validación in vitro. Esta validación experimental consistió en cuantificar el cambio en la afinidad de unión de ALFPm3 y el lípido A cuando se sustituyen individualmente los residuos que de acuerdo a las simulaciones MD eran clave para la interacción de esas moléculas (K39 e Y49) por otros con diferente carga o polaridad. Debido a la similitud de las estructuras del ALFPm3 y LALF y al conocimiento adquirido previamente en el grupo de investigación Procesos Avanzados de Separación (PAS) sobre la unión experimental de LALF y el LPS, se empleó el LALF en lugar del ALFPm3 para la validación experimental de los resultados obtenidos in silico. Para ello, se sintetizaron dos LALFs; en uno de ellos se sustituyó la lisina 37 por un ácido glutámico (K37E-LALF) y en el otro, se reemplazó la tirosina 47 por una fenilalanina (Y47F-LALF). Mientras que el K37E-LALF se pudo sobreexpresar y purificar, el Y47F-LALF solo se pudo sobreexpresar ya que la sustitución Y47F probablemente afecta al plegamiento de la proteína y se requiere un plegamiento adecuado para realizar la purificación mediante la técnica de cromatografía utilizada en este trabajo (IMAC por sus siglas en inglés). Consecuentemente, únicamente se contactaron con el LPS partículas de agarosa funcionalizadas con K37E-LALF. Independientemente de la relación K37E-LALF/LPS ($\phi_{\mathrm{protein/LPS}} \sim 300$ and 400) y del tiempo de contacto (20 o 60 minutos), se obtuvo que la capacidad de captar al LPS de K37E-LALF es considerablemente inferior que la de WT-LALF. Este resultado avala la importancia del aminoácido K37 en la interacción con el LPS y por tanto confirma los resultados obtenidos *in silico*. Asimismo, se contactó el LPS con

partículas de agarosa sin funcionalizar, que tienen iones Ni^{2+} en su superficie y se determinó que la habilidad para captar LPS era intermedia entre WT-LALF y K37E-LALF.

Optimización del rendimiento de CMMSs

Además de diseñar una molécula que capture al LPS con elevada afinidad, la implementación con éxito de MCMDs también requiere el diseño de CMMSs que recuperen completamente las partículas magnéticas mientras procesan elevados caudales. Para abordar la optimización del rendimiento de CMMSs mediante técnicas de CFD se siguieron dos estrategias: optimizar las características geométricas de los microcanales y aumentar el gradiente magnético ejercido a las partículas mediante la selección de una disposición de imanes más adecuada. Por lo tanto, siguiendo el trabajo previamente realizado en el grupo de investigación PAS, se optimizó la geometría de CMMSs con forma de Y a la entrada y a la salida. De las diferentes longitudes y formas de la sección transversal analizadas, se descubrió que los canales con sección rectangular y 10 mm de longitud tenían el mejor rendimiento, ya que proporcionan la captura completa de partículas mientras tratan caudales uno o dos órdenes de magnitud mayor que el resto de configuraciones. De esta forma, en esos microcanales se pueden recuperar las partículas en su totalidad cuando los valores de J (balance de fuerzas que actúan sobre las partículas) y θ (acoplamiento de esas fuerzas con las características geométricas del canal) son 0.011 y 0.45 respectivamente. Sin embargo, alargar el canal no fue suficiente para mejorar considerablemente el rendimiento de CMMSs. Por tanto, una vez que se identificó la geometría del microcanal que proporcionaba la captura completa de partículas a caudales elevados, se abordó el aumento del gradiente magnético ejercido a as l partículas. Para ello, se usó un QMS, que tiene cuatro imanes permanentes dispuestos en orientación cuadrupolar en vez de un CMMSs convencional con entrada y salida en forma de Y con un único imán para generar el campo magnético, para llevar a cabo la recuperación magnética de las partículas. Los resultados demostraron que la configuración de los imanes en el QMS conduce a la generación de gradientes magnéticos considerablemente mayores en el microcanal, y por tanto, las partículas están sometidas a fuerzas magnéticas de un orden de magnitud mayor en el QMS. Consecuentemente, el QMS proporciona recuperación completa de (a) partículas fluyendo a velocidades 4.5 veces superiores, o (b) partículas 2.2

veces más pequeñas. El análisis adimensional reveló que la recuperación completa de partículas se consigue en el QMS cuando J es 0.014 and θ es 0.5; asimismo el valor de ϕ (aprovechamiento de la energía magnética para conseguir la recuperación completa de partículas) es aproximadamente 3.4 $\cdot 10^2$ $m \cdot s^{-1} \cdot kJ^{-1}$ indica que tanto el QMS como el CMMSs convencional tienen una eficiencia simular en cuanto a la utilización de la energía magnética para conseguir la recuperación completa de partículas. La comparación del rendimiento del QMS y del CMMSs convencional confirmó el rendimiento excepcional del QMS comparado con el CMMSs convencional, avalando así su uso para llevar a cabo la etapa de recuperación magnética de procesos de detoxificación sanguínea extracorpórea.

En conclusión, esta tesis proporciona guías metodológicas, combinando diferentes técnicas de simulación avanzadas, es decir, MD y CFD, para abordar el diseño racional de MCMDs. Aunque este trabajo se ha centrado en MCMDs para ser empleadas en la captura de endotoxinas de la sangre, esas guías metodológicas también pueden ser utilizadas para cualquier MCMDs destinado a capturar diferentes compuestos objetivo de medios complejos. Por tanto, el conocimiento y metodologías desarrollados en este trabajo pueden ser claves para avanzar en el diseño de esos MCMDs.

4.4. Retos para futuras investigaciones

Esta tesis tiene como objetivo avanzar en el diseño de nuevas estrategias para la captura de endotoxinas presentes en la sangre combinando la microfluídica y la acción de micro- o nanopartículas magnéticas funcionalizadas. A pesar de los logros descritos a lo largo de este trabajo, todavía quedan algunos retos por abordar para que los MCMDs puedan ser empleados con éxito en casos reales de tratamiento. Específicamente, estos retos se basan en (i) mejorar la capacidad de las moléculas que funcionalizan las partículas para captar al LPS, (ii) mantener la calidad y funcionalidad de la sangre una vez que la molécula ha capturado al LPS, (iii) diseñar un incubador microfluídico donde las partículas magnéticas funcionalizadas secuestren al LPS, (iv) integración de las etapas de incubación y recuperación magnética y (v) paralelización de MCMDs a fin de mejorar aún más la eficiencia de estos sistemas.

Mejorar la habilidad para captar al LPS de las moléculas que funcionalizan las partículas magnéticas

En base a la interacción del lípido A con ALFPm3, se pueden diseñar moléculas con mejor habilidad para secuestrar al LPS. Así, el sitio de unión del lípido A en ALFPm3 puede ser usado como base para añadir o reemplazar aminoácidos para conseguir moléculas con elevada afinidad hacia el LPS. El uso de esas nuevas moléculas para secuestrar la endotoxina conduciría a la reducción del tiempo necesario para captar al LPS de la sangre, mejorando así la eficiencia de los MCMDs.

Mantener la calidad y funcionalidad de la sangre

Asimismo, un aspecto importante a tener en cuenta en el diseño de adsorbentes para aplicaciones biomédicas consiste en mantener la calidad y funcionalidad del biofluido. Por tanto, además de exhibir una elevada capacidad de captura de LPS; las moléculas que funcionalizan las partículas no deben suponer ningún peligro para la salud del paciente. En este sentido, evaluar, por ejemplo, la pérdida de proteínas sanguíneas debido a su secuestro inespecífico por los agentes de captura de LPS es clave.

Diseñar incubadores microfluídicos para realizar la captura de LPS

Siguiendo la metodología desarrollada en este trabajo se puede investigar el equilibrio de adsorción entre la nueva molécula con la que funcionalizar las partículas y el LPS a fin de diseñar un incubador microfluídico donde se pueda realizar la captación del LPS. De las diferentes geometrías propuestas en la literatura para incubadores microfluídicos (por ejemplo, en forma de S, espiral, etc.), se debe seleccionar aquella que permita la captación de LPS con mayor eficiencia mientras se mantienen las propiedades de la sangre.

Integración de las etapas de captura de LPS y recuperación magnética

Una vez que la etapa de incubación está diseñada y optimizada, se puede integrar con el micro-QMS (canal anular con cuatro imanes permanentes dispuestos en orientación cuadrupolar) para abordar en modo continuo la detoxificación sanguínea. Así, el acoplamiento de las etapas de secuestro de LPS y recuperación de las partículas magnéticas dará lugar a un MCMD.

Paralelización de MCMDs

Como se ha comentado a lo largo de esta tesis, las reducidas dimensiones de los microcanales conducen al tratamiento de caudales bajos. Por tanto, para reducir la diferencia entre los rendimientos volumétricos que proporcionan los MCMDs y los que se requieren para tratar la sangre contaminada del paciente durante un tiempo aceptable, se puede realizar la paralelización de los MCMDs. Esta estrategia consiste en el uso de varios MCMDs simultáneamente en paralelo, lo que mejora extraordinariamente la eficiencia de los MCMDs, fomentando la viabilidad de su implementación para tratar la captura de endotoxinas en escenarios reales.

ANNEXES

Supplementary material and scientific contributions

A1. Supplementary material of Chapter 2

Contents:

Table A1.1. Oligonucleotide sequences used for plasmid construction (K37E and Y47F) and for Sanger sequencing (T7 and pT7).

Name	Oligonucleotides 5'-3'
K37E	TGCCACTATCGTATTGAACCCACGTTCCGCCGC
Y47F	CGCCTGAAGTGGAAGTTTAAAGGGAAGTTTTGG
T7	TAATACGACTCACTATAGGG
pT7	GCTAGTTATTGCTCAGCGG

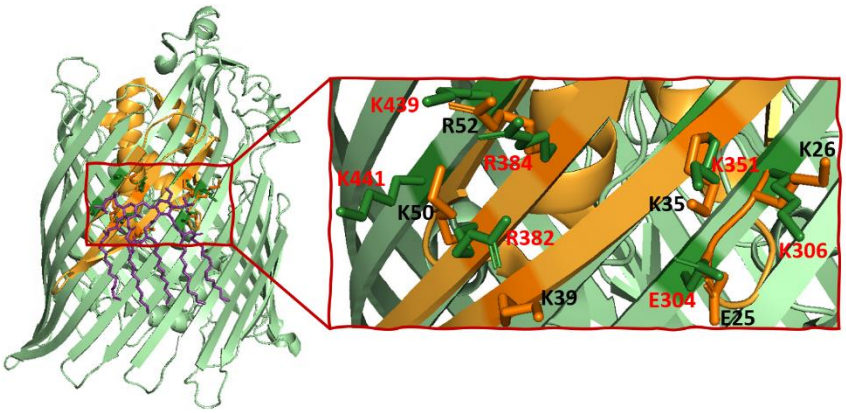

Figure A1.1. Superimposition of ALFPm3 and FhuA structures to derive the initial ALFPm3-lipid A complex structure.

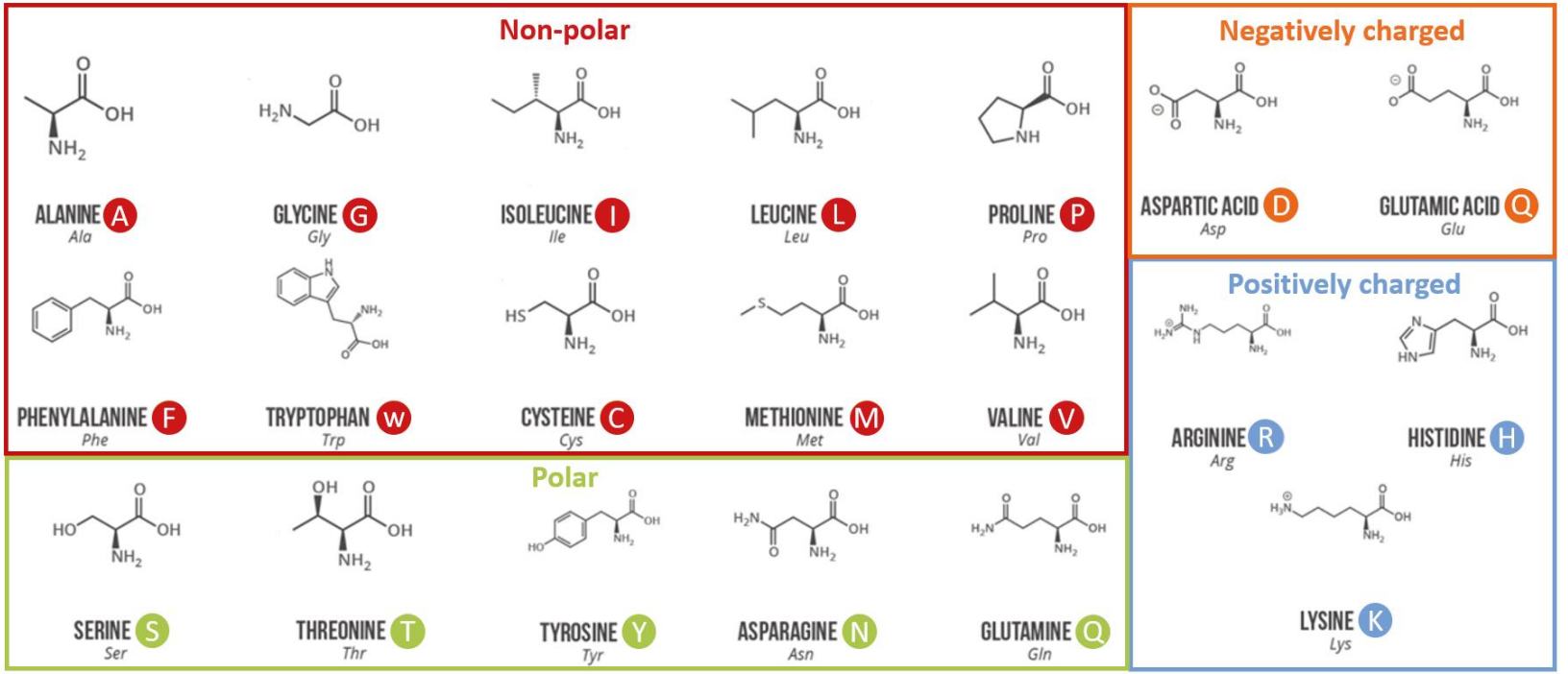

Figure A1.2. Classification of amino acids. Adapted from Compound Interest (https://www.compoundchem.com/2014/09/16/aminoacids/)

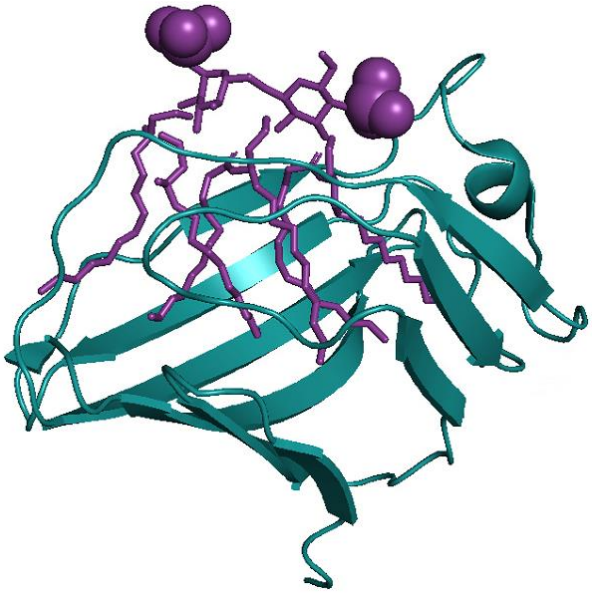

Figure A1.3. Binding pose of MD2 and lipid A (obtained from PDB ID: 3FXI). Note that the lipid acyl chains are buried in the MD2 cavity and that the phosphates are oriented outwards facing the medium.

```
ALFPm3   EAYV-QGWEAVAAAVASKIVGLWRNEKTELLGHECKFTVKPYLKRFQVYYKGRMWCPGWT    59
LALF     ---MDGIWTQLIFTLVNNLATLWQSGDFQFLDHECHYRIKPTFRRLKWKYKGKFWCPSWT    57

ALFPm3   AIRGEASTRSQSGVAGKTAKDFVRKAFQKGLISQQEANQWLSS----     102
LALF     SITGRATKSSRSGAVEHSVRNFVGQAKSSGLITQRQAEQFISQYNLE     104
```

Figure A1.4. Amino acid sequence alignments of ALFPm3 and the LALF synthetised in the ASP research group (Ref. 98 in Chapter 2). Note that K39 and Y49 in ALFPm3 correspond to K37 and Y47 in LALF (highlighted in blue).

A2. Supplementary material of Chapter 3

Contents:

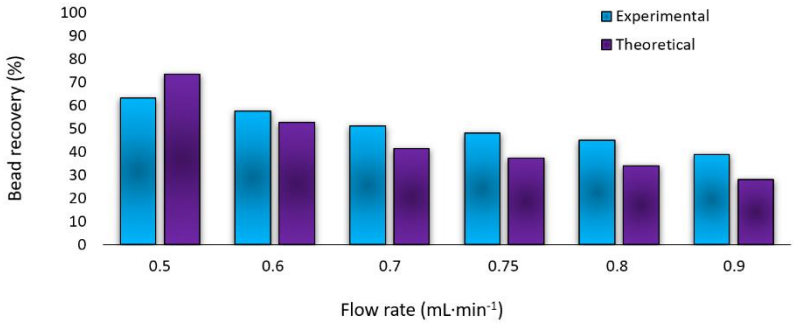

Figure A2.1. Comparison between experimental and theoretical recoveries in a QMS system. The QMS system employed by Moore et al. (Ref. 33 in Chapter 3) for the recovery of deoxygenated red blood cells has been simulated with our numerical model. In the region of flow rates simulated, the experimental and theoretical recoveries are in good agreement. The average absolute error is less than 10% for the flow rate range evaluated and below 5% for some of the flow rate values, which confirms the validity of the numerical model.

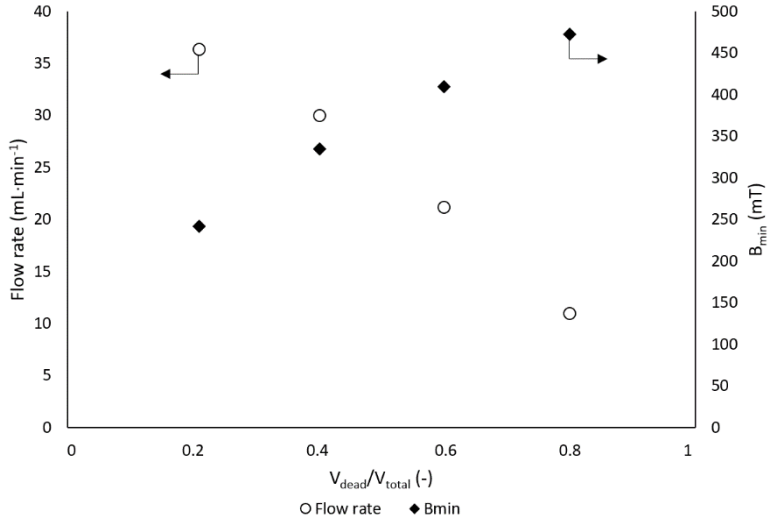

Figure A2.2. Influence of the micro-QMS dead volume (V_{dead}) on both the flow rate that can be processed and the magnetic field at the rod surface (B_{min}). Decreasing the r_{rod} value, and thus, the V_{dead}, increases the cross-sectional area of the device and the flow rate that can be applied. However, V_{dead}/V_{total} should be high enough to work at magnetic field values that saturate the particles (≈ 500 mT).

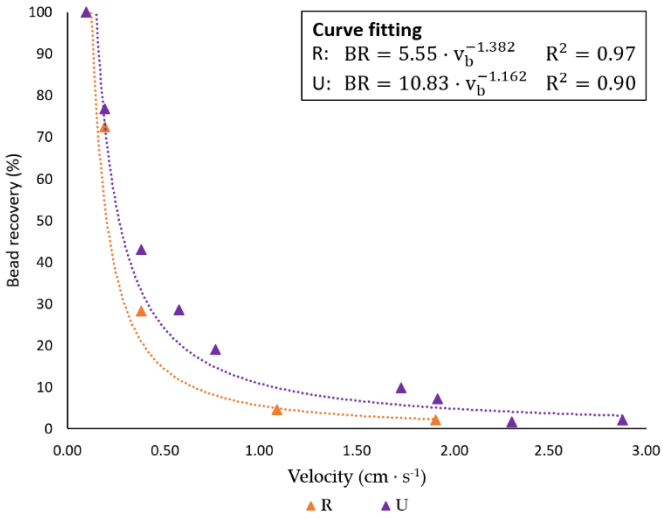

Figure A2.3. Effect of fluid velocity on bead recovery when the same magnetic force ($F_{m,z}$ = 0.011 nN) is applied for rectangular and U-shaped channels.

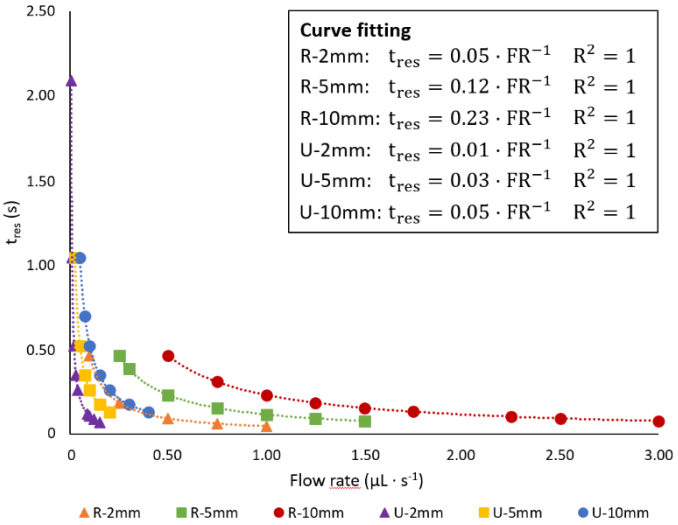

Figure A2.4. Variation of the residence time with the fluid flow rate for all of the studied geometries.

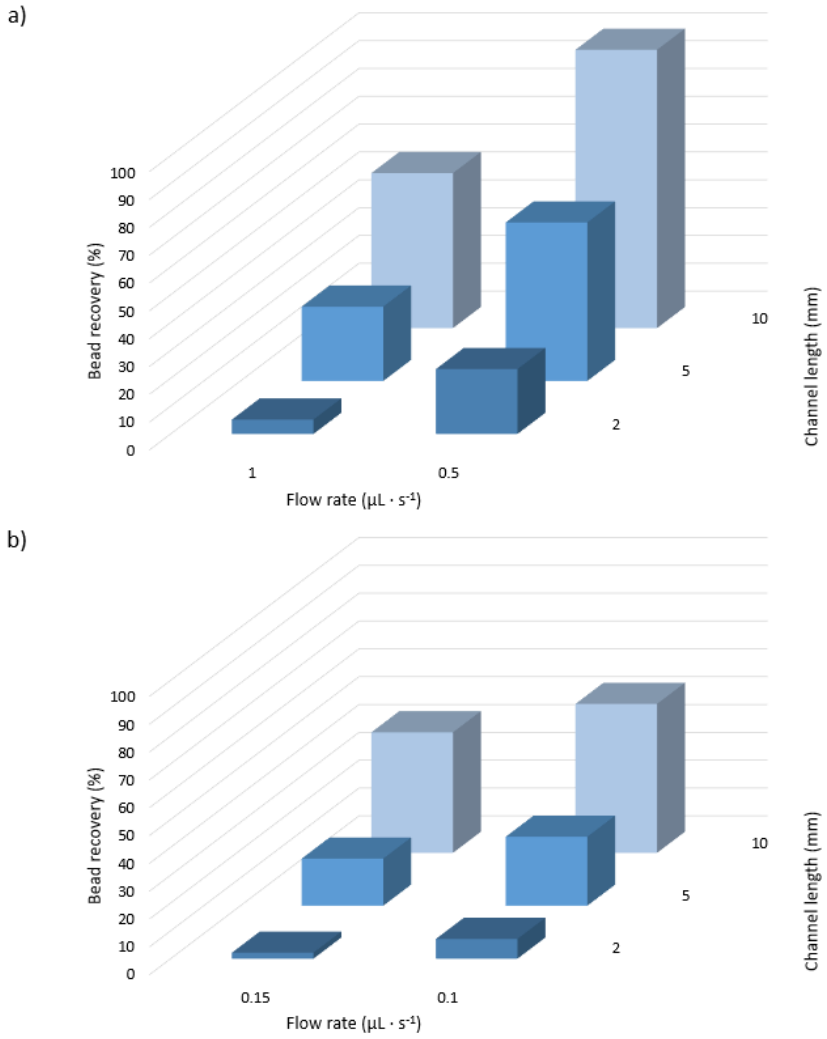

Figure A2.5. Dependence of bead recovery with the channel length and fluid flow rate for (a) rectangular and (b) U-shaped cross section microdevices of fluid velocity.

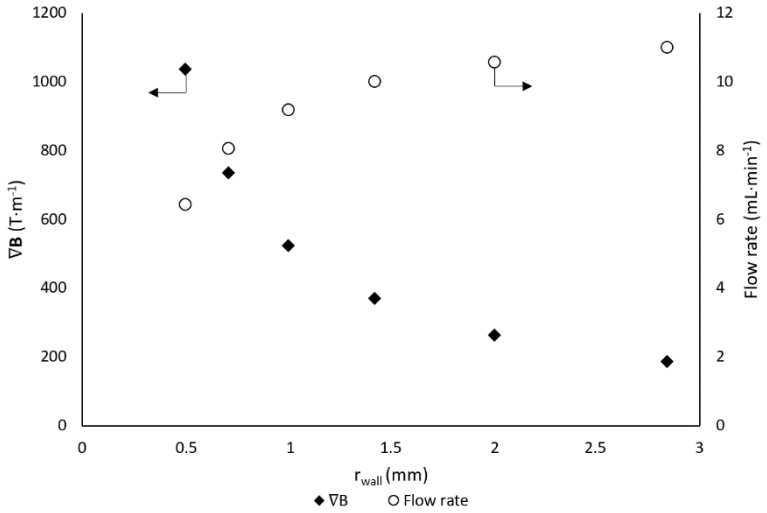

Figure A2.6. Effect of the QMS dimensions (r_{wall}) on the magnetic field gradient and the treated flow rate. Decreasing the r_{wall} of the QMS positively affects the magnetic field gradient achieved inside the system, however, it negatively impacts the flow rate that can be processed since the cross-sectional area depends on the r_{wall} value.

A3. Scientific contributions

Peer-reviewed scientific publications prior to the present thesis:

- Gómez-Pastora, J., **González-Fernández, C.**, Real, E., Iles, A., Bringas, E., Furlani, E. P., & Ortiz, I. (2018). Computational modeling and fluorescence microcopy characterization of a two-phase magnetophoretic microsystem for continuous-flow blood detoxification. *Lab on a Chip 18*(11), 1593–1606.
- Gómez-Pastora, J., **González-Fernández, C.**, Fallanza, M., Bringas, E., & Ortiz, I. (2018). Flow patterns and mass transfer performance of miscible liquid-liquid flows in various microchannels: Numerical and experimental studies Biochemical interactions between LPS and LPS-binding molecules. *Chemical Engineering Journal 344*, 487-497.

Peer-reviewed scientific publications during the present thesis:

- **González-Fernández, C.**, Gómez-Pastora, J., Bringas, E., Zborowski, M., Chalmers, J. J., & Ortiz, I. (2021). Recovery of magnetic catalysts: advanced design for process intensification. *Industrial & Engineering Chemistry Research 60*(46), 16780-16790.
- **González-Fernández, C.**, Basauri, A., Fallanza, M., Bringas, E., Oostenbrink, C., & Ortiz, I. (2021). Fighting against bacterial lipopolysaccharide-caused infections through molecular dynamics simulations: A review. *Journal of Chemical Information and Modeling 61*(10), 4839-4851.
- **González-Fernández, C.**, Gómez-Pastora, J., Basauri, A., Fallanza, M., Bringas, E., Chalmers, J. J, & Ortiz, I. (2020). Continuous-flow separation of magnetic particles from biofluids: How does the microdevice geometry determine the separation performance. *Sensors 20*(11), 3030.
- Roodan, V. A., Gómez-Pastora, J., Karampelas, I. H., **González-Fernández, C.**, Bringas, E., Ortiz, I., Chalmers, J. J, Furlani, E. P., & Swihart, M. T. (2020). Formation and manipulation of ferrofluid droplets with magnetic fields in a microdevice: a numerical parametric study. *Soft Matters 16*(41), 9506-9518.
- Basauri, A., **González-Fernández, C.**, Fallanza, M., Bringas, E., Fernandez-Lopez, R., Giner, L., Moncalián, G., de la Cruz, F., & Ortiz, I. (2020). Biochemical interactions between LPS and LPS-binding molecules. *Critical*

Reviews in Biotechnology 40(3), 292–305.

Publications in conference proceedings during the present thesis:

- **González-Fernández C.,** Basauri, A., Fallanza, M., Bringas E., Ortiz I. **(2019)** Contribution to the design of novel tailor-made magnetic biomaterials for blood detoxification through molecular dynamics simulations. *CASEIB 2019. XXXVII Congreso Anual de la Sociedad Española de Ingeniería Biomédica: libro de actas: Hacia una salud personalizada y universal* 2019, 251-254. (ISBN: 978-84-09-16707-4)
- **González-Fernández C.,** Gómez-Pastora J., Karampelas I.H., Bringas E., Ortiz I. (2019). Optimization of continuous-flow magnetic bioseparators through CFD numerical models. *TechConnect Briefs*, 290-293. (ISBN: 978-0-9988782-8-7)
- Roodan, V.A., Gómez-Pastora J., **González-Fernández C**., Karampelas I.H., Bringas E., Furlani E.P., Ortiz I. (2019). CFD analysis of the generation and manipulation of ferrofluid droplets. *TechConnect Briefs*, 298-301. (ISBN: 978-0-9988782-8-7)
- Gómez-Pastora J., **González-Fernández C.**, Karampelas I.H., Bringas E., Furlani E.P., Ortiz I. (2018). Design of magnetic blood cleansing microdevices through experimentally validated CFD modeling. *Advanced Materials – TechConnect Briefs* 3, 170–173. (ISBN: 978-0-9988782-0-1)

Conference contributions prior to the present thesis:

- Gómez-Pastora J., **González-Fernández C**., Basauri A., Fallanza M., Bringas E., Ortiz I. Contribution to the design of magnetic blood cleansing microdevices. *10th World Congress of Chemical Engineering*, Barcelona (Spain), October 1-5, 2017. Oral presentation.
- **González-Fernández C**.,* Gómez-Pastora J., Bringas E., Ortiz I. Development of microfluidic-magnetophoretic devices for Gram-negative sepsis treatment. *10th World Congress of Chemical Engineering*, Barcelona (Spain), October 1-5, 2017. Oral presentation. *Winner of the best poster award.

Conference contributions during the present thesis:

- **González-Fernández, C**., Gómez-Pastora, J., Bringas, E., Ortiz, I. Magnetophoretic separations as more efficient technologies for the recovery of target solutes. *6th International Symposium on Green and Smart Technologies for a Sustainable Society 2021*. Online. December 9-10, 2021. Video.
- **González-Fernández, C**., Bringas, E., Ortiz, I. On the rational design of magnetophoretic microseparators for blood detoxification: advanced MD and CFD models. *Symposium of the Spanish Royal Society of Chemistry 2021*. Online. September 27-30, 2021. Poster presentation.
- **González-Fernández, C**., Gómez-Pastora, J., Basauri, A., Fallanza, M., Bringas, E., Ortiz, I. Intensified microfluidic separations under magnetic field. 11th International Symposium on Catalysis in Multiphase Reactors (CAMURE-11). Online. March 21-24, 2021. Oral presentation.
- **González-Fernández, C.**, Basauri, A., Fallanza, M., Bringas E., Ortiz I. Contribution to the design of novel tailor-made magnetic biomaterials for blood detoxification through molecular dynamics simulations. *CASEIB 2019. XXXVII Congreso Anual de la Sociedad Española de Ingeniería Biomédica,* Santander (Spain), November 27-29, 2019. Oral presentation.
- **González-Fernández, C.**, Gómez-Pastora, J., Bringas E., Ortiz I. Novel design of magnetophoretic microdevices for extracorporeal sepsis treatment. *The 12th European Congress of Chemical Engineering (ECCE),* Florence (Italy), September 15-19, 2019. Oral presentation.
- **González-Fernández, C.**,* Bringas E., Ortiz I. Molecular design of Lipid A-LBP interaction as a tool for sepsis control. *XXXVI Jornadas Nacionales de Ingeniería Química,* Zaragoza (Spain), September 4-6, 2019. Oral presentation. *Winner of the best presentation award.
- **González-Fernández, C.**,* Gómez-Pastora, J., Bringas E., Ortiz I. Optimized design of novel magnetophoretic-microfluidic devices for biofluids detoxification. *ANQUE ICCE-CIBIC 2019,* Santander (Spain), June 19-21, 2019. Poster presentation. *Winner of the best poster award.
- Basauri, A., **González-Fernández, C.**, Giner, L., Fallanza, M., Bringas E., Moncalián, G., de la Cruz, F., Ortiz I. Micro-separators design for

lipopolysaccharides selective sequestration. *ANQUE ICCE-CIBIC 2019,* Santander (Spain), June 19-21, 2019. Poster presentation.

- **González-Fernández C.,** Gómez-Pastora J., Karampelas I.H., Bringas E., Ortiz I. Optimization of continuous-flow magnetic bioseparators through CFD numerical models. *Nanotech 2019 Conference & Expo*, Boston (USA), June 17-19, 2019. Oral presentation.
- Roodan, V.A., Gómez-Pastora J., **González-Fernández C**., Karampelas I.H., Bringas E., Furlani E.P., Ortiz I. CFD analysis of the generation and manipulation of ferrofluid droplets. *Nanotech 2019 Conference & Expo*, Boston (USA), June 17-19, 2019. Oral presentation.
- Gómez-Pastora J., **González-Fernández C.**, Karampelas I.H., Bringas E., Furlani E.P., Ortiz I. Design of magnetic blood cleansing microdevices through experimentally validated CFD modeling. *Nanotech 2018 Conference & Expo*, Anaheim (USA), May 13-16, 2018. Oral presentation.
- Gómez-Pastora J.,* **González C**., Ramos-Vivas J., Furlani E.P., Bringas E., Ortiz I. Innovative microdevice for extracorporeal sepsis treatment. *VI Doctorate Days and Scientific Dissemination of Group 9 of Universities (G-9)*, Santander (Spain), April 11-13, 2018. Poster presentation. *Winner of the best poster award.

Scientific outreach activities:

- Noche Europea de los Investigadores (2018, 2019, 2020)
- Semana de la Ciencia (2018, 2019, 2020, 2021)
- Día Internacional de la Mujer y la Niña en la Ciencia (2019)

ABOUT THE AUTHOR

Cristina González Fernández was born on 17th September 1994 in Santander (Cantabria, Spain). In July 2016, she completed the Chemical Engineering degree at the University of Cantabria, during which she obtained a collaboration research grant from the Spanish Ministry of Education, Culture and Sport that allowed her to start her research activity at the Chemical and Biomolecular Engineering department. In 2017, she obtained a Master's degree in Chemical Engineering at the Universities of Cantabria and the Basque Country.

Since December 2017, she has been developing her doctoral studies in the PhD program of Chemical Engineering, Energy and Processes under the supervision of Prof. Dr. Inmaculada Ortiz Uribe and Dr. Eugenio Bringas Elizalde in the research group Advanced Separation Processes (ASP). She has obtained two predoctoral contracts ("Concepción Arenal" from the University of Cantabria, and FPU from the Spanish Ministry of Science, Innovation and Universities) and a predoctoral mobility grant from the University of Cantabria.

During her PhD, she has performed two research stays, one for one month at the University of Huelva (Spain) supervised by Prof. Felipe Jiménez Blas (2018) and the other for three months at the University of Natural Resources and Life Sciences (Vienna) under the supervision of Prof. Chris Oostenbrink (2019). Moreover, she has been involved in teaching assignments in the Chemical Engineering degree (2021 and 2022). At the time of writing, she is author of 7 scientific articles and 14 contributions (oral, poster and video) in international, national, and local conferences where she has obtained some awards.

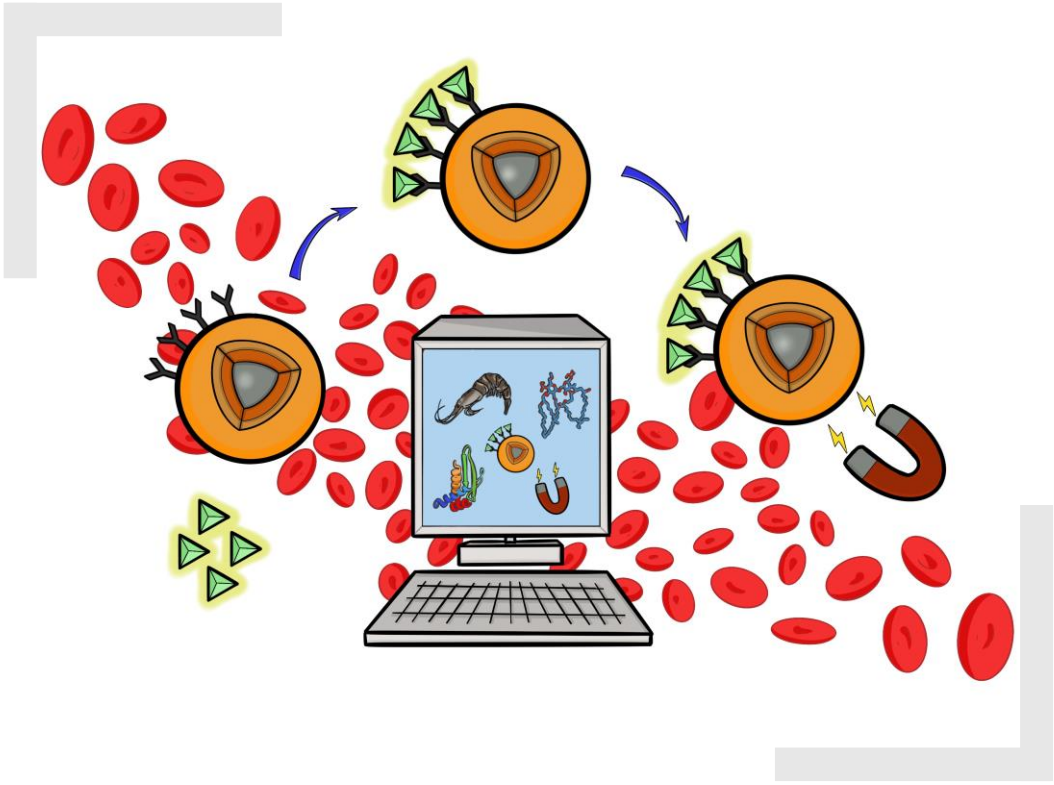

La detoxificación sanguínea extracorpórea empleando microdispositivos magnetoforéticos (MCMDs por sus siglas en inglés) se concibe como una estrategia prometedora para combatir enfermedades infecciosas, alternativa al uso de antibióticos. Los MCMDs, que combinan la microfluídica y las micro- o nanopartículas magnéticas funcionalizadas, permiten captar y eliminar de forma selectiva y eficaz los compuestos tóxicos (el lipopolisacárido, LPS, en este trabajo) de la sangre. La presente tesis doctoral contribuye al diseño asistido por ordenador de MCMDs. De este modo, se ha avanzado en el diseño de moléculas para funcionalizar las partículas magnéticas a través de simulaciones MD, contrastando los resultados de las simulaciones experimentalmente. Asimismo, se ha optimizado la recuperación magnética del complejo LPS-partícula mediante técnicas CFD. En conclusión, el conocimiento y metodologías proporcionados en este trabajo pueden ser claves para avanzar en el diseño de MCMDs para llevar a cabo la captura de endotoxinas de la sangre como parte de tratamientos novedosos para la sepsis.

Extracorporeal blood detoxification using magnetic cleansing microdevices (MCMDs) has been understood as a promising strategy to abate infectious diseases as alternative to the use of antibiotics. MCMDs, which couple microfluidics and functionalized magnetic micro- or nanoparticles, enable the selective and efficient capture and removal of toxic agents (lipopolysaccharide, LPS, in this work) from blood. The present dissertation contributes to the rational computer aided design of MCMDs. Hence, progress in the design of biotargeting agents to functionalize the magnetic beads has been made through MD simulations, validating *in vitro* the *in silico* predictions. Additionally, the magnetic recovery of LPS-bead complexes has been optimized using CFD techniques. Collectively, the insights and methodologies provided in this work might be key for advancing in the design of MCMDs for capturing endotoxins from blood as part of innovative sepsis treatments.

UC UNIVERSIDAD DE CANTABRIA

Escuela de Doctorado